Synthesis, Characterisation and Spectroscopic Studies of Diazine-*N*-oxide Complexes of Iron(II) Towards the Development of Sensors

A thesis submitted in fulfilment of the requirements for the degree of

Master of Science

To

Rhodes University

RHODES UNIVERSITY

By

Unako Bongani Mpiti

Abstract

The characteristic magnetic and spectroscopic features associated with the red monomeric or dimeric, and polymeric pyrazine-*N*-oxide (PyzNO) iron(II) perchlorate complexes; $Fe_n(\mu_{1,1}\text{-pyzNO})_{2n-2}(pyzNO)_{3n+2}(ClO_4)_{2n}$ $(n = \{1, 2\})^*$, and the novel compound $\{Fe(\mu\text{-pyzNO-}\kappa N,\kappa O)_{n-1}(pyzNO\text{-}\kappa N)_2(pyzNO\text{-}\kappa O)_2\}_n(ClO_4)_{2n}$†, respectively, were investigated. These properties are altered substantially when the complexes are hydrated; for instance, by atmospheric exposure. The resulting species; $Fe(pyzNO)_5(H_2O)_3(ClO_4)_2$* and $[Fe(pyzNO\text{-}\kappa N)_4(H_2O)_2](ClO_4)_2{\cdot}2H_2O$†, which have different hues of a bright yellow colour, were found to exhibit strong paramagnetism, in contrast to their anhydrous precursors, which are 'EPR silent'. A low spin → high spin crossover (LS→HS, SCO) transition was therefore proposed to occur as the complexes become hydrated by atmospheric moisture.

The red→yellow colour change is reversible, and dehydration of the yellow species by heating regenerates the red variant, a feature which lends itself to the potential applicability of the system as a sensor. Further emphasis on this potential derives from the fact that the hydration/dehydration process, and its accompanying physical changes, appears reversible even after many such treatments.

It became of interest, then, to determine if these changes were limited to water-exposed samples, or if they occurred under more diverse solvent atmospheres. The reversibility of such exposure on the structure of the novel polynuclear complex was therefore investigated. In general, it was found that there occurred a strong solvent-complex association for the more polar solvents. Red→yellow, LS→HS events were seen when the complex was exposed to the vapours of *p*-dioxane, acetaldehyde and formaldehyde, and to a lesser extent, to that of methanol. In each case, significant structural changes were seen, as evidenced be comparative XRPD and thermo-analytical studies. Some of these changes have however been ascribed to the effects of partial dissolution upon extended exposure of the complex to the associated media.

---

* The complexes $Fe_n(\mu_{1,1}\text{-pyzNO})_{2n-2}(pyzNO)_{3n+2}(ClO_4)_{2n}$ $(n = \{1, 2\})$ and $Fe(pyzNO)_5(H_2O)_3(ClO_4)_2$ will be referred to as Complex1 and Complex5, respectively, in text. The formulas are shown in this way as their structures are not known unambiguously. And it is noted, for Complex1, that such a representation does not inform that the ligand is in two distinct coordination modes. Where n = 1, and n = 2, the structure would condense as $[Fe(\mu\text{-pyzNO-}\kappa N)_3(pyzNO\text{-}\kappa O)_2](ClO_4)_2$ and $[Fe_2(\mu\text{-pyzNO-}\kappa^2 O)_2(pyzNO\text{-}1{:}\kappa^4 N,2{:}\kappa^4 N)_8](ClO_4)_4$, respectively.

† The complexes $\{Fe(\mu\text{-pyzNO-}\kappa N,\kappa O)_{n-1}(pyzNO\text{-}\kappa N)_2(pyzNO\text{-}\kappa O)_2\}_n(ClO_4)_{2n}$ and $[Fe(pyzNO\text{-}\kappa N)_4(H_2O)_2](ClO_4)_2{\cdot}2H_2O$ will be referred to as Complex2 and Complex6. The full formulas will be kept in headings, table titles and figure titles.

Exposure to less polar solvent atmospheres, such as those of cyclohexane, toluene, diethyl ether, etc., showed some signs of mild solvent surface adhesion, but were unaccompanied by discernible magnetic and colour changes.

Another novel complex was produced during attempts to synthesize the PyzNO complexes from a mixture of a 2,2'-dimethoxypropane (DMP) and ethanol (1:1, v/v), rather than the methanol/DMP mixture which had been alternately used. The formula of the resulting complex is $Fe(pyzNO)_6(ClO_4)_2 \cdot 3EtOH$*. This EPR inactive product was orange in colour, and transformed into a bright yellow, strongly paramagnetic species upon atmospheric exposure. Further solvent studies showed that this species interacted significantly with all solvents tested, but generally more strongly with increasing solvent polarity. Orange→yellow colour changes occurred in environments saturated with *p*-dioxane, acetaldehyde and formaldehyde vapours. The DMSO-exposed sample transformed to dark red, due to suspected PyzNO substitution by the solvent.

The red→yellow and orange→yellow colour changes were ascribed to the formal substitution of *O*-coordinated PyzNO (μ-PyzNO in the polymeric complex) by the incoming solvent. The resulting structural and geometric changes stimulated a redistribution of *d* electrons among the new constituent molecular orbitals of altered energy and symmetry. Therefore, although the colour changes were not conventionally solvatochromic - in that the original structure was lost on exposure – data suggested that it was the coordination of species of higher donor strength that produced the observed bathochromic shifts.

A novel 4,4'-bipyridine-*N*-oxide Fe(II) perchlorate complex, $Fe_2(bipyNO)_5(ClO_4)_4 \cdot 6MeOH$†, was also produced, primarily for physicochemical comparison with the PyzNO complexes. No colour or magnetic changes were seen on atmospheric exposure. The original complex was observed to be inherently paramagnetic, and no SCO events occurred upon solvent exposure. Despite this, thermal analyses showed that the complex did exhibit the *strong* uptake of polar solvents in general, but particularly with acetaldehyde. Significant structural changes upon exposure were limited to surface phenomena, with the exception of the acetaldehyde-exposed sample.

---

*,† The structures of $Fe(pyzNO)_6(ClO_4)_2.3EtOH$ and $Fe_2(bipyNO)_5(ClO_4)_4 \cdot 6MeOH$ (Compex3 and Complex4, respectively, in text) are not known unambiguously. Their predicted structures, which are speculated based on the results of indirect methods (as in the case of Complex1 and Complex5), are $[Fe(pyzNO\text{-}\kappa O)_6](ClO_4)_2.3EtOH$ and $[Fe_2(\mu\text{-}bipyNO\text{-}\kappa^2 O)_3(bipyNO\text{-}1{:}\kappa N,2{:}N)_2(MeOH)_4](ClO_4)_4 \cdot 2MeOH$.

Acknowledgements

My sincerest thanks are conveyed to the following:

- Prof G.M. Watkins, for his guidance and supervision through the course of this study.
- Prof Z.R. Tshentu and Dr A.S. Ogunlaja, Chemistry Department, Nelson Mandela Metropolitan University, for their immense and invaluable contributions towards sculpting this thesis in its structural aspects, and in terms of the related chemistry.
- Prof R. Krause, Chemistry Department, Rhodes University, for providing his editorial expertise, as well as for his substantial financial and administrative support.
- Mr Francis Chindeka, Chemistry Department, Rhodes University, for obtaining the microanalytical data.
- Dr Jonathan Britton, Nanotechnology Innovation Centre, Rhodes University, for his assistance in obtaining the XRPD patterns.
- Dr Usmani Imran, Nanotechnology Innovation Centre, Rhodes University, for his help with deconvolution software.
- Dr Eric Hosten, Chemistry Department, Nelson Mandela Metropolitan University, for his assistance is obtaining single crystal diffraction data.
- Dr John Mack, Nanotechnology Innovation Centre, Rhodes University, for his assistance in conducting the EPR analyses.
- Ms Shirley Pinchuck, Electron Microscopy Unit, Rhodes University, for her assistance in obtaining the SEM micrographs of the complexes.
- Mr André Adriaan and Mr Rubin Douglas, Chemistry Department, Rhodes University, for the glass-blowing of specialist glassware and the construction and assembly of the N_2-line for Schlenk-type syntheses.
- Lab-mates: Wesley Feldmann, Siyabonga Hulushe, Ivan Hodgson, Bukonola Oguntade, Magaji Ilu-Barde, Vitalis Tshiza and Tafadzwa Murinzi for their aid and motivation.
- Nomvula Mpiti, Siphokuhle Mpiti and Sakhono Mpiti, for their constant and consistent support and encouragement throughout the course of my studies.

- Simon Lipworth, Lauren Hawkins, David Taylor, Bantubonke Ntsaluba and Shannon Chetty, for being the very best friends that one could ask for.
- Rhodes University and the Department of Chemistry, for providing a ‘home away from home’ for the past 7 years.
- Sasol, for the funding of my Masters studies.

Contents

List of Figures

List of Schemes

List of Tables

Abbreviations & Definitions

Bipy	=	4,4'-Bipyridine (dipyridyl)
BipyNO	=	4,4'-Bipyridine-*N*-oxide (dipyridyl-*N*-oxide)
$BipyNO_2$	=	4,4'-Bipyridine-*N*,*N*'-dioxide
DMP	=	2,2'-Dimethoxypropane
EtOH	=	Ethanol
MeOH	=	Methanol
MepyzNO	=	Methylpyrazine-*N*,*N'*-dioxide
Pyz	=	Pyrazine
PyzNO	=	Pyrazine-*N*-oxide
$PyzNO_2$	=	Pyrazine-*N*, *N´*-dioxide
2-MepyzNO	=	2-Methylpyrazine-*N*-oxide
3-MepyzNO	=	3-Methylpyrazine-*N*-oxide

ν	=	Stretch
α	=	Inplane bend (of heterocyclic ligand)
γ	=	Out-of-plane bend (of heterocyclic ligand)
δ	=	Inplane bend
π	=	Out-of-plane bend
τ	=	Twist
ω	=	Wag
ρ	=	Rock

BE	=	Binding Energy
DSC	=	Differential Scanning Calorimetry
LIESST	=	Light-Induced Excited Spin State Trapping
SCO	=	Spin Crossover
TGA	=	Thermal Gravimetric Analysis
TG-FTIR	=	Thermogravimetry-Fourier Transform Infrared
T_{sc}	=	Spin Crossover Temperature
$T_{1/2}$	=	Temperature at which 50 % of SCO active nuclei are Low Spin configured, whilst the remaining 50 % are in their High Spin state

---

Note: While the word '*sub-endotherm*' is neither official, nor conventionally used, it will appear with some frequency in this text, and refers to one of several unresolved or overlapping endotherms on a DSC thermogram.

Chapter 1

Introduction

1.1 The Spin Crossover Effect

1.1.1 Background and a Few Postulated Mechanisms

One of the momentous triumphs of crystal field theory was its success in describing the magnetic properties of coordination complexes [1]. The description was established upon the notion that there exists a competition in the coordination sphere between paired and unpaired sets of electrons to occupy the available energy levels (or orbitals) whose initial degeneracy was lifted by the application of a geometrical crystal field [1, 2]. The event was termed the splitting of the d-orbitals in a crystal field (*d-d* splitting). It was postulated that in circumstances wherein the energy associated with this splitting was much higher than the inter-electronic repulsion energy of the d electrons, a spin paired electron configuration would be preferred for a stable ground state of the resulting complex [1, 3-5]. And where the d-d splitting was comparatively smaller than the inter-electronic repulsion, a spin free configuration would predominate [3-5]. These 'spin-states' would come to be known, respectively, as the low spin (LS) and high spin (HS) electron configurations [1].

It was then realised that there existed a few compounds whose crystal field splitting energy was approximately intermediate between those associated with HS and LS complexes, such that the simultaneous population of both spin states within certain well defined temperature ranges occurred. This class of complexes was given the name 'spin crossover (SCO) compounds'.

SCO compounds are described as a subset in a variety of functional molecular materials whose properties include at least two labile electron configurations such that they can reversibly adopt either one on application of appropriate external stimuli [1, 4-6]. The phenomenon occurs in some metal complexes wherein the spin state of the complex changes due to external stimuli such as a variation of temperature, pressure, light irradiation or the influence of a magnetic field [1-6]. Hence, the LS state could be converted to the HS state by

applying heat to the material. Moreover, adsorption, phase transition and ligand substitution (ligand field strength fluctuations) may induce such electron configuration changes [7].

The use of heat to convert the LS to the HS state is referred to as thermally-induced SCO, and was seen to occur only in instances where the ground state configuration was LS [1]. This necessity arises from the higher degeneracy of the HS state in comparison with its low spin counterpart, to the extent that the LS to HS transition has a positive entropy [1]. This transition can only occur when the HS energy (E_{HS}) is higher than the LS energy (E_{LS}) which only occurs at positive absolute temperatures. Fig. 1.1 shows a gradual temperature-driven SCO process, the completion of which spans some 250 ^{o}C.

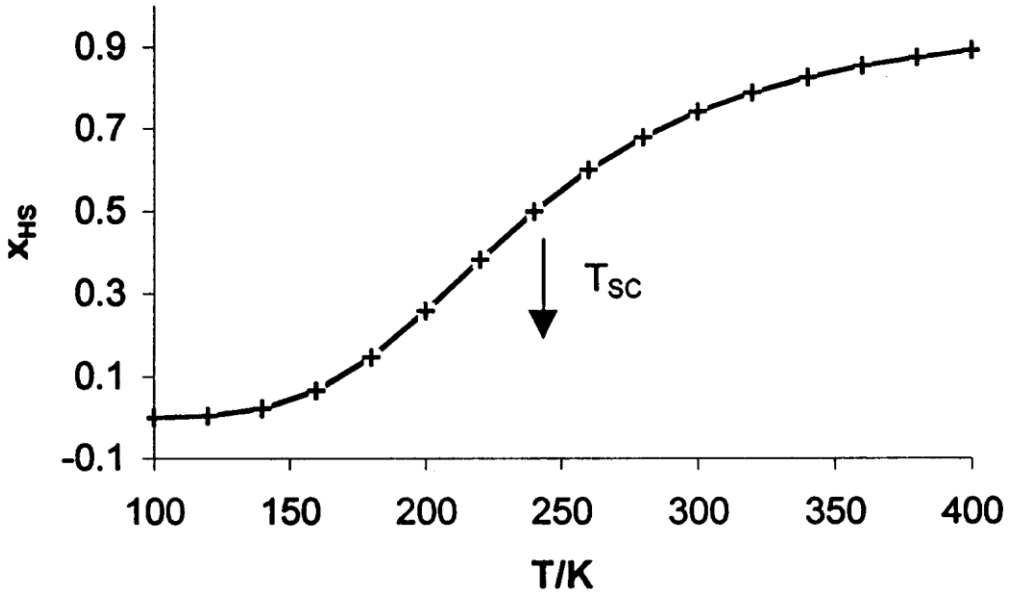

Figure 1.1: Simulated SCO depicting a hypothetical LS→HS transition (Spin crossover temperature (T_{sc}) = 240 K, enthalpy change on SCO (ΔH_{sc}) ≈ 10.5 J.mol^{-1}) (reproduced from Linert and Kudryavtsev [1]).

Consequently, it was found that species in their HS configuration could not be converted to their LS state by heating even when the excited LS state was observed to be stable at a measurably higher *kT* than the HS form [1, 3, 8-10]. This form of SCO was only observed when non-thermal strategies were employed towards that end. One example of such a strategy is the excitation of the HS species by irradiation with an appropriate wavelength of light, followed by subsequent non-radiative relaxation into the LS state. The LS to HS transition was found to also be responsive to light stimulation, and when performed at sufficiently high temperature could produce a metastable HS with substantial longevity [4, 5, 9-11]. This

phenomenon was termed the light-induced excited spin state trapping effect (LIESST) [1], and will be elaborated upon briefly in section 1.4. Figure 1.2 shows two hypothetical potential energy wells associated with the LS and HS ions between which a temperature-dependent/light induced SCO transition may occur [1]. The two spin states are shown in equilibrium, and only the lowest vibrational energy level is depicted for simplicity.

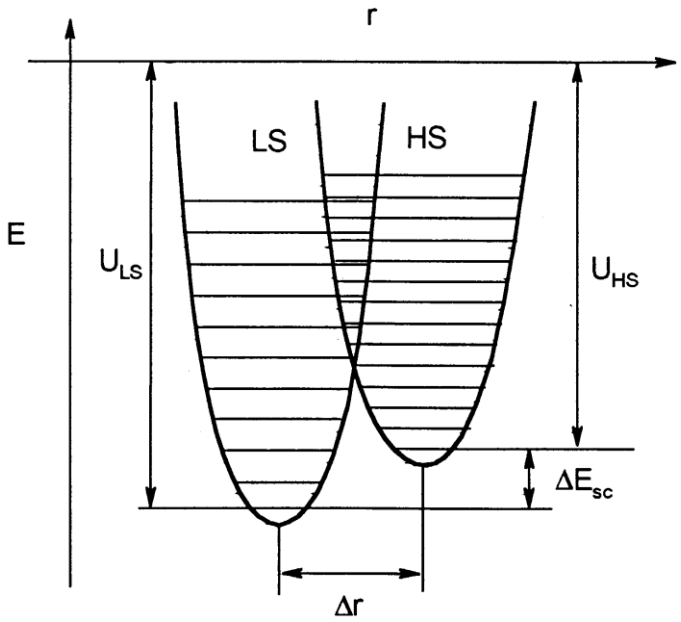

Figure 1.2: Potential energy wells of LS and HS spin states in SCO equilibrium showing only the ground state vibrational energy levels (reproduced from Linert and Kudryavtsev [1]).

The first spin crossover (SCO) compounds based on iron(II) were reported some 5 decades ago around the early 1960's [7]. Since then, extensive research has been invested in terms of the elucidation of the SCO mechanism, as well as the development of novel such compounds for technological utilization [7].

SCO materials are known for their vast application, or applicability, resulting from the exploitation of their switching properties [6]. Their application spans a myriad technological genres, wherein the development and fine-tuning of their memory transduction potential and switching properties have been the objectives of much rigorous research. Their technological and scientific significance for high performance devices includes their employment as molecular switches, for information storage, display devices, and, in context of this work, as chemical sensors of the host-guest type [12-14].

According to Gaspar *et al.* [11], the substantial majority of described SCO materials comprise Fe(II) and Fe(III) complexes, and to a significantly lesser extent, Co(II) coordination compounds. Noteworthy also is the applicability, in a few cases, of some Mn(III) and Cr(II) compounds [12].

The great advantage the molecule-based bistability of SCO compounds is its diversity with respect to the aforementioned stimuli that confer to the bulk material a variety of observable manifestations that stem, ultimately, from transformations of the electronic and geometrical states of individual molecules [12]. That is, these microscopic modifications to these materials, as well as the macroscopic changes to which they give rise, occur under variable imposed conditions. And a readily measurable change in attributes such as magnetism, dielectric and optical properties, colour and structure is characteristic of the aforementioned HS to LS (or LS to HS) transition [1-12].

At the most fundamental level, in terms of the underlying physical chemistry, the SCO phenomenon is equated to an 'intra-ionic electronic transfer' involving the e_g and t_{2g} *d*-orbitals of associated (octahedral) nuclei, accompanied by a molecular structural reorganization [12, 14, 15].

It has been suggested that the SCO event in condensed phases does not assume the form of a typical Boltzmann-type equilibrium between the two spin states, or spin energy levels [14]. Rather, it is said to be an entropically driven phenomenon at a temperature where the higher vibrational and configurational entropy of the high spin state ultimately overcomes (or overwhelms) the otherwise more favourable higher enthalpy of the strong M-L bonds characteristic of the low spin form [14, 15]. For example, both axial and planar Fe-ligand bond lengths can be reduced by as much as 0.10-0.20 Å on transition from the HS to the LS state [12]. This occurs because the inter-electronic repulsion associated with M-L molecular orbitals (e_g* hybrid orbital) is significantly greater in the former case due the doubly occupied nature of the e_g set (d_z^2, $d_{x^2-y^2}$). The change may then be reflected not only where spectral (*d-d* and charge transfers bands, etc) and magnetic features are concerned, but can be observed in X-ray diffraction patterns [16] and Infrared data, etc. Fig. 1.3 shows how pronounced these changes in M-L bond lengths due to HS↔LS transitions can be [16].

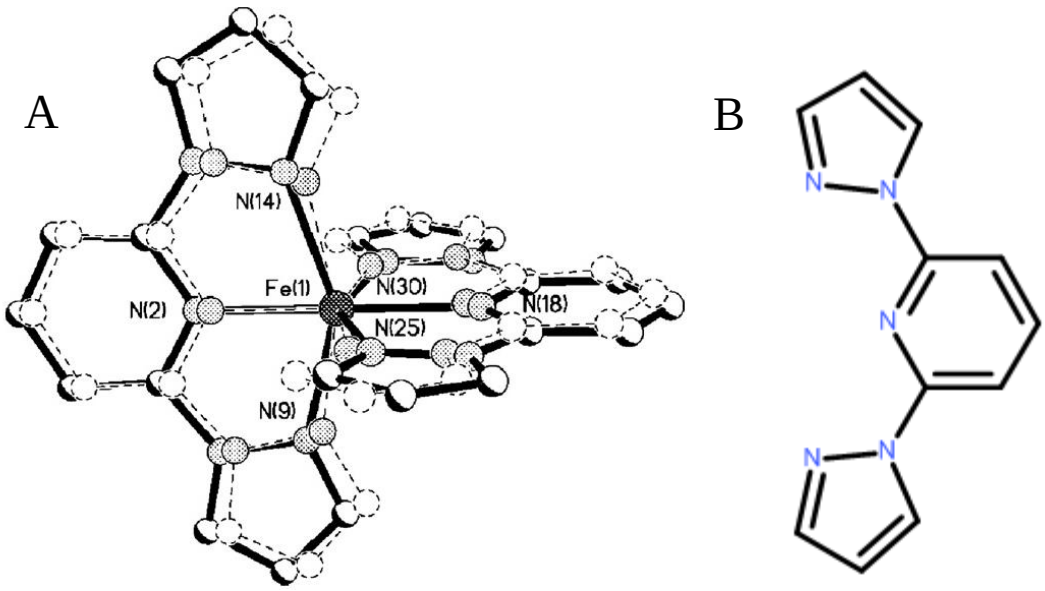

Figure 1.3: Ball and stick model of $[Fe(L)_2](BF_4)_2$ (A) (Counterion omitted; L = 2,6-bis(pyrazol-1-yl)pyridine), showing the variation in Fe-*N* bond lengths on the LS (dotted lines) ↔ HS (solid lines) transition. The structure of the ligand (L) alone is shown for clarity (B) (adapted from Olguin and Brooker [16]).

It becomes clear then that the coordination of a ligand that offers greater enthalpy to the system, in terms of the strength of the generated M-L bond may tip the sliding scale in the reverse direction in accordance with the above described analysis [12]. The change in the crystal field stabilization energy associated with the LS to HS transition may be sufficient to induce such a transition, accompanied by the reduced overall inter-electronic repulsion in the coordination sphere. It can be seen then that it becomes a considerable challenge to tune the system to undergo the desired spin transition under given circumstances. Olguin and Brooker [16] reviewed several reported structures in which various structural analogues of 'L' in Fig. 1.3 above were employed in order to produce a series of SCO-active Fe(II) complexes. The resulting complexes were found to exhibit substantially varied electronic characteristics, particularly with respect to the SCO event; even with relatively little ligand structural change.

Four examples of the ligands evaluated are shown in Fig. 1.4, accompanied by a table of associated '-R' group structures. In each case, the position of T_{sc} and $T_{1/2}$ were found to vary significantly with each sequential alteration of the ligand. Additionally, the changes were accompanied by changes in the geometric dimensions of the associated unit cell. XRD data revealed marked variations within each complex, in the Fe-*N* bond lengths and angles of their

respective LS/HS variants; and in some cases, significant structural changes due to the SCO event itself. The latter changes were in accordance with the theme described above in terms of LS↔HS induced effects in M-L bond lengths [16].

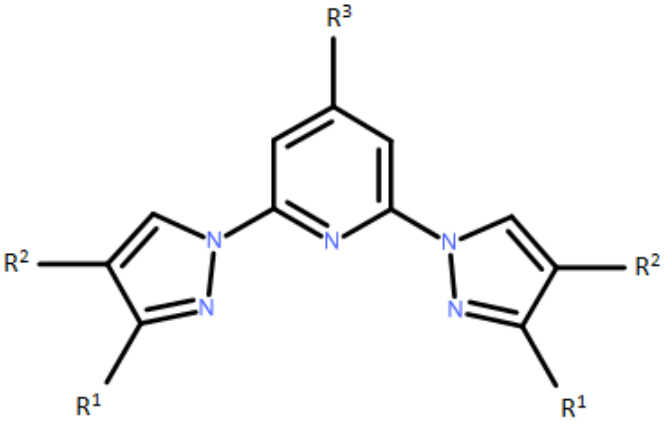

Ligand Designation	'R' group substituents		
	R^1	R^2	R^3
L^2	-H	-H	$-CH_2OH$
L^3	-H	$-CH_3$	H
L^4	-H	Cl	H

Figure 1.4: Examples of some variations to the 'L' ligand towards the design of SCO-active Fe(II) complexes isostructural to $[Fe(L)_2](X)_2$ (L = 2,6-bis(pyrazol-1-yl)pyridine; X = ClO_4^- or BF_4^-) (adapted from Olguin and Brooker [16]).

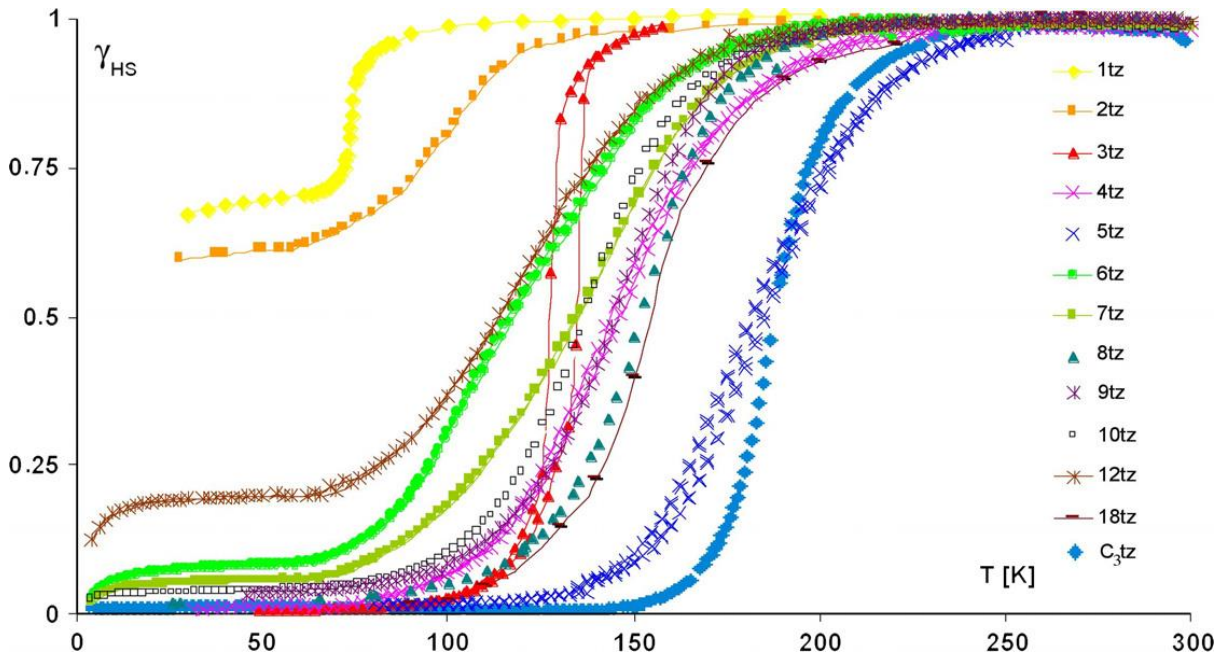

Figure 1.5: HS/LS ratio as a function of temperature of $[Fe(C_3tz)_6](BF_4)_2$, compared to *n*-alkyl substituted $[Fe(nC_3tz)_6](BF_4)_2$ (*n* = the number of carbon atoms in the alkyl substituents) (reproduced from Gaspar *et al.*. [11]).

As shown above (Fig. 1.5), it is clear that even relatively unpronounced changes in ligand structure can produce marked alterations in the temperature-related electronic properties,

especially in terms of T_{sc} and $T_{1/2}$. To that extent, SCO may occur extremely gradually, or be altogether suppressed in one species relative to an isostructural analogue. In terms of the latter situation, the HS configuration is found to be maintained independently of the imposed ambient temperature.

1.1.2 The Cooperativity of the Spin Crossover Effect

As aforementioned, it is known that many of these described changes may occur cooperatively [12]. That is, they are not necessarily confined to individual nuclei (in discrete mononuclear *and* polymeric arrangements) but can effect changes to the bulk material. A stimulus can be thought of as being generated by the structural changes mediated by SCO in a localised nucleus, and these are sequentially or exponentially propagated to neighbouring nuclei by interactions collectively referred to as cooperative effects, in a process analogous to dominos [17]. This cooperativity has been ascribed primarily to hydrogen bonding patterns, π-π interactions, and in the case of polymers, to the electronic effects associated with covalent bonding between active SCO Fe(II) centres [12, 13]. The advantages of cooperativity then become immediately apparent in that it not only confers additional stability to the adopted spin states of the bistable Fe(II) centres, but can positively influence the functionality of SCO materials [17]. That is, SCO events are no longer confined molecular-scale occurrences, and as such, give rise to increased sensitivity to subtle changes in the magnitude of the previously mentioned external stimuli [12].

The applicability of these systems, both current and potential, where data processing, sensors, and display devices are concerned, is said to be driven by the elastic nature of the aforementioned cooperative effects [18].

Figure 1.6 (A) shows the crystal packing diagram of $[Fe(C_3tz)_6](BF_4)_2$ [12], a monomeric complex; showing the potential through-space electronic interaction of proximal ligand groups, that facilitate or enhance SCO cooperativity effects. Fig. 1.6 (B) shows the molecular packing of $[Fe(qnal\text{-}12)_2].2C_6H_6$ [17], highlighting the π-π stacking *via* which SCO cooperativity effects

are mediated in that particular system. In both cases, LS↔HS transitions are transmitted between proximal nuclei despite the lack of covalent linkages connecting them.

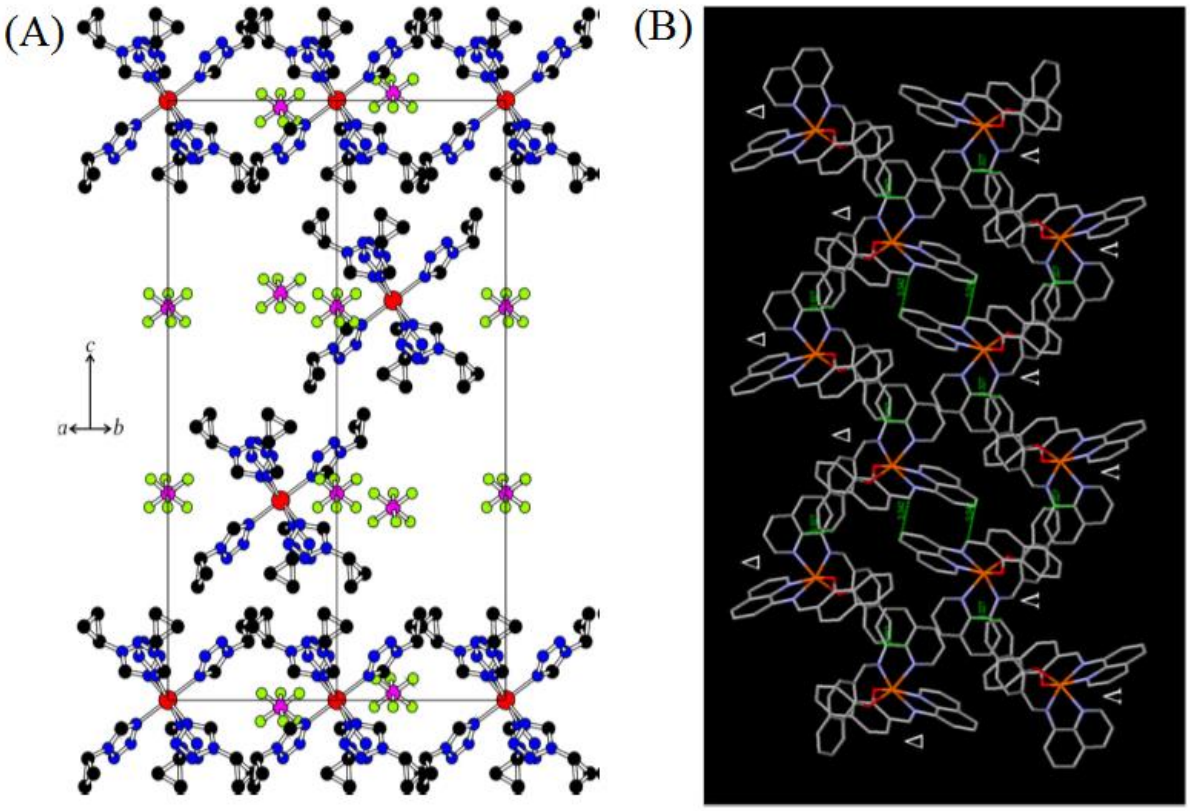

Figure 1.6: Packing diagrams of $[Fe(C_3tz)_6](PF_6)_2$ (A) (viewed along the (110) direction, omitting H atoms), and $[Fe(qnal\text{-}12)_2].2C_6H_6$ (B), (viewed from the *a* direction, omitting solvate C_6H_6 moieties) (adapted from Soliman *et al.* [6], and Kuroda-Sowa *et al.* [17], respectively).

1.1.3 Spin Crossover Hysteresis

It has been reported that the substantial difference in the bond lengths associated with the two spin states may give rise to thermal and light induced hysteresis [16, 18]. Hysteresis is the process whereby the state of a system may be influenced by an environment wherein the system was at a past time. That is, the system may be said to be dependent not only on its current environment, but on one within which the system was held in the past [18]. In this context, then, the systemic configurations associated with the complexes, characterised by certain physical attributes, can be re-attained in the future if they are subjected to identical

stimuli. In simple terms, the environment may convey a memory effect to the materials under consideration [18].

The above described hysteresis need not necessarily be confined to photo- or thermally induced SCO, and, in general, can theoretically be extended to the general spectrum of stimuli capable of inducing reversible SCO.

The potential SCO under investigation in this work is mediated by exposure to certain solvents, and reversed by their subsequent removal. Therefore, even minute changes in the quantities thereof could theoretically be detected, were the systems to be appropriately fine-tuned to be responsive to such subtle variations in stimulus levels.

As aforementioned, the spin crossover (SCO) mechanism of iron(II) complexes is extensively described in the literature [1-18], and is typified by a characteristic colour change. However, it is often characterised by the less than ideal spectral shift of red (LS) to orange (HS) in pyrazine-*N*-oxide (pyzNO) iron(II) complexes $\{Fe(pyzNO)_3(ClO_4)_2 + H_2O \rightarrow (Fe(pyzNO)_3(OH_2)(ClO_4)_2\}$ [19]. To a substantially lesser extent, there are cases wherein a red to yellow colour change has been observed [20]. The latter is of particular interest in this case as the associated species are more readily distinguishable. And so, since the system could potentially be employed in sensor applications, particularly of the host-guest type, the most readily discernible change in a given property on exposure to a stimulus (guest molecule) is desirable. Such a change should ideally occur under mild conditions (viz. room temperature and pressure) in order that the energy to generate a required spin configuration be minimized [13]. As such, the reversal of SCO events would warrant the expenditure of relatively low energies.

1.1.4 The Light-induced Excited Spin State Trapping (LIESST) and Reverse-LIESST Effects.

The induction of the HS – LS spin state transition by a variation in temperature, pressure, or light irradiation has already remarked upon, and has become the quintessential feature of Fe(II) spin cross-over compounds [21]. Decurtins and co-workers were the first to report the

susceptibility of some Fe(II) spin cross-over compounds to the photomagnetic effect [22]. They were able to successfully convert $[Fe(ptz)_6](BF_4)_2$ (ptz = 1-propyltetrazole) from its stable LS state ($^1A_1$ or t_{2g}^6) to its metastable HS state ($^5T_2$ or $t_{2g}^4e_g^2$) at -263.15 ^oC using irradiation of the sample with green light. The mechanism by which they were able to achieve this is now referred to as the light-induced excited spin state trapping effect or, simply, LIESST. The reverse-LIESST effect was subsequently reported by Hauser independently, wherein the conversion of $[Fe(ptz)_6](BF_4)_2$ back to the LS state was achieved by irradiation of the compound with red light [23].

The potential utility then of the induction of reversible spin cross-over simply by employing a different (complementary) wavelength of light at temperatures below $T_{1/2}$ or T_c [24] of the associated initial spin state, becomes apparent. Among others, the potential utilization of such materials as optical switches and for magneto-optical storage has been the subject of much investigation [24]. Above $T_{1/2}$ (referred to as the critical LIESST temperature or T_c by Létard *et al.* [24]) there is sufficient thermal energy available in the system, such that the energy barrier between the two spin states can be readily overcome, and relaxation to the lower energy LS state rapidly occurs after the radiation source has been removed. At those temperatures and above, LIESST cannot be achieved. Hauser then, using optical spectroscopy, found a very strong correlation between the lifetime of the LIESST (HS) state and the thermal spin-crossover temperature ($T_{1/2}$) [25]. He found, based on the non-adiabatic multiphonon theory proposed by Buhks *et al.* [26], that the essential components of his relaxation model were the energy difference (termed ΔE^o_{HL}) between the lowest vibrational energy levels of the HS and LS states, and the change in M-L bond length accompanying the spin state transition (termed Δr_{HL}), or, more specifically, the relative Cartesian displacements of the HS and LS potential energy wells [24]. Hauser showed the inverse proportionality of the logarithm of the LIESST lifetime with $T_{1/2}$, a phenomenon that is now referred to as the inverse-energy-gap law [25].

The drawback in this regard, however, is that the full characterisation of such, and analogous systems, requires a complete kinetic evaluation of the temperature independent tunnelling-induced relaxation region up to the thermally activated region [25]. And this is

perhaps the largest contributor to the fact that only a limited number of compounds exhibiting the LIESST effect have thus far been fully described [24, 25].

1.1.5 Design of Novel Spin Crossover Compounds

Research into this field has afforded a continued fine-tuning and refinement of the understanding underlying the SCO mechanism in myriad diverse systems. And having developed techniques by which the process of spin transitions could be controlled, particularly in solid (crystalline) materials, concerted efforts have been invested towards the design of novel SCO compounds in recent times. This is been inspired principally by the potential practical applicability of these materials. The major aim has been to synergistically combine the spin transition behaviour inherent to SCO materials under appropriate conditions with other physical and chemical properties [27]. A few examples among these latter features may include magnetic exchange, non-linear optics, liquid-crystal properties, ligand isomerisation, and perhaps particularly relevant in the context of this work; host-guest chemistry [12].

The ‘molecular character’ of the spin crossover event in many compounds is the sight for potential exploitation, and may be used for the reversible storage of information at the molecular level, by methodically varying the ambient pressure and/or pressure, or by exposure of either the LS or HS states to an appropriate wavelength of light in order to stimulate the associated spin transition [27]. According to Atmani *et al.* [27], the SCO phenomenon presents substantially higher transition temperatures, as ‘single molecule magnets (SMM)’, relative to competing proposed systems for molecular level memory storage. As such, the design and fabrication of novel materials that exhibit SCO has indisputable relevance and provides one of the most exciting areas in current coordination chemistry, and in particular the field of magnetic molecular materials.

As has been briefly elaborated upon above in terms of these ‘electronic switching materials’, when the ligand field strength approaches the thermal spin transition energy, the magnetic state of the associated molecular SCO centres can be tuned towards preference of

either of the spin states (LS/HS) by the application of an appropriate external stimulus [28, 29]. This includes the lattice adsorption of amenable guest molecules.

Tuning can be extended in general to d^n (where n= 4 - 7) transition metal complexes, of which the most extensively investigated is the d^6 configured Fe(II) ion; for which the paramagnetic-diamagnetic, LS (S=0) to HS (S=2) transition is typically seen. Of these, complexes with the form FeN_6 have undergone the most comprehensive scrutiny because the coordination environment generated by 6 bonded nitrogen atoms has an associated ligand field that is close to the thermal spin transition energy [27].

There are various mechanisms to which the SCO phenomenon is thought to be collectively attributable; among which are π-π stacking, π-delocalisation, hydrogen bonding, Van der Waals interactions, and so on. These have been extensively investigated, as well as some features characteristic of SCO; such as cooperativity, T_c (LIESST) [24] and $T_{1/2}$. However, new synthetic strategies towards the design and development of novel such compounds have been comparatively scarcely reported [27].

1.1.6 Analogous Literature Reported SCO Structures

Atmani *et al.* [27] provided a comprehensive review in which they presented new SCO compounds of the FeN_6 form using different polynitrile ligands to tune the SCO transition temperature to values above room temperature.

They showed the use of neutral SCO complexes of the type $[Fe(abpt)_2X_2]$, where X was a variable series of coordinated polynitrile ligands (abpt = 4-amino-3,5-bis(pyridin-2-yl)-1,2,4-triazole). They reported a significant variation in the SCO transition temperature on the variation of group X in terms of structure and/or charge. More importantly in the context of this current work, however, they report the novel SCO chain compound formulated $[Fe(abpt)_2(tcpd)]_n$ ($tcpd^{2-}$ = 2 dicyanomethylene-1,1,3,3-tetracyanopropanediide); which exhibits the same colour changes (red to yellow) on the LS→HS transition, as the pyrazine-*N*-oxide complexes synthesised here. They were able to exploit the potential bridging ability of the polynitrile ligand $tcpd^{2-}$ (analogous to the PyzNO ligand used in this work), instead of using

terminal axial polynitrile ligands as they had previously done, in order to build a polynuclear material (analogous to the $\{Fe(\mu\text{-pyzNO-}\kappa N,\kappa O)_{n-1}(pyzNO\text{-}\kappa N)_2(pyzNO\text{-}\kappa O)_2\}_n(ClO_4)_{2n}$ complex (Complex2) reported in this work) that exhibits the SCO phenomenon. They found that each $tcpd^{2-}$ ligand was shared by two Fe(II) centres such that a polymeric structure of the form $[Fe(abpt)_2(tcpd)]_n$ was ultimately the result [27]. The structure of this complex is shown in Fig. 1.7.

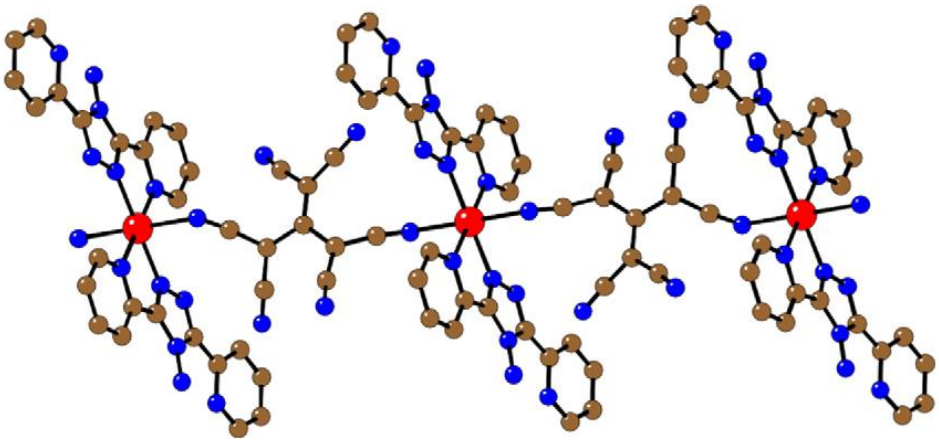

1.7: Chain structure of the SCO compound $[Fe(abpt)2(tcpd)]_n$. The bridging ligand is disordered, and is thus placed in one of its two statistically possible orientations. Colour code: red = Fe(II), brown = C, blue = N (reproduced from Atmani *et al.* [27]).

As Figure 1.8 shows, the complex fully maintained the HS configuration at room temperature (yellow), and the average Fe-*N* bond length was 2.159(2) Å; well within the normal range for HS configured FeN_6 complexes [30]. Lowering of the temperature to 10 K by flash cooling lead to a 50% conversion of SCO centres of the LS state (now red), with a corresponding average bond length of 2.065 Å. Irradiation of the sample with 534 nm light at 10 K recovered the RT bond length values (2.156(3) Å) and the yellow colour was likewise regenerated, indicating that LIESST was in effect. After relaxation, the bond lengths were reduced to 2.018(3) Å, which showed that 25% of the SCO centres had remained HS configured at low temperature [27].

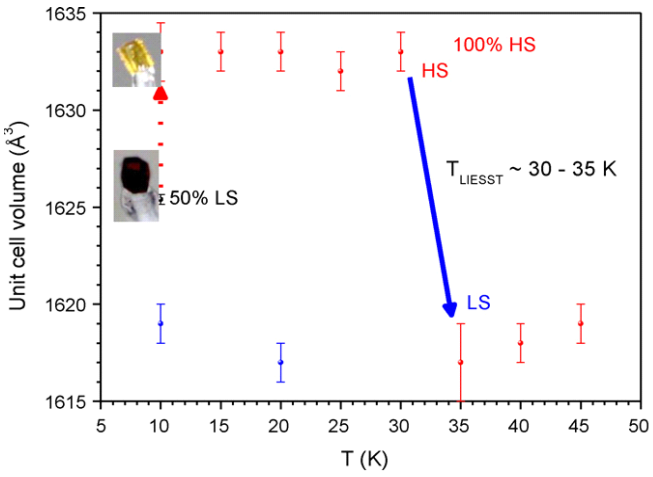

Figure 1.8: Evolution of the unit cell volume of $[Fe(abpt)_2(tcpd)]_n$ under irradiation at 534 nm (red points) and after relaxation (irradiation off, blue points) (reproduced from Atmani *et al.* [27]).

In the case of our current study, all of the aforementioned changes occur above room temperature, and are as yet proposed to be mediated principally by exposure to certain solvents (future LIESST studies would need to be conducted). The LS state is produced first as it is the preferred spin configuration of complex's original structure. The stimulus, solvent exposure then, and the accompanying solvation processes that follows, stimulate the structural and/or electronic reconfiguration of the coordination sphere that induces the spin transition to the HS state. Removal of the stimulus, by volatilisation of the solvent by heating or pressure reduction, or its chemical removal, regenerates the LS state [28, 29].

Other structures that were of interest are tabulated in table 1.1, including some noteworthy properties thereof. Particularly interesting is the apparent correlation between the number of close π-π contacts with the resulting SCO behaviour. No SCO was seen to occur when there were less than three close π-π contacts between proximal nuclei (in the unit cell) [27].

Table 1.1: Neutral SCO *active* complexes of the general formula $[Fe(abpt)_2X_2]$ (abpt = 4-amino-3,5-bis(pyridin-2-yl)-1,2,4-triazole). Shown are π-π overlap modes and some SCO parameters (SCO type and $T_{1/2}$)

Compound	Phase	X*	π-π overlap mode	Number of close π-π contacts	SCO type	$T_{1/2}$ (K)	Ref.
$[Fe(abpt)_2X_2]$	A	NCS^-	Frontal	>5	Gradual	180	[30]
,,	B	$NCSe^-$	Sideways	<3	None (HS)	-	[31, 32]
,,	B(Fe1)	$N(CN)_2^-$	Frontal	>5	Incomplete	86	[33, 34]
,,	A	$tcnq^-$	Frontal	>5	Gradual	280	[35, 36]
,,	A	$C(CN)_3^-$	Frontal	>5	Gradual	336	[37]
,,	A	$tcnome^-$	Sideways	<3	None (HS)	-	[37]
,,	B	$tcnoet^-$	Frontal	>5	Gradual	383	[37]
,,	A	$tcnopr^-$	Frontal	>5	Incomplete	>400	[27]
,,	A	$tcnoEtOH^-$	Frontal	>5	Incomplete	>400	[27]
,,	A	$tcnopr3OH^-$	Frontal	>5	Gradual	360	[27]

*Some of the ligands, whose structures may be unclear based on their abbreviations, are shown in Fig. 1.9. Only four ligands are shown as the other two are simple derivatives of those shown

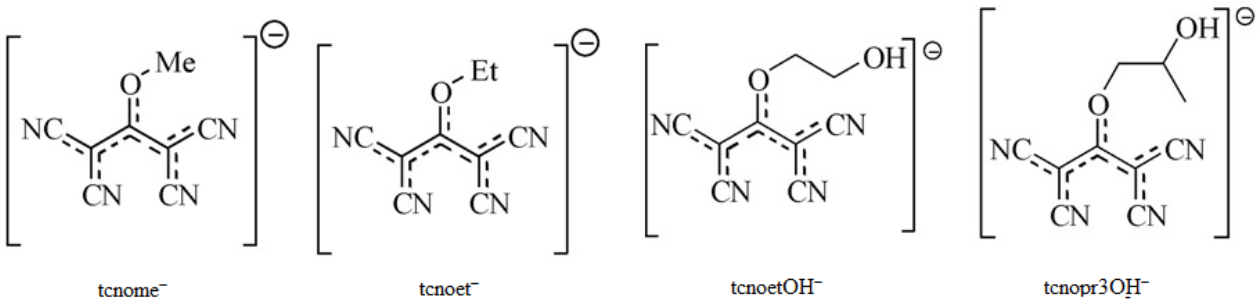

Figure 1.9: Examples of some polynitrile ligands, as per the complexes tabulated in table 1, whose structure may be uncertain based on their abbreviations (reproduced from Atmani *et al.* [27]).

1.1.7 Some Potentially Problematic Features

It has been reported that, in the solid state, SCO materials can be tuned such that their SCO mechanism is responsive to a number of extrinsic stimuli [38, 39]. The spin transition can be influenced markedly by a number of these, among which are; the presence and nature of

counter ions, the degree of hydration (or, in general, solvation) as well as its variation, trace paramagnetic contaminants of which Fe(III) is known to be the most significant [40], and the synthesis strategy employed (e.g. whether or not acidic or ionisable groups are protonated, even if their associated heteroatoms are not directly involved in coordination, such as imidazole hydrogen sites, and so on) [38]. Many of these become significant in the interpretation of data such as that obtained from infrared, EPR and NMR spectra, as unanticipated SCO events may lead to seemingly anomalous results [39-42].

1.2 Solvatochromism

1.2.1 General Mechanism by which Solvatochromism occurs

The phenomenon of solvatochromism is one that continues to inspire a great deal of interest as a consequence of both attempts to understand the physical chemistry of solvation [43, 44], and the relentless efforts towards deriving solvent parameters that can be generally applied [44-48] . Solvatochromism occurs when the energy of the electronic transitions of a compound; and hence the associated excitation wavelength, depend on the solvent employed for dissolution [45]. There are in general two types; positive and negative solvatochromism [44]. The former is said to have occurred if the electronic transition under consideration undergoes a bathochromic shift when the solute of interest is exposed to a particular solvent. That is, a diminished energy gap between the transition-associated energy levels (orbitals), results from solvent exposure, such that the corresponding excitational photons assume longer wavelengths [44]. In contrast, the opposite occurs in negative solvatochromism.

There are a variety of mechanisms by which this phenomenon occurs, and these in general will differ depending on the particular case under consideration. For instance, in the investigation of some carbonyl tungsten organometallic complexes by Kaim *et al.* [44], in which they were primarily concerned with the associated metal-to-ligand charge transfer (MLCT) transitions of the compounds produced in that work, they detailed instances in which both forms of spectral shifting occurred. They were able to rationalise both negative and positive solvatochromism in terms of the following description.

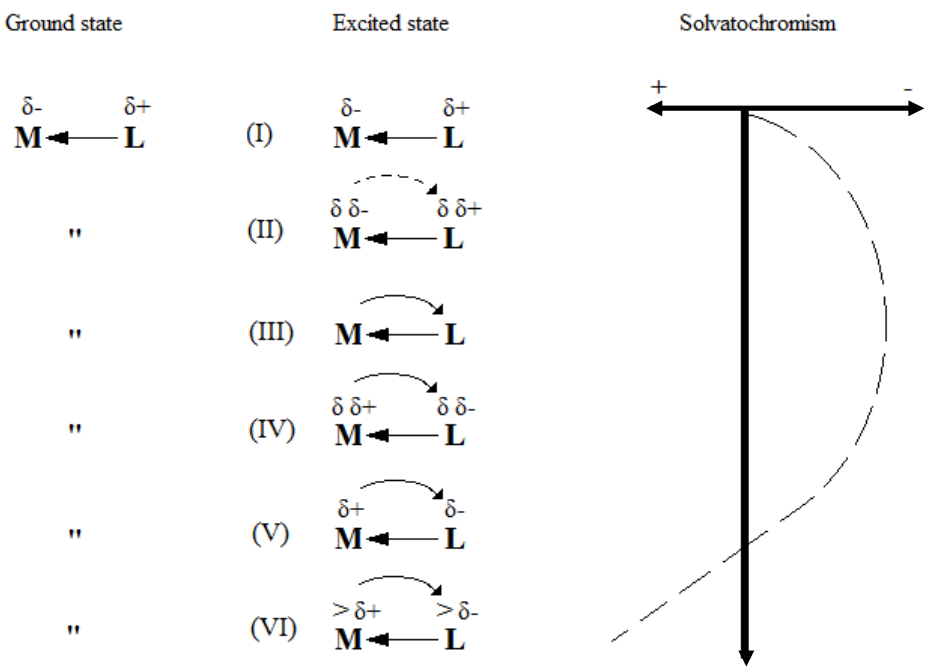

Figure 1.10: Effect of increasing metal-to-ligand charge transfer in the excited state on the metal–ligand bond polarization (or polarizability) with that of the ground state assumed to be constant. The sign and magnitude of solvatochromism is dependent on the difference in the polarizability of the metal-ligand bond between the ground and excited states (adapted from Kaim *et al.* [44]).

Figure 1.10 shows how the MLCT can affect the metal-ligand (M-L) bond polarisation in a complex of the general form ML_n. Although this simplified description, strictly speaking, deals with a diatomic ML complex, the rationale can be extended with reasonable success to more complex systems, of which the vast majority of coordination compounds will tend to be [44].

The scheme depicts the inherent polarity of the M-L bond due the nature of the dative covalent bond and the manner in which it is formed. Since the shared electron pair originates from the ligand (has predominant ligand character), the ligand will be partially electron deficient. With the metal centre being comparatively electron rich, the resulting bond has a definite dipole moment. MLCT transitions will transiently replenish the ligand electron density, thereby reducing the M-L bond polarity in the excited state. This correlation is seen in (II) of Fig. 1.10. In this case, polar solvents will stabilize the ground state energy level to a greater extent than the excited state. As a result, the associated energy difference between these two states increases; to the extent the appropriate excitation photon need necessarily have a higher energy to induce the transition to the excited state. The correspondingly shorter wavelength of the aforementioned photon is the reason that solvatochromism by this mechanism, and with this

result, is said to be negative. In (III) of Fig. 1.10, the increased MLCT completely offsets (or "compensates") the M-L bond polarization of the ground state. The resulting difference in the extent to which the polar solvent stabilizes the non-polar excited state and the ground state produces increasingly negative solvatochromism. In other words, the essentially non-existent stabilization of the excited state in combination with substantially stabilized ground state produces an energy gap between the two which requires especially energetic photons (significantly lower λ) to stimulate the equivalent transition. Fig. 1.10 (IV) shows that further increases in MLCT eventually result in a reversal of the polarity of the M-L bond, with the ligand now assuming the electron rich role. With the M-L bond now resuming its polar nature, albeit it reversed, the excited state then becomes more stabilized than was the case in Fig. 1.10 (III), such that the gap between ground and excited states becomes diminished in comparison. And so, as the Figure shows, the negative solvatochromism becomes less pronounced.

Figure 1.10 (V) shows MLCT occurring so strongly that in addition to the reversal of M-L bond polarity in the excited state, the magnitude of the charges at the two poles cannot be distinguished from those of the ground state. Therefore, since the two dipoles (ground and excited states) are essentially identical from an electronic perspective, the difference in the stabilization of the ground and excited states does not change on exposure of the complex to increasingly polar solvents, and so no accompanying solvatochromism is observed. Finally, further increases in MLCT may not only completely reverse the polarization, but enhance the magnitude of the charge separation in the resulting dipole, such that the excited state is stabilized to a greater extent by more polar solvents that the ground state. The net reduction of the ground and excited state energy gap gives a corresponding positive wavelength shift of the required excitation photon; hence the phenomenon is termed positive solvatochromism in this instance [46].

1.2.2 Primary Factors which Effect Solvatochromism

The solvation phenomena under discussion have been shown to be largely dependent on a few characteristic properties of the solvents that have thus far been evaluated [49]. Among these highlighted features are the solvent's electron pair donor and acceptor strength (Lewis basicity

and acidity, respectively), its polarity, and in some cases, possibly its polarizability [49-54]. This simplification then permits the use of manageable empirical models to describe the effects of solvents on the different experimentally determined physicochemical properties of species in solution [54-59]. Even relatively subtle variations in these properties where magnitude is concerned can produce pronounced physical effects. Dramatic colour changes have be seen to occur when the dissolution the complex is performed in solvents of increasing donor strength, particularly when the latter approaches the value for one of the coordinated anions. Further increases may result in the solvolytic substitution of the particular ligand, a process which is generally accompanied by significant colour changes. Fig. 1.11 shows this sort of relationship. In particular, the Figure shows the dependence of the relative energies of the *d* orbitals in the coordination sphere (and the corresponding *d-d* transitions between them) on donor strength of the bonded anion versus that of the solvent [60]. Linert *et al.* [60] evaluated a mixed ligand Cu(II) system; with acetylacetonato (acac) and *N*,*N*,*N*',*N'*-tetramethyl-ethylenediamine (tmen) ligands.

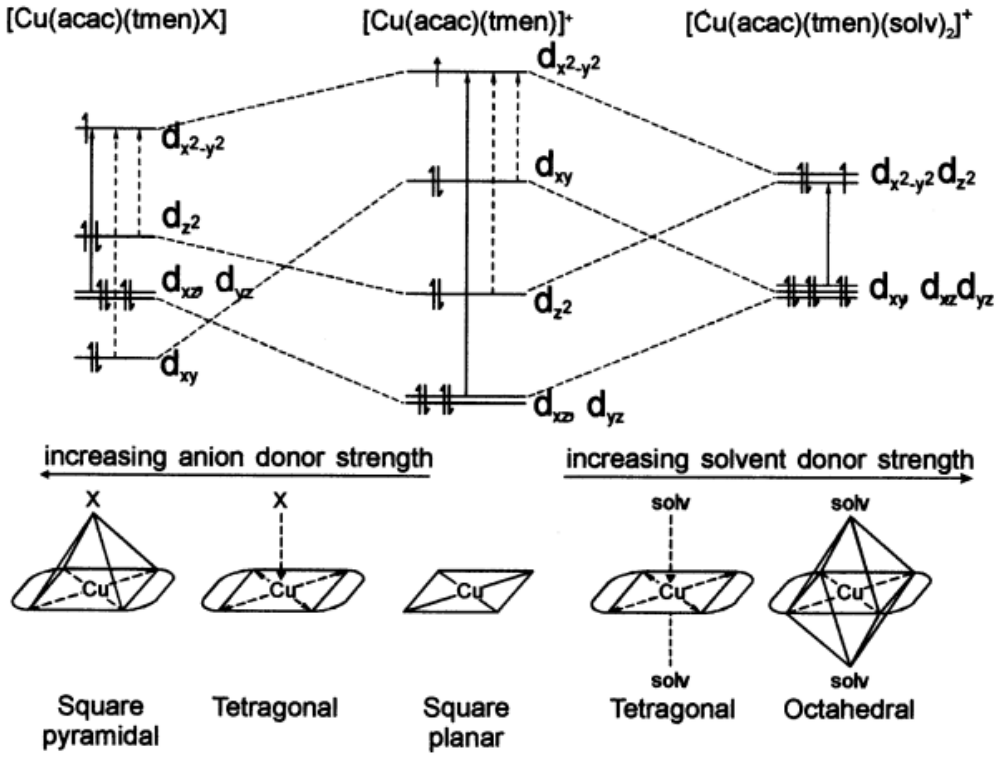

Figure 1.11: The scheme shows the dependence of the resulting orbital energy diagram on the relative donor strengths of the (axial) ligand and the solvent (reproduced from Linert *et al.* [60]).

As mentioned above, this difference can produced dramatic colour changes. Fig. 1.12 shows the resulting colours which can in general be expected of mixed-ligand copper of complexes of the type: $[Cu(dike)(diam)]^+$ (where dike = β-diketonate; diam = *N*-alkylated diamines). In the case of these complexes however, no spin energy barrier has to be overcome on increasing solvent donor strength, and the *continuous* colour change seen occurs *via* a Jahn-Teller effect-mediated mechanism [60].

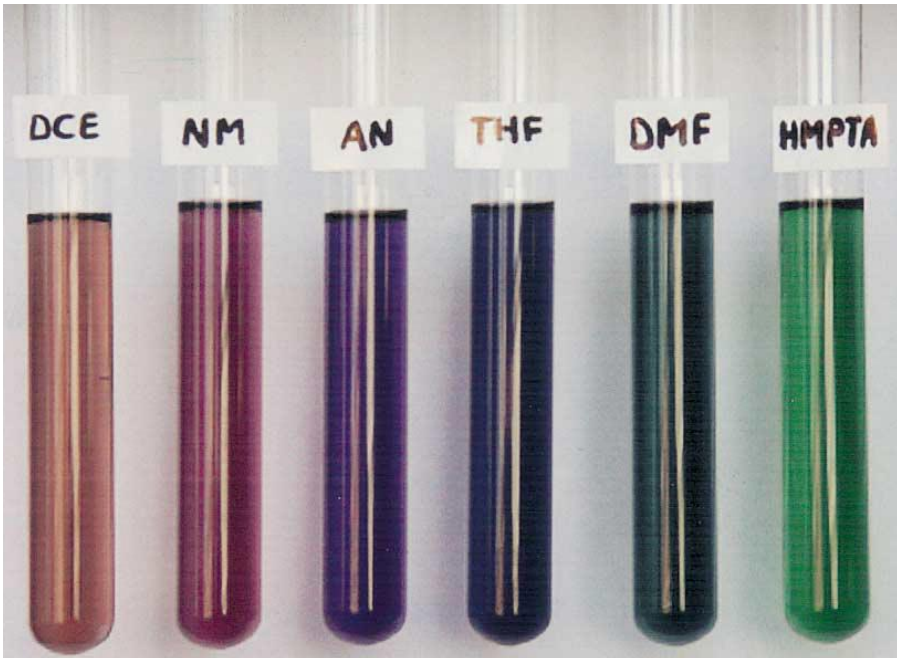

Figure 1.12: Photograph showing the colour change of solvatochromic mixed-ligand $[Cu(dike)(diam)]^+$ complexes (DCE = dichloroethylene, NM = nitromethane, AN = acetonitrile, THF = tetrahydrofuran, DMF = dimethylformamide, HMPTA = hexamethylphosphorictriamide acid (reproduced from Linert *et al.* [60]).

It has been suggested that these physicochemical properties and their related parameters are, to a certain approximation, linear functions of features which characterise the numerous different properties of the solvents themselves [49, 51-53]. These properties and related parameters include adsorption/emission spectra, NMR chemical shifts, ion activity coefficients, enthalpies and entropies of solvation, redox potentials, reaction rates, equilibrium constants, and so on [49, 52, 53].

As aforementioned, studies have shown Lewis basicity and acidity (donor and acceptor strength, or H-bonding ability), polarity and polarizability, to be the chief properties which dominate all of the other parameters that collectively give rise to solvent effects [49, 59-61].

1.2.3 The Utility of Solvatochromic Phenomena

There are a variety of complexes which have been found to be strongly influenced by solvent effects in terms of their manifest colours, upon exposure. These resulting colours were found to be particularly susceptible to even mild changes in donor/acceptor strength of the associated solvent [60]. As such they have found extensive application as Lewis-acid and Lewis-base indicators. Particularly noteworthy among this class of complexes are $[Cu(acac)(tmen)]^+$, $[Ni(acac)(tmen)]^+$, $[Fe(phen)_2(CN)_2]$ and [Cu(acac)(tmen)Cl] (acac = acetylacetonato; tmen = *N*,*N*,*N*',*N'*-tetramethyl-ethylenediamine; and phen = 1,10-phenanthroline) [60]. Their structures are shown below.

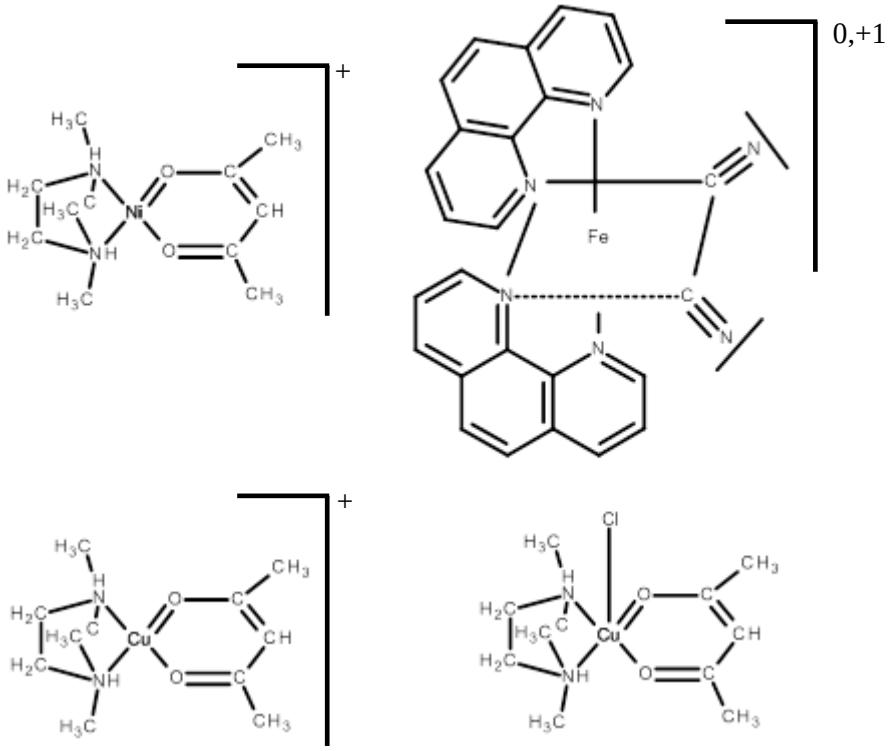

Figure 1.13: Examples of four solvatochromic complexes used as Lewis acid/base indicators (reproduced from Linert *et al.* [60]).

This is just one example of the ways in which solvatochromic effects can be exploited successfully. Others may include the determination of solvent purity, degree of hydration, the

relative volumes (qualitatively) of two or more components of a composite solvent mixture, and so on.

The iron(II) complex depicted in Fig. 1.13 undergoes solvatochromism by the interaction of the lone pairs of electrons on the uncoordinated nitrogen atoms of its cyano- ligand. Linert *et al.* [60] suggested that there may be formal coordination of these groups to incoming Lewis-acid species. The mode of coordination is shown in Fig. 1.14.

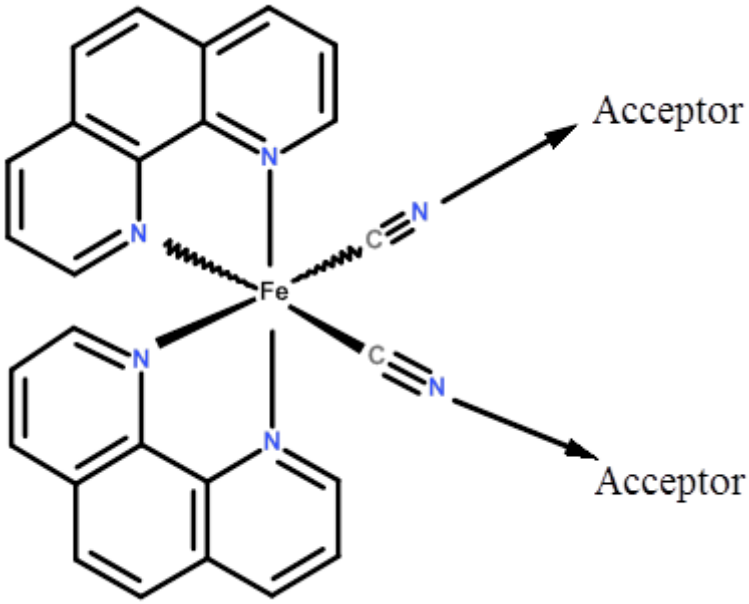

Figure 1.14: Proposed coordination of $[Fe(phen)_2(CN)_2]$ with Lewis acid molecules *via* the uncoordinated cyano- group nitrogens (reproduced from Linert *et al.* [60]).

1.3 Potential Mis-assignment of Solvatochromism as Spin Crossover

Among the many attractive features of coordination compounds, in both the literal and figurative sense, is the vast range of different colours by which the many complexes in existence are characterised. Additionally, these varying colours can reversibly interconvert as a consequence of a variety of chemical reactions, or more aptly in this context, by altering the parameters of the local environment in which the associated chromophore is situated [59, 60].

Among those parameters that may reversibly influence spectral properties, as has been discussed, are temperature, pressure light irradiation, and solvents. 'Chromotropism' is the generally recognised term which encompasses all of these reversible colour changes, in response to some or other appropriate stimulus [60]. The difficulty arises in the specific assignment of the origin or mechanism of a colour change, especially considering that most chromotropic phenomena and their associated stimuli may potentially overlap. For example, Linert *et al.* noted that it is not an unusual situation for a compound to exhibit both solvato- and thermochromism [60]. And so it is perhaps not an unreasonable assertion to make that what may have been assigned as a spin crossover mediated colour change may in fact be a consequence of solvent effects, particularly in the absence of supporting magnetic susceptibility data. For instance, a compound whose hygroscopic nature has not been characterised may be exposed to some wavelength of light, and be seen to gradually undergo a colour change.
In lieu of the colour change being brought about by the irradiation; leading to its assignment as charge transfer or intersystem crossing, or indeed spin crossover, further analyses may reveal that adsorption of atmospheric moisture, accompanied by enhanced H-bonding, dipole-dipole effects, etc., may in fact be the underlying cause of the absorption/emission spectral shift. That is, the observed physical changes would in that instance be due to solvatochromic effects. In addition, these solvent effects may induce spin crossover, to the extent that the light irradiation itself was in fact of no perceivable long-lived consequence.

It is just this latter mechanism which is believed to be responsible for the colour changes observed for the pyrazine-*N*-oxide iron(II) and cobalt(III) perchlorate complexes [19, 20]. For the former, this perspective is confirmed in this work as the result of a combined interpretation of the elemental microanalysis data, infrared data, UV-Vis absorption data, powder X-ray diffraction data, as well as the results from the thermal analyses of both the mono- and polynuclear complexes.

The difficulty in conducting a direct systematic evaluation of these diazine-*N*-oxide iron(II) complexes in terms of solvatochromic phenomena stems from their insolubility in the majority of organic or relatively non-polar solvents. Among these are those solvents with decidedly low to intermediate dielectric constants; such as those ranging from the non-aqueous alkanes and their absolute alcohols to the chlorinated organic solvents [59, 60]. This limitation

is augmented by the potential (and likely) coordination of their polar counterparts by addition or solvolytic mechanisms [62], to produce solvate complexes unlike the original synthetic products, and which are likely to be characterised by wholly different spectral features [63-65].

1.4 The Ligands

One of the key parameters which determines the magnitude crystal field stabilisation energy (CFSE; commonly referred to as Δ_o, or 10Dq in cubic crystal fields) is the donor strength (and acceptor strength, in the context of π-backbonding) of the bonded ligands. That is, the ligand field splitting energy (LFE/CFE) is inexorably a reflection of the Lewis basicity and proximity of the ligands to the metal centre, with all other influences ignored [1, 2, 4].

These parameters (collectively referred to as the ligand field strength), although based on approximations derived from idealistic models, can be extrapolated or built upon, with other significant interactions considered, to accurately reflect the underlying physicochemistry of coordination (MOT).

Owing to this splitting, in d^4 to d^7 systems of octahedral symmetry (cubic crystal field), the ligand field strength is the foremost influential factor in the determination of both magnetic and spectroscopic properties [12] (assuming that the metal centre and its chemical attributes are kept invariant). Correspondingly, the derivation of the resulting spectroscopic terms can then be used as a rudimentary basis upon which some of properties typical of coordination complexes can be rationalised [3].

Many reported FeN_6 complexes with conjugated aromatic heterocycles have such a value for 10Dq that interconversion between LS and HS states, occurs readily under requisite stimuli [17, 27]. That is, these FeN_6-type iron(II) complexes are characterised, in many cases, by their ability to undergo SCO [27].

The compatibility of iron(II) and *N*-donor ligands in terms of the latter's typically considerable donor strength and π-acceptor ability, with respect to generating a complex that can undergo reversible ligand→guest substitution, was considered an attractive combination, and one which, in part, motivated the use of pyrazine-*N*-oxide (PyzNO) for the fabrication of such a complex. The possibility of generating a PyzNO-bridged polymeric complex, thereby

potentially enabling the exploitation of intramolecular cooperativity effects towards high analyte sensitivity, was also considered a highly desirable prospect.

Of primary concern in this study was the treatment, on molecular orbital theory terms, of the d^6 system. The electronic configurations that manifest with fluctuating ligand field strength, as well as the spectral and magnetic properties they impart on the resulting complexes, provides the rationale behind the use of PyzNO and its isostructural analogues; 4,4'-bipyridine-*N*-oxide (bipyNO) and 2-methylpyrazine-*N*-oxide as ligands in this work.

Whether they exhibit paramagnetism or diamagnetism, the positions of the *d* - *d* , L→M and M→ L charge transfer bands, and so on, will be a prime function of the LFSE, provided the nature of the iron(II) centre (oxidation state) remains unchanged [12-16].

1.5 The Metal Centre

The use of Fe(II) as the complexes' metal centre has already been fully motivated above. It is worth noting again, however, that the d^6 electronic configuration thereof provides one of two readily distinguishable states on coordination; the fully spin paired or low spin (LS) state, or the spin free or high spin (HS) state. The two states are individually characterised by the substantially different physical and chemical properties to which they give rise. For example; whereas one state may be strongly paramagnetic (HS), its counterpart will be strongly diamagnetic (LS), a difference which has inspired rigorous research for the development of magneto-optical switches, and so on.

In combination with the chosen ligands then, the idea is to tune the ligand field strength so that it is very close to the thermal spin transition energy. Consequently, subtle change in a stimulus (viz. solvent-mediated increased hydrogen bonding, dipole-dipole and π-π interactions, etc.) would, in principle, be sufficient to induce the spin crossover event.

The intramolecular SCO of some low spin *N*-heterocyclic ferrous perchlorate compounds such as those of the pyrazines, its *N*-oxides and those of polypyridyl ligands have been studied [66-68]. Spectroscopic analyses suggest the formation of a $^5T_2$ excited state following the photo-excitation of the low spin Fe(II) complexes. The $^5T_2$ state is formed in 700 fs following ^{1}MLCT $^1A_1$ excitation [68]. McCusker *et al.* [68] suggested that the mechanism of $^5T_2$

formation proceeds *via* "direct" ^{1}MLCT $^{5}T_2$ conversion at or near the Franck-Condon configuration for the ^{1}MLCT $^{1}A_1$ excitation [68-72]. As mentioned, although LIESST studies are yet to be undertaken, strong MLCT behaviour may aid to produce substantial solvatochromic effects; particular in highly polar solvents which greatly stabilize the excited state (MLCT*).

As previously noted, the principal complexes of interest comprise an iron(II) (d^6) metal centre coordinated to a number of pyrazine-*N*-oxide (pyzNO) ligands, and perchlorate serving either purely as a counterion, or, at least potentially, as both a ligand and a counterion [20]. The perchlorate ion is known to be a very weakly coordinating ligand [73-76] in that it generally forms highly kinetically labile complexes. This result would be expected to be more pronounced in the context of iron(II) complexes since bonding would involve a hard ligand and a soft metal. As such, its substitution by a stronger Lewis base in the coordination sphere should be a spontaneous or readily occurring process (thermodynamically favourable in terms of hard and soft acid-base theory). This substitution should ideally be readily detectable by significant changes in both the spectral and magnetic properties of the complexes, provided the difference in Lewis base strengths is sufficient to drive the reaction significantly to the desired side of the equilibrium.

1.6 Objectives of this Study

The objectives of the study were as follows:

- To synthesize and fully characterise the mononuclear and polynuclear pyrazine-*N*-oxide iron(II) perchlorate complexes herein designated Complex1 and Complex2, and glean some insight into their respective structures, including any observed differences.

- To characterise the hydrated forms of the above complexes and determine their molecular structure as well as understand any differences, subtle or pronounced, in their hydrated variants.

- To understand the mechanism underlying the substantial change in colour (red to yellow) observed on hydration of these complexes. That is, whether the colour change is purely solvatochromic in origin, or occurs as a consequence of the spin crossover phenomenon, or a synergistic combination of the two processes.

- To determine whether the colour change is limited to exposure to water, or if exposure to other solvents would induce similar spectral shifts. Additionally, to determine the overall impact and the strength of interaction of various solvents with the complexes.

- To synthesize and characterise a similar, or isostructural complex, by varying the primary ligand, and conduct comparative solvent studies on the resulting product in order to understand the ligand's role in the observed properties of the complexes.

- To synthesize a pyrazine-*N*-oxide complex using a different solvent system, so as to contrast it with Complex1 and Complex2 in terms of its spectral and magnetic properties, as well as its thermal behaviour upon solvent exposure.

References

[1] **Linert, W.; Kudryavtsev, A.B**. Isokinetic and isoequilibrium relationships in spin–crossover systems. *Coord. Chem. Rev*. **190–192** (1999), 405–420.

[2] **Guetlich, P.; Hauser, A.; Spiering, H**. Thermally and optically switchable iron(II) complexes. *Angew. Chem*. **106**(20) (1994), 2109-2113.

[3] **Kahn, O**. *Molecular Magnetism*, VCH, New York (1993).

[4] **Guetlich, P.; Hauser, A**. Thermal and light-induced spin crossover in iron(II) complexes. *Coord. Chem. Rev*. **97** (1990), 1-19.

[5] **Toftlund, H.** Spin equilibria in iron(II) complexes. *Coord. Chem. Rev*. **94** (1989), 67-74.

[6] **Madeja, K.; Koenig, E**. Binding ratio in complex compounds of iron(II) with 1,10-phenanthroline. *J. Inorg. Nucl. Chem*. **25** (1963), 377-381.

[7] **Hoselton, M. A.; Wilson, L. J.; Drago, R. S**. Substituent effects on the spin equilibrium observed with hexadentate ligands on iron(II). *J. Am. Chem. Soc*. **97** (1975), 1722-1726.

[8] **Reeder, K. A.; Dose, E. V.; Wilson, L. J.** Solution-state spin-equilibrium properties of the tris[2-(2-pyridyl)imidazole]iron(II) and tris[2-(2-pyridyl)benzimidazole]iron(II) cations. *Inorg. Chem.* **17** (1978), 1071-1074.

[9] **Simmons, M. G.; Wilson, L. J.** Magnetic and spin lifetime studies in solution of a $\Delta S1$ spin-equilibrium process for some six-coordinate bis(*N*-R-2,6-pyridinedicarboxaldimine)cobalt(II) complexes. *Inorg. Chem.* **16** (1977), 126-128.

[10] **Addison, A. W.; Burman, S.; Wahlgren, C. G.; Rajan, O. A.; Rowe, T. M.; Sinn, E.** New iron(II) spin-crossover complexes with heterocyclic amine-derived ligands and STEPS experiments on photogenerated metastable high-spin states. *J. Chem. Soc. Dalton Trans*. **11** (1987), 2621-2624.

[11] **Gaspar, A. B.; Seredyuk, M.; Gutlich, P**. Spin crossover in iron(II) complexes: Recent advances. *J. Mol. Struct.* **924-926** (2009), 9-15.

[12] **Soliman, A. A.; Khattab, M. M.; Reissner, M.; Weinberger, P.; Werner, F.; Linert, W**. Synthesis, structure, spectroscopic and magnetic characterization of a novel spin-crossover iron(II) complex with 1-cyclopropyltetrazole ligands. *Inorg. Chim. Acta*. **360** (2007), 398-399.

[13] **Leita, B. A.; Moubaraki, B.; Murray, K. S.; Smith, J. K**. Spin-crossover in dimeric hydrogen-bonded iron(II) 2-(pyrazolyl)-pyridine and 2-(imidazolyl)-pyridine complexes. *Polyhedron*. **24** (2004), 2165-2168.

[14] **Halcrow, M. A**. The spin-states and spin-transitions of mononuclear iron(II) complexes of nitrogen-donor ligands. *Polyhedron*. **26** (2007), 352-256.

[15] **Nihei, M.; Shiga, T.; Maeda, Y.; Oshio, H**. Spin crossover iron(III) complexes. *Coord. Chem. Rev*. **251** (2007), 2607-2610.

[16] **Olguin, J.; Brooker, S**. Spin crossover active iron(II) complexes of selected pyrazole-pyridine/pyrazine ligands. *Coord. Chem. Rev*. **255** (2011), 204-207.

[17] **Kuroda-Sowa, T.; Kimura, K.; Kawasaki, J.; Okubo, T.; Maekawa, M**. Effects of weak interactions on spin crossover properties of iron(II) complexes with extended π-conjugated Schiff-base ligands. *Polyhedron*, **30** (2011), 3189-3192.

[18] **Krivokapic, I.; Enachescu, C.; Bronisz.; Hauser, A**. Spin transition and relaxation dynamics coupled to a crystallographic phase transition in a polymeric iron(II) spin-crossover system. *Chem. Phys. Lett.* **455** (2008), 192-194.

[19] **Speca, A.N.; Karayannis, N.M.; Pytlewski, L.L.** Transition metal perchlorate complexes with pyrazine-*N*-oxide. *J. Inorg. Nucl. Chem*. **35** (1973), 3113-3125.

[20] **Watkins, G.M**. (1988) *Ligand Isotope Vibrational Studies of Metal(II) Complexes*. Doctoral thesis. Cape Town: University of Cape Town.

[21] **Gaspar, A.B.; Agusti, G.; Martinez V.; Munoz, M.C; Levchenko, G.; Real, J. A**. Spin crossover behaviour in the iron(II)-2,2-dipyridilamine system: Synthesis, X-ray structure and magnetic studies. *Inorg. Chim. Acta*. **358** (2005), 4089-4092.

[22] **Decurtins, S.; Gütlich, P.; Hauser, A.; Spiering, H**. Light-induced excited spin state trapping in Fe(II) complexes. *Photochem. Coord. Compd*. **105** (1984), 1-3.

[23] **Hauser, A.** Reversibility of light-induced excited spin state trapping in $Fe(ptz)_6(BF_4)_2$ and the Zn_1-x-$Fe_x(ptz)_6(BF_4)_2$ spin-crossover systems. *Chem. Phys. Lett.* **124** (1986), 543-546.

[24] **Létard, J.-F., Capes, L., Chastanet, G., Moliner, N., Létard, S., Real, J. A., Kahn, O**. Critical temperature of the LIESST effect in iron(II) spin crossover compounds. *Chem. Phys. Lett.* **313** (1999), 115-119.

[25] **Hauser, A**. Intersystem crossing in iron(II) coordination compounds. *Coord. Chem. Rev*. **111** (1991), 275-279.

[26] **Buhks, E. Navon, M., Bixon, J., Jortner, J**. Spin conversion processes in solution. *Am. Chem. Soc*. **102** (1980), 2918-2920.

[27] **Atmani, C.; El Hajj, F.; Benmansour, S.; Marchivie, M.; Triki, S.; Conan, F.; Patinec, V.; Handel, H.; Dupouy, G.; Gómez-García, C.J.** Guidelines to design new spin crossover materials. *Coord. Chem. Rev*. **254** (2010), 1559-1568.

[28] **Buchan, T.; Gütlich, P**. Thermal and light-induced spin crossover in iron(II) complexes with monodentate tetrazole ligands carrying long alkyl chains in the 1-position. *Chem. Phys. Lett*. **220** (1994), 262-264.

[29] **Gütlich, P.; Goodwin, H.A.** Spin crossover metal compounds III. *Top. Curr. Chem*. **235** (2004), 268-270.

[30] **Guinneau, M.; Marchivie, M.; Bravic, G.; Létard, J.-F.; Chasseau, D.** Structural aspects of spin crossover. Example of the $[Fe(II)L_n(NCS)_2]$ complexes. *Top. Curr. Chem*. **234** (2004), 97-100.

[31] **Moliner, N.; Muñoz, M. C.; Létard, S.; Létard, J-F.; Solans, X.; Burriel, R. Castro, M. Kahn, O. Real, J-A**. Spin-crossover in the $[Fe(abpt)_2(NCX)_2]$ (X=S, Se) system: structural, magnetic, calorimetric and photomagnetic studies. *Inorg. Chim. Acta*. **291** (1999), 278-279.

[32] **Gaspar, A.B.; Muñoz, M. C.; Moliner, N.; Ksenofontov, V.; Levchenko, G. Guetlich, P. Real, J. A**. Polymorphism and pressure driven thermal spin crossover phenomenon in $[Fe(abpt)_2(NCX)_2]$ (X = S, and Se): Synthesis, structure and magnetic properties *Monatsh. Chem*. **134** (2003), 285-287.

[33] **Sheu, C. F.; Pillet, S.; Lin, Y. C.; Chen, S. M.; Hsu, I.J.; Lecomte, C.; Wang, Y**. Magnetostructural relationship in the spin-crossover complex t-$[Fe(abpt)_2(NCN)_2]_2$: Polymorphism and disorder phenomenon. *Inorg. Chem.* **47** (2008), 10866-10870.

[34] **Pillet, S. Lecomte, C. Sheu, C.F. Lin, Y.C. Hsu, I.J. Wang, Y.** Light induced modulated structure of the spin crossover compound $[Fe(abpt)_2(NCN)_2]_2$. *J. Phys.: Conf. Ser*. **21** (2005), 221-222.

[35] **Kunkeler, P.J.; Van Koningsbruggen, P. J.; Cornelissen, J.P.; Van der Horst, A.N.; Van der Kraan, A.M.; Spek, A.L.; Haasnoot, J.G.; Reedijk, J.** Novel hybrid spin systems of 7,7‘,8,8‘-tetracyanoquinodimethane (TCNQ) radical anions and 4-amino-3,5-bis(pyridin-2-yl)-1,2,4-triazole (abpt). Crystal structure of [Fe(abpt)2(TCNQ)2] at 298 and 100 K, Mössbauer spectroscopy, magnetic properties, and infrared spectroscopy of the series [M(II)$(abpt)_2(TCNQ)_2$] (M = Mn, Fe, Co, Ni, Cu, Zn). *J. Am. Chem. Soc*. **118** (1996), 2190-2195.

[36] **Cornelissen, J.P.; Van Diemen, J. H.; Groeneveld, L. R.; Haasnoot, J. G.; Spek, A. L.; Reedijk**, **J.** Synthesis and properties of isostructural transition-metal (copper, nickel, cobalt, and iron) compounds with 7,7',8,8'-tetracyanoquinodimethanide(1-) in an unusual monodentate coordination mode: crystal structure of bis(3,5-bis(pyridin-2-yl)-4-amino-1,2,4-triazole)bis(7,7',8,8'-tetracyanoquinodimethanido)copper(II). *Inorg. Chem.* **31** (1992), 198-200.

[37] **Dupouy, G.; Marchivie, M.; Triki, S.; Sala-Pala, J.; Salaün, J. Y.; Gómez-García, C. J.; Guionneau**, **P.** The key role of the intermolecular π–π interactions in the presence of spin crossover in neutral [Fe$(abpt)_2A_2$] complexes (A = Terminal monoanion N ligand) *Inorg. Chem.* **47** (2008), 8921-8922.

[38] **Boca, R.; Baran, P.; Dlhan, L.; Fuess, H.; Haase, W.; Renz, F.; Linert, W.; Svoboda, L.; Wemer, R**. Crystal structure and spin crossover studies on bis(2,6-bis(benzimidazol-2-yl)pyridine) iron(II) perchlorate. *Inorg. Chim. Acta*. **260** (1997), 129-131.

[39] **Isley, W. C.; Zarra, S.; Carlson, R. K.; Bilbeisi, R. A.; Ronson, T. K.; Nitschke, J. R.; Gagliardi, L.; Cramer, C. J**. Predicting paramagnetic ^{1}H NMR chemical shifts and state-energy separations in spin-crossover host-guest systems. *Phys. Chem. Chem. Phys.* **16** (2014), 10620-10623.

[40] **Speca, A.N.; Pytlewski, L.L.; Karayannis, N.M**. Pyrazine-*N*-oxide complexes with 3d metal chlorides. *J. Inorg. Nucl. Chem*. **35** (1973), 4029-4036.

[41] **Nakamoto, K**. *Infrared and Raman Spectra of Inorganic and Coordination Compounds*. 6th ed. John Wiley and Sons, Inc., New Jersey, USA (2009).

[42] **Nyquist, R. A. and Kagel, R. O**. *Handbook of Infrared and Raman Spectra of Inorganic Compounds and Organic Salts*, vol. 4. Academic Press, Inc., Chestnut Hill, Massachusetts, USA (1997).

[43] **Reichardt, C.** *Solvent Effects in Organic Chemistry*. Verlag Chemie, Weinheim, Germany (1979).

[44] **Kaim, W.; Kohlmann S.; Ernst, S.; Olbrich-Deussner, B.; Bessenbacher, C.; Schulz, A.** What determines the solvatochromism of metal-to-ligand charge transfer transitions? A demonstration involving 17 tungsten carbonyl complexes. *J. Organomet. Chem*. **321** (1987), 215–224.

[45] **Dogonadze, R. R.; Kalman, E.; Kornyshev, A. A.; Ulstrup J.** (Eds.), *The Chemical Physics of Solvation., Pt. A: Theory of Solvation* . Elsevier, Amsterdam, Netherlands (1985).

[46] **Kamlet, M.J.; Abboud, J.L.M.; Taft, R.W**. An examination of linear solvation energy relationships. *Prog. Phys. Org. Chem.* **13** (1981), 485-488.

[47] **Abboud, J. L. M.; Taft, R. W.; Kamlet, M. J**. Linear solvation energy relationships. Part Correlations of additional solvent property scales with the solvatochromic parameter, π*. *J. Chem. Res*. **3** (1984), 98-100.

[48] **Taft, R.W.; Abboud J.L.; Kamlet, M.J**. Linear solvation energy relationships. 28. An analysis of Swain's solvent "acidity" and "basicity" scales. *J. Org. Chem*. **49** (1984), 2001-2002.

[49] **Burger, K.; Horvath, I.** Solvatochromism in Mössbauer spectroscopy. Effects of solvents on structure and electronic structure of iron and tin compounds. *Inorg. Chim. Acta*. **196** (1992), 47-55.

[50] **Burger, K.** *Solvation, Ionic and Complex Formation Reactions in Non-aqueous Solvents*. Elsevier, Amsterdam, Netherlands (1983).

[51] **Gutmann, V.** *The Donor-Acceptor Approach to Molecular Interactions.* Plenum, New York, USA (1978).

[52] **Gutmann V.** *Coordination Chemistry in Non-aqueous Solutions*. Springer, Vienna, Austria (1968).

[53] **Fawcett, W. R.; Krygowski, T. M.** Complementary Lewis acid-base description of solvent effects. II. Dipole-dipole interactions. *Aust. J. Chem*. **28** (1975), 2115-2117.

[54] **Krygowski, T. M.; Fawcett, W. R.** Complementary Lewis acid-base description of solvent effects. I. Ion-ion and ion-dipole interactions. *J. Amer. Chem. Soc*. **97** (1975) 2143-2147.

[55] **Kamlet, M. J.; Taft, R. W.** Linear solvation energy relationships. Part XVII. Some further correlations with the solvatochromic parameters. *Pol. J. Chem*. **55** (1981) 1337-1339.

[56] **Kamlet, M. J.; Carr, P. W.; Taft, R. W.; Abraham, M. H**. Linear solvation energy relationships. 13. Relationship between the Hildebrand solubility parameter, δH, and the solvatochromic parameter, π*. *J. Amer. Chem. Soc*. **103** (1981), 6062-6066.

[57] **Koppel, I.; and. Palm, V. A. in N. B. Chapman and J. Shorter** (Eds.). *Advances in Linear Free Energy Relationships*. Plenum, New York, USA (1972), Ch. 5.

[58] **Reichardt, C.; Harbusch, E.; and Muller, R.; Bertini, I.; Lunazzi, L.; Dei, A**. (Eds.). *Advances in Solution Chemistry*. Plenum, New York, USA (1981).

[59] **Spencer, J. N.; Ganunis, T. F.; Zafar, A. I.; Salata, C. M.; Gupta, S.; Puppala, S.; Eppley, H. J.; Ealy, J. L.; Yoder, C. H.** Enthalpy and entropy contributions to solvent effects on adduct formation . *J. Phys. Chem*. **95** (1991) 4910-4912.

[60] **Linert, W.; Fukuda, Y.; Camard, A.** Chromotropism of coordination compounds and its applications in solution. *Coord. Chem. Rev*. **218** (2001), 113-116.

[61] **Reichardt, C.** *Solvents and Solvent Effects in Organic Chemistry*. 2nd ed, Verlag Chemie, Weinheim, Germany (1988).

[62] **Sone, K.; Fukuda, Y.** (Eds.). *Ions and Molecules in Solution*. Elsevier, Amsterdam, Netherlands (1983).

[63] **Linert, W.; Taha, A. J**. Coordination of solvent molecules to square-planar mixed-ligand nickel(II) complexes: a thermodynamic and quantum-mechanical study. *J. Chem. Soc. Dalton Trans*. (1994), 1091-1093.

[64] **Linert, W.; Bauer, G.; Jameson, R.F.; Taha, A**. Estimation of the acceptor numbers of cations by means of an acid-base indicator. *J. Coord. Chem*. **42** (1997), 211-215.

[65] **Iwamoto, E.; Nishimoto, J.; Yokoyama, T.; Yamamoto, K.; Kumamaru, T**. Increased basicity and hydrogen-bonding donor ability of water by hydrogen bonding to dimethyl sulphoxide and its coordination to 1,4,8,11-tetramethyl-1,4,8,11-tetraazacyclotetradecanenickel(II) in nitrobenzene. *J. Chem. Soc., Faraday Trans.,* **87** (1991), 1537-1540.

[66] **Nordlander, E.; Whalen, A. M.; Prestopino, F**. Iron 1993. *Coord. Chem. Rev*. **146** (1995), 229-241.

[67] **Brown, A. M.; McCusker, J. K.; Catherine, E**. Spectroelectrochemical identification of charge-transfer excited states in transition metal-based polypyridyl complexes. *Dalton Trans*. **201** (2014), 17635–17637.

[68] **McCusker, J. K.; Walda, K. N.; Dunn, R. C.; Simon, J. D.; Magde, D.; Hendrickson, D. N**. Sub-picosecond ^{1}MLCT → $^{5}T_2$ intersystem crossing of low-spin polypyridyl ferrous complexes. *J. Amer. Chem. Soc*. **115** (1993), 298-299.

[69] **Twigg, M. V.** Kinetics and thermodynamics of solvolysis of tris(2,2'-bipyridine)iron(II) perchlorate in dimethylsulfoxide. *Trans. Met. Chem*. **18** (1993), 175-176.

[70] **McCusker, J. K.; Toftlund, H.; Rheingold, A. L.; Hendrickson, D. N**. Ligand conformational changes affecting $^{5}T_2 \rightarrow {}^{1}A_1$ intersystem crossing in a ferrous complex. *J. Amer. Chem. Soc*. **115** (1993), 1797-1802.

[71] **Klaeui, W.; Eberspach, W.; Guetlich, P**. Spin-crossover cobalt(III) complexes: steric and electronic control of spin state. *Inorg. Chem.* **26** (1987), 3977-3980.

[72] **Habib, F.; Luca, O. R.; Vieru, V.; Shiddiq, M.; Korobkov, I.; Gorelsky, S. I.; Takase, M. K.; Chibotaru, L. F.; Hill, S.; Crabtree, R. H**. Influence of the ligand field on slow magnetization relaxation versus spin crossover in mononuclear cobalt complexes. *Angew. Chemie.* **52** (2013), 11290-11294.

[73] **Matsumoto, T.; Newton, G. N.; Shiga, T.; Hayami, S.; Matsui, Y.; Okamoto, H.; Kumai, R.; Murakami, Y.; Oshio, H**. Programmable-state switching in a mixed-valence iron grid. *Nat. Comm*. **5** (2014), 3865-3869.

[74] **Gruden-Pavlovic, M.; Stepanovic, S.; Peric, M.; Guell, M.; Swart, M.** A density functional study of the metals. *Phys. Chem. Chem. Phys.* **16** (2014), 14514-14516.

[75] **Woodward, F.; Gibson, P.J.; Jameson, G.; Landee, C.P.; Turnbull, M.; Willet, R.D**. Two-dimensional Heisenberg antiferromagnets: Syntheses, X-ray structures, and

magnetic behavior of $[Cu(pz)_2](ClO_4)_2$, $[Cu(pz)_2](BF_4)_2$, and $[Cu(pz)_2(NO_3)](PF_6)$. *Inorg. Chem.* **46** (2007), 4256-4266.

[76] **Vela, S.; Jornet-Somoza, J.; C.P.; Turnbull, M.M.; Feyerherm, R.; Novoa, J.J.; Deumal, M**. Dividing the Spoils: Role of Pyrazine Ligands and Perchlorate Counterions in the Magnetic Properties of Bis(pyrazine)diperchloratecopper(II), $[Cu(pz)_2](ClO_4)_2$. *Inorg. Chem.* **52** (2013), 12924-12929.

Chapter 2

Experimental

2.1 Synthesis of the Ligands

The general protocol for the synthesis of the ligands was taken from Watkins [1]. Pyrazine-*N*-oxide (PyzNO) was synthesised as described, while the protocol employed to produce 4,4'-bipyridine-*N*-oxide (BipyNO) bears only stoichoimetric and temperature modifications to procedure outlined therein (see section 2.1.2). This was necessary as the procedure employed by Watkins was tailored towards the synthesis of the 2,2'-bipyridine-*N*-oxide isomer, as per the requirements of that particular study.

PyzNO was also purified as described therein [1]. The purification of BipyNO, however, employed a prep plate in lieu of the recrystallization procedure described by Watkins [1].

All reagents ('HPLC grade'; 98-99% isotopic purity) used in this work were purchased from Sigma-Aldrich.

The peroxy-acid mediated mono-*N*-oxidation of aromatic diazines (imines in general), in this case Pyz, Bipy and mePyz, was employed in the preparation of the ligands; PyzNO, BipyNO and mePyzNO, respectively. To that end, standardization of the H_2O_2 to be used in syntheses was required due to its steady decomposition on storage. Standardization was performed against 0.0258 mol.dm^{-3} $KMnO_4$ (0.8170 g (5.168 mmol) in a total aqueous volume of 200 mL) (standard was made intentionally dilute to avoid the formation of MnO_2 due to incomplete +7 to +2 Mn reduction). Titration of 1000 μL of H_2O_2 (acidified with 6 mol.dm^{-3} H_2SO_4) required 144.70 mL of $KMnO_4$ standard to reach equivalence. The concentration of H_2O_2 was found to be 9.333 mol.dm^{-3} and 18.750 mol.dm^{-3} for the syntheses of PyzNO and BipyNO, respectively.

2.1.1 Synthesis of Pyrazine-*N*-oxide

To 6.0981 g of Pyz (76.14 mmol) was added 22.44 mL of glacial acetic acid (380.5 mmol) and 8.155 mL of 9.333 mol.dm^{-3} H_2O_2 (76.1 mmol). The solution was heated at 70 ^{o}C for 3 hours

under reflux. A further 8.155 mL of 9.333 mol.dm^{-3} H_2O_2 (total ratio 2:1 H_2O_2:Pyz) was added, and heating continued for a further 5 hours. The solution was cooled and the volume reduced to approximately half of the original volume. The solution was neutralised using Na_2CO_3 whereupon PyzNO was extracted into chloroform 5 times over using an approximate 2:1 per volume ratio of organic to aqueous phase. After removal of the chloroform by rotary evaporation (rotavap) (35 ^oC), the cream-white and fluffy crude product was purified by vacuum sublimation (50-60 ^oC, ca. 0.5 mmHg) to yield pure-white, moderately transparent, needle-shaped pyrazine-*N*-oxide single crystals. Yield: 0.6672 g (41%). The compound was characterised by CHNS microanalysis, DSC, TGA*, TG-IR EGA*, mid-infrared spectroscopy, ^1H and ^{13}C NMR, FT-Raman*.

2.1.2 Synthesis of 4,4'-Bipyridine-*N*-oxide

To 2.7546 g of 4,4'-bipyridine (17.64 mmol) was added 5.206 mL of glacial acetic acid and 1.010 mL of 17.45 mol.dm^{-3} H_2O_2 (17.64 mmol). The solution was heated at 50 ^oC for 5 hours under reflux (starting bipy:H_2O_2 ratio 1:1). The temperature was then lowered to 45^oC for 6 days whilst monitoring the progress by TLC every 12 h. 200 µL additions of H_2O_2 were made every 8 h for a total of a 3.5:1 H_2O_2:bipy ratio in order to encourage maximal conversion to the *N*-oxide whilst keeping the BipyNO_2 at a minimum. When the Bipy precursor could no longer be seen by TLC, the reaction was stopped and neutralized with Na_2CO_3 followed by the complete removal of solvent by rotary evaporation at 32^oC. Precipitation of sodium acetate occurred almost immediately but the solvent was allowed to evaporate completely notwithstanding, without filtration. The resulting solid yellow mixture was mulled in a pestle and mortar and then stirred in a large excess of warm absolute ethanol (~ 32 ^oC) for 30 min. It was then filtered and washed with a further excess of solvent. The filtrate was then reduced to approximately 5 mL by rotary evaporation followed by the loading of the intense golden mixture onto a normal phase prep plate TLC while hot for a maximum load width of 1 cm. A 1:1 (v/v) EtOH/$CHCl_3$ mobile phase was used to produce three well resolved bands. Analytical TLC confirmed that the band of intermediate chromatographic affinity was the desired bipyNO product, whilst those with greatest and lowest mobility were bipy and bipyNO_2, respectively.

*See Appendix in supplementary CD-ROM for PyzNO characterization by TGA, FT-IR-EGA and FT-Raman.

The final light brown powder was weighed (0.684 g (3.972 mmol), 22.56% yield) and characterised by Microanalysis (CHNS), DSC, FT-IR, ^{1}H and ^{13}C NMR, and TG-IR EGA*.

Several minor refinements† were made to improve the exceptionally low yield. The highest recorded yield was 0.8165 g (24.67%) using 3.0067 g of Bipy. A total mass of 2.839 g of pure BipyNO for complexation was generated over the course of 6 separate reactions. Microanalysis data, ^{1}H and ^{13}C NMR were consistent with the depicted spectra and the literature [2].

2.2 General Remarks on the Ligand Syntheses

It was concluded from the close correlation of analysis results obtained for PyzNO to literature values [3], in terms of the measured melting points, DSC data, ^{1}H NMR spectra, ^{13}C NMR spectra, infrared spectra (and FT-Raman, see Appendix), that the various syntheses were successful. As such, complex synthesis with pure ligand commenced.

With regards to BipyNO, there was initial difficulty in resolving the composite product mixture into its constituent parts. The major side product, whose formation could not be suppressed despite attempting a wide variety of different reaction conditions, was $BipyNO_2$. Attempts at recrystallizing the desired product from a variety of solvents, ranging from the very polar to the non-polar, including various mixtures of solvents in different ratios were made, but were largely unsuccessful due to either an exceptionally low product yield (still bearing residual di-*N*-oxide), or insolubility of the crude product at the onset.

A precipitation strategy that attempted to eliminate $BipyNO_2$ as the protonated di-chloride salt also proved unsuccessful. The milky precipitate formed in this case rapidly re-dissolved, which was likely due to its decomposition by acid catalysed hydrolysis to regenerate the soluble diazine precursor. Finally, the preparative TLC plate method ultimately attempted proved to be a success. Instrumental characterisation of the pure BipyNO product gave all of the expected features in the resulting spectra. The drawback, however, was that the yield could not be improved substantially in individual syntheses in spite of several modifications of the

* See Appendix on CD-ROM for BipyNO characterization by FT-IR EGA.

† These included minor temperature and volume adjustments.

protocol to that end. Ultimately, the reaction had to be conducted repeatedly many times over to generate sufficient product for complex syntheses.

$PyzNO_2$* was successfully synthesised with very little difficulty. As the reaction conditions, and the large excess of oxidant resulted in the formation of only one product, purification did not entail countless tedious and largely inefficient solvent extractions as was the case with the other ligands. The yield (0.52 g from 0.99 g Pyz precursor, 37.5 %) may be however improved with perhaps several minor alterations to the protocol. A qualitative solubility evaluation of the product showed that of the solvents tested, it was only soluble in water, *N*,*N*-dimethylformamide (DMF), and dimethylsulphoxide (DMSO), and only sparingly soluble in hot ethanol (60 ^{o}C), and to an even lesser extent in hot methanol at the same temperature. The crystalline $PyzNO_2$ product appeared completely insoluble in toluene, hexane, cyclohexane, cyclohexene, chloroform, acetone, dichloromethane, pent-1-ol, and 1,1-dichloroethylene. At this point, it was thought that it would exhibit consistently poor solubility in all non-polar to moderately polar solvents. The major disadvantage of this was the fact that the product could then not be used as a ligand for complexation. That is, it could not be dissolved in the methanol/2,2-dimethoxypropane and ethanol/2,2-dimethoxypropane solvent systems in which the other complexation reactions were conducted.

The synthesis of 2-methylpyrazine-*N*-oxide† from methylpyrazine precursor was also conducted. However, although the *N*-oxidation reaction was concluded successful, it produced both 2-methyl and 3-methyl isomers of the resulting *N*-oxide. Structural inspection of the two isomers shows that the former may experience significant steric strain due to its proximal oxide and methyl groups. It may form only as the result of the increased nucleophilicity of the ring nitrogen due to the neighbouring methyl group, and is thus likely the thermodynamic product [2-6]. Its counterpart, the 3-methyl isomer, in contrast, should not experience the same measure of steric hindrance to *N*-oxidation, as the associated oxide and methyl groups are in the 1, 3 positions. It is expected therefore that it should be the kinetic product [4-6]. Molecular modelling, or thermodynamic/kinetic experiments in which the systematic variation of

* See Appendix in CD-ROM for the synthesis and characterization of pyrazine-*N,N'*-dioxide.

† See Appendix in CD-ROM for the synthesis and characterization of methylpyrazine-*N*-oxide.

parameters such as reaction temperature, reagent concentration, etc. is undertaken, would be required to validate the above theoretical speculation [5, 6].

This mixture could not ultimately be resolved by all above mentioned methods, however, a complexation reaction was attempted with the $Fe(ClO_4)_2$ salt notwithstanding. Unfortunately, the ligand synthesis reaction produced very low yields (≈ 0.16 g from 1 mL of precursor, 13.2 %). Lower still was the yield from the complex forming reaction. Consequently, due to limited precursor, an extensive study of the resultant (potentially) mixed ligand complex was unfeasible given time constraints. However, atmospheric exposure for arbitrarily long periods showed no discernible impact on the material of the sort described above.

2.3 Preparation of the Complexes

Metal perchlorates are explosive and need to be handled with care. For this reason, the complexes were synthesised in small quantities, requiring repeat syntheses in order to obtain sufficient material for investigation [1].

2.3.1 Synthesis of $Fe_n(\mu_{1,1}\text{-}pyzNO)_{2n-2}(pyzNO)_{3n+2}(ClO_4)_{2n}$ (n = {1, 2})

All syntheses reported in this chapter were either taken directly from Watkins [1], or bear minor variations in temperature and stoichoimetry from those therein outlined.

A solution of 0.1888 g (7.411×10^{-1} mmol) the iron(II) perchlorate (as the hydrated salt, M_r: 254.75 $g.mol^{-1}$) in 7 mL of dry methanol/2,2-dimethoxypropane (MeOH/DMP, 1:1, v/v) was stirred for ca. 24 h before being added with stirring to a similarly prepared solution of 0.4911 g PyzNO (5.111 mmol, ~ 7:1 ratio). Schemes 1a to 3 (section 2.5) show the technique used to generate crystalline product. The product was isolated as red micro-crystallites, and characterised by microanalysis, FT-IR, XRPD, UV/Vis*, DSC, TGA, SEM and EPR.

* UV/Vis characterization was considered largely inconclusive as, owing to insolubility of the complexes in non-polar, non-coordinating solvents, DMSO had to be used for dissolution. The high potential for DMSO to coordinate, thereby altering the original complex, inspired a reluctance to make definitive statements in the interpretation of the resulting spectra. The spectra are nevertheless included in the appendix as supplementary material.

Of the 16 syntheses conducted, this was the trial which produced the highest yield. The recorded mass was 0.1092 g (1.485 x 10^{-1} mmol) giving a yield of 20.04 % (assuming a M_r of 735.1886 g.mol^{-1} (Complex1). The lowest recorded yield was 3.46 %.

2.3.2 Synthesis of {Fe(μ-pyzNO-κ*N*,κ*O*)$_{n-1}$(pyzNO-κ*N*)$_2$(pyzNO-κ*O*)$_2$}$_n$(ClO$_4$)$_{2n}$

A solution of 0.4996 g (1.961 mmol) of iron(II) perchlorate (as the hydrated salt, M_r: 254.75 g.mol^{-1}) in 12 mL of dry MeOH/DMP (1:1, v/v) was stirred for 24 h before being added with stirring to a similarly prepared solution of 0.5666 g PyzNO (5.897 mmol, ~ 3:1 ratio). The protocol as described from scheme 1a to 3 was then employed in the preparation of the product.

The crystals were isolated as deep/blood red rhombus-shaped aggregates with a recorded yield of 2.629 g (60.65 %). The product was characterised by microanalysis, FT-IR, XPS, XRD-single crystal, XRPD, UV/Vis*, DSC, TGA, TG-IR-EGA, SEM and EPR.

Complex1 and Complex2 products were allowed to become hydrated by exposure to the atmosphere. A time-dependent mid-IR hydration study was conducted. The fully hydrated species of Complex1 was thereafter characterized by microanalysis, Mid-IR, XRPD, DSC, TGA, SEM and EPR. The hydrated form of Complex2, [Fe(pyzNO-κ*N*)$_4$(H$_2$O)$_2$](ClO$_4$)$_2$·2H$_2$O, was characterised by single crystal XRD, microanalysis, Mid-IR, XPS, XRPD, DSC, TGA, TG-IR-EGA, SEM and EPR.

2.3.3 Attempted Syntheses of Fe$_n$(μ$_{1,1}$-pyzNO)$_{2n-2}$(pyzNO)$_{3n+2}$(ClO$_4$)$_{2n}$ (n = {1, 2}) and {Fe(μ-pyzNO-κ*N*,κ*O*)$_{n-1}$(pyzNO-κ*N*)$_2$(pyzNO-κ*O*)$_2$}$_n$(ClO$_4$)$_{2n}$ from EtOH/DMP Mixture

A solution of 0.2091 (8.208 x 10^{-1} mmol) of iron(II) perchlorate (as the hydrated salt, M_r: 254.75 g.mol^{-1}) in 12 mL of dry ethanol/2,2-dimethoxypropane (EtOH/DMP) (1:1, v/v) was stirred for 24 h before being added with stirring to a similarly prepared solution of 0.5571 g PyzNO (5.797 mmol, ~ 7:1 ratio). The product rapidly precipitated out of solution as a bright orange solid. It was filtered under N_2, transferred into a dry, N_2-purged vial, recorded (0.8546 g; 8.815 x 10^{-1} mmol, 61% yield) and characterized by Microanalysis, FT-IR, XPS, XRPD, DSC, TGA, TG-IR-EGA, SEM and EPR.

The attempted synthesis of Complex2 from this solvent mixture was similarly performed, varying only the mole ratio of reagents. A solution of 0.3692 (1.449 mmol) of iron(II) perchlorate (as the hydrated salt, M_r: 254.75 g.mol^{-1}) in 12 mL of dry EtOH/DMP (1:1, v/v) was stirred for 24 h before being merged with stirring with a similarly prepared solution of 0.5571 g PyzNO (5.798 mmol, ~ 4:1 ratio). The product rapidly precipitated out of solution as a bright orange solid (0.5479 g, 5.651 x 10^{-1} mmoles, 39% yield).

As with the BipyNO complexes, microanalysis, mid-IR, DSC and FT-IR-EGA analyses showed that the two products were generated from these syntheses were identical and gave the formula $Fe(pyzNO)_6(ClO_4)_2 \cdot 3EtOH$ (Complex3). The results of their characterization were therefore likewise combined.

The hydrated form of this complex was characterized in the same way as those of the 'MeOH/DMP' complexes, and the EPR spectra of its 'dry' and 'wet' species are depicted together in Fig. 5.38 for ease of comparison.

2.3.4 Attempted Syntheses of $[Fe(bipyNO)_5](ClO_4)_2$ and $[Fe_n(bipyNO)_{5n}](ClO_4)_{2n}$

A solution of 0.1997 g (7.839 x 10^{-1} mmol) the iron(II) perchlorate (as the hydrated salt, M_r: 254.75 g.mol^{-1}) in 7 mL of MeOH/DMP (1:1, v/v) was stirred for 24 h before being added with stirring to a similarly prepared solution of 0.9459 g bipyNO (5.493 mmol, bipyNO : $Fe(ClO_4)_2$ ~ 7:1 ratio). Schemes 1a and 1b show the experimental setup for the above described preparation.

An orange precipitate was generated the instant the ligand and metal salt solutions were merged. The resulting suspension was allowed to stand for an hour in order to maximise product yields. The solid product was filtered and dried under N_2, recorded and stored in a desiccator. Further cooling of the filtrate in an ice bath afforded a further small amount of precipitate. The precipitates were combined, recorded and stored in a desiccator awaiting analysis. A yield of 0.9606 g (6.211 x 10^{-1} mmol, 79.23 %) was recorded (assuming a M_r of 1546.6559 g.mol^{-1} ($\{Fe_2(bipyNO)_5(ClO_4)_4 \cdot 6MeOH\}$)). The compound was characterised by microanalysis, mid-IR, XPS, XRPD, DSC, TGA, TG-IR-EGA, SEM and EPR.

The attempted synthesis of $[Fe_n(bipyNO)_{5n}](ClO_4)_{2n}$ was similarly undertaken, changing only the mole ratio of reagents. A solution of 0.1872 g (7.348 x 10^{-1} mmol) the iron(II) perchlorate (as the hydrated salt, M_r: 254.75 g.mol^{-1}) in 7 mL of (MeOH/DMP, 1:1, v/v) was

stirred for 24 h before being added with stirring to a similarly prepared solution of 0.4710 g bipyNO (2.735 mmol, ~ 3.7:1 ratio bipyNO : $Fe(ClO_4)_2$).

An orange precipitate of the same physical consistency as that produced in the attempted preparation of $[Fe(bipyNO)_5](ClO_4)_2$ immediately formed in the reacting solution (0.2160 g, 1.395 x 10^{-1} mmol, 51%). Mid-IR, DSC and TG-IR-EGA results indicated that the products from the two syntheses were the same. The results from their characterisation have therefore been combined and reported as one.

2.4 Chemical Dehydration Process

It was observed that in the synthesis of the complexes Complex1 and Complex2 in an inert, anhydrous or dehydrating medium, followed by crystal growth by the method of vapour diffusion-assisted crystallization, yields blood red crystals [1]. The dehydrating medium employed was a solvent system comprising a 1:1 v/v mixture of dry methanol and 2,2'-dimethoxypropane (DMP). DMP is a chemical dehydrating agent which reacts with water to produce acetone and methanol. One possible mechanism by which water is broken down by DMP is shown in Fig. 2.1.

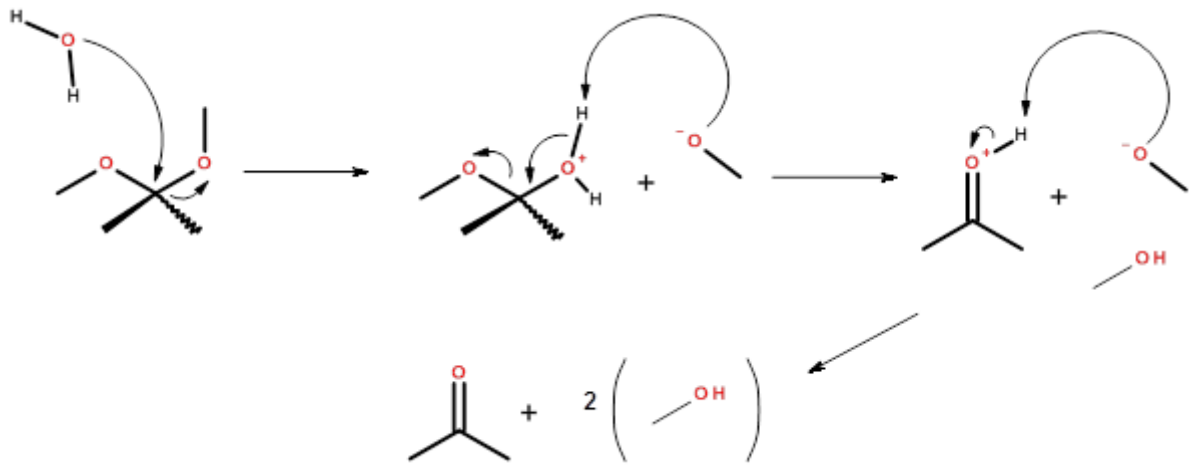

Figure 2.1: Possible schematic pathway showing the process whereby DMP reacts with water to produce acetone and methanol.

The methanol component of the solvent system is used to facilitate the dissolution of the metal salt, which is otherwise insoluble in pure DMP. As the two solvents are readily miscible, their combination made for a suitable mixture for this type of synthesis.

2.5 Glassware and Reagent Pre-treatment Protocol

Two Schlenk-tubes (one for the ligand solution and the other for the metal salt solution) were washed and dried with acetone, and thereafter stored in an autoclave at 60 ^{o}C for 24 h. The Schlenk-tubes were then fitted hot onto a N_2 gas line and immobilized using metallic clamps. They were then allowed to cool whilst simultaneously being purged with dry N_2 gas, after which they were rinsed with a small volume of 2,2-dimethoxypropane (DMP). The gas flow was allowed to persist until all the DMP had evaporated.

Similarly prepared magnetic stirrer bars were introduced, whereupon the Schlenk tubes were stoppered with quick-fit glass stoppers, on which a small amount of Silicone-based vacuum grease had been applied. A moderate vacuum was applied to the Schlenk-tubes *via* taps 1 and 3, ensuring that all other taps (except 2) were tightly shut. When the bubbler indicated no further evacuation, N_2 gas was allowed into the Schlenk tubes. The glass stoppers were then removed for 1 minute, in order to permit a strong N_2 gas flow through the Schlenk tubes, after which the entire process was repeated. Sequential pump and purge cycles were repeated 4 times.

The N_2 gas flow was resumed when the stoppers were removed in order to introduce appropriately weighed solid reagents into their respective Schlenk tubes.

A suitable volume of methanol/DMP (1:1, v/v) solvent mixture (previously stored over 3Å molecular sieves in an inert vessel) was introduced. The Schlenk-tubes were then sealed with rubber septa, followed by magnetic stirring for 24 h to allow complete H_2O decomposition. Positive N_2 pressure was maintained using an N_2-filled balloon connected to a syringe.

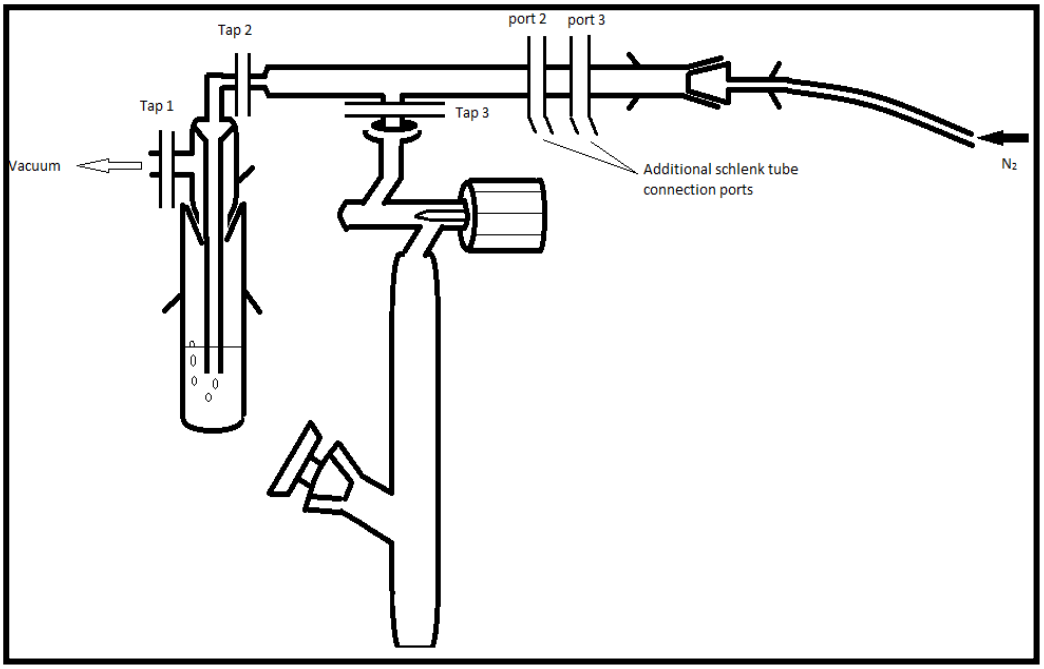

Scheme 1a: Schlenk-type experimental setup employed in the preparation of the individual reagent solutions prior to their merger; towards the synthesis of the anhydrous complexes (only one tube is shown, the other was connected to 'port 2' in the scheme).

2.6 Techniques by which the Crystalline Products were Generated

After a 24 h stirring period, the reagents were merged by means of a cannula, as shown in scheme 1b.

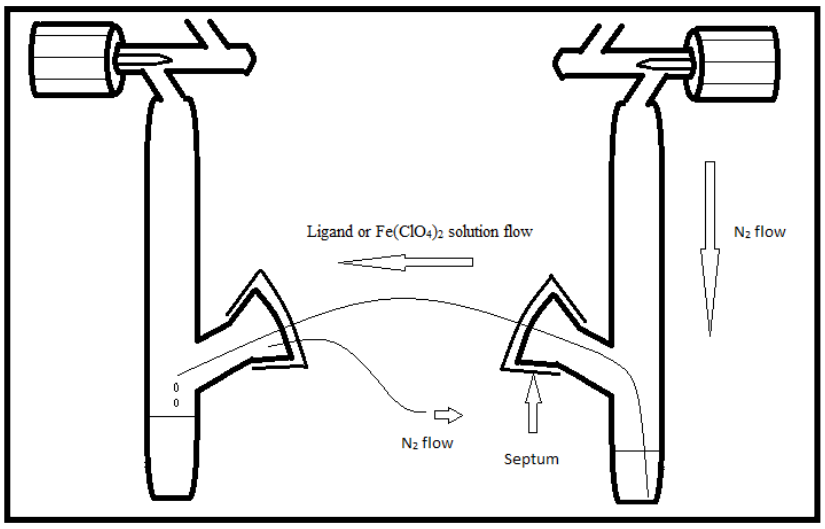

Scheme 1b: Schlenk-type experimental setup employed in the synthesis of the anhydrous complexes, depicting the air-free process by which the reagents are mixed.

The method by which a suitable environment for crystal growth was generated can be outlined as follows:

20 mL of distilled toluene was bubbled with N_2 gas for 30 min, whereupon 2 mL of DMP was added, and bubbling continued for a further 5 min. The dry toluene was then poured into a clean and dry 250 mL Büchner flask. Three sample vials per Büchner flask were then introduced (only one is shown is scheme 2a). The vial-bearing Büchner flask was then flushed with nitrogen for 15 min. The Büchner flask was then sealed and stoppered with a rubber septum. An N_2 filled balloon/syringe (see scheme 2a) was then used to maintain a positive N_2 pressure in Büchner flask interior.

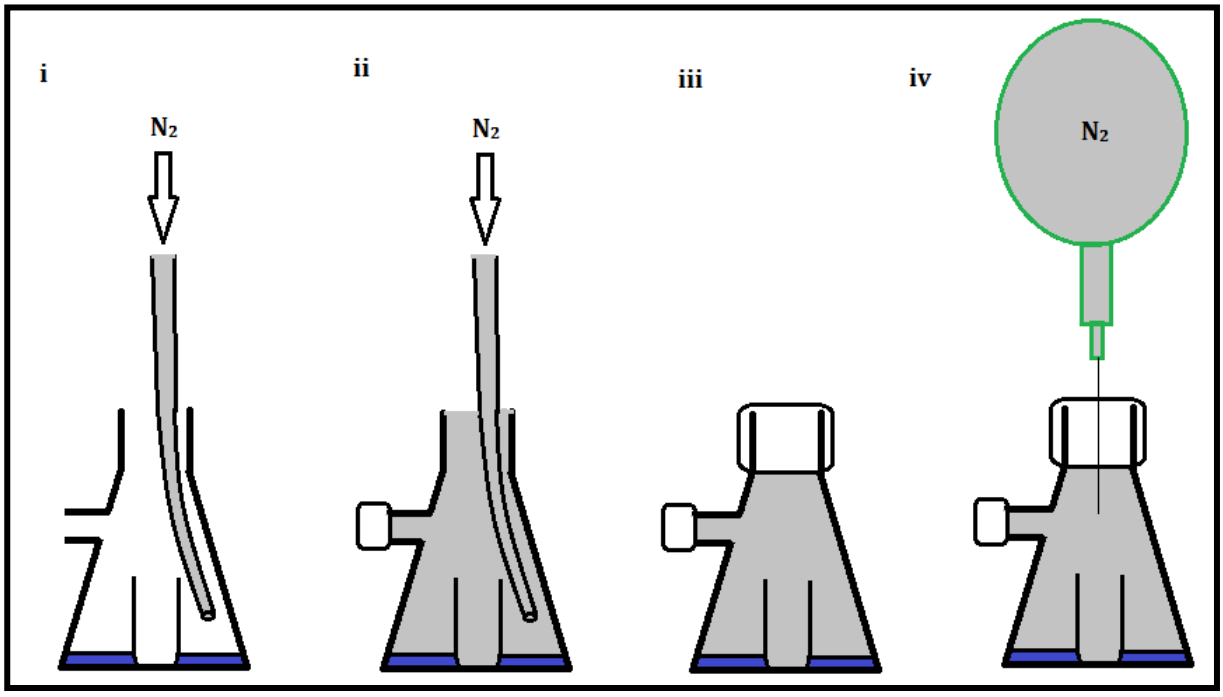

Scheme 2a: Diagrammatic outline of the technique used to saturate (with N_2 gas) the vessel in which the vapour diffusion-assisted crystal growth is facilitated, in order to maintain the inertness of the environment to which the crystals are exposed.

The solution containing the complex was transferred to the vial *via* cannula for vapour diffusion-assisted crystal growth, as shown in scheme 2b. In the preparation of Complex2, minute red crystals became visible after approximately 48 h (as indicated in the scheme), whereas, in the case of Complex1, crystals became visible on storage for 24 h. In the former case, the crystals were allowed to grow for 5 to 6 weeks, whereupon no further growth in size

was readily observed. In the case of Complex1, no further discernible product formation was seen after ~ 14 days.

When the crystals were deemed to have grown sufficiently large (i.e. when no further gain in size could be seen with time), they were filtered under N_2 pressure using a sintered glass disk funnel, (scheme 3), washed with the methanol/DMP mixture, and then dried under N_2. They were transferred to a clean weighing vial (rinsed with DMP, autoclave-dried (60 ^oC, 2 h) and purged with dry N_2 gas, prior) and *immediately* put into a desiccator. Great care was taken throughout this process due to the hygroscopic nature of the products.

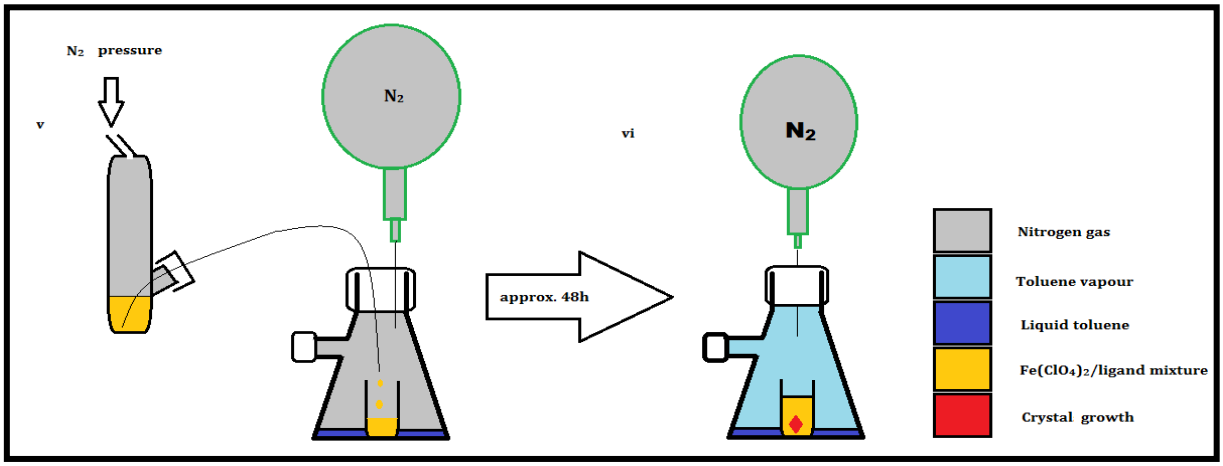

Scheme 2b: Diagrammatic outline of the technique used to transfer the reaction solution from the Schlenk tube for slow vapour diffusion-assisted crystal growth.

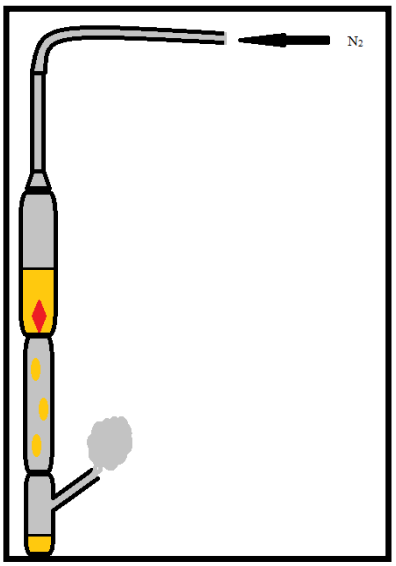

Scheme 3: Diagrammatic outline of the technique used to filter, wash, and dry the crystals generated in the vapour diffusion-assisted method. Colour coding from scheme 2b is used here.

Another technique which was found to be effective for product formation, although the resulting solid product precipitated out of solution as a very fine powder, is shown in Scheme 4. The metal salt and ligand mixture, in lieu of being introduced into the sample vials housed in the Buchner flasks, as detailed above, was introduced into 'B' of scheme 4, using cannula technique. Vessels 'A' and 'B' are boiling tubes which were previously dried, purged with N_2 gas and stoppered with rubber septa. Vessel 'C' is a test tube.

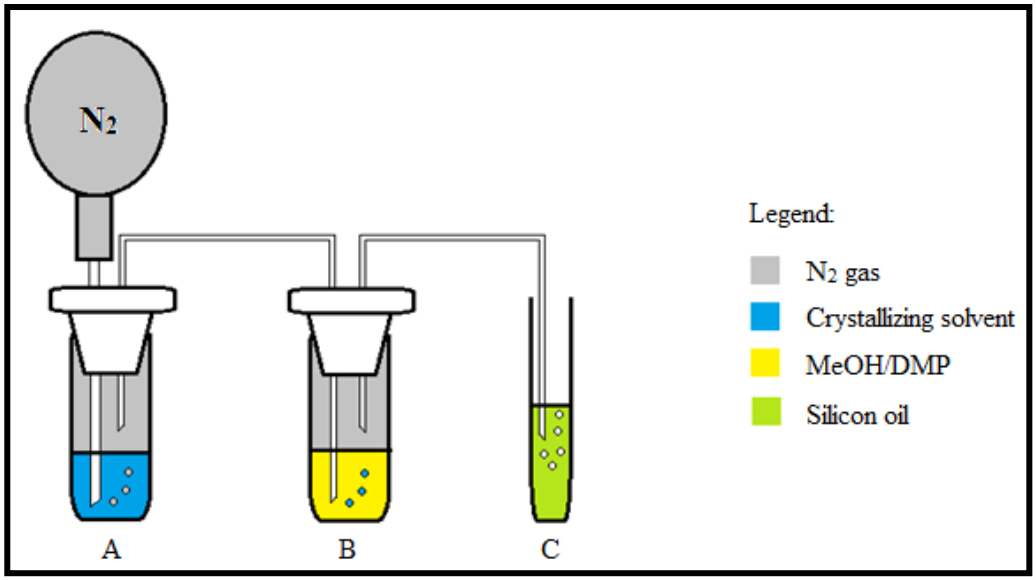

Scheme 4: Diagrammatic depiction of the simultaneous evaporation of the reaction solvent and addition of the crystallizing solvent, in an inert environment.

2.7 Complexes Successfully Synthesised in this Current Work

Four pure iron(II) complexes were successfully synthesised in this work, three of which were seen to undergo significant colour changes upon their exposure to the atmospheric moisture. Of these, three are pyrazine-*N*-oxide (PyzNO) iron(II) perchlorate complexes, whilst the fourth complex was synthesized with 4,4'-bipyridine-*N*-oxide (BipyNO) as the primary ligand. They have been named Complex1 ($Fe_n(\mu_{1,1}\text{-pyzNO})_{2n-2}(pyzNO)_{3n+2}(ClO_4)_{2n}$ (n = {1, 2}); section 2.3.1), Complex2 ($\{Fe(\mu\text{-pyzNO-}\kappa N,\kappa O)_{n-1}(pyzNO\text{-}\kappa N)_2(pyzNO\text{-}\kappa O)_2\}_n(ClO_4)_{2n}$ (n ≥ 2); section 2.3.2), Complex3 ($Fe(pyzNO)_6(ClO_4)_2 \cdot 3EtOH$; section 2.3.3) and Complex4 ($Fe_2(bipyNO)_5(ClO_4)_4 \cdot 6MeOH$; section 2.3.4).

Hydration of Complex1 and Complex2, by exposure to an environment bearing water vapour, produced $Fe(pyzNO)_5(H_2O)_3(ClO_4)_2$ and $[Fe(pyzNO\text{-}\kappa N)_4(H_2O)_2](ClO_4)_2{\cdot}2H_2O$, which have been named Complex5 and Complex6, respectively.

Attempts at growing Complex5 and Complex6 from solution were unsuccessful, despite vigorous scratching and arbitrary solvent reduction procedures. Instead, suspensions of the metal salt and the hexaaqua complex were eventually generated, leaving PyzNO in solution.

Crystallographic studies were undertaken after one week of atmospheric exposure to ensure complete hydration. As the process is ordinarily seen to go to completion within 1 hour (see Fig. 5.10), a week was deemed more than sufficient to ensure complete hydration.

Unfortunately, synthesis of Complex1 (see section 2.3.1) produced very low yields. This made the comprehensive undertaking of comparative studies (especially solvent studies) difficult. Moreover, the success of synthesis was achieved in only 3 of the 16 attempted trials. In the other 13 trials, Complex2 was generated instead, as evidenced by preliminary IR characterization. Many remedial attempts were made to obtain sufficient sample to conduct solvent studies after the appropriate characterization of the product, most of which bore little success. Due to limited precursor availability, and time-constraints, emphasis was directed to the analysis of the Complex2 species. Further solvent studies of the Complex1, beyond the characterization of its hydrated variant, have therefore been reserved for future work.

The PyzNO complexes were all seen to exhibit a substantial colour change upon atmospheric exposure; ascribed to either a hydration-induced spin crossover event, or perhaps purely to solvation effects (solvatochromism). The latter mechanism would not be characterised by an accompanying redistribution of *d* electrons. Rather, a solvation-associated shift in the spectral position of M↔L charge transfer bands would give rise to the observed colour change, with no accompanying change in the complexes' magnetic properties. A synergistic combination of the two processes was considered as a third possible mechanism by which the observed hydration associated spectral shifting could be occurring overall. The aim then, was the assignment of this underlying mechanism by available techniques, as well as to ascertain whether the observed spectral shifting could be extended to other solvents [7-9]. How these complexes in particular came to be generated can be motivated as follows:

SCO can be tuned to exhibit required characteristics ($T_{1/2}$, chromatism, hysteresis, etc.) by modifying the metal centre, the coordinating ligands, the counterions present and the nature of the solvent employed in the synthesis [8-11]. It was therefore of great interest to quantify the significance of these features in terms of the spectral and magnetic behaviour of the resulting species, particularly towards solvent exposure. This motivated the use of the two different solvent systems for the synthesis of the PyzNO complexes. In lieu of the methanol/2,2'-dimethoxypropane (MeOH/DMP) mixture used in the preparation of the first PyzNO complexes, the same syntheses using mixtures of DMP with various other solvents were attempted. Those mixtures included chloroform, acetone, 1,1-trichloroethylene and ethanol. Several others were attempted, however, due to their immiscibility with DMP, those trials were abandoned. Of the aforementioned solvent systems, only the ethanol/DMP (EtOH/DMP) mixture provided adequate dissolution of the $Fe(ClO_4)_2$ metal salt. As a result, this was the only other solvent mixture from which a PyzNO complex could be produced. The resulting complex, herein designated Complex3 (see section 2.3.3), was orange in colour, unlike the bright and deep reds of its respective Complex1 (section 2.3.1) and Complex2 (section 2.3.2) analogues. At this stage, it was clear that the choice of solvent played a strongly influential role in the resulting physical properties of product in this context. The next step then became finding the underlying cause of this, as well as to determine if any other differences existed, subtle or pronounced, that could ultimately be traced back to the method of synthesis.

The PyzNO structural analogue, BipyNO was used in an attempt to synthesize a complex which would be isostructural to the pyzNO complexes. BipyNO bears the general features of PyzNO, the essential difference being that the former has an extended delocalized π-cloud. The two ligands could be said to be isoelectronic, and were thus expected to behave somewhat similarly when placed in the same coordination environment. Any manifest differences in the physical properties of the two types of complexes, particularly with regard to their interaction with various solvents, would then be a reflection of some necessary property of PyzNO (in terms of its complex's behaviour).

As a means towards a more comprehensive ligand-based comparison, pyrazine-*N*,*N*-dioxide ($PyzNO_2$*) and 2-methylpyrazine-*N*-oxide (MePyzNO*) were also synthesized. $PyzNO_2$

* See Appendix on CD-ROM for the synthesis and characterisation of these ligands

was successfully characterized by DSC and ^{1}H NMR to verify its purity. However, upon the attempted synthesis of its Fe(II) perchlorate complexes, it was found to be insoluble in both MeOH/DMP and EtOH/DMP solvent mixtures, even on heating to boiling. Consequently, the synthesis of its associated anhydrous Fe(II) complexes by the technique outlined in sections 2.5 and 2.6 was discontinued. Additionally, the tendency for coordinated $PyzNO_2$ to be readily displaced by water with first series transition metals [1] made the synthesis of an anhydrous complex from an aqueous solution unfeasible.

In the synthesis of MePyzNO, it was found by ^{1}H NMR that the 3-methylpyrazine-*N*-oxide isomer formed in comparable concentration as the desired product. Suppression of the formation of this *side product* was attempted by reagent concentration and temperature variation of the initial synthesis protocol. When these measures were ultimately deemed futile, attempts at the chromatographic separation of the two components were undertaken, also unfortunately with no fruitful outcome. It appeared that the two isomers were virtually indistinguishable in terms of their associated partition coefficients among the mobile and stationary phases (in normal and reverse chromatographic phases). When, as a final measure, recrystallization methods using a variety of different solvents also failed, the synthesis of MePyzNO Fe(II) perchlorate complexes was reserved for future work.

To begin to understand the impact of the counterion on the PyzNO complexes synthesis, an attempt was made at synthesising the PyzNO complexes using iron(II) tetrafluoroborate as the metal salt. However, again owing to difficulties in the solubility of the metal salt in the MeOH/DMP solvent mixture, further progress in this regard could not be made.

Lastly, the synthesis of a cobalt(III) perchlorate PyzNO complex was undertaken in order to determine if the observed spectral and magnetic properties were limited to the PyzNO complexes of iron(II) perchlorate. Cobalt(II) tetrafluoroborate was the only available metal salt, therefore its H_2O_2 oxidation was carried out, followed by the substitution of the counterion for perchlorate by a column-based ion exchange procedure. Recrystallization of the product from methanol afforded purple needle-shaped crystals which were then used for the preparation of the complex as done with the Fe(II) complexes. The resulting red solid was a mixture of various components, with the major product being an orange-red microcrystalline powder as

later confirmed by SEM. In addition, there was a colourless cube-shaped material of unknown composition (presumably the sodium perchlorate salt). The cobalt species was observed to exhibit a colour change to pale orange-yellow upon prolonged atmospheric exposure. The preliminary (qualitative) conclusion was that Co(III) PyzNO perchlorate complexes undergo similar structural and spectral changes as their Fe(II) analogues upon solvent exposure, as later evidenced by mid-IR data. Nevertheless, further characterisation and solvent studies of this complex have been left to future studies.

2.8 Characterisation Techniques

2.8.1 Nuclear Magnetic Resonance

All ligands synthesised in this work were characterised, in part, by Nuclear Magnetic Resonance (NMR) Spectroscopy using a Bruker Biospin 600 MHz Avance Spectrometer.

NMR is a technique whereby the details concerning the structure and interactions of a range of molecules of varying complexity, as well as the kinetics and thermodynamics of their reactions and composite mixtures, can be elucidated; often with unparalleled resolution [11].

In essence, NMR relies on the Zeeman interaction of the magnetic moments of the nuclei of certain amenable atomic species (with half integer spin) to acquire information about the characteristics of the local magnetic field at those positions. The expression for the Zeeman interaction is:

$\mathcal{H}_z = -\mu_n.\mathbf{H}_n$ and $\mu_n = h.\gamma_n\mathbf{I}_n/2\pi$,

where $\mathbf{H}_n$ is the local magnetic field value and μ_n is the nuclear magnetic moment. γ_n and $\mathbf{I}_n$ are the gyromagnetic ratio and the nuclear spin, respectively [11-13].

Generally, a resonance signal is obtained at the Larmor frequency, which corresponds to transitions between adjacent energy levels ($\omega_{NMR} = \gamma_n H_n$), which are initially approximately degenerate, but are split in an applied magnetic field due to the Zeeman effect. With γ_n having been previously accurately determined from calibration on a suitable reference standard, this permits for the very precise measurement of $\mathbf{H}_n$, and therefore, the induced hyperfine field:

$\mathbf{H}_{hf} = \mathbf{H}_n - \mathbf{H}_0$. ($\mathbf{H}_0$ is the applied magnetic field)

The hyperfine field is produced by the sum of electromagnetic interactions between the nucleus and its surrounding electrons, and is thus a unique and diagnostic signature which is characteristic of the local electronic environment. This information can then be exploited to gather detailed compositional and structural insight about materials, including the type and nature of the associated bonding, the geometry, intra- an intermolecular electrostatic interactions, among a myriad of other useful features [11, 12].

In the case of this work, solution-state measurements were performed in a time constant magnetic field with strength on the order of 13.1 T, which was homogeneous over the entire sample volume.

2.8.2 CHNS Microanalysis

CHNS elemental analysis was performed on a Vario MICRO V1.6.2 elemental analysis system. CHNS analysis, or just microanalysis, is a form of thermal gravimetric analysis in which an analyte of interest is separated from all other elements present in a given sample by converting the former into a gas of known chemical composition [10]. This may be done, for example, by the oxidation of the analyte in an O_2 gas-purged electric furnace. The mass of this gas, against that of the remaining mass of the sample from which it was evolved, then serves as a measure of the concentration of the analyte within the sample. In this manner, the weight percentages of carbon, nitrogen, hydrogen and sulphur (by the technique employed in this work), may be obtained.

These experimental percentage masses were then compared to theoretical, calculated values for a variety of hypothesised potential structures which were deemed chemically and logically possible. The best empirical correlation with percentage masses was then identified. The posited structure, from which the best alignment of experimental and theoretical percentage composition was obtained, was made, pending corroborating evidence. This, in combination with mid-infrared, XPS and thermo-analytical data, was the primary source of the proposed structures in this work, where confirmation by single crystal XRD was not possible.

2.8.3 Infrared Spectroscopy

All infrared spectra reported in this work, excluding those from TG-IR analyses, where recorded using a Perkin Elmer Spectrum 100 FT-IR spectrometer with an ATR attachment. The spectra were recorded in the 4000 cm^{-1} to 650 cm^{-1} range. Instrument resolution was consistently kept at 4 cm^{-1} for a total of four scans per sample. All spectra shown were baseline auto-corrected and smoothed using Spectrum version 6.3.5 software.

Infrared spectra originate from transitions between the vibrational ground and excited states within the electronic energy levels of a molecule, and are observed as absorptions in the infrared region [10, 11, 14, 15]. These typically occur between 10000 and 100 cm^{-1}, with the 4000 – 650 cm^{-1} mid-infrared subset falling well within this range. The number, position and relative intensity of these transitions is a characteristic property of each individual analyzed sample, and reflects the unique overall structure of the molecule of interest [15]. Accordingly, the summation of all these observations may then be used as a diagnostic validation of a certain proposed structure [11, 14]. However, symmetry considerations in the context of actual physical molecules in the crystalline state often make the technique less than adequate towards the determination of structure. Symmetry, being generally lower in these cases than in the ideal gas state; as a consequence of intermolecular interactions, causes the complication of experimental spectra beyond theoretically predicable levels. As a result, quantitative assertions made principally by recourse to IR data, without complementary corroboration, may often be less than accurate [15, 16].

The infrared band of main interest in this study is that due to the symmetric N-O (*N*-oxide) stretching vibration, ν_s(N-O), which typically occurs around 1300 cm^{-1}. A shift in position and intensity of this band on complexation, or exposure of the resulting complexes to various solvents, is taken to reveal something of interest. It may indicate a strong intermolecular interaction of the solvent with an uncoordinated *N*-oxide moiety, or the former's substitutive covalent attachment to the coordination sphere itself, and so on [17].

Also of interest are the asymmetric and symmetric stretching vibrations, and the bending vibration of water; ν_a(O-H), ν_s(O-H) and δ(O-H), respectively. The stretches span the range

from 3500 cm^{-1} to 2500 cm^{-1}, and typically indicate strong hydrogen bonding interactions [10, 11].

Lastly, the very strong, broad vibration ascribed to the ClO_4^- anion spanning 1150 cm^{-1} to 850 cm^{-1} is also of some interest. It encompasses both the ν_s(Cl-O) and ν_a(Cl-O) modes, and gives some insights about its possible symmetry, and therefore its chemical environment can generally be gleaned by inspection of the associated FT-IR spectrum [10, 11].

2.8.4 X-ray Photoelectron Spectroscopy

The XPS scans shown in this work were obtained using a Kratos Axis Ultra DLD X-ray photoelectron spectrometer, equipped with a monochromatic aluminium anode, and a charge neutraliser. All scans were performed at an operating pressure of the order of 5,0 x 10^{-9} torr.

Wide XPS scans were performed with an emission current of 10 mA, with the anode (HT) set at 15 kV. A hybrid lens was used and a resolution of 160 eV pass energy was used to acquire the survey scans in slot mode. The centre used for the scans was at 700 eV with a width at 1205 eV. A step size of 1 eV was used, with a dwell time of 0.500 seconds. The resolution was changed to 40 eV pass energy for high resolution scans in slot mode, with a step size of 0.1 eV, and corresponding dwell times of 0.500 s for each analyte.

Tabulated below are the corresponding scan centres and widths for the high resolution scan of each analyte of interest.

The centre and width energies for each of the high-resolution XPS runs

Element	**Centre [eV]**	**Width [eV]**
C 1s	287.5	23.1
N 1s	399.5	21.1
O 1s	533.0	18.1
Cl 2p*	201.5	13.1
Fe 2p	721.0	38.1

*The ‘undeconvoluted’ scans of the complexes’ Cl 2p regions are included in the Appendix for completeness, but had limited diagnostic utility insofar as the determination of structures was concerned.

X-ray photoelectron spectroscopy is based on the principles underlying the photoelectric effect. That is, the process whereby a photon of sufficient energy may remove an electron from a sample if this energy is greater than the electron binding energy (BE). By bombarding the sample with a stream of such photons, and subsequently measuring the energy of ejected electrons, the corresponding BE of the latter can be determined [16]. The measured BE of the electron is dependent on the element; and the associated sub-shell, the element's oxidation state, and chemical environment of the atom from which the electron was ejected. Therefore, XPS may be used as a technique by which to understand differences in the chemical environment of various atoms within the sample, including speciation effects, and so on [16].

In terms of this current work, of particular interest was the iron(II) ion (2p), and the carbon (1s), nitrogen (1s) and oxygen (1s) atoms within the complexes; and any possible differences between the hydrated and anhydrous variants in terms of binding energies and peak intensities. Included also (appendix), for the purposes of completeness, are the high resolution scans of chlorine 2p region.

Origin version 6.1 software was used for the deconvolution of the high resolution scans where appropriate, in order to resolve overlapping peaks.

2.8.5 X-ray Powder Diffraction

A Bruker D8 Discovery X-ray powder diffractometer was used to conduct the X-ray powder diffraction studies, using copper K_α radiation (λ_1 = 1.54060 Å, λ_2 = 1.54439 Å, ratio = 0.5), and a nickel filter to minimize X-ray divergence. The generator tube was operated at a potential of 40 kV with a current of 40 mA. The divergence slit width was 0.6 mm and the primary Soller slit was 4.0°.

The general principle upon which powder X-ray diffractometry is based as a means towards the evaluation of the molecular physical dimensions, by which a material is characterised, relies on the scattering of X-ray photons incident upon it, by its unique pattern and distribution of electron density. When an X-ray beam of suitable wavelength approaches an arbitrary crystalline material, it is scattered by the latter's constituent atoms in a manner that conforms to the Laue equations [18]. It is generally more practically useful to envisage the X-

rays as being reflected off the crystal lattice planes of the material. On this view, Bragg's law; which relates the wavelength of the incident X-rays (λ), the X-ray angle of incidence (θ), the interplanar separation of successive lattice planes (d), and n, an integer, by the following simple equation: $n\lambda = 2dsin\theta$, may be used. Operationally then, the positions of the reflections (*viz.* θ) as measured by the detection apparatus, can be used to uncover the dimensions of the unit cell; the basic repeating unit upon which the macroscopic structure is generated [19, 20].

These dimensions within the unit cell may include (but are not limited to) bond angles, torsion angles, bond lengths, the relative positioning of its constituent atoms, as well as its overall size. Therefore, this technique often provides an excellent indication of any structural changes that an analyte may have incurred subject to some or other stimulus, by collecting the diffraction pattern before and after exposure [18, 19, 21].

In this work, X-ray powder diffraction is used as a qualitative means by which to detect any structural influences exerted by a variety of different solvents on the pyrazine-*N*-oxide* and bipyridine-*N*-oxide complexes produced. In particular, the solvent's impact on the size of the unit cell is of interest. Since the position of the each X-ray reflection is a property of certain elements or features of the unit cell, a change in the former indicates that various structural changes will have occurred, including the size and shape of the latter. It is these differences (if any) which were sought after upon the exposure of the complexes to each solvent.

2.8.6 Differential Scanning Calorimetry

A Perkin Elmer Differential Scanning Calorimeter DSC 6000 was used to record the DSC thermograms reported in this thesis. Calorimetric power-compensation is the configurational principle upon the system operates. Pyris version 11.0.3.0470 software was used for instrument setup, as well post-analysis data processing. Powdered samples of predetermined mass, using a microbalance apparatus, were heated to varying temperatures, depending upon the aim of the analysis. Generally, a 30 ^{o}C – 445 ^{o}C heating profile was employed for preliminary analyses.

*The XRPD pattern of the Complex1 powder was obtained after the sample was mixed with a small amount of petroleum jelly. This was done in order to exclude atmospheric moisture, which was otherwise found to result in the yellow species during previous analyses.

Upon determination of the decomposition temperature (typically 170 ºC to 250 ºC), suitable truncation of the previous range was preferred in order to save time, particularly in the solvent studies. The reference material was an empty sample pan of the same material as that in which the sample was held. Sample masses ranged from 2 to 4 mg, using a heating rate of 10°C.min^{-1} under a nitrogen atmosphere throughout. The N_2 gas flow was kept at 20 mL.min^{-1}, whilst continuously recording the difference in the power supplied to the sample and the reference, in the DSC furnace.

Power-compensating DSC instruments maintain a constant temperature where the sample and the reference material are concerned, throughout a preset temperature programme [22]. Processes in a sample that inherently require, or give off energy (endothermic and exothermic, respectively) tend to change the sample's local temperature, either negatively or positively. These processes occur often at tandem during a heating profile, and require alternating higher and lower power investments, respectively, in order to suppress temperature fluctuations [23]. A reference material (an empty sample pan in this case) is chosen which maintains a constant base line heat flow throughout the preset thermal profile. Alternatively, the instrument is calibrated such that any heat transfer processes associated with the reference material, are taken to represent the baseline. Therefore, the power required to change its temperature linearly, is typically 'constant'. The difference then, in the power that is supplied by the instrument in order to maintain a constant temperature in both sample and reference materials is recorded. This is then translated into the form of a heat flow (endo or exo) versus temperature thermogram. Determination of the peak area for a given process in such a thermogram is undertaken, and its value is taken to be proportional to the associated enthalpy change (ΔH) [22, 23].

In this work, the enthalpy associated with the loss of various guest solvent molecules, either held by physical or chemical adsorption, was of particular interest. This enabled the quantification of the extent and reversibility of their interaction with the complexes under study. Some solvents were seen to change the overall structure of the complexes altogether, either by way of complete dissolution, or by the substitution of bound ligand in the coordination sphere. Ultimately, the nature and origin of any solvatochromic effects observed as a consequence of the solvent/complex association could at least be partly gleaned by the

examination of their corresponding thermal profiles. In general, large enthalpy changes were taken to indicate a strong interaction, whereas small such changes meant that the solvent was relatively loosely held by the complexes. Any colour changes in the latter cases were then likely only surface localised effects, mediated principally by weak intermolecular interactions. Additionally, some solvents were seen to either stabilize or destabilize the complexes towards thermal decomposition. This was reflected in a change in the temperature of the associated exotherms.

2.8.7 Thermal Gravimetric and Evolved Gas Analyses

A Perkin-Elmer TGA 4000 fitted with an FT-IR attachment was used to conduct the thermal gravimetric analysis. Pyris version 11.0.3.0470 software was used for data processing, including the calculation of the depicted first derivative curves. Temperature programs employed were varied between 30°C to 350°C, 30°C to 400°C and 30°C to 900°C depending upon the specific result sought after, and the product under analysis. A fixed heating rate of 10°C.min^{-1} was used for all analyses, with an accompanying nitrogen purge gas flow rate of 20 mL.min^{-1}.

The FT-IR unit used is a Perkin Elmer Frontier FT-IR spectrometer with an ATR attachment. The wavenumber range between 4000 cm^{-1} and 650 cm^{-1} was scanned. Perkin Elmer Spectrum TimeBase software version 3.1.2.0041 was used for instrument configuration and processing of evolved gas infrared data. A Perkin Elmer TL 8000 TG-IR-GCMS interface was used to pump effluent evolved gases (TG exhaust) from the TG furnace to the FT-IR for analysis.

The thermal gravimetric analysis (TGA) thermogram ordinate and abscissa units employed were percentage weight (% mg) and sample temperature (^{o}C), respectively, and were recorded throughout the heating profile.

TGA is an analytical technique whereby the weight of a sample is accurately measured against its temperature, or the temperature of its surroundings (TG furnace), in a controlled, often inert environment. An ‘initial sample mass’ is necessarily measured at the onset of a TG experiment, such that the percentage of the sample remaining throughout the heating profile can be calculated. The transfer of heat generated by the TG furnace into the sample has the

impact of volatilising increasingly strongly held components of the latter, as a function of temperature. These evolved fractions are then carried away by the purge gas at a fixed flow rate, such that the mass of the remaining solid can be related to the specific temperature at which the evolution took place [22-24]. A typical TG temperature program is often configured to include the final decomposition of the analyte of interest. As a result, one may assess the impact of the treatment of a material, chemical or otherwise, on its associated thermal stability.

In the context of this work, TGA is used to evaluate the extent (if any) of the solvent interaction or uptake of the various complexes of interest, as well the solvents' impact on the complexes stability towards thermal decomposition.

The above technique is then used in combination with its FT-IR attachment in an attempt to determine the nature and identity of the aforementioned evolved fractions. This latter unit employs a pump, the flow rate of which can be programmed so as to compliment the TG gas flow rate, which extracts evolved gases from the TG furnace for infrared analysis. The FT-IR can be programmed to records an infrared spectrum per desired or appropriate unit of time (or temperature) throughout the TG heating profile.

It therefore becomes possible (ideally) to determine the identity of each evolved fraction. This technique is however often limited by the fact that different gases often coincide, with respect to the temperature at which they are evolved by the analyte. Complex infrared spectra, which are difficult to interpret, may then result. This is especially the case at sample decomposition, as the process may expel a myriad difference gases simultaneously, making the resulting spectrum nearly impossible to ascribe to any manageable number thereof.

There is also an inherent lag between the time (and temperature) at which gas evolution in the TG furnace takes place, and that at which the FT-IR records a spectrum. This lag is a consequence of the length of the tube that connects the two instruments, and varies as an inverse function of the pump rate used. The pumping rate cannot however greatly exceed the TG N_2 gas flow, as this may have one of two potential consequences. Firstly, if the furnace is sealed well, a partial vacuum may result thereby increasing the vapour pressure of evolved gases such that the associated weight losses occur at lower temperatures, giving unreliable thermograms. Secondly, if the furnace is not completely sealed, the resulting pressure differential against the TG exterior results in the inflow of air making the sample susceptible to various O_2-mediated oxidative processes. Another consequence of the second possibility would

be the detection of atmospheric components (especially H_2O and CO_2) by the FT-IR attachment, thereby producing misleading EGA results.

Finally, sample preparation, as with most analytical techniques plays a crucial role in obtaining reliable and consistent TG data. A sample characterised by a broad particle size distribution must necessarily be rendered uniformly powdered before analysis [20]. A TG profile may reveal even subtle differences in grain size, which might appear as broad, apparently continuous weight loss steps, depending upon the thermal conductivity of the sample. The use of fine powders may circumvent this due to their inherently greater thermal conductivity relative to loosely packed grains of varying size [22-24]. For this reason, the crystalline compounds were powdered before being introduced into the TG furnace. In terms of the solvent studies, the milling took place before the introduction of samples to the solvent vapour-saturated vessels, prior to TGA. All milling processes were conducted under N_2 gas flow in order to minimize atmospheric exposure.

2.8.8 Scanning Electron Microscopy

The SEM micrographs of the complexes were taken using a TESCAN Vega TS 5136LM electron microscope. In vacuo gold sputter-coating of the samples was employed in order to enhance surface conductivity and the resolution of the resulting micrograph.

SEM is an analytical technique by which the surface topography of a suitable solid substrate can be determined. This is achieved by scanning a beam of electrons over the conducting material. When the substrate is ‘struck’ by the electron beam it either releases secondary electrons resulting from the excitation, thereby becoming ionized in the process, or it scatters the incoming beam by inter-electronic elastic repulsion [25, 26]. Other signals which are produced include characteristic X-rays, which are measured in energy dispersive X-ray spectroscopy. The secondary and back-scattered electrons (BSE’s) arrive at a detector, and the variation in their energy and intensity is related strongly to the position and atomic number of the elements at or near the substrate surface. Consequently, they are used to generate its 2-D topographical and compositional surface structure [16, 25, 26].

Substrates are generally coated with a sub-micron thick layer of suitable conducting material in order to improve their conductivity. The improved conductivity enables a better interaction between the beam and substrate. That is, it enhances the signal-to-noise ratio of BSE's and secondary electrons arriving at the detector, thereby producing an image of improved resolution [25, 26].

2.8.9 Electron Paramagnetic Resonance Spectroscopy

The EPR spectra shown were recorded on a Bruker EPR 300E X-band (10 GHz) spectrometer equipped with a flat quartz cell. As the G-parameters were unable to be calculated due to a failure in obtaining a conventional, resolved EPR spectrum, spin Hamiltonian parameters could not be simulated. A static field of 3400 G was used, with the center field being varied according to the sample under analysis. The modulation amplitude was kept constant at 19.19 G, while a time constant of 10.24 ms and an accompanying conversion time of 5.12 ms was used. The resolution was varied between 1024 and 10000 pts, with the modulation frequency held constant at 100 kHz. Both 298 K and 77 K studies were conducted.

EPR spectroscopy is based upon the exploitation of the Zeeman Effect; which is the lifting of the degeneracy of the two spin states ($+\frac{1}{2}$ and $-\frac{1}{2}$) of a *free* electron by the application of a homogeneous external magnetic field. The resulting difference in the energies of the two spin states is proportional to the strength of the applied field. Irradiation of this system with photons, whose energy is equal to this energy difference, then may stimulate resonance between the two spin states. That is, photons of this energy will be absorbed by the sample, such that at this wavelength, an intensity diminution will be observed at a suitable detector, when the sample is placed in the path of beam [27]. As the Zeeman splitting is very small, oftentimes impossible to detect even in strong magnetic fields, the radiation employed is of the subset of microwaves.

Operationally, two possible EPR modes are possible in principal. The first would employ the maintenance of constant magnetic field strength, whilst varying the frequency of the microwave beam until resonance occurs. And the second keeps the microwave frequency constant while varying the field strength. In practice, the latter mode is found to be more

convenient (readily available microwave sources produce a relatively small number of different wavelengths), and is thus preferred in conventional EPR [16, 28, 29].

As electrons are never ‘free’ their properties are constant reflections of the (chemical) environment in which they are held. And the electromagnetic influences of the latter; including other electrons, nearby nuclei, and so on, confer to the ‘analyte’ electron features that may be distinguished by an EPR experiment. The technique therefore, although limited to paramagnetic species, can often provide a wealth of information of the chemical nature and molecular configuration of a material.

Of significance in this work is the demonstration of the solvent-induced low spin (LS) to high spin (HS) crossover; posited as the mechanism underlying the associated red-yellow and orange-yellow absorbance/emission spectral shifts. The drawback, however, is the phenomenon of zero-field splitting (zfs) associated with S = 2 ions. The inherent lifting of the aforementioned spin state degeneracy due to inter-electronic interactions, often complicates their EPR spectra beyond workable levels. This is caused by anisotropic orbital angular momentum contributions in reduced symmetry environments, which, even without an applied magnetic field, remove degeneracy of the ‹S,M_S| level [28]. Generally, if one has a sufficiently sophisticated EPR instrument such that the detection of the HS signal is even possible in the first place, the more unpaired electrons are present, the more complicated the resulting spectrum. This is the purported explanation for the highly complicated spectra of the HS complexes (S = 2) herein reported.

2.8.10 Solvent Studies

In preparation for FT-IR and thermal analysis, each crystalline complex (pyrazine-*N*-oxide complexes) was milled under nitrogen gas flow using a Schlenk-type apparatus using a spatula. This was done in order to maximally exclude the atmosphere in order to circumvent the effects of exposure to atmospheric water vapour. The procedure was deemed unnecessary for the 4,4’-bipyridine-*N*-oxide complex, as well as that derived from the ethanol/2,2’-dimethoxypropane solvent system; as these products precipitated out of solution as fine powders upon their syntheses. Thereafter, the powders were placed on clean, dry DSC sample pans and then

introduced into a sample vial saturated with the solvent vapour of interest. Fig. 2.2 shows an example of the vapour saturated vessels in which the samples were placed for solvent exposure.

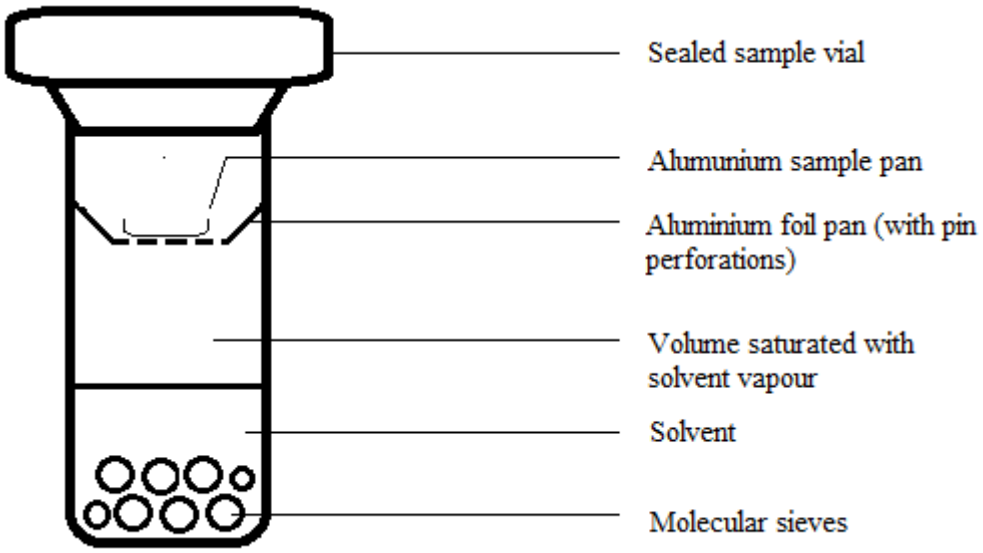

Figure 2.2: Solvent vapour-saturated sample vial employed for solvent studies.

The pyrazine-*N*-oxide samples were placed in these vessels for a period of 72 hours in order to permit the solvent to sufficiently permeate the solid mass, with the following exceptions. Preliminary studies revealed that exposure for extended periods in vessels saturated with acetonitrile, acetaldehyde, dimethylsulphoxide, ethanol, formaldehyde, formamide, methanol and *N*,*N*'-dimethylformamide, resulted in the complete dissolution of the complexes. Therefore, exposure time for these solvents was limited to 90 minutes. The 4,4'-bipyridine-*N*-oxide complex did not exhibit this behaviour upon exposure to all the solvents evaluated except gradually in DMSO. For this reason, all solvent exposure for this complex was kept at 72 hours, but with the exception, where it was limited to 5 hours. After these periods of exposure, sufficient sample was weighed on the microbalance, whereupon characterisation by thermal analysis was *immediately* conducted.

The same procedure was employed for characterisation by EPR and XRPD, although in these cases, a few representative solvents were chosen due to limited instrument availability.

Thermoanalytical solvent studies of Complex3-acetaldehyde were unsuccessful due to the rapid and complete dissolution of the material in the solvent vapour saturated atmosphere.

References

[1] **Watkins, G.M.** (1988). *Ligand Isotope Vibrational Studies of Metal(II) Complexes*. Doctoral thesis. Cape Town: University of Cape Town (1988).

[2] **McKay, S. E.; Lashlee, R. W.; Maina, L. W.; Wheeler, K. A.; Brown, A. B**. Synthesis of bipyridine-*N*-oxides and bipyridine-*N,N'*-dioxides. *Heterocyc. Commun.* **13** (2009), 186.

[3] **Klein, B.; Berkowitz, J**. Pyrazines. I. Pyrazine *N*-oxides. Preparation and spectral characteristics. *J. Amer. Chem.* **81** (1959), 5160-5165.

[4] **Carey, F. A.; Sundberg, R. A**. *Advanced Organic Chemistry*. 5th ed. Springer, New York, USA (2007).

[5] **Eicher, T.; Hauptmann, S.; Speicher, A.** *The Chemistry of Heterocycles: Structures, Reactions, Synthesis, and applications*. 3rd ed. (rev), Wiley-VCH, Weinheim, Germany (2013).

[6] **Royer, J** (Ed.). *Asymmetric Synthesis of Nitrogen Heterocycle*s. Wiley-VCH, Weinheim, Germany (2009).

[7] **Isley, W. C.; Zarra, S.; Carlson, R. K.; Bilbeisi, R. A.; Ronson, T. K.; Nitschke, J. R.; Gagliardi, L.; Cramer, C. J**. Predicting paramagnetic ^{1}H NMR chemical shifts and state-energy separations in spin-crossover host-guest systems. *Phys. Chem. Chem. Phys.* **16** (2014), 10620-10621.

[8] **Speca, A.N.; Pytlewski, L.L.; Karayannis, N.M**. Pyrazine-*N*-oxide complexes with 3d metal chlorides. *J. Inorg. Nucl. Chem*. **35** (1973), 4029-4031.

[9] **Nordlander, E.; Whalen, A. M.; Prestopino, F**. Iron 1993. *Coord. Chem. Rev*. **146** (1995), 229-249.

[10] **Skoog, D. A.; West, D. M.; Holler, F. J.** *Fundamentals of Analytical Chemistry*. 7th ed. Saunders College Publishing, Orlando, Florida, USA (1996).

[11] **Banwell, C.N.** *Fundamentals of Molecular Spectroscopy*. 2nd ed. McGraw-Hill Book Company (UK) Ltd., Maidenhead, Berkshire, England (1972).

[12] **Berthier C.; Horcatic, M.; Julien, M.-H.; Mayaffre, H.; Kramer, S.** Nuclear magnetic resonance in high magnetic field: Application to condensed matter physics. *C. R. Physique.* **18** (2017), 331-340.

[13] **Mlynarik, V.** Introduction to nuclear magnetic resonance. *Anal. Biochem*. **529** (2017), 4-9.

[14] **Nakamoto, K**. *Infrared and Raman Spectra of Inorganic and coordination compounds*. 6th ed. John Wiley and Sons, Inc., New Jersey, USA (2009).

[15] **Nyquist, R. A. and Kagel, R. O**. *Handbook of Infrared and Raman Spectra of Inorganic Compounds and Organic Salts*, vol. 4. Academic Press, Inc., Chestnut Hill, Massachusetts, USA (1997).

[16] **Scott, R. A. and Lukehart, C. M.** *Application of Physical Methods to Inorganic and Bioinorganic Chemistry*. 1st ed., John Wiley & Sons Ltd., New York, USA (2007).

[17] **Thornton, D. A. and Watkins, G. M.** An assessment of the assignment of characteristic N-O vibrations in aromatic *N*-oxides. *Spectrosc. Lett*. **25** (1992), 1023-1031.

[18] **Bloss, F. D**. *Crystallography and Crystal Chemistry*. Holt, Rinehart and Winston, Inc., New York, USA (1971).

[19] **de Jong. W. F**. General *Crystallography: A Brief Compendium*. W.H. Freeman and Company, New York, USA (1959).

[20] **Azároff, L. V. and Buerger, M. J**. *The Powder Method in X-ray Crystallography*. McGRAW-HILL book company, New York, USA (1958).

[21] **Cullity**, **B. D.** *Elements of X-ray Diffraction*. 2nd ed. Addison-Wesley. Massachusetts, USA (1978).

[22] **Brown, M. E**. *Introduction to Thermal Analysis Techniques and Applications*. 2nd ed. Kluwer Academic Publishers, Dordrecht, Netherlands (2001).

[23] **Haines**, **P. J.** *Thermal Methods of Analysis: Principles, Applications and Problems*. 1st ed., Blackie Academic and Professional, an imprint of Chapman Hall, Glasgow, Scotland (1995).

[24] **Wunderlich, B**. *Thermal Analysis*. Academic Press Inc., San Diego, California, USA (1990).

[25] **Goldstein, J.; Newbury, D.; Joy, D.; Lyman, C.; Echlin, P.; Lifshin, E.; Sawyer, L.; Micheal, J.** *Scanning Electron Microscopy and X-ray Microanalysis*. Springer, New York, USA (2003).

[26] **McMullan., D.** Scanning Electron Microscopy 1928-1965. *SCANNING*. **17** (1995), 175-178.

[27] **Weil, J. A. and Bolton, J. R.** *Electron Paramagnetic Resonance: Elementary Theory and Practical Applications*. 2nd ed., John Wiley & Sons Ltd, New Jersey, USA (2006).

[28] **Harriman, J. E. and Loebl, E. M.** *Theoretical Foundations of Electron Spin resonance*. Phys. Chem.: A Series of Monographs, **37**, New York, USA (1978).

[29] **Krzystek. J.; Smirnov, D.; Schlegel, C.; van Slageren, J.; Telser, J**. High-frequency and –field EPR and FDMRS study of the $[Fe(H_2O)_6]^+$ ion in ferrous fluorosilicate. *J. Mag. Res*. **213** (2011), 158-159.

Chapter 3

Characterisation of the Ligands

3.1 Pyrazine-N-oxide

3.1.1 Microanalysis

Table 3.1: CHNS microanalysis of PyzNO product

Trial number	Experimental (%)				Calculated (%)			
	C	H	N	S	C	H	N	S
1	49.88	4.181	29.14	0	49.99	4.196	29.15	0
2	49.74	4.279	28.94	0				
Average	49.81	4.230	29.04	0				
Δ (%)$_{exp\ vs\ calc}$	-0.18	+0.034	-0.11	-				

The CHNS microanalysis of PyzNO shows excellent agreement with the calculated values of the anhydrous product (M_r: 96.088 g.mol^{-1}). The small negative deviations shown by the C (-0.18%) and N (-0.11%) values, and accompanying the small positive shift in the H (0.034%) value is likely due the adsorption of a trace atmospheric moisture by the product. This is evidenced by the ^{1}H NMR spectrum, and to a lesser extent, by thermogravimetric FT-IR evolved gas analysis (TG-IR EGA) stack plot* of the product. The marginal decreases in the C and N values, and the corresponding increase in the H value between successive CHNS runs, also corroborate this, and are due to the *prolonged* handling of the sample outside a desiccator.

The melting point found for PyzNO, using a capillary tube oil-based apparatus and visual inspection to determine any physical changes, seemed at the onset to agree excellently with the literature [1]. A melting point of 110 – 112 ^{o}C was found by this method.

* See Appendix on CD-ROM

3.1.2 Differential Scanning Calorimetry

Differential scanning calorimetry (DSC) revealed some interesting physical properties in the thermal profile of the compound which placed uncertainty in the literature melting point values. Some of these features will be discussed in the DSC characterisation section below.

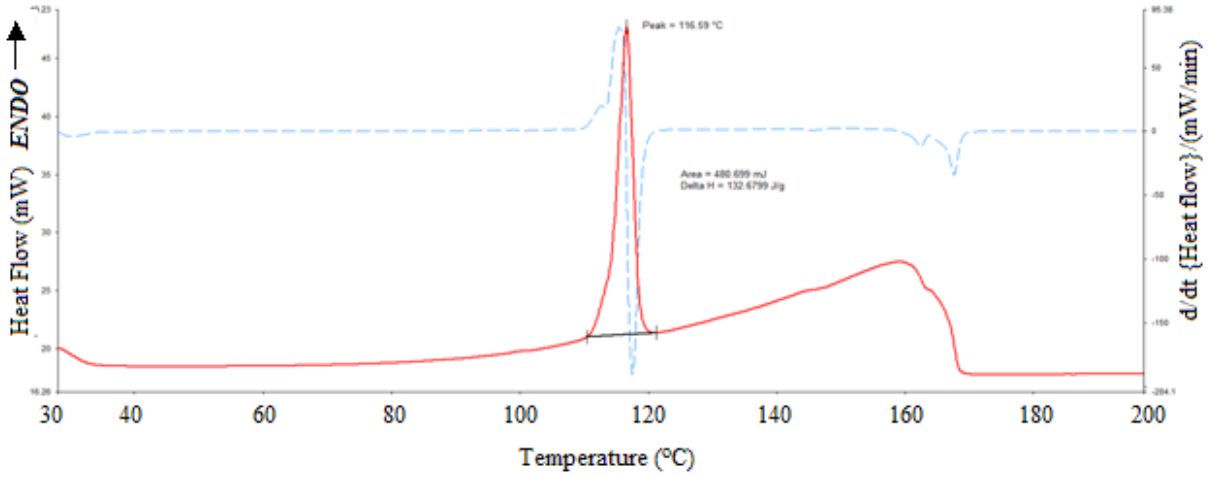

Figure 3.1: DSC thermogram (temperature range: 30 – 200 °C, heating rate: 10 °C.min^{-1}) of intact crystals of PyzNO (red). Derivative curve is shown in dashed blue. ΔH M.P. = 132.68 J.g^{-1} (12.749 kJ.mol^{-1}).

The melting point of PyzNO was given as 104 °C by Speca *et al.* [2] and as 112 – 113 °C by Thornton and Watkins [3]. In this work, DSC gave a melting point of 111 °C (T_{onset}), which is within the latter range. The single peak corroborates the purity of the ligand. The broad endotherm after the melting point is due to the gradual evaporation of liquid PyzNO from the open DSC sample in the furnace, which is completely lost at 168 °C. No discernible residue remained on the sample pan upon inspection, after the latter had been allowed to cool to room temperature.

3.1.3 Mid-IR Spectroscopy

Shown consecutively in Fig. 3.2 are the mid infrared spectra of pure pyrazine (Pyz), the crude product after the H_2O_2 *N*-oxidation reaction, the pyrazine-*N*-oxide (pyzNO) product, and finally, the residue after vacuum sublimation. The Figure shows the appearance of an intense band (not present in pyrazine and of medium intensity in the residue). The systematic

comparison of the FT-IR spectra after each consecutive treatment in the synthesis of PyzNO ligand revealed the sought after differences that indicated the success of the *N*-oxidation reaction.

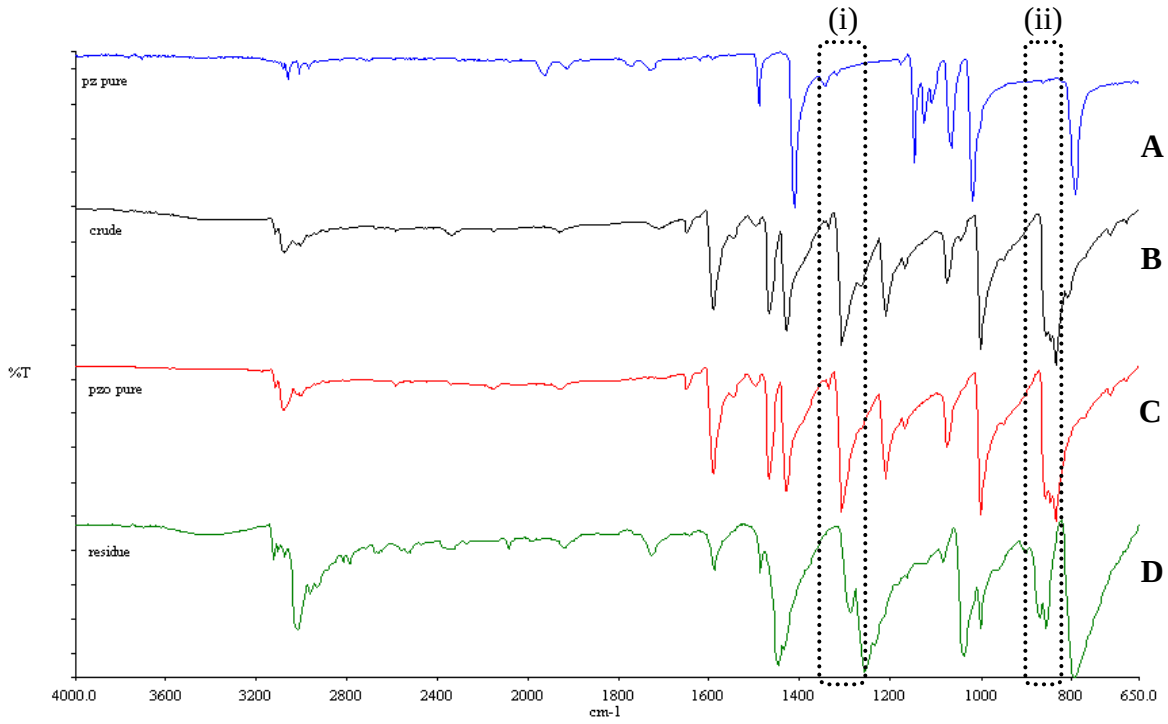

Figure 3.2: Split-display FT-infrared spectra (4000.0 – 650 cm^{-1}) of pure pyrazine (A), crude product (B), pure pyrazine-*N*-oxide after vacuum sublimation (C), and the remaining non-volatile residue (D). Boxed are the regions containing the (ν(NO) + ν(ring)) bands; (i) and (ii).

The mid-infrared spectrum recorded for PyzNO is in very good agreement with the literature in terms reported assignments of the associated fundamentals [3]. As mentioned above, what was of particular diagnostic significance was the appearance of the characteristic symmetric ν(NO) band at 1309 cm^{-1} that was not found in the precursor Pyz. This feature was deemed sufficient to make the preliminary conclusion that the *N*-oxidation reaction was for the most part successful, and no undesired side products were present in quantity. The further comparison of the IR spectrum of the product with the residue resulting from the purification of the crude mixture by vacuum sublimation further corroborates this view. The 'fingerprint' region; which perhaps bears most of the subtle vibrations that ascribe to a compound its uniqueness in mid-infrared spectroscopy, is fully assigned [1, 3, 4] with one exception, the strong band at 847 cm^{-1}. All assignments, including those of the spectra recorded for the PyzNO products in further syntheses, are tabulated in table 3.2.

Table 3.2: Infrared assignment (650-4000 cm^{-1}) of Pyrazine-*N*-oxide [3, 4]

PyzNO	Assignment
3079 mbr	ν(C-H)
1650 w	α(ring)
1593 s	α(ring)
1468 s	ν(C-H)
1431 s	ν(ring)
1338 w	Unassigned
1309 s	ν(N-O) + ν(ring)
1211 s	ν(ring)
1075 m	α(C-H)
1003 s	ν(ring)
859 s	ν(ring) + ν(N-O)
847 s	Unassigned
836 vs	γ(C-H)

w = weak; m = medium; mbr = medium broad; s = strong; vs = very strong.

3.1.4 ^{1}H and ^{13}C Nuclear Magnetic Resonance Spectroscopy

For the purposes of completeness, ^{1}H and ^{13}C nuclear magnetic resonance (NMR) data were deemed important, especially in determining the purity of the PyzNO product conclusively.

Fig. 3.3 (i) shows the 600 MHz ^{1}H NMR spectrum of PyzNO with the precursor pyrazine included for the comparison their respective chemical shifts. Fig. 3.3 (ii) shows the spectrum of PyzNO alone.

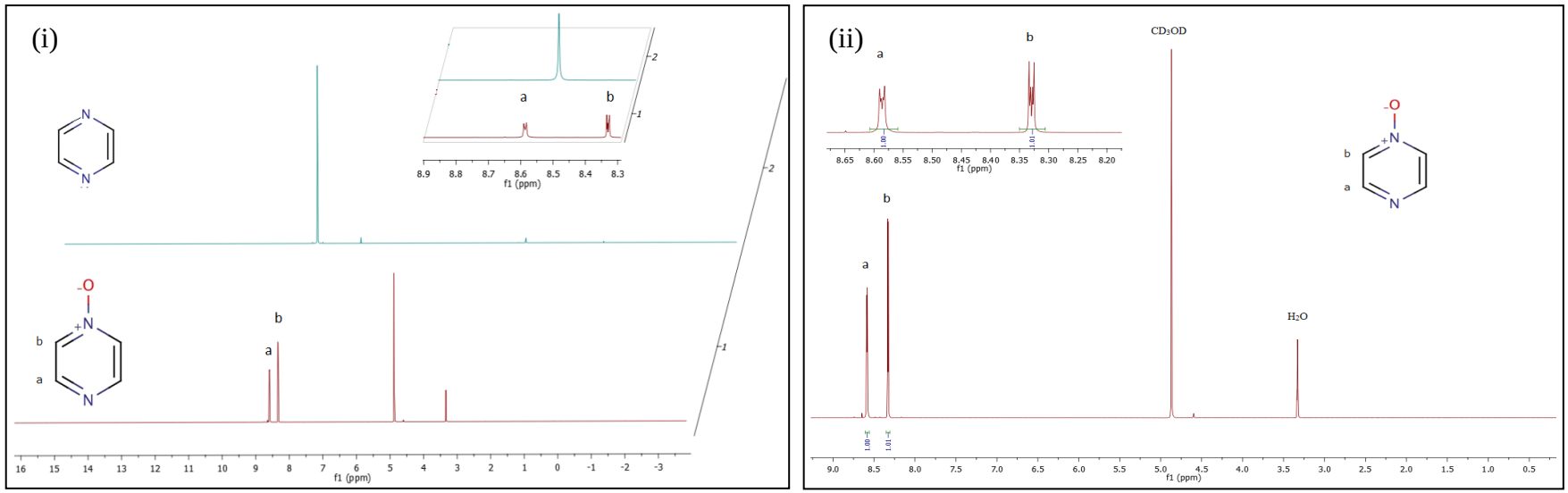

Figure 3.3: (i) shows the 600 MHz ^{1}H NMR spectrum of pyrazine-*N*-oxide product with pH 8 correction (in CD_3OD), with the spectrum of pyrazine included for comparison above; δ doublet 8.44 ppm (2H, J = 4.8 Hz), doublet 8.11 ppm (2H, J = 5.4 Hz). (ii) shows the PyzNO ^{1}H spectrum depicted alone for clarity; signal integrals are included below the spectrum (left to right 1.00, 1.01) as well as an enhanced view of the aromatic region (insert).

The number and position of the doublet signals on the ^{1}H NMR spectrum of PyzNO agree with the literature [4, 5], and support the conclusion that a highly pure product was generated by the vacuum sublimation procedure. Moreover, the absence of both a residue after DSC and TGA (see Appendix), and a melting point endotherm around 58 ºC on the DSC thermogram, confirms the exclusion of sodium acetate in both its anhydrous and trihydrate forms. As the acetate anion may otherwise potentially coordinate to Fe(II) to give an undesired mixed ligand system with PyzNO, its exclusion was preferred. The success of this strategy is also evidenced by Figs. 3.3 and 3.4.

Additionally, syntheses (not shown here) wherein the pH of the reaction was taken to approximately 9 and above prior to extraction, were conducted, each time with no apparent effect on the ultimate complex synthesis reactions. Fig. 3.4 shows the ^{13}C NMR spectrum of PyzNO product.

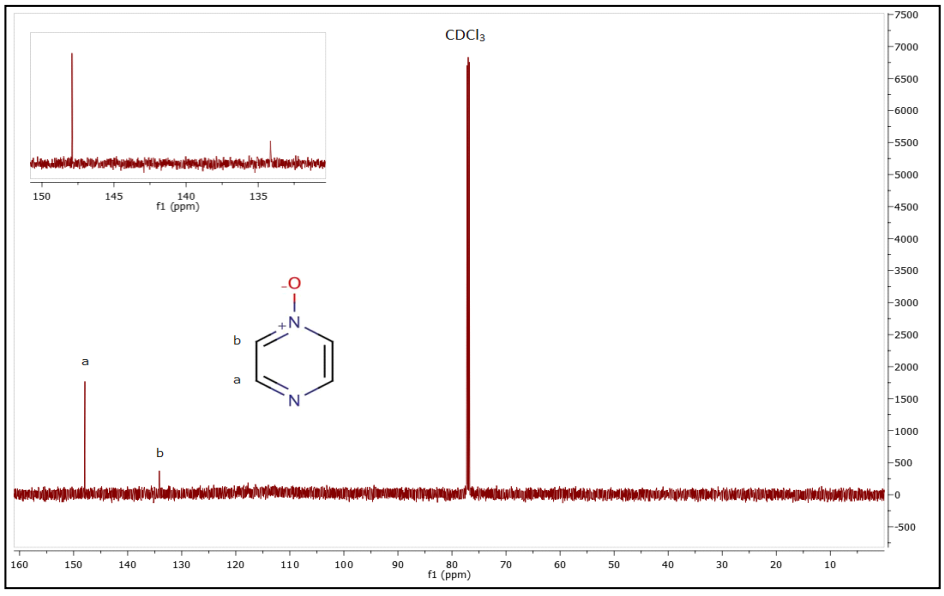

Figure 3.4: 600 MHz ^{13}C NMR spectrum of pyrazine-*N*-oxide product in $CDCl_3$; δ 147.92 ppm (2C), 134.16 ppm (2C). Enhanced view of aromatic region is included for clarity (top left).

The ^{13}C NMR spectrum of the product is as expected, showing signals resulting from the resonance of the two chemically distinct aromatic carbons, as well as the $CDCl_3$ solvent signal. There are no extraneous signals due to carbon-containing contaminant materials such as unreacted pyrazine, pyrazine-*N,N'*-oxide ($PyzNO_2$), co-extracted sodium acetate or acetic acid.

The good agreement with the literature [1-5], of the temperature (and range) of the recorded melting point, the DSC and TGA data, the ^{1}H NMR, and the FT-IR spectrum, all corroborate the purity of the desired PyzNO product. Therefore, this PyzNO product was used for the synthesis of the iron(II) perchlorate complexes described in the chapters 2 and 5.

3.2 4,4'-Bipyridine-*N*-oxide

3.2.1 Microanalysis

Table 3.3: Experimental versus theoretical microanalyses of 4,4'-bipyridine-*N*-oxide product (best fitting rows highlighted in yellow correspondingly)

Trial number	Experimental (%)				Calculated (%)				
	C	H	N	S	Waters	C	H	N	S
1	62.09	5.374	14.39	0.010	1.25	61.68	5.436	14.38	0
2	61.87	5.547	13.93	0					
Average	61.98	5.461	14.16	0.005					
Δ (%)$_{exp\ vs\ calc}$	-0.30	-0.025	+0.22	-0.005					

The microanalysis (CHNS) shown in table 3.3 is in very good agreement with what was expected for a theoretical calculation of $C_{10}H_{10,5}N_2O_{2.25}$ for BipyNO with 1.25 waters per formula unit (M_r: 194.7075 g.mol^{-1}). If the small amount of detected sulphur (due to instrumental column contamination by prior analyses) in 'run 1' was also corrected for, it would bring the experimental values yet marginally closer to the calculated values.

3.2.2 Differential Scanning Calorimetry

DSC thermal analysis was then employed in order to verify the purity of the BipyNO product as suggested by the close correlation of the theoretical calculated CHNS percentage masses with the experimental values. The resulting thermogram is shown in Fig. 3.5.

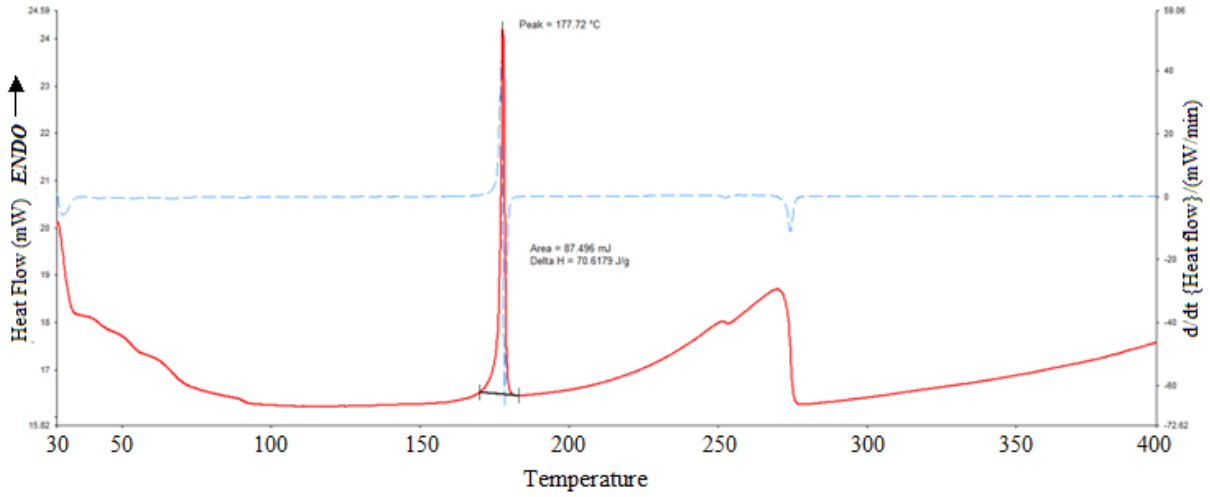

Figure 3.5: Differential Scanning Calorimeter thermogram (heating rate: $10^{o}.min^{-1}$) of BipyNO (red) with derivative curve (dashed blue). m.p. 170 ^{o}C (443 K). $\Delta H_{m.p.}$ = 70.6 $J.g^{-1}$ (0.4 $J.mol^{-1}$).

The DSC thermogram in Fig. 3.5 shows a broad endotherm with at least four unresolved peaks embedded within it is seen, in the 30 - 100 ^{o}C range. This is due to the evaporation of the physically adsorbed (or crystallization) waters described in the interpretation of the microanalysis data. The thermogram also shows a single sharp melting point, with T_{onset} at 170 ^{o}C. The literature reported values for the melting point of BipyNO vary somewhat widely. While Brunner *et al*. [6] reported a value of 170 ^{o}C, Moran *et al*. [7] reported a range of 174 – 176 ^{o}C, and McKay *et al* a range of 177 - 178 ^{o}C [8]. Amongst the highest values reported is 180 ^{o}C by Fielden and Summers [9]. These considerable discrepancies therefore made assertions regarding purity, on this view alone, unreliable.

The remaining endotherm shows the evaporation of the resulting bipyNO liquid to completion at around 275 ^{o}C. No residue was found on the uncrimped DSC sample pan post-analysis of BipyNO (30 – 280 ^{o}C).

3.2.3 Mid-IR Spectroscopy

The mid-infrared spectrum of the BipyNO product was recorded and compared with its Bipy precursor in order to identify the characteristic strong ν_s(NO) vibration. The spectra are shown in split display in the Fig. 3.6.

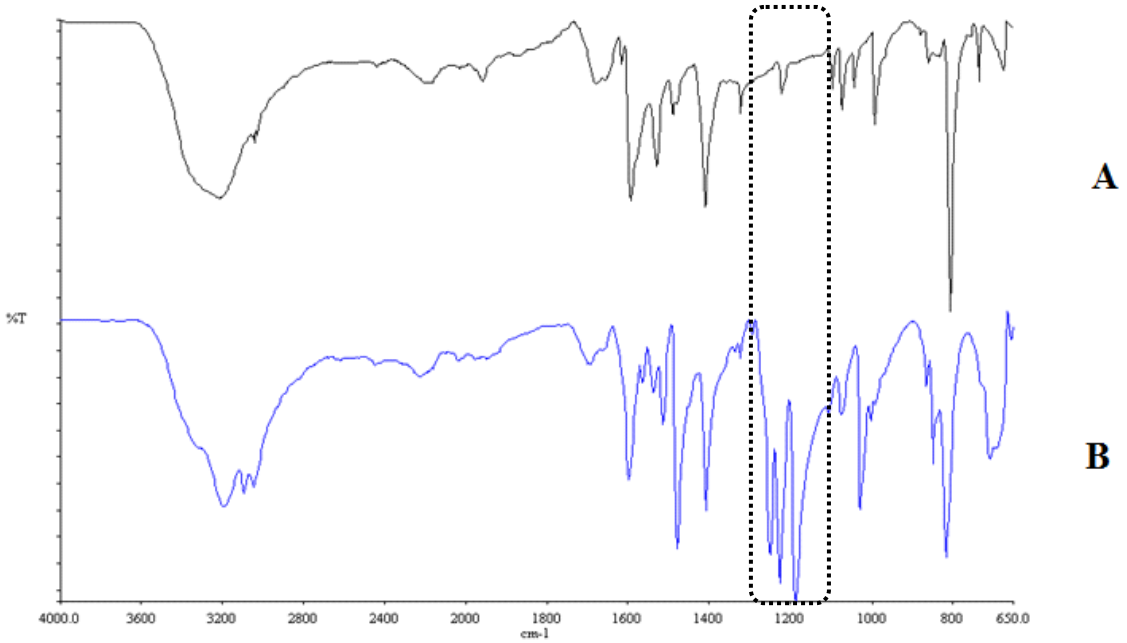

Figure 3.6: Mid-IR spectra of Bipy (A), and BipyNO product (B). Boxed is the characteristic diazine *N*-oxide ν(NO) and δ(NO) region.

Fig. 3.6 (B) shows three very strong bands of increasing intensity in the order 1256, 1229 and 1185 cm^{-1}. The first band has been assigned to the symmetric *N*-oxide stretch, ν_s(NO), while the second and third have been assigned to δ(NO) vibrations [5]. Thornton and Watkins [10] reported a mean value of 1255 cm^{-1} for the *ν*(N-O) vibration of 2,2'-bipyridine-*N*-oxide. Additionally, they indicated, following the behaviour of substituted benzenes as vibrational analogues, that the *ν*(N-O) vibration is strongly coupled with the 'Star of David' ring breathing modes. This coupling produces a pair of N-O sensitive bands, each member of which is split into two by in-phase and out-of-phase coupling, to produce a total of four bands: two N-O bands above 2000 cm^{-1}, and two ring modes below 850 cm^{-1}. The presence of only one N-O moiety in the case of BipyNO produces only one *ν*(N-O) stretch [5].

The medium strong, broad, composite band centred at approximately 3200 comprises the ν_a(OH), ν_s(OH) and δ(OH) vibrations of physisorbed water; trapped primarily *via* the aqueous synthesis protocol (waters of crystallization) [11, 12]. Additionally, surface waters may be acquired through atmospheric exposure, due to the hygroscopic nature of the product. This agrees with both the microanalysis and DSC data previously discussed.

3.2.4 ^{1}H and ^{13}C Nuclear Magnetic Resonance Spectroscopy

The final techniques employed towards the complete characterisation of the product were ^{1}H and ^{13}C NMR analyses. Fig's. 3.7 (i) and (ii) show the ^{1}H NMR spectra of the BipyNO and Bipy, and BipyNO alone, respectively.

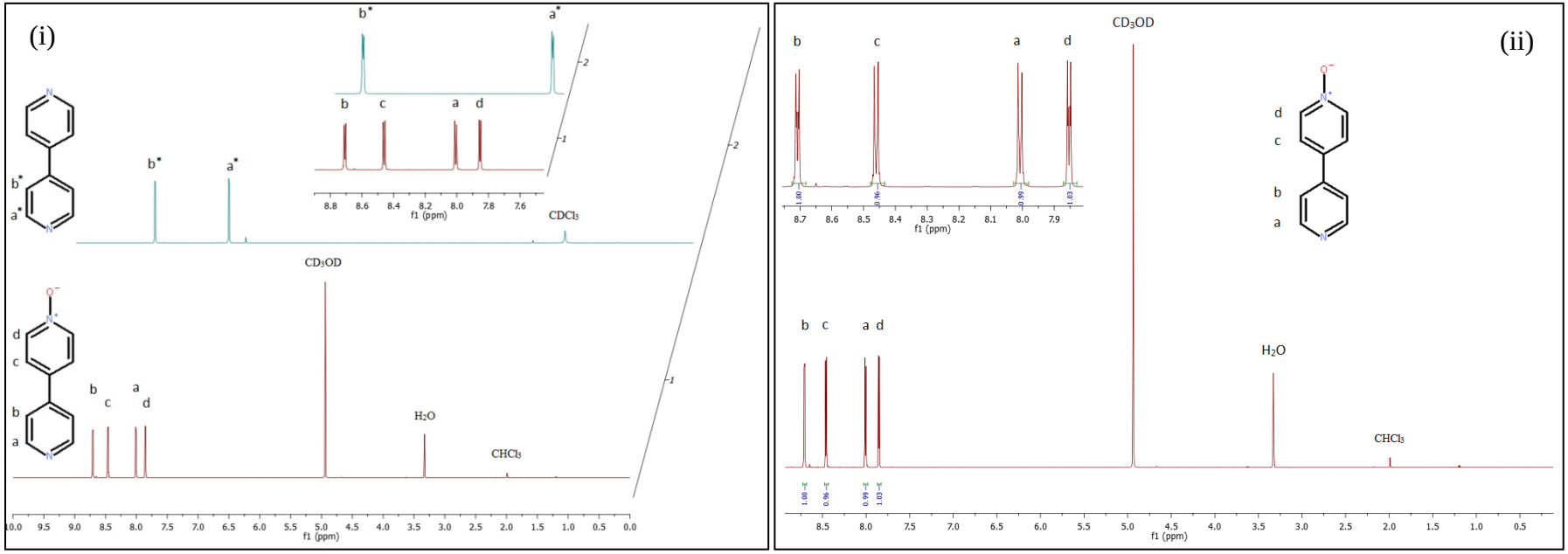

Figure 3.7: (i) shows the 600 MHz ^{1}H NMR spectra of Bipy in $CDCl_3$ (top), and BipyNO in CD_3OD (bottom). Enhanced views of the aromatic regions of both spectra are provided, with the signals assigned to the corresponding nuclei (letters a*-b* for Bipy, and a-d for BipyNO). And (ii) shows the spectrum of BipyNO alone; doublet 8.72 ppm (2H, J = 6 Hz), doublet 8.46 ppm (2H, J = 7.2 Hz), doublet 8.01 ppm (2H, J = 7.2 Hz), doublet 7.85 ppm (2H, J = 6.6 Hz). Peak integrals are also shown for BipyNO (left to right; 1.00, 0.96, 0.99, 1.03).

The ^{1}H NMR spectrum in Fig. 3.7 confirms the success of the *N*-oxidation reaction of Bipy in producing BipyNO [5, 8]. The set of four doublets in the aromatic region corresponding to the different dipyridyl protons (δ 8.72 ppm (2H, J = 6 Hz), 8.46 ppm (2H, J = 7.2 Hz), 8.01 ppm (2H, J = 7.2 Hz) and 7.85 ppm (2H, J = 6.6 Hz)) can be seen. It also corroborates the conclusions drawn from the microanalysis and the DSC data in terms of the water content (H_2O signal at 3.32 ppm). The ^{13}C NMR spectrum of the product is shown below.

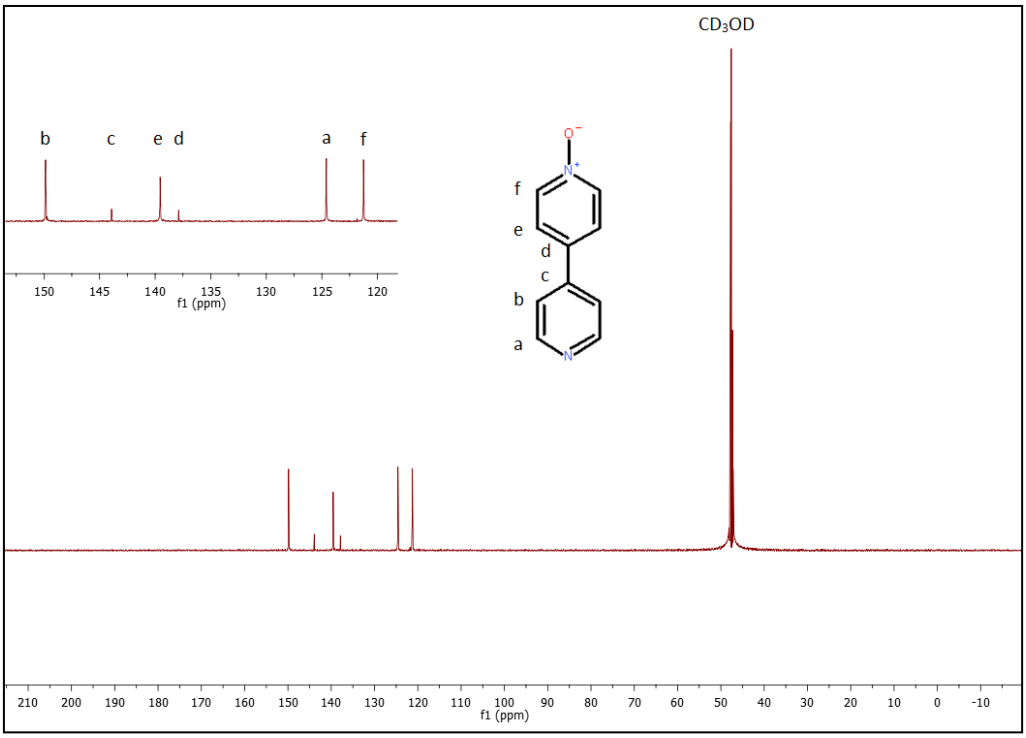

Figure 3.8: 600 MHz ^{13}C NMR spectrum of BipyNO product in CD_3OD (δ 149.75 ppm (2C), 143.93 ppm (1C), 139.55 ppm (2C), 137.89 ppm (1C), 124.59 ppm (2C), 121.26 ppm (2C)). Enhanced view of aromatic region provided, with the signals assigned to the corresponding nuclei (letters a-f, CD_3OD).

The ^{13}C NMR spectrum also indicates the success of the reaction showing signals at δ 149.75 ppm (2C), 143.93 ppm (1C), 139.55 ppm (2C), 137.89 ppm (1C), 124.59 ppm (2C) and 121.26 ppm (2C) corresponding to the six different dipyridyl aromatic carbons [5, 8]. That there are no other carbon signals detected other that the solvent peak, which reflects the high purity of the generated product.

References

[1] **Klein, B.; Berkowitz, J**. Pyrazines. I. Pyrazine *N*-oxides. Preparation and spectral characteristics. *J. Amer. Chem.* **81** (1959), 5160-5165

[2] **Speca, A.N.; Pytlewski, L.L.; Karayannis, N.M**. Transition metal perchlorate complexes with pyrazine-*N*-oxide. *J. Inorg. Nucl. Chem*. **35** (1973), 3113.

[3] **Thornton, D. A. and Watkins, G. M.** An assessment of the assignment of characteristic N-O vibrations in aromatic *N*-oxides. *Spectrosc. Lett*. **25** (1992), 1023-1031.

[4] **Thornton, D. A.; Verhoeven, P. F. M.; Watkins, G. M.; Desseyn, H. O.; van der Veken, B. J.** Isotope labelling studies of some aromatic *N*-oxides – Part II. A full vibrational assignment of the infrared and Raman spectra (4000 cm^{-1} – 50 cm^{-1}) of pyrazine-*N*-oxide and its fully deuterated analogue. *Bull. Chim. Soc. Belg.* **100** (1991), 211 – 220.

[5] **Aakeröy, C. B.; Epa, K.; Forbes, S.; Schultheiss, N.; Desper, J.** Ranking relative hydrogen-bond strengths in hydroxybenzoic acids for crystal-engineering purposes. *Chem. Eur. J.*, **19** (2013), 14998-15003.

[6] **Brunner, H.; Störiko, R.; Rominger, F.** Novel chiral oxazoline ligands for potential charge-transfer effects in the Rh(I)-catalysed enantioselective hydrosilylation. *Eur. J. Inorg. Chem.*, **1998** (1998), 772-779.

[7] **Moran, D.B.; Morton, G.O.; Albright, J.D.** Synthesis of (pyridinyl)-1,2,4-triazolo[4,3-a]pyridines. *J. Heterocycl. Chem.*, **23 (**1986), 1074-1076.

[8] **McKay, S. E.; Lashlee, R. W.; Maina, L. W.; Wheeler, K. A.; Brown, A. B**. Synthesis of bipyridine-*N*-oxides and bipyridine-*N,N'*-dioxides. *Heterocyc. Commun.* **15** (2009), 183-187.

[9] **Fielden, R.; Summers, L.** Chemical constitution and activity of bipyridylium herbicides. Part IX. *N*-alkoxy quaternary salts of 4,4′bipyridyl. *J. Heterocycl. Chem.*, **11** (1974), 299-300.

[10] **Thorton, D. A.; Watkins, G. M.** Isotope labelling studies of some aromatic *N*-oxides – Part III. A full vibrational assignment of the infrared spectra (4000-50 cm^{-1}) of 2,2'-bipyridine *N*,*N*'-dioxide and its fully deuterated analogue. *Bull. Chim. Soc. Belg.* **100** (1991), 221-223.

[11] **Banwell, C.N.** *Fundamentals of Molecular Spectroscopy*. 2nd ed. McGraw-Hill Book Company (UK) Ltd., Maidenhead, Berkshire, England (1972).

[12] **Nakamoto, K**. *Infrared and Raman Spectra of Inorganic and coordination compounds*. 6th ed. John Wiley and Sons, Inc., New Jersey, USA (2009).

.

Chapter 4

Characterisation of the Complexes

Only the crystal structure of Complex2 and the hydrated Complex6 ($[Fe(pyzNO)_4(H_2O)_2](ClO_4)_2 \cdot 2H_2O$) could be solved by single crystal X-ray crystallography, as the other complexes produced in this work were too small (microcrystals) to be mounted in the instrument. Therefore, all other structures of the complexes depicted were proposed after the analysis of data from studies such as microanalysis (CHNS), infrared spectroscopy (mid-IR), X-ray photoelectron spectroscopy (XPS), thermal analyses (TG, DSC and TG-IR-EGA), and strengthened by X-ray powder diffraction data.

4.1 $[Fe_n(\mu_{1,1}\text{-}pyzNO)_{2n-2}(pyzNO)_{3n+2}](ClO_4)_{2n}$ (n = {1, 2}) (Complex1)

The structure of Complex1 could not be solved by single crystal X-ray crystallography because of its microcrystalline nature. Although the complex has the apparent consistency of an amorphous powder, close inspection over a suitable light source does reveal the minute needle-like crystals. This was later confirmed by XRPD and scanning electron microscopy (SEM). As a result, the structure had to be inferred by alternative means.

The structure of Complex2 was first predicted using mid-IR and microanalysis data, and then later confirmed crystallographically. This complex gave an almost identical CHNS microanalysis to that of Complex1, which led to the preliminary conclusion that the two were the same complex. However, comparison of their mid-IR spectra revealed key differences in the region in which the coupled (ν(N-O) + ν(ring)) stretching vibration of aromatic diazine-*N*-oxides is typically found. This occurs at approximately 1300 cm^{-1} for free PyzNO [1, 2].

The mid-IR spectrum of Complex1 showed the splitting of this band into two, unlike with free PyzNO; which shows only one strong sharp band. This is consistent with alternating *N*- and *O*- PyzNO coordination. *O*-coordination is expected to decrease the N-O's double bond character, while *N*-coordination is expected to enhance it. Therefore, negative and positive vibrational frequency shifts are expected due to the two respective modes of bonding, resulting

in two distinct *ν*(NO) bands [3, 4]. In contrast, the mid-IR spectrum of Complex2 showed the splitting of this band into three. This indicated that in addition to the two aforementioned modes, there was a third mode which gave rise to its own associated *ν*(NO) frequency. It was predicted that the structure was a polymeric $\mu_{1,5}$-PyzNO complex with alternating *O*- and *N*-coordination. This was later confirmed crystallographically (Fig's. 4.9 and 4.10).

The possibility of $\mu_{1,5}$-PyzNO bridging was excluded by the absence of the 'third' aforementioned *ν*(NO) band in the IR spectrum of Complex1.

The broad $\nu_a ClO_4^-$ band remains largely featureless in the IR spectra of both complexes, and does not show any distinct splitting behaviour which might be ascribed to ClO_4^- coordination. As the crystal structure of Complex2 showed no such coordination, the same is considered to be true for Complex1.

The above would seem to suggest that Complex1 is a monomeric five-coordinate species. Square-based pyramidal and trigonal bipyramidal geometries (Fig. 4.1 A) were considered, and potentially, an equilibrium between the two in which interconversion could be achieved by mechanism of Berry pseudorotation [5]. Generally, a highly distorted intermediate geometry often results [5]. On the pure basis of ligand repulsions, whether considered as entirely electrostatic or due to Pauli repulsions of the associated bonding pairs, the trigonal bipyramidal geometry is often favoured, being somewhat more stable than square pyramidal [6]. Given that five-coordinate geometries in Fe(II) *N*- and *O*-donor complexes are usually found with chelating ligands, due to restrictive ligand bonding patterns, it was considered that it may be an anomalous result that Complex1 assumed this sort of configuration [7].

Therefore, an alternative structure* was proposed which is considered more likely to have been the product of the reaction detailed in section 2.3.1. The proposed structure is a dimeric bis($\mu_{1,1}$-pyzNO) complex with distorted pseudo-octahedral geometry (Fig. 4.1 B), and is consistent with both the microanalytical data and the mid-IR spectrum of Complex1. Regarding the latter, the monodentate ligands would have a ν_s(NO) of higher frequency due to the enhanced N-O double bond character that would result from coordination through the ring nitrogen. In contrast, the N-O bond of the doubly coordinated oxygen of each μ-pyzNO would experience significant electron withdrawal, giving a ν_s(NO) band of lower frequency [8].

* It should be emphasised that all depicted structures of the compound 'Complex1' are proposed provisionally, and as such, require confirmation by single crystal data.

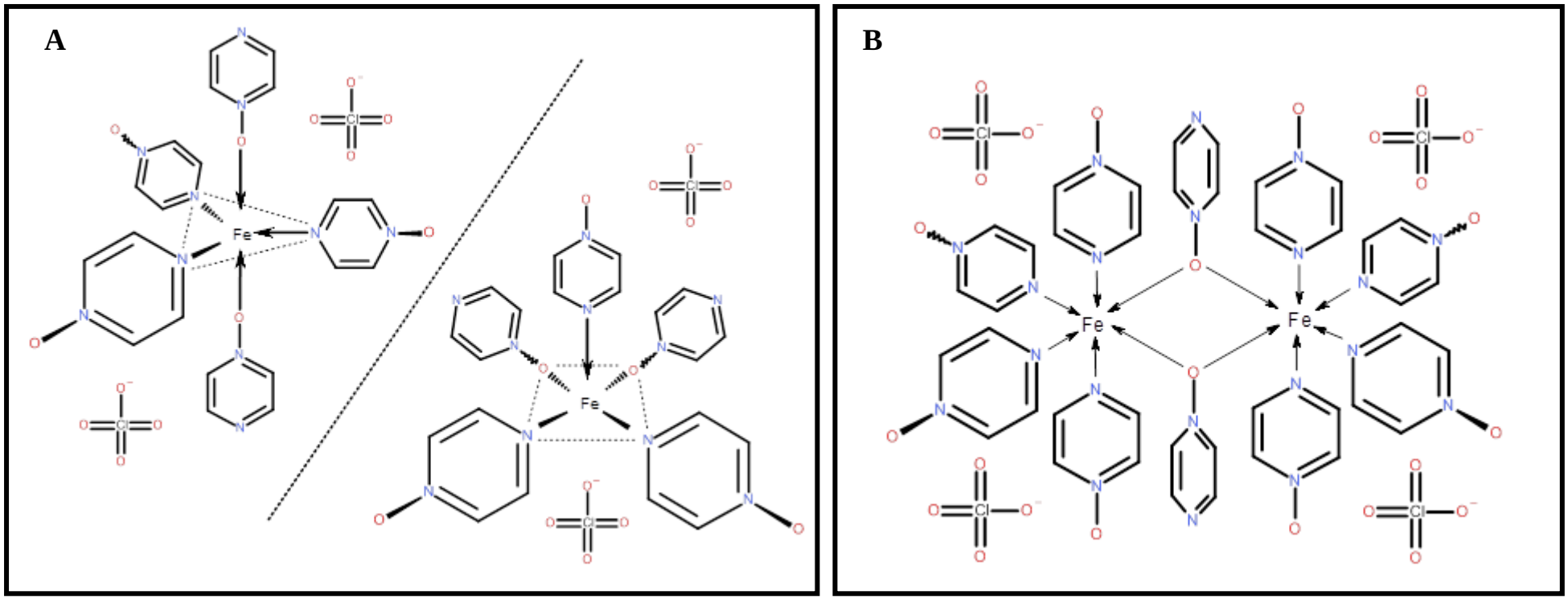

Figure 4.1: Representation of the proposed possible structures of the Complex1.

4.1.1 Microanalysis and Mid-IR Spectroscopy

Table 4.1: Experimental versus calculated microanalysis values for $Fe_n(\mu_{1,1}\text{-pyzNO})_{2n-2}(pyzNO)_{3n+2}(ClO_4)_{2n}$ (n = {1, 2}) (Complex1)

Trial number	Experimental values (%)				Calculated values (%)			
	C	H	N	S	C	H	N	S
1	32.99	2.868	18.69	0	32.67	2.742	19.05	0
2	32.71	2.912	18.77	0				
Average	32.85	2.890	18.73	0				
Δ (%)$_{exp\ vs\ calc}$	-0.18	-0.148	+0.32	0				

The experimental microanalysis data of this product agrees with the calculated values for Complex1 (M_r: 735.189 g.mol^{-1}). Any theoretical introduction of additional components (PyzNO fractions, water, etc.) was found to result in unacceptable discrepancies between of the calculated and experimental values.

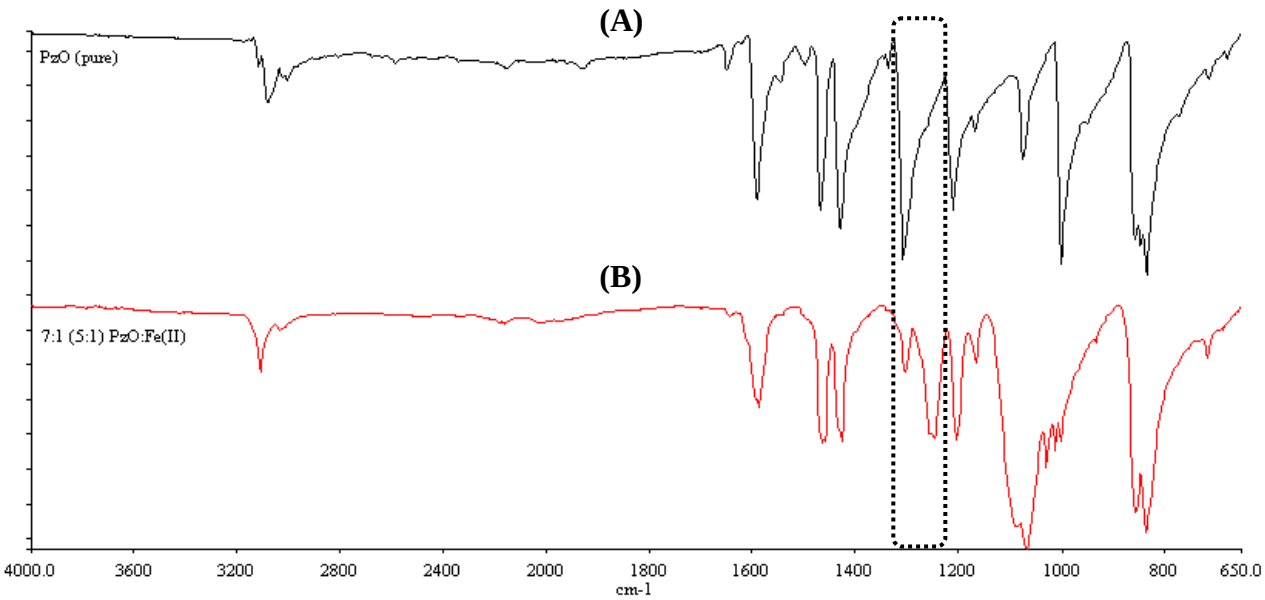

Figure 4.2: Mid-infrared spectra (4000 – 650 cm^{-1}) of PyzNO (A), and $Fe_n(\mu_{1,1}\text{-pyzNO})_{2n-2}(pyzNO)_{3n+2}(ClO_4)_{2n}$ (n = {1, 2}) (B) (Complex1). Boxed is the region where the coupled (ν(NO) + ν(ring)) vibration is found.

A comparison of the IR spectrum of the complex with that of pure PyzNO, in Fig. 4.2, reveals the success of the complexation reaction. This conclusion is based on the splitting and loss of intensity of the initially very strong and sharp coupled *ν*(NO) + *ν*(ring) band of pure PyzNO at 1309 cm^{-1}. The resulting bands, appearing at 1303 cm^{-1} and 1248 cm^{-1}, are suggestive of simultaneous (alternating) *N*- and *O*-coordination. Pure *N*- or *O*- coordination should retain the single *ν*(NO) stretch, accompanied only by a shift in the band's frequency. *N*-coordination may theoretically induce either a positive or negative *ν*(NO) frequency shift, resulting from the withdrawal of the electron density *via* the ring nitrogen. This withdrawal of electron density would create partial electron deficiency in the ring. In alignment with a positive *ν*(NO) frequency shift, this loss would be replenished by the *N*-oxide moiety's oxygen atom, favouring N-O with increased double bond character. Alternatively, the electronegative O atom may persistently retain most of the *N*-oxide moiety's electron density (favouring N-O single bond character), such that a negative *ν*(NO) frequency may be seen on *N*-coordination.

In contrast, *O*-coordination is expected to be exclusively characterised by a negative shift in the *ν*(NO) frequency as it diminishes the capacity for the oxygen to donate electron density back into the ring, thereby enhancing the single bond character (decreasing d/bond character) of the N-O bond [8]. It is suggested that a combination of the two latter possibilities is in effect. The bands have thus been assigned as *N*→Fe (1303 cm^{-1}) and N-*O*→Fe (1248 cm^{-1}) [7-9].

4.1.2 X-ray Powder Diffraction

The XRPD pattern of Complex1 was collected after a necessary sample preparative step wherein the powder was mixed with a small amount of anhydrous petroleum jelly. In a preliminary analysis, the untreated sample was found to undergo the red → yellow colour change during the experiment, albeit incomplete. The intense amorphous peak in the ~ 12 – 26 $^{o}2\theta$ range is due to reflections associated with background scattering resulting from the silicate sample holder. This effect is exacerbated by the dilution of the crystalline sample which results from merging it with the petroleum jelly component of the mull [9, 10]. This amorphic background is usually suppressed by the comparatively intense crystalline reflections when sufficient analytical material is available. Fig. 4.3 shows the X-ray powder diffraction pattern of Complex1.

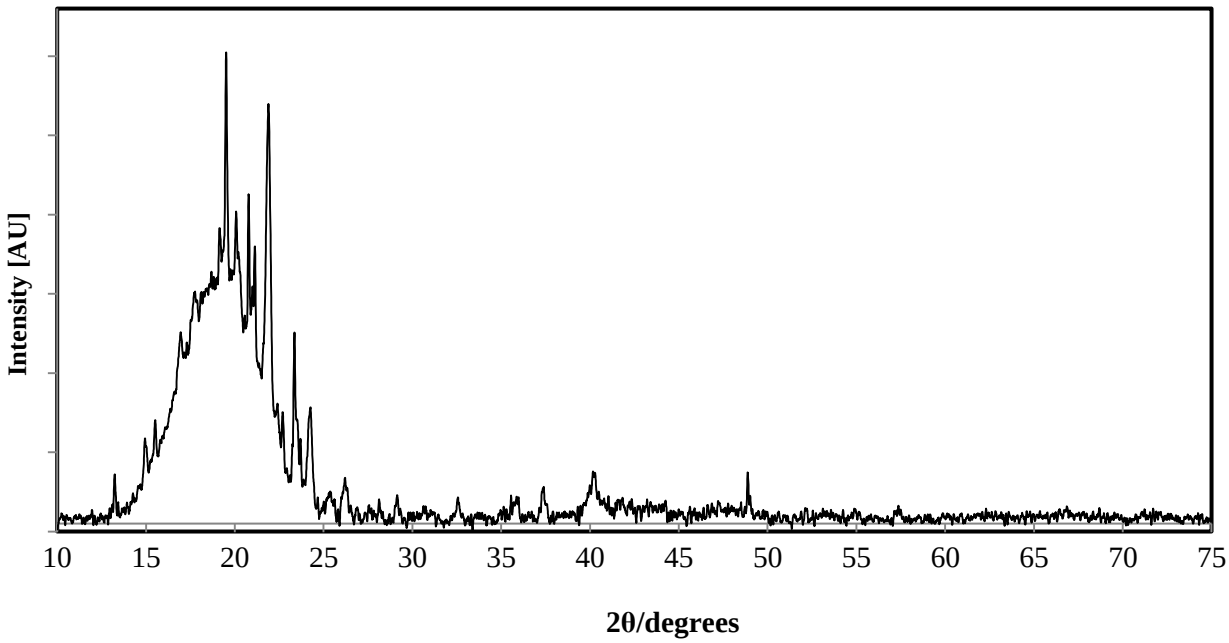

Figure 4.3: X-ray powder diffraction pattern (10^o-75^o 2θ) of the anhydrous petroleum jelly mull of $Fe_n(\mu_{1,1}\text{-pyzNO})_{2n-2}(pyzNO)_{3n+2}(ClO_4)_{2n}$ (n = {1, 2}) (Complex1).

Omitting the large amorphous peak, the XRPD pattern of Complex1 shows very well defined and narrow peaks, which is indicative of relatively large crystallite sizes [10, 11].

The first reflections of quantitative intensity appear at low 2θ values, which generally suggests a large unit cell size. The comparison of this pattern with that of the hydrated complex (Fig 5.4) shows positive shifts in the first peaks of the latter. This is consistent with a reduction in the unit cell dimensions.

The structural transformation associated with the PyzNO→H_2O ligand substitution reaction invariably introduces new analytical phases, and thus new corresponding peaks due to their potentially unique reflections. Nevertheless, on a facile view, the increased inter- and intramolecular H-bonding and dipole-dipole interactions accompanying the introduction of water into the coordination sphere is, expected to diminish the unit cell volume [10]. Table 4.2 shows the d-spacing values calculated for each quantitative reflection.

Table 4.2: 2θ (degrees) and corresponding d-spacing (Å) values for $Fe_n(\mu_{1,1}\text{-pyzNO})_{2n-2}(pyzNO)_{3n+2}(ClO_4)_{2n}$ (n = {1, 2}) (Complex1).

$Fe_n(\mu_{1,1}\text{-pyzNO})_{2n-2}(pyzNO)_{3n+2}(ClO_4)_{2n}$ (n = {1, 2})	
2θ (º)	***d*-Spacing (Å)**
13.233	6.685
14.682	6.028
14.941	5.924
15.516	5.706
16.946	5.228
19.507	4.547
20.064	4.422
20.774	4.272
21.129	4.201
21.886	4.058
22.692	3.915
23.354	3.806
23.690	3.752
24.256	3.666

$$d = \lambda/(2\sin\theta) \qquad (1.1)$$

4.1.3 Differential Scanning Calorimetry and Thermogravimetry

The DSC thermogram of the complex is shown in Fig. 4.4. The spectrum was collected in the range 30 – 300 ºC. Thermal decomposition of the complex was complete at 250 ºC, leaving only a carbon and metal oxide residue.

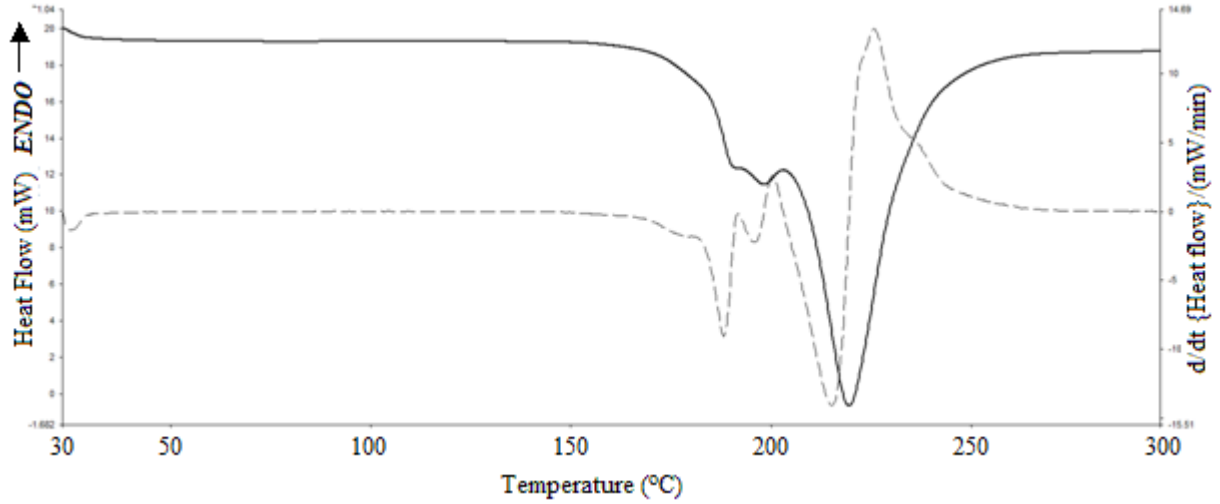

Figure 4.4: DSC thermogram (temperature range: 30 – 300 °C, heating rate: 10 °C.min^{-1}) of $Fe_n(\mu_{1,1}\text{-}pyzNO)_{2n-2}(pyzNO)_{3n+2}(ClO_4)_{2n}$ ($n = \{1, 2\}$) (Complex1).

The DSC thermogram of Complex1 shows the absence of any distinct thermal events from 30 °C until the onset of decomposition at ~ 150 - 170 °C, indicating the thermal stability of this temperature range. The thermolysis of the complex manifests as a 3-step exotherm spanning the 175 – 250 °C range. The first two steps are due to the partial decomposition of PyzNO into CO and CO_2 gases. The partial loss of the PyzNO fraction destabilizes the ClO_4^- component of the remaining Fe-PyzNO-ClO_4 species. The major exotherm spanning the 205 – 250 °C range results from the explosive decomposition of this component (205 – 230 °C), which subsequently ignites residual PyzNO (230 °C). The remaining black solid is likely a FeO/Fe_2O_3/carbon residue mixture, the latter component being due partial oxidation of PyzNO moiety. The incomplete oxidation is due to the inert conditions in the N_2 gas-purged DSC furnace. The TG-IR-EGA (EGA) of the complex could not be performed due to limited sample. As a result, these assignments were inferred from the analysis of the EGA of the polymeric complex.

The TGA thermogram supports the above interpretation, and shows no sample weight loss until 140 °C, whereupon a gradual decline is observed. A 12.27% weight loss is seen between 140 and 180 °C, which is ascribed to the loss of one PyzNO ligand per formula unit (this is more readily seen in the first derivative TG curve) (calc.: 13.05%). However, in contrast to the DSC profile, the explosive decomposition occurs at 180 °C on the TG thermogram. The suggested origin of this *premature* decomposition is the loss of PyzNO at 140 – 160 °C in the open TG ceramic sample crucible. This PyzNO fraction remains trapped in crimped and sealed

DSC sample pan, thereby ostensibly providing additional stabilization of ClO_4^-, until the former's thermolysis as per the description of the DSC profile. As a result, decomposition is seen to occur at a lower temperature in the TGA than on the DSC profile.

The TGA thermal profile of Complex1 is shown in Fig. 4.5.

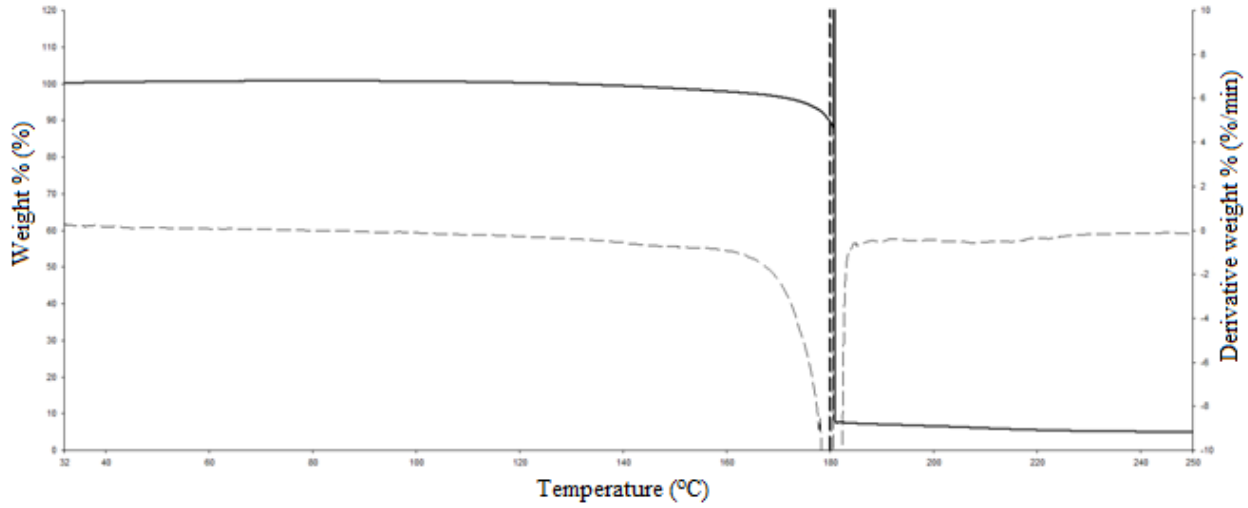

Figure 4.5: TG thermogram (temperature range: 30 – 250 °C, heating rate: 10 °C.min^{-1}) of $Fe_n(\mu_{1,1}\text{-pyzNO})_{2n-2}(\text{pyzNO})_{3n+2}(ClO_4)_{2n}$ ($n = \{1, 2\}$) (Complex1).

4.1.4 Scanning Electron Microscopy

The SEM micrograph of Complex1 in Fig. 4.6 shows the elongated monoclinic structure of the complex. Initial inspection may lead one to hastily conclude that the crystals have a triclinic geometry. However, closer inspection of Fig. 4.6 (i) shows that the crystals have two parallel lateral planes connected by a pair of two intersecting diagonal planes; one on each longitudinal side of the elongated structure. A drawn diagram of a cross-section of a 'hypothetical' Complex1 crystal is provided in Fig. 4.7 to clarify this description.

The growth of single crystals of Complex1of suitable size for single crystal XRD proved elusive. Alternative methods of crystal growth towards that end, and subsequent crystallographic characterization have therefore been put under the scope of future work.

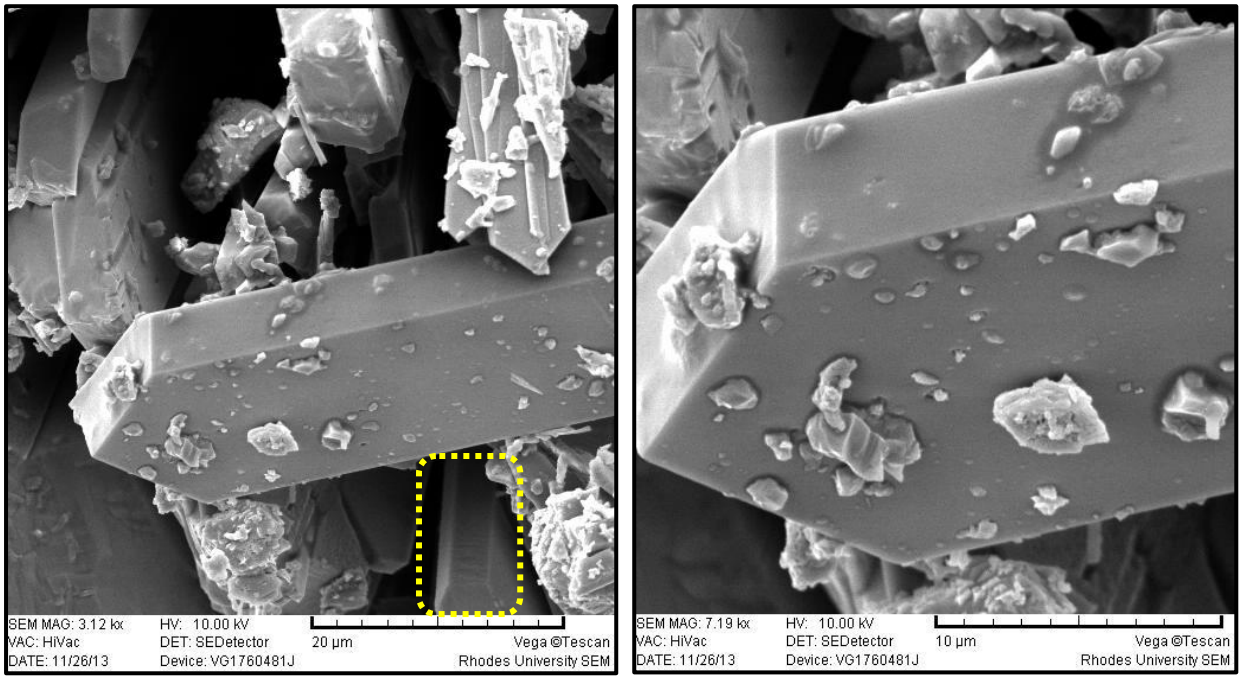

Figure 4.6: SEM of $Fe_n(\mu_{1,1}\text{-pyzNO})_{2n-2}(pyzNO)_{3n+2}(ClO_4)_{2n}$ (n = {1, 2}) (Complex1) at (i) 1600x magnification, and at (ii) 3600x magnification. Boxed in yellow in the bottom of (i) is the crystal which confirms their monoclinic geometry.

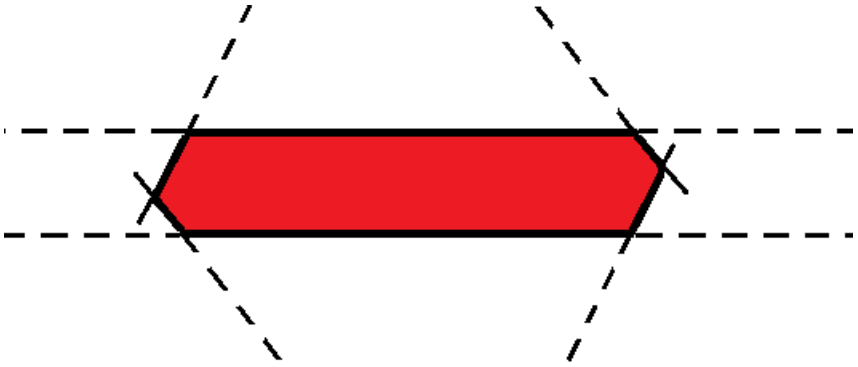

Figure 4.7: Drawn diagram (front view cross-section) of a 'hypothetical' $Fe_n(\mu_{1,1}\text{-pyzNO})_{2n-2}(pyzNO)_{3n+2}(ClO_4)_{2n}$ (n = {1, 2}) crystal showing the intersecting planes previously described.

4.1.5 Electron Paramagnetic Resonance Spectroscopy

The EPR spectrum Complex1 showed no detectable resonance features at 77 K and at room temperature; despite multiple sequential increases in resolution and scan width. This is consistent with what would be expected of a low spin (LS) iron(II) complex. In contrast, the

EPR spectrum of its hydrated form revealed the latter's marked paramagnetism, thereby confirming the LS→HS transition on exposure to a moist environment. The spectra of the anhydrous and hydrated species – both collected at 77 K – are shown in Fig. 4.8.

Figure 4.8 clearly shows the lack of paramagnetic resonance in the anhydrous complex, while strong resonance is detected in the hydrated species. The major peak has a line width of ~ 534 G, and is split into five peaks of unequal spacing by a combination of spin-orbit coupling and hyperfine interactions [12-14].

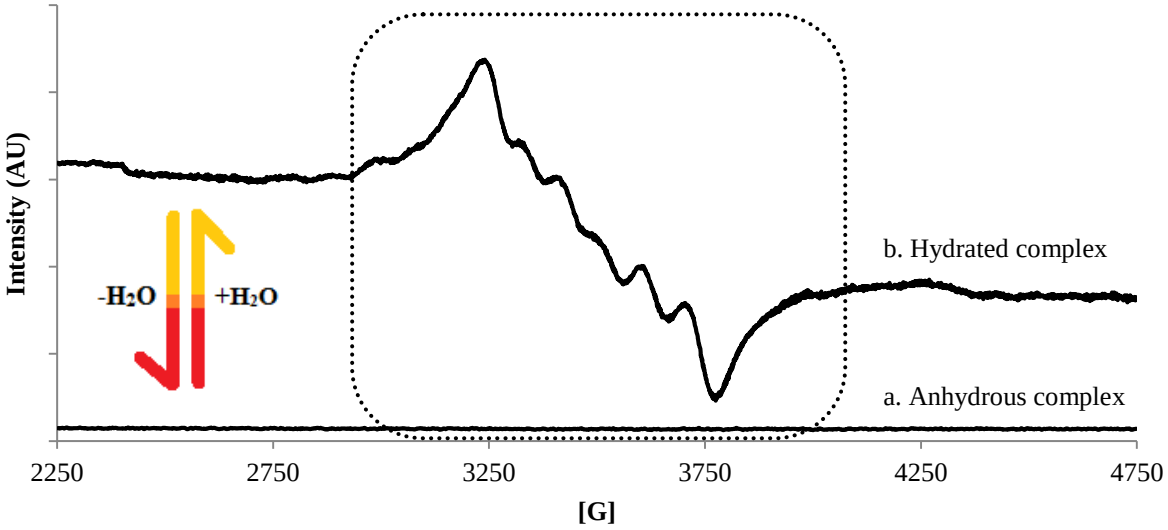

Figure 4.8: EPR spectra of (a), the original anhydrous $Fe_n(\mu_{1,1}\text{-pyzNO})_{2n-2}(pyzNO)_{3n+2}(ClO_4)_{2n}$ (n = {1, 2}) complex (Complex1) versus (b), its hydrated variant. The magnetic field range in which the observable resonances occur is boxed (HS species). Both spectra were recorded at 77 K.

The poor resolution of these overlapping lines made it impossible to make a comprehensive evaluation of hyperfine structure of the complex. Simulation studies will be undertaken for future work, but are expected to have limited utility, considering the complexity of HS d^6 EPR spectra. These are generally recorded using low temperature high-frequency and field techniques, in order to *overcome* the effects of zero-field splitting [12-14], or alternatively, to determine its magnitude [13-16]. The electron g factor (g_e) was approximated at 2.0130 using an experimental centre field of 3468 G. The equation used to calculate the approximate g_e value is:

$$g_e = \frac{h\nu}{\beta_e . \mathrm{B}_0} \; ; \qquad (1.2)$$

where *h* is Planck's constant, *ν* is the frequency of analytical microwave radiation, β_e is the Bohr Magneton and B_o is the strength of the applied magnetic field in Gauss.

4.2 {Fe(μ-pyzNO-κ*N*,κ*O*)$_{n-1}$(pyzNO-κ*N*)$_2$(pyzNO-κ*O*)$_2$}$_n$(ClO$_4$)$_{2n}$

4.2.1 X-ray Single Crystal Diffraction

The crystal structure of Complex2 is shown in Fig's. 4.9 A and B, with an enhanced view of an arbitrary polymer chain given in Fig 4.10.

Fig's. 4.9 A and B show the parallel orientation of the proximal polymeric chains of Complex2.

The *O*-coordinated PyzNO moieties of one chain are arranged at tandem with the *N*-coordinated species of neighbouring polymeric chains. The interaction of these moieties is suspected to be mediated primarily by π-π stacking to produce a three-dimensionally rigid structure. A dipole-dipole contribution is expected to arise from the 'anti-parallel' orientation of such moieties, thereby further diminishing, to negligible minima, the extent to which individual chains can move relative to one another in any given direction. This potential contribution would therefore enhance the rigidity of the resulting supramolecular structure.

The perchlorate units are equidistant from any two arbitrarily chosen Fe(II) nuclei (from neighbouring chains) with a lowest mutual spacial separation (Fe-Cl contact distance is 3.655(3) Å). That is, they are equally spaced between successive polymer chains with no apparent partiality.

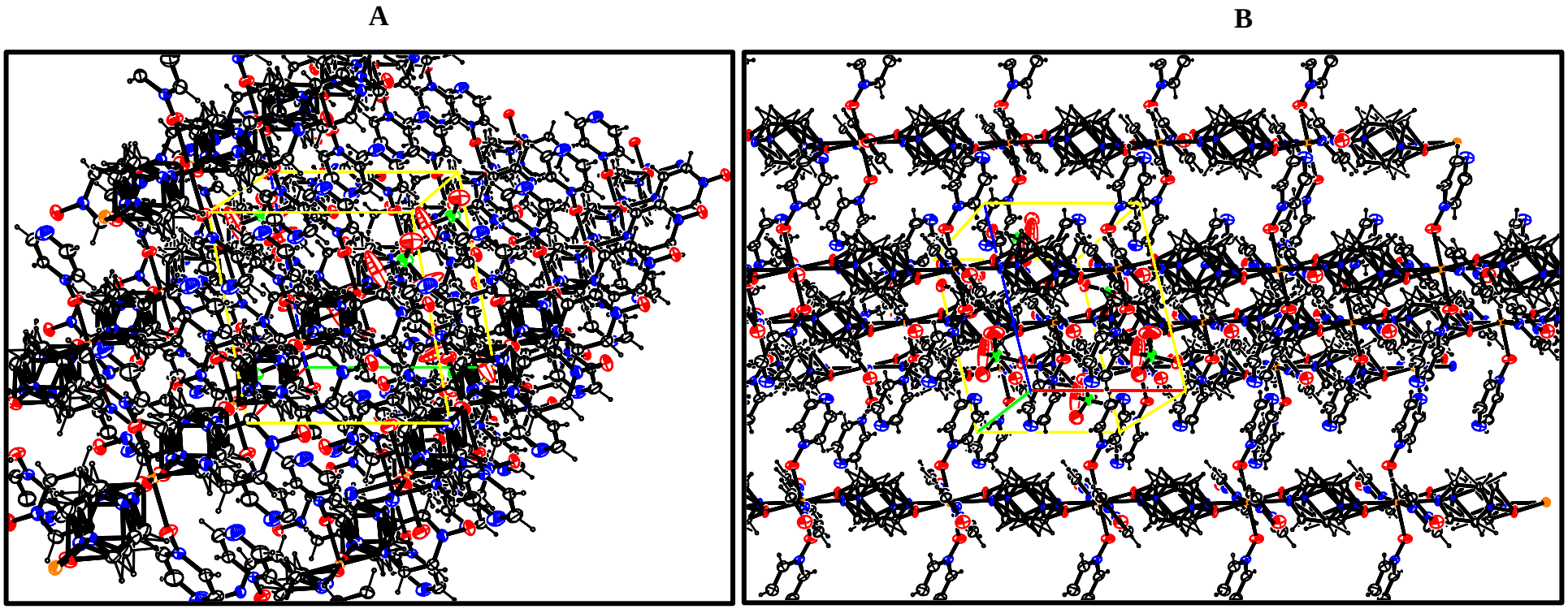

Figure 4.9: The crystal structure (A: Normal to (100), and B: Normal to (010)) of $\{Fe(\mu\text{-}pyzNO\text{-}\kappa N,\kappa O)_{n-1}(pyzNO\text{-}\kappa N)_2(pyzNO\text{-}\kappa O)_2\}_n(ClO_4)_{2n}$ (Complex2). Colour coding: yellow box = unit cell; Atoms: yellow = Fe, black = C, blue = N, red = O, green = Cl.

Despite the close packing of the unit cell, Fig. 4.9 A and B reveal definite volumetric 'voids' in the crystal lattice of the anhydrous complex. These are suspected to provide access to individual Fe(II) nuclei for the incoming water upon atmospheric exposure or, equivalently, treatment with a suitable solvent of interest.

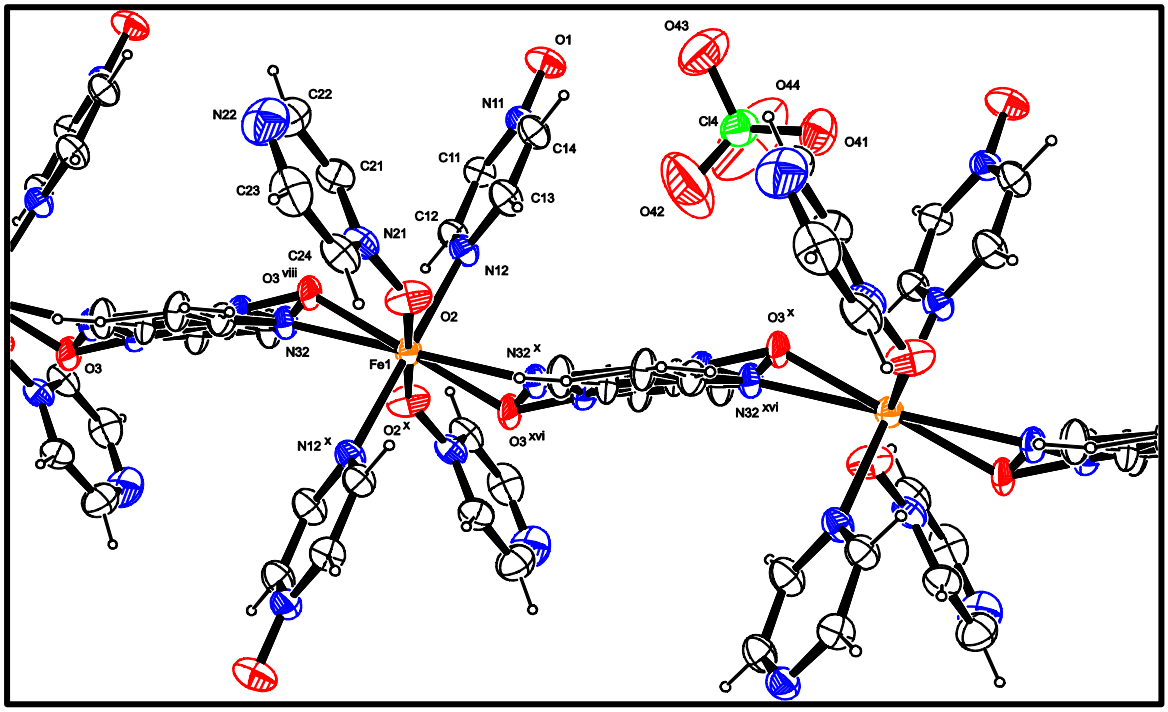

Figure 4.10: The crystal structure of $\{Fe(\mu\text{-pyzNO-}\kappa N,\kappa O)_{n-1}(pyzNO\text{-}\kappa N)_2(pyzNO\text{-}\kappa O)_2\}_n(ClO_4)_{2n}$ (Complex2) showing atomic numbering in the basic repeating unit. Colour coding: yellow = Fe, black = C, blue = N, red = O, green = Cl.

The crystal structure of Complex2* shows its polymeric nature. There are four equatorially bound PyzNO ligands per Fe(II) nucleus, two of which are *N*-coordinated, while the other two are *O*-coordinated. The Fe(1)-O(2)-N(21) bond angle (equatorially *O*-coordinated PyzNO) is 135.50(19) °, while the equivalent bond angle generated by $\mu_{1,5}$-PyzNO (Fe(1)-O(3)-N(32)) is 137.5(4) °. The Fe(1)-O(3) and Fe(1)-O(2) bond lengths are 2.035(5) Å and 2.0814(19) Å, respectively; while equatorial (Fe(1)-N(12)) and μ-*N*-Fe (Fe(1)-N(12)) bond lengths are, correspondingly: 2.1793(19) and 2.291(7) Å.

*An alternative depiction to Fig. 4.10 with enhanced clarity is included in the Appendix (Fig. 2.2).

The $\mu_{1,5}$-PyzNO ligand is disordered between successive Fe(II) nuclei, and either one of the two possible orientations may exist without preference (1:1 disorder). The structures depicted in Fig's. 4.9 and 4.10 have both orientations shown simultaneously.

Although only one is shown here in Fig. 4.10, there are two perchlorate groups per Fe(II) center, both of which serve purely the role of counterions. The resulting structure is a quasi-octahedral PyzNO-bridged coordination polymer comprising *n* Fe(II) nuclei, 5*n* PyzNO ligands, and 2*n* perchlorate; where $n > 2$. The most accurate formula for the structure is $\{Fe(\mu\text{-pyzNO-}\kappa N,\kappa O)_{n-1}(\text{pyzNO-}\kappa N)_2(\text{pyzNO-}\kappa O)_2\}_n(ClO_4)_{2n}$, which reflects the fact that one of the terminal Fe(II) centers per polymer chain is five-coordinate, while the other is fully saturated. This was suggested by microanalytical data and then confirmed crystallographically. The full name of Complex2, using kappa notation, is μ-pyrazine-*N*-oxide-κ*O*:κ*N*bis(pyrazine-*N*-oxide-κ*N*)bis(pyrazine-*N*-oxide-κ*O*)iron(II) perchlorate.

Table 4.3 shows the crystal structure data of the complex.

Table 4.3: Crystal data of the $\{Fe(\mu\text{-pyzNO-}\kappa N,\kappa O)_{n-1}(\text{pyzNO-}\kappa N)_2(\text{pyzNO-}\kappa O)_2\}_n(ClO_4)_{2n}$ complex (Complex2).

Property	$\mathbf{[Fe_{2n}(\mu_{1,5}\text{-pyzNO})_{2n-1}(pyzNO)_{8n+1}](ClO_4)_{4n}}$
Crystal system	Triclinic
Space group	$P\bar{1}$
a (Å)	8.1003(3)
b (Å)	9.5432(3)
c (Å)	10.0862(3)
α (°)	100.368(2)
β (°)	103.900(2)
γ (°)	109.009(1)
Volume ($Å^3$)	687.71(6)
$Density_{calc}$ ($g.cm^{-1}$)	1.778

4.2.2 Microanalysis and Mid-IR Spectroscopy

Table 4.4: Experimental versus calculated microanalysis values for $\{Fe(\mu\text{-pyzNO-}\kappa N,\kappa O)_{n-1}(pyzNO\text{-}\kappa N)_2(pyzNO\text{-}\kappa O)_2\}_n(ClO_4)_{2n}$ (Complex2).

Trial number	Experimental values (%)				Calculated values (%)			
	C	H	N	S	C	H	N	S
1	32.20	2.459	18.96	0	32.67	2.742	19.05	0
2	32.42	2.411	18.72	0				
Average	32.31	2.435	18.84	0				
Δ (%)$_{exp\ vs\ calc}$	-0.36	-0.307	-0.29	0				

The experimental microanalysis data of Complex2 agrees with the calculated values. The molecular mass of the repeating unit, upon which the calculated values were based, was found to be 735.21 g.mol^{-1} by single crystal XRD.

The structure of Complex2, as predicted by microanalysis and mid-IR (Fig. 4.11), was confirmed by the single crystal structure (Fig's. 4.9 and 4.10). As previously mentioned, a PyzNO-bridged complex had been suspected based on the interpretation mid-IR data. The characteristic coupled ν(NO) + ν(ring) vibration is highlighted.

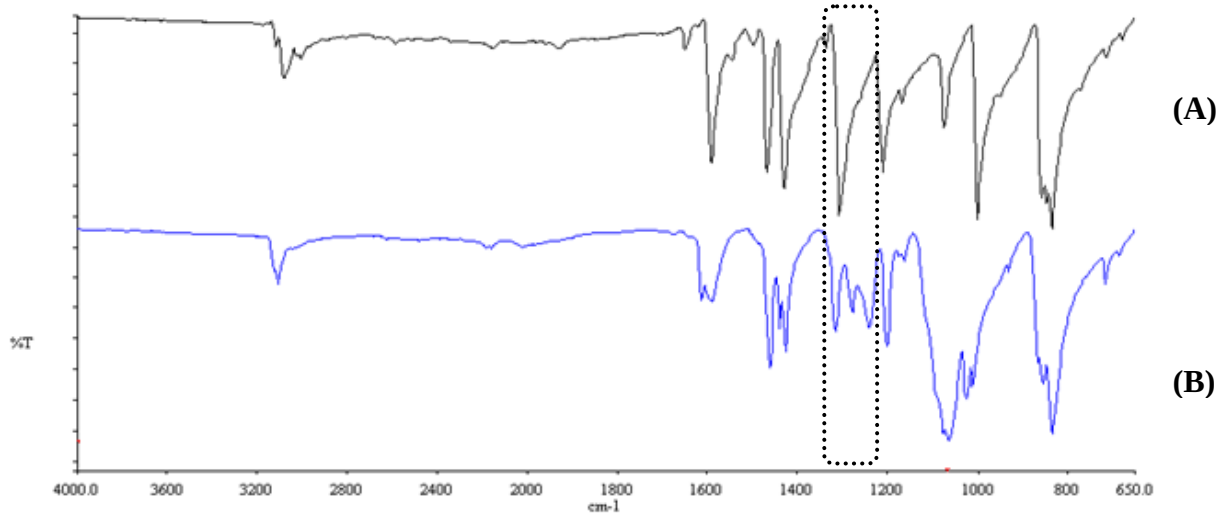

Figure 4.11: Mid-infrared spectra (4000 – 650 cm^{-1}) of PyzNO (A), and $\{Fe(\mu\text{-pyzNO-}\kappa N,\kappa O)_{n-1}(pyzNO\text{-}\kappa N)_2(pyzNO\text{-}\kappa O)_2\}_n(ClO_4)_{2n}$ (Complex2) (B). Boxed is the region where the (ν(NO) + ν(ring)) band is found.

The mid-IR spectrum of the complex shows the splitting of the ν(NO) + ν(ring) band into three bands. The three bands have been assigned to *N*-coordinated PyzNO (1317 cm^{-1}), *O*-coordinated PyzNO (1279 cm^{-1}), and μ-PyzNO (1241 cm^{-1}).

4.2.3 X-ray Photoelectron Spectroscopy

The wide scan XPS spectrum of the complex designated Complex2 indicates the presence of iron, carbon, nitrogen, oxygen and chlorine, as expected. The spectrum is given in Fig. 4.12.

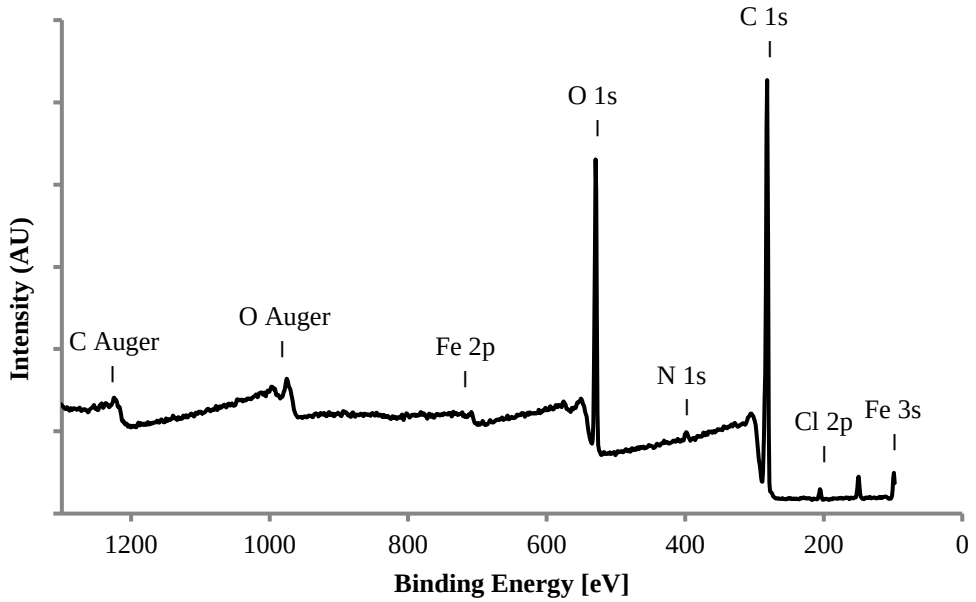

Figure 4.12: Wide scan XPS spectrum of $\{Fe(\mu\text{-pyzNO-}\kappa N,\kappa O)_{n-1}(pyzNO\text{-}\kappa N)_2(pyzNO\text{-}\kappa O)_2\}_n(ClO_4)_{2n}$ (Complex2) collected in the range 97.5 eV – 1302.5 eV

Several additional peaks can also be seen, and have been assigned as shown on the Fig. 4.12. They are due to the iron 3s orbital at ~ 99.0 eV, as well as oxygen and carbon auger electrons at 979.0 and 998.5 eV, and 1225.0 eV, respectively [17].

High resolution scans of the C 1s, N 1s and O 1s regions were also obtained and are shown in Fig. 4.13. In all three spectra, deconvolution of the experimental data was undertaken to reveal the underlying curves. Theoretical Gaussian-Lorentzian functions were then fitted to the original and the deconvoluted curves.

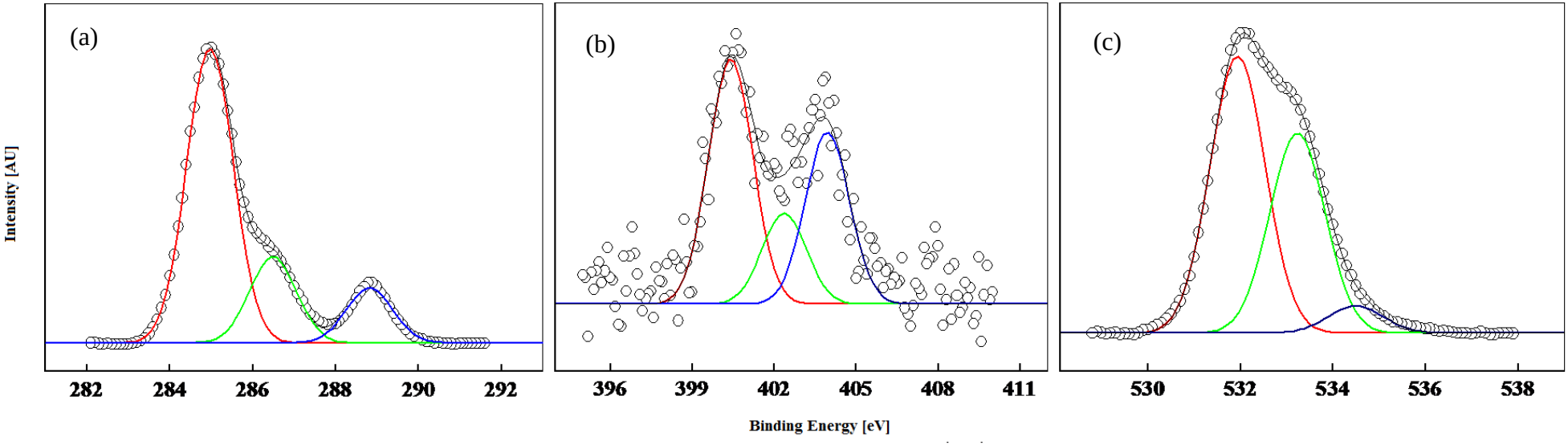

Figure 4.13: Deconvoluted high resolution XPS spectra of {Fe(μ-pyzNO-κ*N*,κ*O*)$_{n-1}$(pyzNO-κ*N*)$_2$(pyzNO-κ*O*)$_2$}$_n$(ClO_4)$_{2n}$ (Complex2) showing the (a) C 1s, (b) N 1s and (c) O 1s regions.

The high resolution XPS spectrum of the C 1s region shows three peaks; two of which show a significant degree of overlap. The three peaks indicate that the carbon (aromatic) detected is in at least three different chemical environments [18-21]. The peak centred at 289.0 eV (highest BE) is due to the C atoms of bridging PyzNO. As μ-PyzNO has the most electron deficient pi cloud due to simultaneous *N*- and *O*- modes of coordination, its C atoms will be the most *oxidized*. Core shells are therefore expected to experience the highest affinity for the higher residual effective nuclear charge. Consequently, the binding energy (BE) of 1s electrons is expected to be higher [12, 17, 18-23]. The middle peak, centred at 286.5 eV is due to the carbons of *O*-coordinated PyzNO. Lastly, the peak on the left, centred at 285.0 eV is due to the carbons of *N*-coordinated PyzNO. The rationale behind these two assignments is as follows:

The *O*-coordination mode is expected to diminish the π-electron cloud density to a greater extent that does the *N*- mode. The loss of PyzNO's N-O double bond character in the former mode, accompanying the oxidation of the O atom; which in itself diminishes the ring's electron 'richness', further increases the C atoms' core electron ionization energy [20, 21]. This is reflected in a correspondingly higher work function; that is, increased energy required to stimulate electron photo-ejection [21, 24]. In contrast, *N*-coordination increases N-O double bond character, thereby replenishing some of the electron density initially forfeited towards the formation of the dative covalent bond (M-L hybrid molecular orbitals). This in turns results in a comparatively greater electron 'richness' of the aromatic ring carbons, and correspondingly lower core electron BE [21, 22]. Additionally, the '*N*- mode peak' has far greater intensity than the other two peaks. This is consistent with expectation because, as previously discussed, Fe(II) is more compatible with aromatic *N*-donor ligands than with their *O*- counterparts [25].

The last point, which lends substantial credence to these assignments, is that the first peak (289.0 eV) is absent entirely in the C 1s region XPS spectrum of the [Fe(pyzNO-κ*N*)$_4$(H$_2$O)$_2$](ClO$_4$)$_2$·2H$_2$O complex (see 5.1.2.3). This is due to the liberation of the μ-PyzNO ligand on hydration of the complex. These changes will be further discussed in the characterisation of the hydrated complex.

The N 1s region of the spectrum shows three peaks centred at 404.0 eV, 402.4 eV and 400.5 eV, respectively. The peaks have been correspondingly assigned as due to PyzNO's μ-, *O*- and *N*- coordination modes. The rationale outlined above for the C 1s region interpretation supports these assignments excellently.

The O 1s region reveals that the major curve comprises three overlapping peaks centred at 534.5 eV, 533.4 eV and 531.9 eV, respectively. Correspondingly, these peaks are due to the oxygen atoms of μ-PyzNO, *O*-coordinated PyzNO and *N*-coordinated PyzNO. The BE's are shifted from that of elemental oxygen, which is 543.1 eV [19, 22, 23].

The O 1s signal of the ClO_4^- counterion was expected to be distinct and substantially more intense than all other O 1s peaks. However, it may be that it overlaps completely with the peak at 531.9 eV, and the two can thus not be distinguished. Alternatively, a positive BE shift of the ClO_4^- O 1s peak to beyond the scanned region; due to extensive electron withdrawal by the electronegative Cl atom and the *high* positive charge density of each formula unit, has been considered. It does however remain unconfirmed. In future investigations, and upon instrument availability, an increase in scan width will need to be employed.

XPS analysis of the $Fe(ClO_4)_2$ for comparison was considered. However, circumspection dictated otherwise, as it was thought that the salt may be potentially unstable under ultra high vacuum (UHV) conditions. The thermal effects of photon bombardment during analysis further exacerbated this concern. The possible explosive decomposition of the salt on the XPS sample stage was therefore necessarily avoided.

The high resolution spectrum of Fe 2p region was also collected and is shown in Fig. 4.14. Deconvolution was unnecessary in that instance as the constituent peaks were sufficiently resolved for a meaningful interpretation of the spectrum.

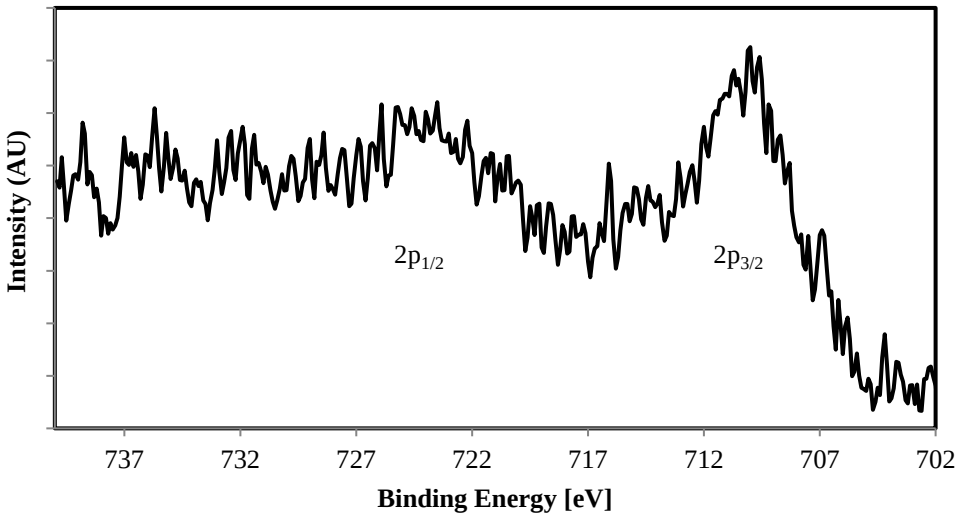

Figure 4.14: High resolution XPS spectrum of $\{Fe(\mu\text{-pyzNO-}\kappa N,\kappa O)_{n-1}(pyzNO\text{-}\kappa N)_2(pyzNO\text{-}\kappa O)_2\}_n(ClO_4)_{2n}$ (Complex2) showing only the Fe 2p region.

.

The Fe 2p region shows two peaks centred at 710.1 eV, and 724.5 eV. These peaks are attributed to resonances associated with Fe $2p_{3/2}$ and Fe $2p_{1/2}$ states*, respectively [17, 20, 22, 23]. The spin state doublets, which arise from the mixing of a 2p-vacancy with an unfilled 3d subshell, are not properly resolved in the untreated spectrum. However, the positions (BEs) of the two states with total moments $j = {}^3/_2$ and $j = {}^1/_2$ is sufficiently convincing of a pure Fe(II) complex [22, 23].

4.2.4 X-ray Powder Diffraction

The XRPD pattern of Complex2 is shown in Fig. 4.15. No sample preparative was necessary in the analysis of this complex as no colour change was seen to occur during preliminary trials. This is likely the result of the comparatively higher resistance to hydration exhibited by the polymeric complex; as evidenced by the time-dependent mid-IR profiles of the two complexes. In addition the ambient temperature of the instrument (~30 ^oC) may slow the adsorption of atmospheric moisture significantly.

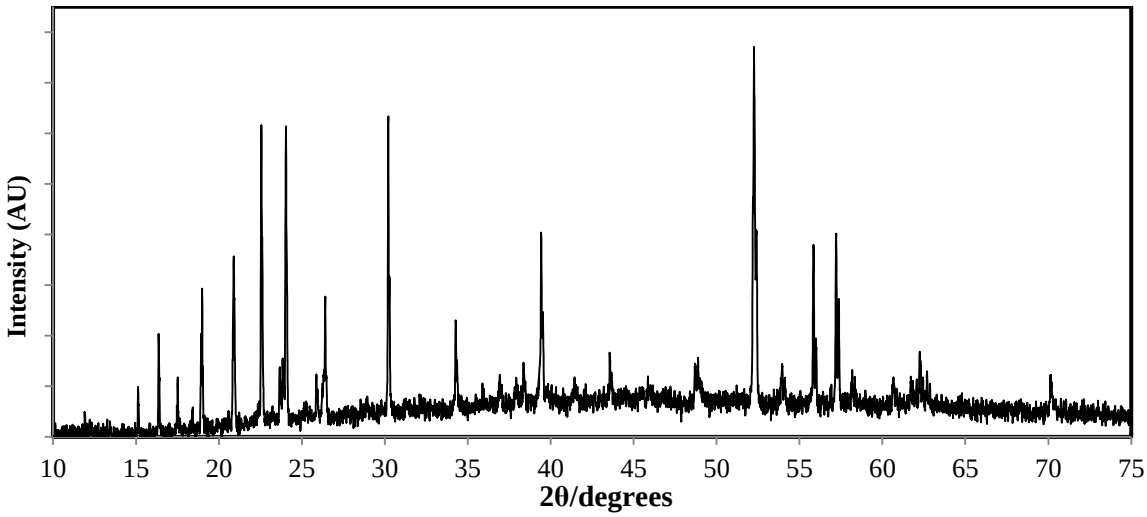

Figure 4.15: X-ray powder diffraction pattern of {Fe(μ-pyzNO-κ*N*,κ*O*)$_{n-1}$(pyzNO-κ*N*)$_2$(pyzNO-κ*O*)$_2$}$_n$(ClO$_4$)$_{2n}$ (10 – 75 $^o2\theta$) (Complex2).

*Deconvolution would be essential in order to properly reveal the spin-doublet components. However, supplementation by the C, N and O 1s regions' spectra was deemed sufficient to adequately characterise the complex by XPS. This also applies to the high resolution spectra of the Fe 2p region of the other XPS-characterized complexes in this work.

In contrast with the XRPD pattern of Complex1, Fig. 4.15 shows the first peaks of quantitative intensity appearing at after 15 $^{o}2\theta$ (15.085 $^{o}2\theta$). This suggests somewhat smaller unit cell size of the polymeric species. Additionally, the latter's diffraction pattern has peaks which are significantly narrower in comparison with Fig. 4.3, which indicates that Complex2 has markedly larger crystallites. This is consistent with expectation, as Complex1 has an inherently powder-like consistency, whereas the polymer requires milling before analysis. Intense sharp peaks span almost the entire 10 – 75 $^{o}2\theta$ range, which suggests the absence of any amorphous phases in the lattice [10, 11]. Table 4.5 shows the 2θ and corresponding *d*-spacing values.

Table 4.5: 2θ (degrees) and corresponding d-spacing (Å) values for $\{Fe(\mu\text{-pyzNO-}\kappa N,\kappa O)_{n-1}(pyzNO\text{-}\kappa N)_2(pyzNO\text{-}\kappa O)_2\}_n(ClO_4)_{2n}$ (Complex2).

$\{Fe(\mu\text{-pyzNO-}\kappa N,\kappa O)_{n-1}(pyzNO\text{-}\kappa N)_2(pyzNO\text{-}\kappa O)_2\}_n(ClO_4)_{2n}$	
2θ (º)	***d*-Spacing (Å)**
15.085	5.868
16.351	5.417
17.512	5.060
19.191	4.621
21.167	4.194
22.558	3.938
23.326	3.810
24.208	3.673
26.587	3.350
30.204	2.956
34.349	2.609
39.414	2.308
43.904	2.061
48.883	1.862

$$d = \lambda/(2\sin\theta)$$

Table 4.5 Continued: 2θ (degrees) and corresponding d-spacing (Å) values for $\{Fe(\mu\text{-pyzNO-}\kappa N,\kappa O)_{n-1}(pyzNO\text{-}\kappa N)_2(pyzNO\text{-}\kappa O)_2\}_n(ClO_4)_{2n}$ (Complex2).

$\{Fe(\mu\text{-pyzNO-}\kappa N,\kappa O)_{n-1}(pyzNO\text{-}\kappa N)_2(pyzNO\text{-}\kappa O)_2\}_n(ClO_4)_{2n}$	
2θ (°)	***d*-Spacing (Å)**
52.250	1.749
53.948	1.698
56.251	1.634
57.815	1.593
58.179	1.584
62.539	1.484
70.045	1.342

4.2.5 Differential Scanning Calorimetry, Evolved Gas Analysis and Thermogravimetry

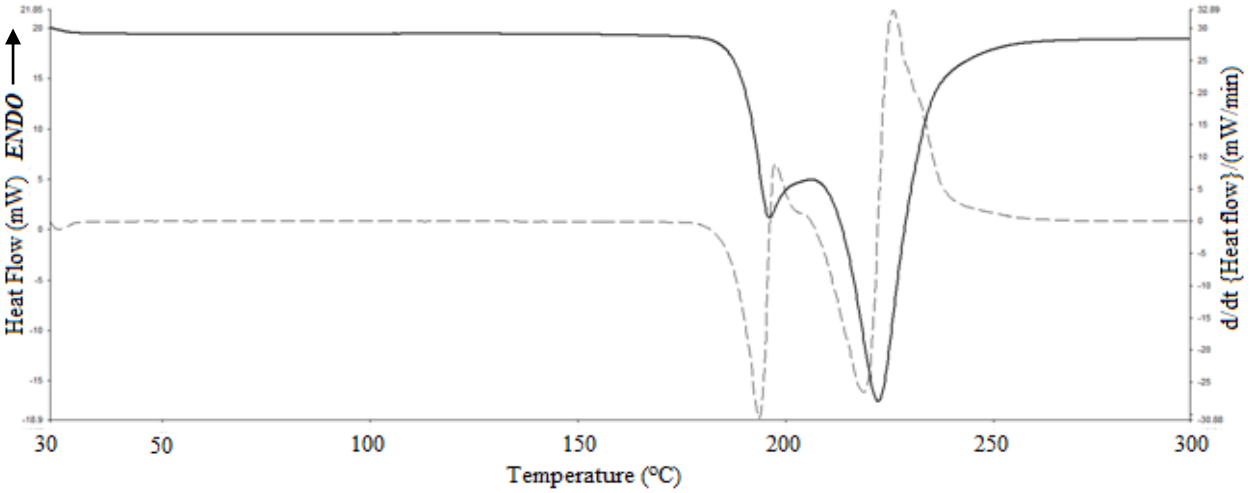

Figure 4.16: DSC thermogram (temperature range: 30 – 300 °C, heating rate: 10 °C.min^{-1}) of $\{Fe(\mu\text{-pyzNO-}\kappa N,\kappa O)_{n-1}(pyzNO\text{-}\kappa N)_2(pyzNO\text{-}\kappa O)_2\}_n(ClO_4)_{2n}$.(Complex2).

The DSC thermogram of Complex2 shows no distinct thermal events from 30 °C until the onset of decomposition at ~ 180 °C. The thermolysis of the complex occurs in a 2-step process in the 180 – 250 °C range. The first step is due to the partial decomposition of PyzNO into H_2O, CO and CO_2 gases. As with Complex1, it is the partial loss of the PyzNO fraction destabilizes the

ClO_4^- component of the remaining Fe-PyzNO-ClO_4 species. Again, the major exotherm spanning the 210 – 250 ^oC range is due to the explosive decomposition of this component, leaving a carbon/FeO/Fe_2O_3 residue.

The EGA of the complex (Fig. 4.17) shows an explosive decomposition producing H_2O, CO and CO_2 gases at 200 ^oC. The shockwave of rapid gas expansion accounts for the anomalous breaking of the background at this temperature. This is due to ClO_4^- thermolysis, and the concomitant combustion of PyzNO. There are no detected evolved gases until the complex's decomposition, with the exception of small peaks at 185 - 200 ^oC, due to partial PyzNO decomposition.

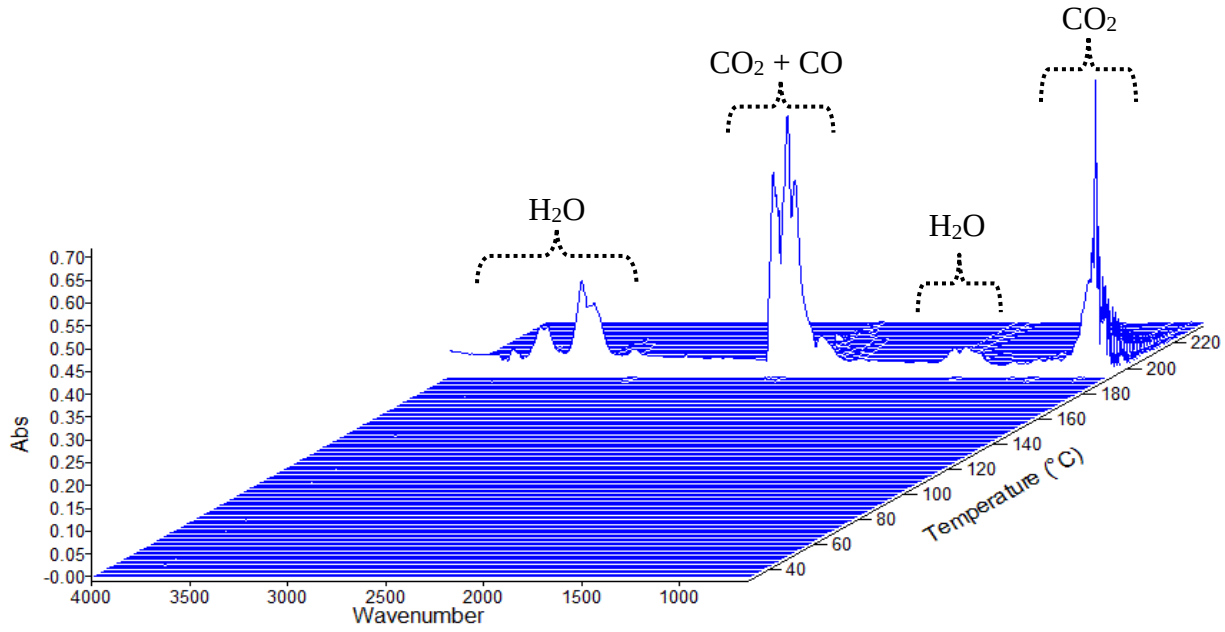

Figure 4.17: EGA stack plot of {Fe(μ-pyzNO-κ*N*,κ*O*)$_{n-1}$(pyzNO-κ*N*)$_2$(pyzNO-κ*O*)$_2$}$_n$(ClO_4)$_{2n}$.(Complex2) (temperature range: 30-230 ^oC).

Fig. 4.18 shows the TG thermogram of Complex2. The thermogram supports the above interpretation, and shows no sample weight loss until 160 ^oC, whereupon a gradual decline is observed. At this stage, the concentration of the evolved H_2O/CO/CO_2 mixture is suspected to be below the lower detection limit of the FT-IR instrument. The explosive ClO_4^- is seen to occur at 183 ^oC. The reason for the difference in the DSC and TG values for decomposition is as described for Complex1. The difference in the TG and EGA values is due to the inherent system lag as evolved gases are transported from the TG furnace to FT-IR component *via* the

connecting tube. This lag was calculated at approximately 20 °C (~ 2 min), although it may potentially vary, as ClO_4^- decomposition possibly causes a temporary pressure increase in the furnace.

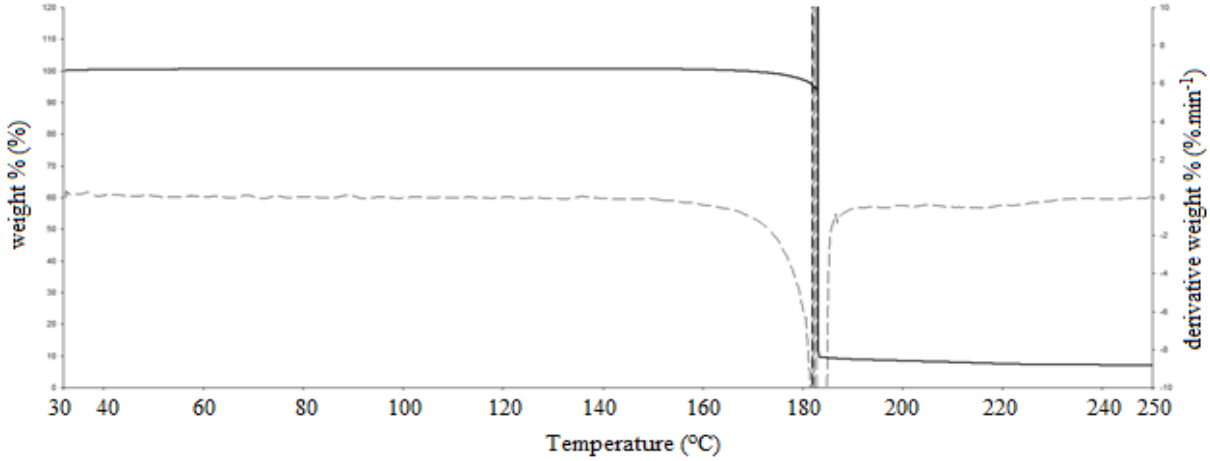

Figure 4.18: TG thermogram (heating rate: 10 °C.min^{-1}) of {Fe(μ-pyzNO-κ*N*,κ*O*)$_{n-1}$(pyzNO-κ*N*)$_2$(pyzNO-κ*O*)$_2$}$_n$(ClO$_4$)$_{2n}$.(Complex2).

4.2.6 Scanning Electron Microscopy

The SEM micrographs of Complex2 show several interesting surface features. These include the minute, seemingly regularly shaped, and repeating 'perforations' that be clearly seen in Fig's. 4.19 (c) and (d). These features are ascribed to lattice defects*. As these potentially exist throughout the crystalline mass, they may well be a significant contributor to the uniform red→yellow conversion of the material upon atmospheric exposure. Diffusion of water vapour through the solid might otherwise take substantially longer to occur to stimulate SCO. A synergy between these morphological features, and the cooperativity phenomenon ascribed to the SCO event is good candidate to explain the crystals' rapid and uniform colour transformation.

As aforementioned, the crystals are characterized by their tendency to form aggregates during their growth, thereby limiting to the size of individual 'single' components. The extent of this can be clearly visualized in Fig. 4.19 (a).

* The largest of these lattice defects (Fig. 5.19 (iv)) has an area of approximately 4.18 μm^2 at the crystal surface.

(i) (ii) (iii) (iv)

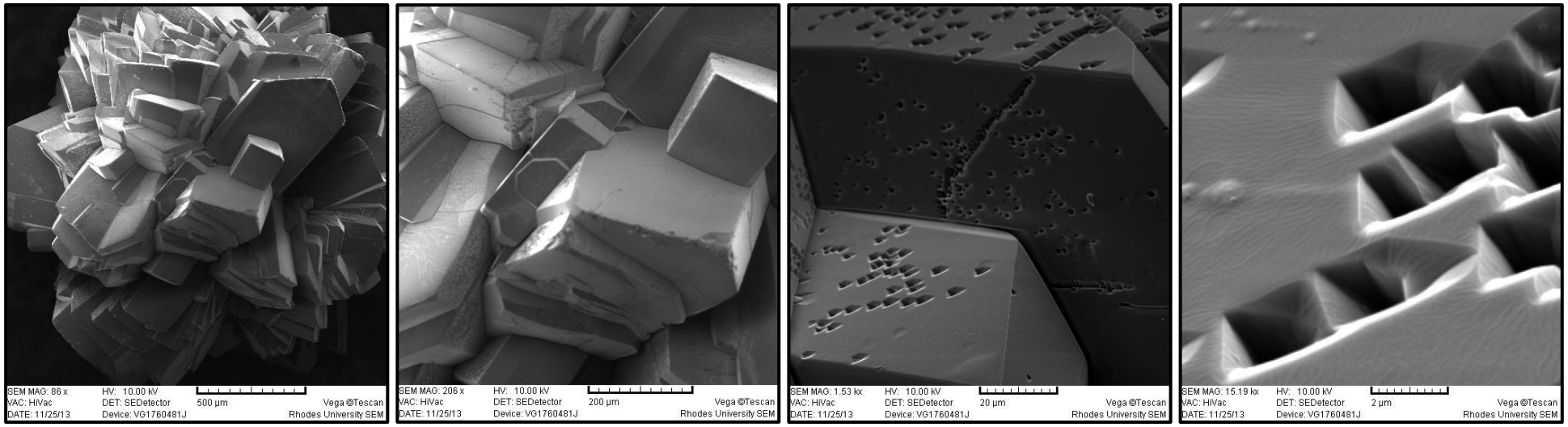

Figure 4.19: SEM micrographs of {Fe(μ-pyzNO-κ*N*,κ*O*)$_{n-1}$(pyzNO-κ*N*)$_2$(pyzNO-κ*O*)$_2$}$_n$(ClO_4)$_{2n}$ (Complex2) crystal aggregate at increasing magnification: (i) = 34x , (ii) = 85x, (iii) = 600x, and (iv) = 6000x.

4.2.7 Electron Paramagnetic Resonance Spectroscopy

As with that of Complex1 (Fig. 4.8), the EPR spectrum Complex2 showed no detectable resonances both at 77 K and at room temperature. Again, this aligns well with what is expected of a LS complex. The EPR spectrum of its hydrated form revealed the substantial paramagnetic behaviour, thereby confirming a hydration-induced LS→HS transition. The spectrum of the anhydrous species was recorded at77 K, while that of the hydrated species was recorded at both 77 K (ii) and at 298 K (i). All three spectra are shown in Fig. 4.17

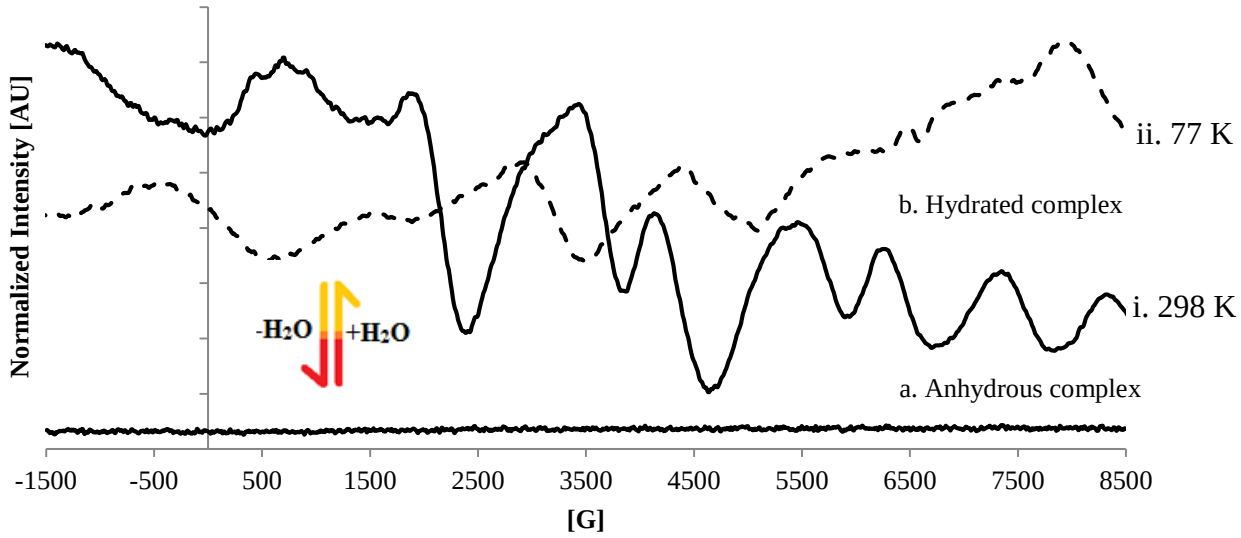

Figure 4.20: EPR spectra of (a), the original anhydrous $\{Fe(\mu\text{-pyzNO-}\kappa N,\kappa O)_{n-1}(pyzNO\text{-}\kappa N)_2(pyzNO\text{-}\kappa O)_2\}_n(ClO_4)_{2n}$ complex (Complex2) versus (b), its hydrated variant $[Fe(pyzNO\text{-}\kappa N)_4(H_2O)_2](ClO_4)_2{\cdot}2H_2O$. The spectra of the hydrated complex were recorded at (i) room temperature and (ii) at 77 K (liquid N_2 cold-finger dewar).

As stated above, the EPR spectrum of Complex2 shows no resonance features, despite numerous arbitrary increases in instrument resolution and scan width. The hydrated complex, on the other hand, showed intense activity. The spectrum could unfortunately not be resolved into its constituent lines by lowering the temperature to 77 K. The spectrum taken at 77 K does however appear to indicate a lower number of excitations. Whether this is a consequence of the reduction of thermal tumbling, or a reflection of some underlying anisotropic behaviour, is yet to be resolved. What has however been confirmed is the SCO event that occurs on hydration.

4.3 $Fe(pyzNO)_6(ClO_4)_2 \cdot 3EtOH$

The orange compound called Complex3, otherwise designated $Fe(pyzNO)_6(ClO_4)_2 \cdot 3EtOH$, has the proposed structure which is given in Fig. 4.21. The major contributing techniques to the proposed structure were microanalysis (CHNS), mid-IR and XPS. Of the many hypothetical structures and geometries that were envisaged, the one depicted made empirical sense (least deviation from the experimental results in terms of the elemental percentage values).

Mid-IR, showed one *v*(NO) band (1270 cm^{-1}), with a *subtle* shoulder (1251 cm^{-1}). Complete splitting of this band was seen in the other complexes, which indicated both *O*- and *N*- coordination modes; with a third band indicating PyzNO bridging in the polymeric complex. Therefore, the shoulder was assigned as the *v*(CO) vibration of solvate ethanol, which is typically found between 1050 and 1260 cm^{-1}. The broad band between 3000 and 3600 cm^{-1} was to interpreted to confirm the presence of solvate ethanol (*v*(OH)). As with the other complexes, the negative shift of the *v*(NO) band was deemed to indicate the *O*-mode of PyzNO coordination [1, 2, 26, 27].

The XPS high resolution scan of O 1s region showed only 1 peak*, which is consistent with exclusively *O*-coordinated PyzNO. This again was in contrast with the spectra of the other PyzNO complexes, which showed additional peaks, thereby confirming the simultaneous occurrence of other coordination modes.

* The XPS detection of solvate ethanol is uncommon; as it readily desorbs under UHV conditions.

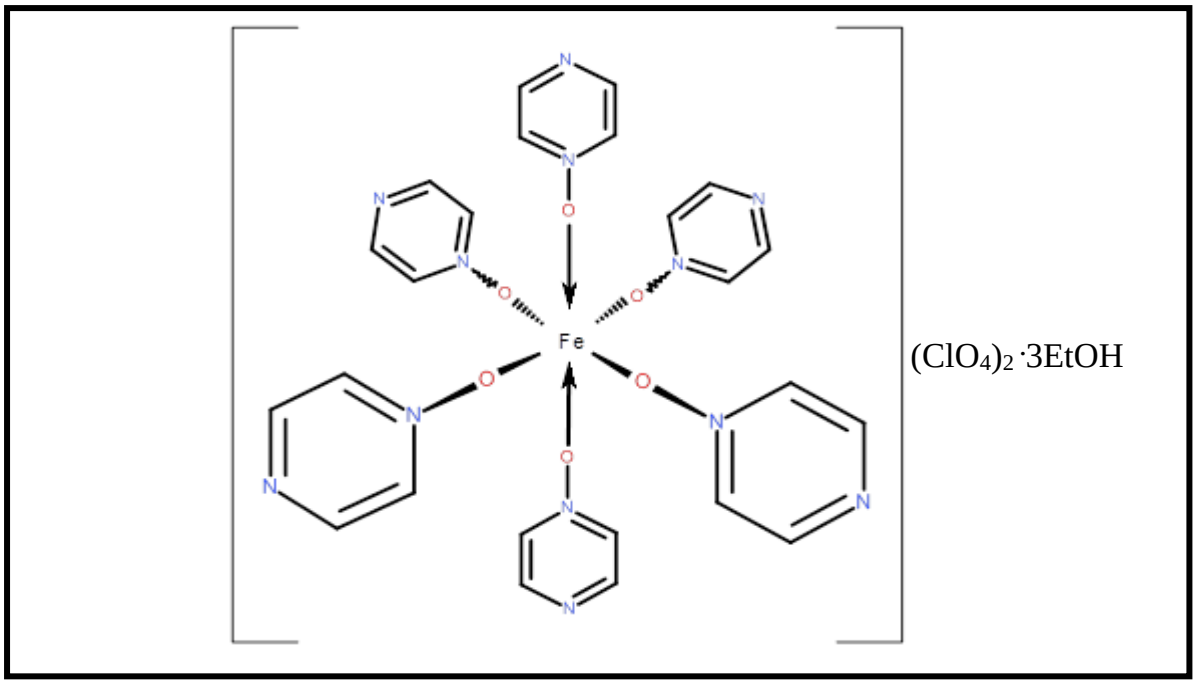

Figure 4.21: Representation of the proposed structure of Complex3: $[Fe(pyzNO\text{-}\kappa O)_6](ClO_4)_2 \cdot 3EtOH$.

4.3.1 Microanalysis and Mid-IR Spectroscopy

Table 4.6: Experimental versus calculated microanalysis values for $Fe(pyzNO)_6(ClO_4)_2 \cdot 3EtOH$ (Complex3).

Trial number	Experimental values (%)				Calculated values (%)			
	C	H	N	S	C	H	N	S
1	37.71	3.560	16.98	0.024	37.17	3.743	17.34	0
2	37.45	3.610	17.02	0				
Average	37.58	3.585	17.00	0.012				
Δ (%)$_{exp\ vs\ calc}$	+0.41	-0.185	-0.34	+0.012				

The experimental microanalysis data shows good agreement with the calculated values for a Complex3 complex (M_r: 969.4847 g.mol^{-1}). The carbon value varies by almost half a percent from the experimental value. This discrepancy is likely ascribable to the detected quantity of sulphur, the source of which is can only be instrument contamination in prior analyses, given the absence of a sulphur source in the synthesis pathway. As with the other complexes, a myriad alternative structures and geometries were considered as potential candidates. The

proposed structure, as shown in Fig. 4.21, was the closest fit with respect the CHNS data, amongst others.

The mid-IR spectrum of the complex is shown in Fig. 4.22. The coupled ν(NO) + ν(ring) vibration is negatively shifted from 1309 cm^{-1}, to produce a band centred at 1270 cm^{-1} on complexation. The new band has a shoulder at 1251 cm^{-1}, which could indicate two similar, but distinct ν(NO) frequencies in the complex in this region; suggesting *O*-mode and bridging PyzNO coordination. However, complete splitting would be expected in this situation, as seen for Complex2; with monodentate PyzNO having a ν(NO) of higher frequency. It is therefore suspected instead that the shoulder may be due to the ν(CO) vibration of solvate ethanol, leaving exclusive *O*-coordination of PyzNO. This analysis agrees with O 1s XPS spectrum of the complex, which shows only one peak - as solvate ethanol is expected to desorb under UHV. It has therefore been suggested that the electron-rich oxygen of solvate ethanol stabilizes the build-up of positive charge on the ring nitrogen of the *N*-O moiety, thereby facilitating the formation of the monodentate N-O→Fe bond. Rearrangement to form the more stable *N*→Fe bond (for a mixture of PyzNO *N*- and *O*-coordination) upon UHV ethanol desorption does not appear to be accomplished in the solid state, as evidenced by Fig. 4.24(c).

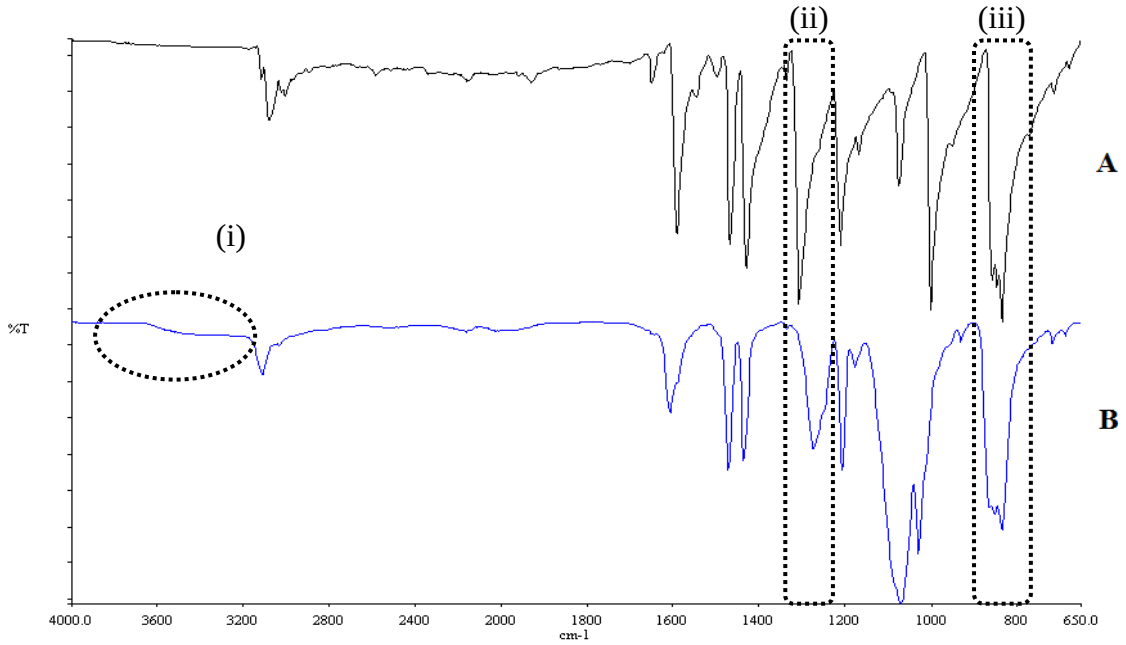

Figure 4.22: Mid-IR spectra (4000 – 650 cm^{-1}) of PyzNO (A), and $Fe(pyzNO)_6(ClO_4)_2 \cdot 3EtOH$ (Complex3) (B). The boxed regions are (i): ν(OH) of ethanol, (ii) and (iii), are those in which the coupled ν(NO) + ν(ring) PyzNO vibrations occur.

4.3.2 X-ray Photoelectron Spectroscopy

The wide scan XPS spectrum of Complex3 indicates the presence of iron, carbon, nitrogen, oxygen and chlorine, as expected. The spectrum is given in Fig. 4.23.

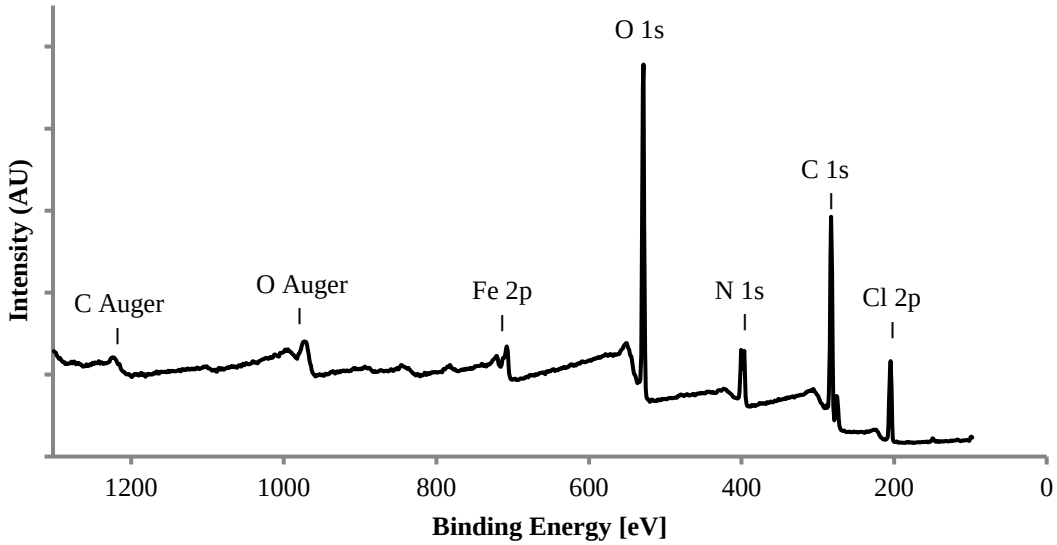

Figure 4.23: Wide scan XPS spectrum of $Fe(pyzNO)_6(ClO_4)_2 \cdot 3EtOH$ (Complex3) collected in the range 97.5 eV – 1302.5 eV.

High resolution scans of the C 1s, N 1s and O 1s regions were also collected (Fig. 4.24), whilst employing the appropriate deconvolution and theoretical Gaussian-Lorentzian curve fitting where appropriate.

The original high resolution spectrum (no deconvolution) of Fe 2p region is shown separately in Fig. 4.26.

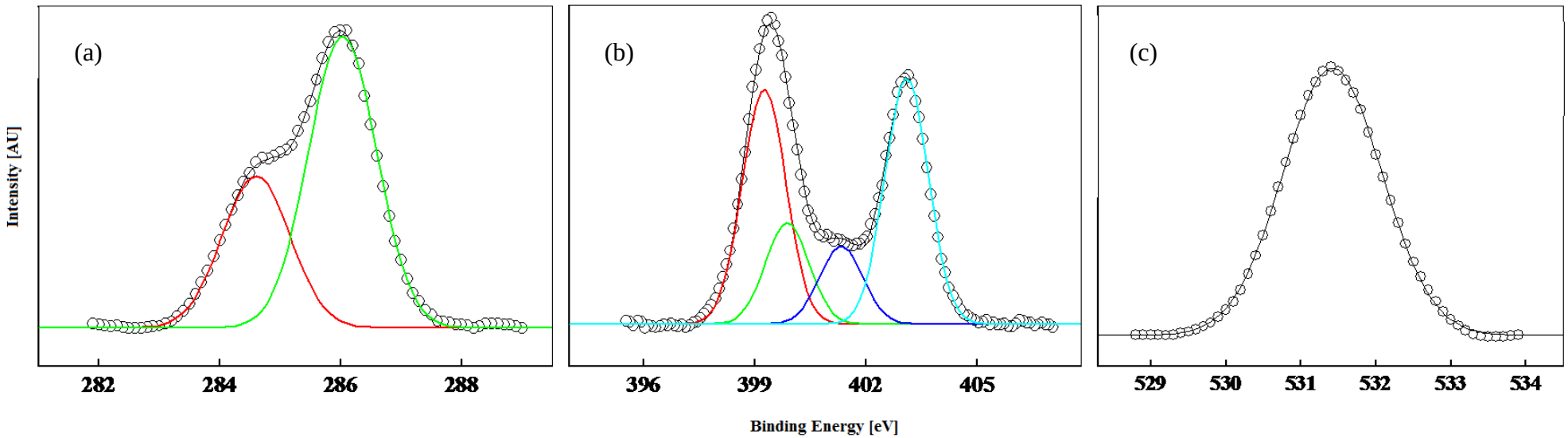

Figure 4.24: Deconvoluted high resolution XPS spectra of $Fe(pyzNO)_6(ClO_4)_2 \cdot 3EtOH$ (Complex3); showing the (a) C 1s, (b) N 1s and (c) O 1s regions.

The attempted deconvolution of the C 1s region of Complex3 failed to refine the peaks labelled (i) and (ii) in Fig. 4.25, due to software limitations. For this reason, only partial deconvolution could be achieved in Fig. 4.24 (a). The entire *undeconvoluted* spectrum is given in Fig. 4.25.

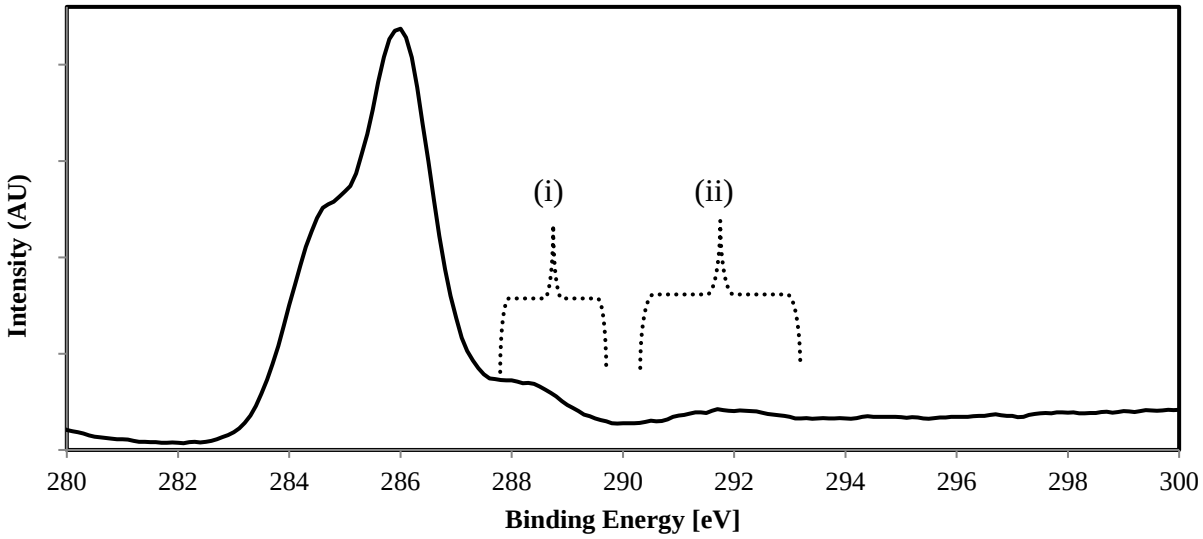

Figure 4.25: High resolution XPS spectrum of the $Fe(pyzNO)_6(ClO_4)_2 \cdot 3EtOH$ complex's (Complex3) C 1s region; showing the peaks 'missing' in the deconvoluted curve (dashed brackets).

Fortunately, the peak centred at 291.8 eV; which could not be included in the deconvoluted spectrum, is completely resolved (ii). Though this is not the case with second omitted peak (i), it is well enough separated from the major peak to at least reasonably estimate the value of the associated BE (288.3(2) eV).

The four peaks detected in the C 1s region indicate that the carbon is in at least four different chemical environments. This is thought to be a consequence of the lesser degree of ring stabilization due to ethanol desorption under UHV. That is, the aromatic carbons nearest the N-O→Fe moiety may experience a greater degree of electron deficiency, such that the C 1s resonance occurs at a higher BE [17, 19-23, 27]. Distortion from ideal octahedral geometry due to steric effects is also possible. Moreover, axial and equatorial PyzNO ligands may in this instance experience distinguishable electronic effects, hence the correspondingly different BE values. This would account for the four observed peaks. The peaks have therefore been

assigned as follows: 291.8 eV→ axial PyzNO 'N-O→Fe carbons*'; 288.3(2) eV→ carbons attached to axial N→Fe bonded PyzNO; 286.0 eV→ carbons attached to equatorial N-O→Fe bonded PyzNO; and 284.6 eV→ carbons attached to equatorial N→Fe bonded PyzNO.

The four peaks in the spectrum of the N 1s region can also be rationalised in the same way; with splitting caused by axial versus equatorial coordination, and N-O→Fe bonding versus bonding *via* the nitrogen atom opposite the N-O moiety (N→Fe). They have thus been assigned as follows: 403.0 eV→ axial PyzNO N-O→Fe nitrogens; 401.3 eV→ equatorial PyzNO N-O→Fe nitrogens; 399.9 eV→ axial PyzNO N→Fe nitrogens; and 399.2 eV→ equatorial PyzNO N→Fe nitrogens.

The spectrum of the O 1s region shows only peak, which suggests only one oxygen phase (or 2; possibly including ClO_4^- O1s peak overlap). This suggests that only one mode of PyzNO coordination in present. Comparison with mid-IR data has led to the conclusion that the exclusively preferred mode is *O*-coordinated PyzNO.

The high resolution XPS spectrum of the Fe 2p region on Complex3 is shown in Fig. 4.26 and has been assigned as was that of Complex2 shown in Fig. 4.1.4 (see 4.2.3).

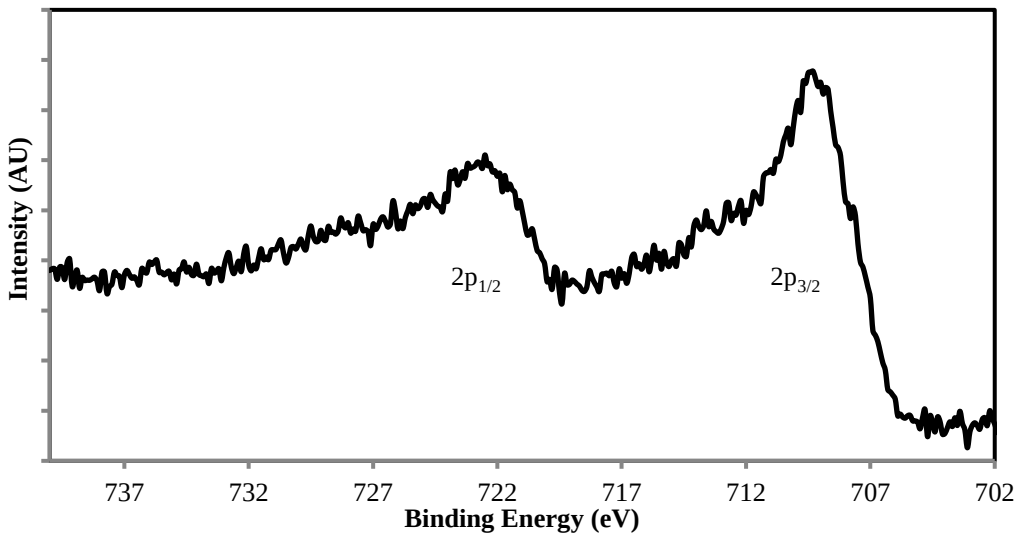

Figure 4.26: High resolution XPS spectrum of $Fe(pyzNO)_6(ClO_4)_2 \cdot 3EtOH$ (Complex3) showing only the Fe 2p region.

*,† This is to say: 'The carbon atoms directly bonded to nitrogen atoms in these groups'.

4.3.3 X-ray Powder Diffraction

The XRPD pattern of Complex3 is shown in Fig. 4.27. The complex's spectrum shows substantially broader peaks in comparison with those of the other PyzNO complexes. This suggests markedly smaller mean crystallite sizes, as well as significant amorphous character. The rapid precipitation of the product from solution upon the merging of the ligand and metal salt solutions is likely a significant contributor to these features.

The broad peak beneath the sharper reflections in the 19 – 31° 2θ range is due to background scattering by the silicate sample holder (see also Fig. 4.3). The first intense reflection occurs at 5.959° 2θ, indicating a very large unit cell size. Its broadness (as well as that of most other reflections in Fig. 4.27) suggests that it was produced by an amorphous aggregate, rather than an ordered crystalline arrangement of atoms. Unfortunately, the phases of interest are yet to be uniquely identified.

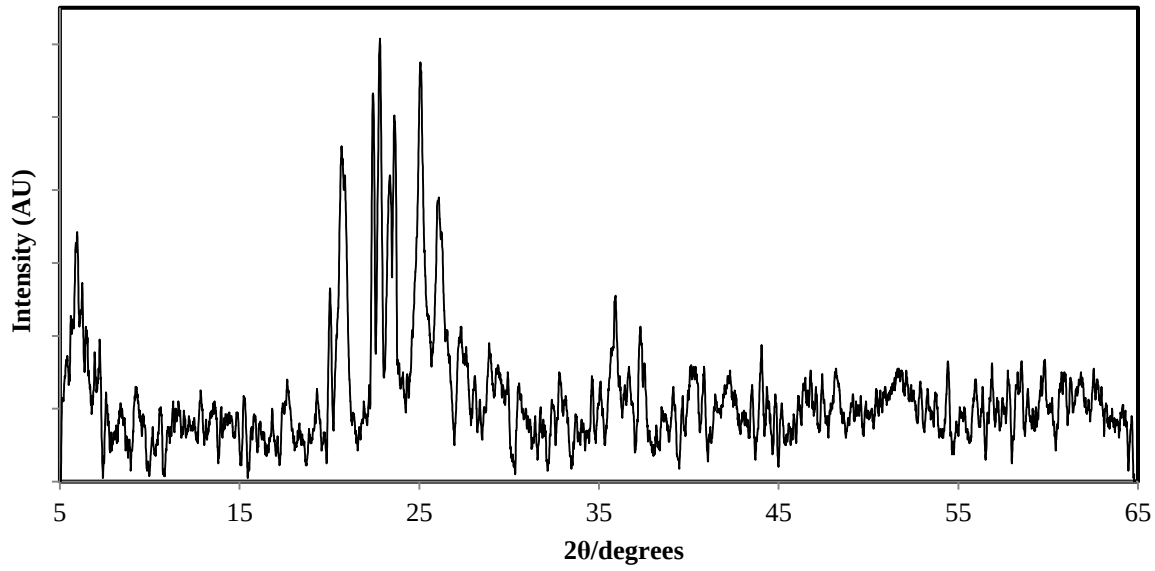

Figure 4.27: X-ray powder diffraction pattern (5° - 65° 2θ) of $Fe(pyzNO)_6(ClO_4)_2 \cdot 3EtOH$ (Complex3).

Table 4.7: 2θ versus *d*-spacing values for $Fe(pyzNO)_6(ClO_4)_2 \cdot 3EtOH$ (Complex3).

$Fe(pyzNO)_6(ClO_4)_2 \cdot 3EtOH$	
2θ (º)	***d*-Spacing (Å)**
5.959	14.819
6.238	14.157
7.203	12.292
20.033	4.429
20.665	4.295
22.748	3.906
22.796	3.898
23.602	3.766
25.060	3.550
26.087	3.413
27.334	3.260
35.891	2.500
37.602	2.390
44.046	2.054

4.3.4 Differential Scanning Calorimetry, Evolved Gas Analysis and Thermogravimetry

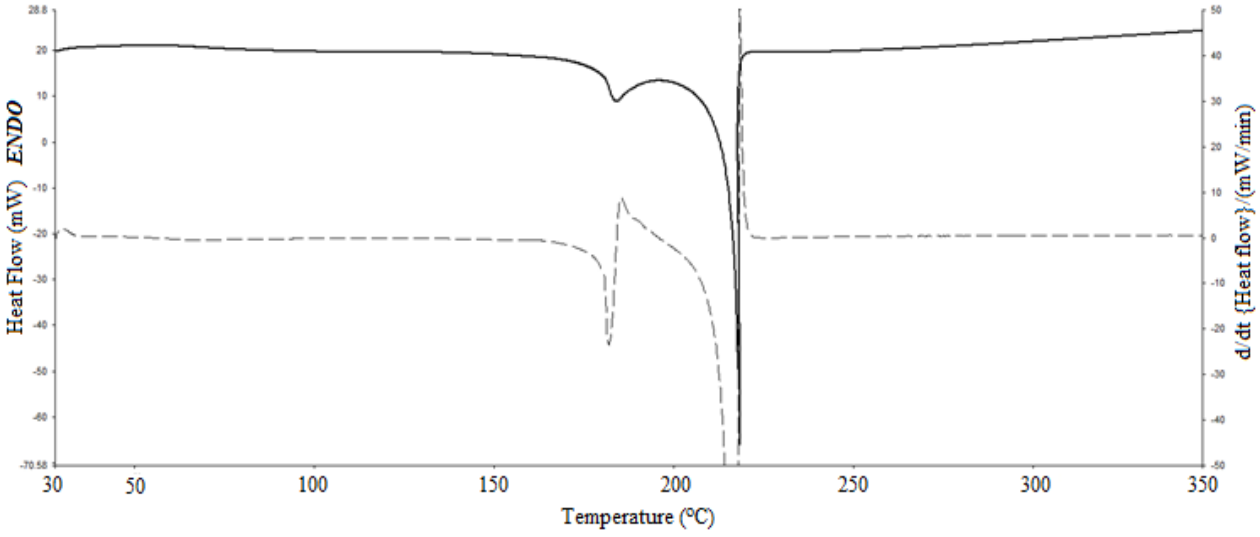

Figure 4.28: DSC thermogram (temperature range: 30 – 350 °C, heating rate: 10 °C.min^{-1}) of $Fe(pyzNO)_6(ClO_4)_2 \cdot 3EtOH$ (Complex3).

The DSC thermogram of Complex3 shows a broad endotherm between 30 and 95 ^{o}C, due to desorption of solvate ethanol. TG shows a 4.5% weight loss, which corresponds to the loss of 1 EtOH molecule per formula unit (theoretical: 4.75 %). The slow, continuous loss of 1 EtOH in the 50 - 160 ^{o}C range drops below the detection limit of the EGA (Fig. 4.29). The first decomposition step at 160 ^{o}C is the loss of half an EtOH per formula unit (seen on EGA) with an exothermic event (seen on DSC). TG shows an associated weight decline of 2.5% due to this loss (theoretical: 2.37%). This triggers the explosive decomposition of the complex (the shockwave displacement of the EGA baseline) in an extremely exothermic event (DSC), releasing the remaining 1.5 EtOH solvate units, and PyzNO as H_2O, CO and CO_2 (see EGA). This is also seen in the violent instantaneous depression of the balance mechanism in the TG (Fig. 4.30); a short-lived event immediately after which a sharp drop in weight is recorded, leaving a carbon/FeO/Fe_2O_3 residue.

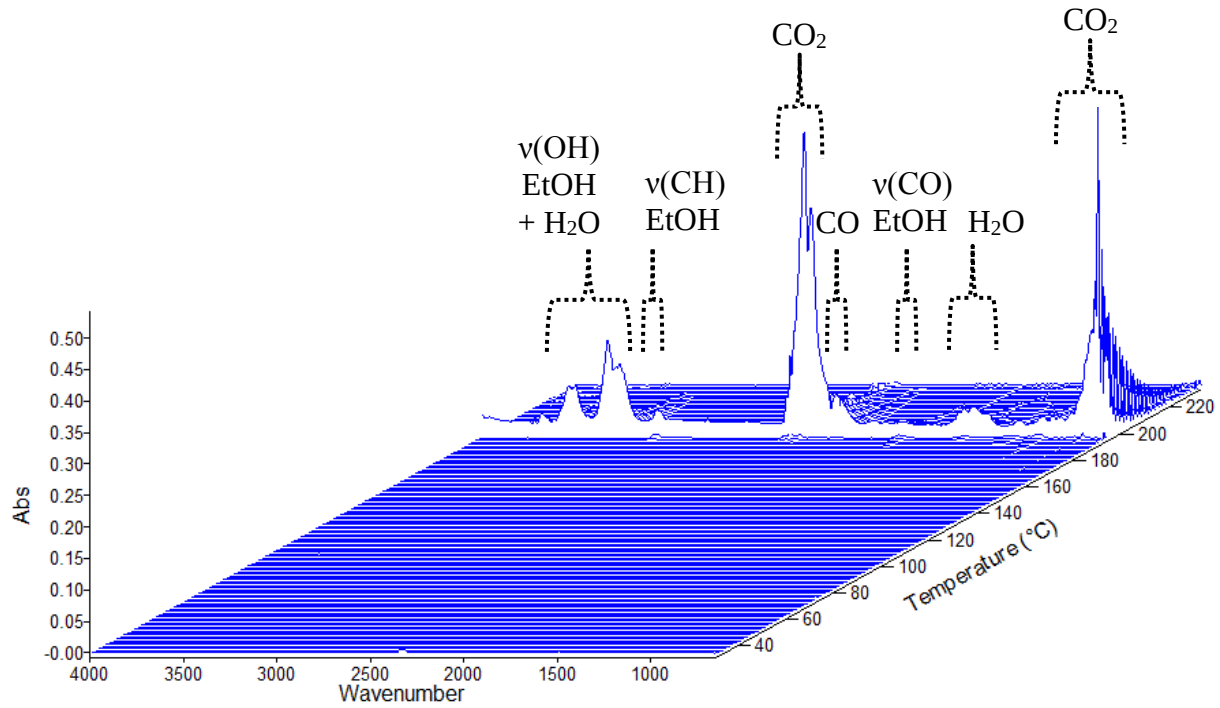

Figure 4.29: EGA stack plot of $Fe(pyzNO)_6(ClO_4)_2 \cdot 3EtOH$ (Complex3) (30-230 ^{o}C).

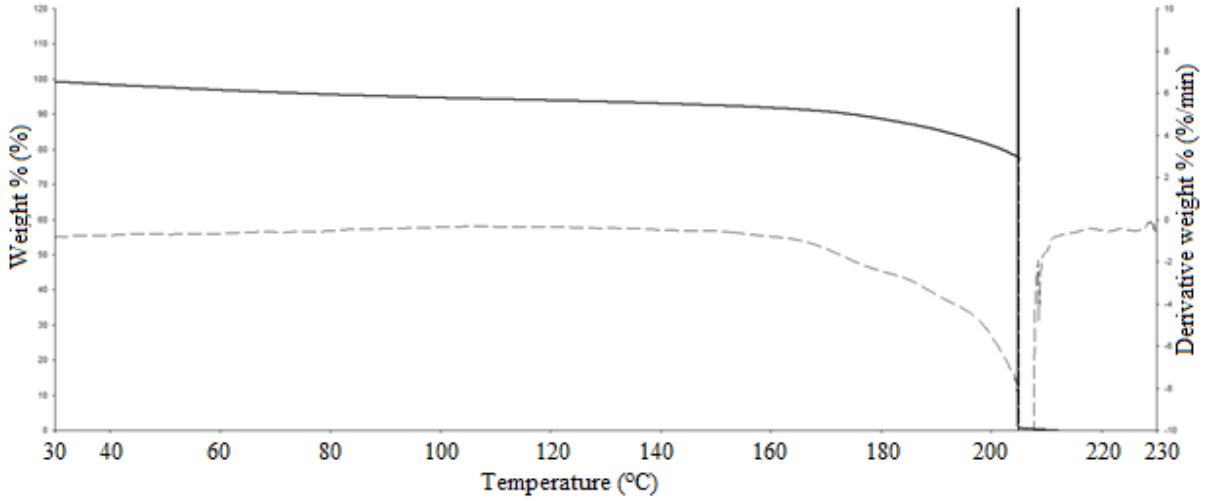

Figure 4.30: TG thermogram (heating rate: 10 $^{o}C.min^{-1}$) of $[Fe(pyzNO)_6](ClO_4)_2 \cdot 3EtOH$ (Complex3).

4.3.5 Scanning Electron Microscopy

The SEM micrographs (Fig. 4.31 (i) – (iii)) of Complex3 show its significant amorphous character, as also evidenced by XRPD (Fig. 4.27). The micrographs do not show any discernible single crystallites, but a preponderance of ‘clumpy’ agglomerated material. The images show elongated structures, but with very little apparent ‘ordered plane’ features; of which pure crystals are generally characteristic. As aforementioned, this morphological consistency is likely a consequence of the rapid manner in which the product forms, which perhaps affords insufficient time for the crystalline arrangement of atoms, to form an ordered lattice.

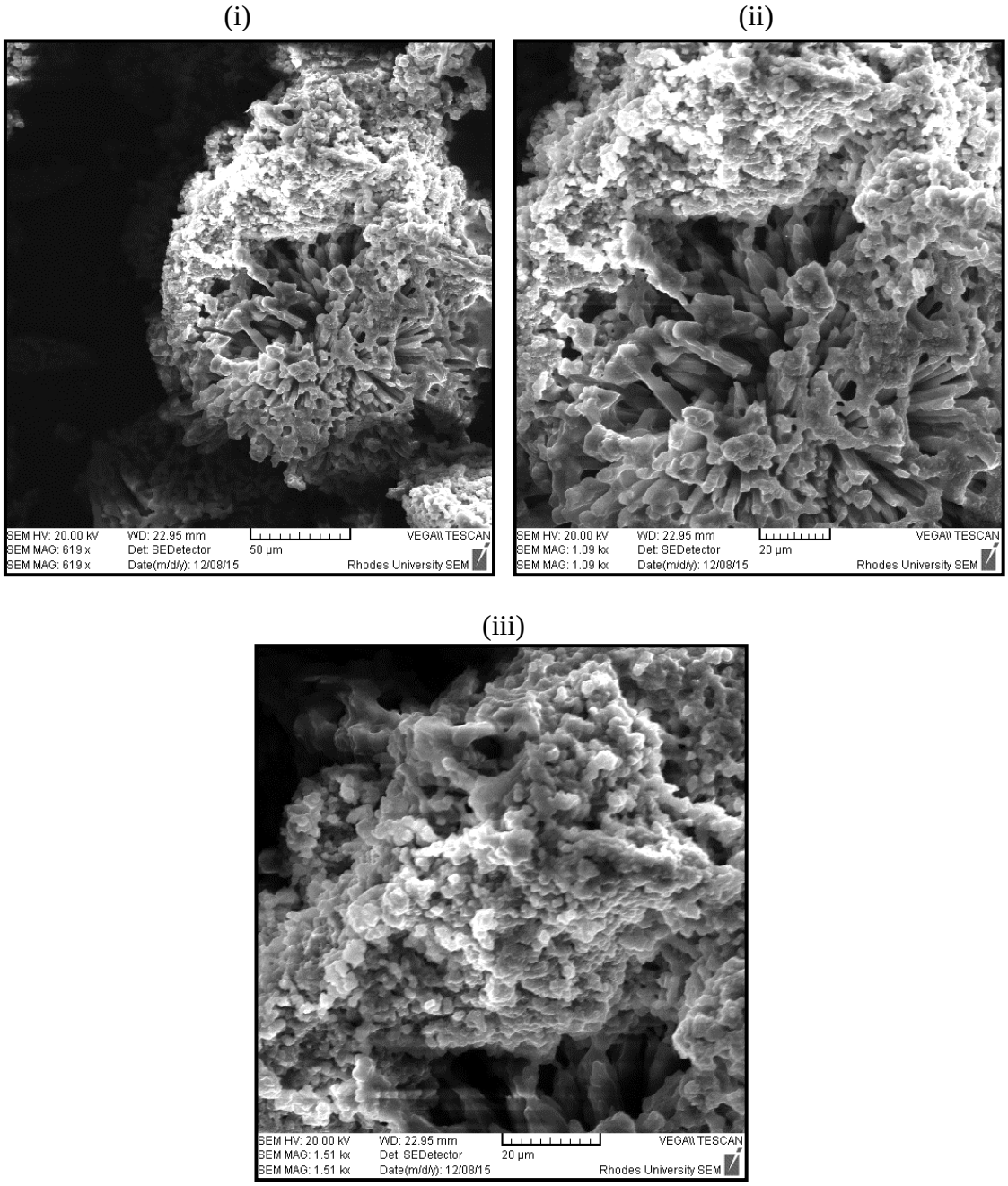

Figure 4.31: SEM micrographs of $Fe(pyzNO)_6(ClO_4)_2 \cdot 3EtOH$ (Complex3) at increasing magnification: (i) = 280x , (ii) = 500x, and (iii) = 700x.

4.3.6 Electron Paramagnetic Resonance Spectroscopy

The EPR spectrum of Complex3 compared to that of its atmosphere-exposed counterpart shows similar behaviour as that seen for Complex1 and Complex2. The LS anhydrous variant shows no detectable resonance features, whereas upon hydration, strong paramagnetic behaviour manifests accompanying its orange → yellow colour change.

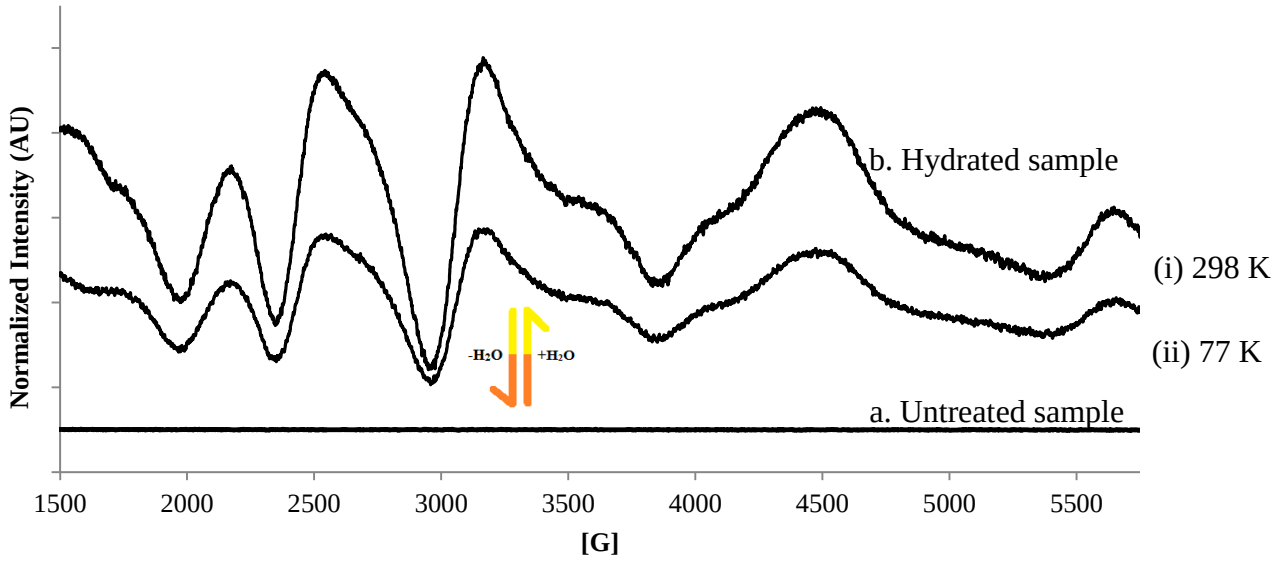

Figure 4.32: EPR spectra of (a), the original anhydrous $Fe(pyzNO)_6(ClO_4)_2 \cdot 3EtOH$ complex (Complex3) versus (b), its hydrated form. The spectra of the hydrated complex were recorded at (i) room temperature and (ii) at 77 K (liquid N_2 cold-finger dewar).

The EPR spectrum of the hydrated variant, much like that of the hydrated form of Complex2, could not be resolved into *discrete* lines. The evaluation of the associated g-parameters could not be undertaken. It was construed to suffice for a preliminary study, however, to demonstrate that a SCO event could be linked with the hydration process. Although the colour change is not as pronounced in comparison with the red complexes, the hydrated form of Complex3 was seen to have a yellow colour of significantly 'lighter' hue. This was considered to be a consequence of *O*-PyzNO and H_2O coordination, which may afford enhanced stabilization of the HOMO, to noticeably shift the charge transfer emission band. Unfortunately, as the B_o value could not be accurately found, the corresponding g_e value could likewise not be properly estimated.

4.4 $Fe_2(bipyNO)_5(ClO_4)_4 \cdot 6MeOH$

The proposed structure of the BipyNO Fe(II) complex (Complex4) was based on the interpretation of thermo-analytical, mid-IR, microanalysis and XPS data. This structure was comparatively complicated to predict as the mid-IR data was not as clear as in cases involving the PyzNO complexes. The greater general complexity of the primary ligand introduces new vibrational modes, as well as combinations thereof that make the *ν*(N-O) bands less readily identifiable. Nevertheless, with the aid of DSC, TGA, and TG-IR EGA data, a logical structure was proposed. DSC showed a large endotherm spanning the 85 to 145 ^oC temperature range, a feature which was not present in the thermograms of the original PyzNO complexes. In the same temperature range, TG-IR EGA showed distinct and significant activity in four regions: 900 – 650 cm^{-1}, 1200 – 950 cm^{-1}, 1600 – 1300 cm^{-1}, and 4000 – 3400cm^{-1}. This activity is consistent with the evolution of methanol vapour by the complex. A very small, but broad endotherm was seen between 30 and 100 ^oC on the DSC thermogram of the complex. This is due to the gradual volatilization of 2 solvate methanols per formula unit; acquired by the complex from the solvent system (MeOH/DMP; 1:1, v/v) used in its synthesis. DSC shows the loss of four coordinated methanols in the 100 – 160 ^oC temperature range, leading to the decomposition of the proposed dimeric 'pseudo-octahedral' structure.

The infrared spectrum of Complex3 provided support for the presence of methanol even after long periods of storage under ambient conditions. The technique showed strong activity in the 2700 – 3700 cm^{-1} region; which is due to the O-H stretching and bending vibrations of solvate and coordinated methanol groups. The proposed structure is shown in Fig. 4.33.

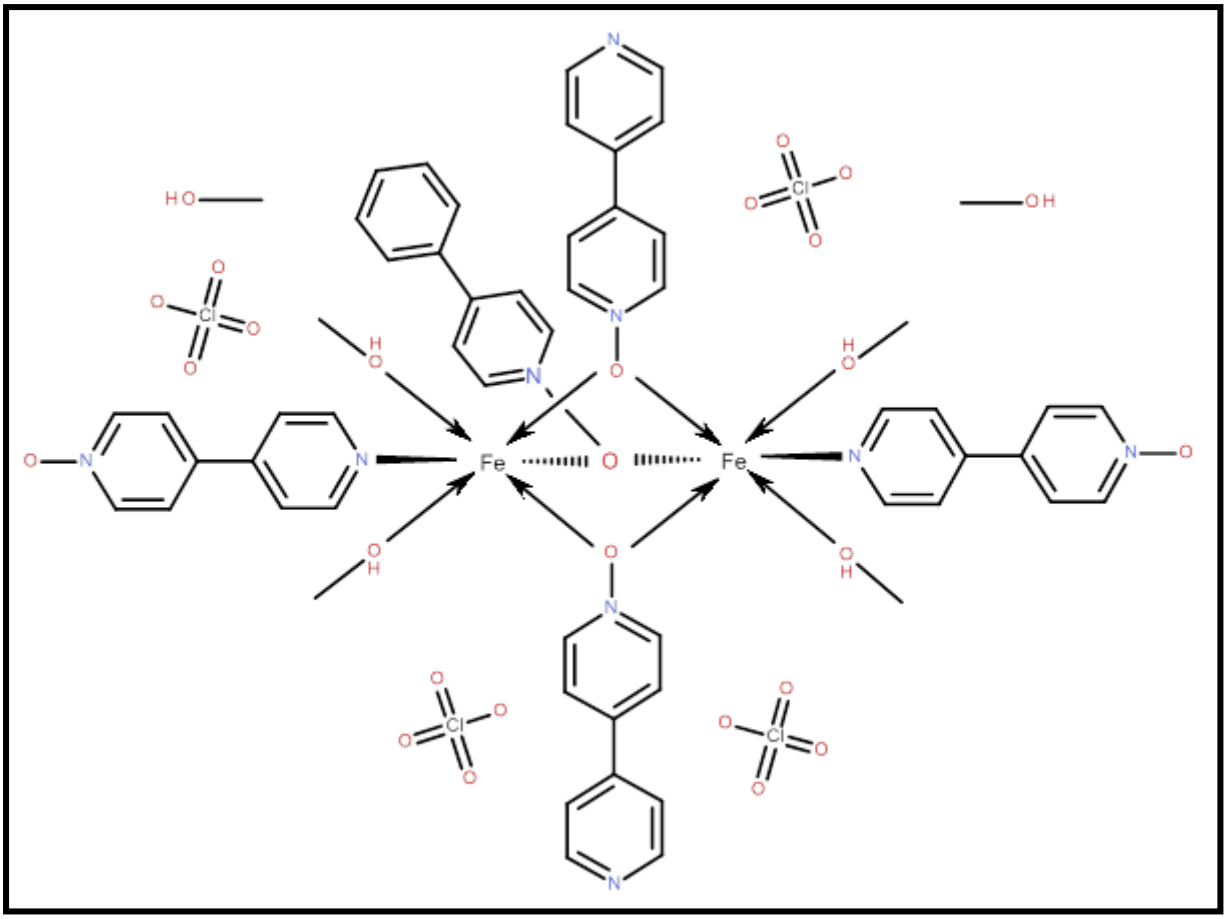

Figure 4.33: Representation of the proposed structure of the Complex4: $[Fe_2(\mu\text{-bipyNO-}\kappa^2O)_3(\text{bipyNO-}1{:}\kappa N,2{:}N)_2(MeOH)_4](ClO_4)_4{\cdot}2MeOH$.

It was initially suspected, upon scrutiny of the microanalysis data, that the complex could be polymeric. However, all such envisaged structures were ultimately empirically irreconcilable with microanalytical and XPS data. Given that the complex was expected to be octahedral, the six-coordinate dimeric structure shown in Fig 4.33 was proposed.

ClO_4^- coordination was ruled out as the IR spectrum of the complex (Fig. 4.34) provided no evidence for presence of both coordinated and free ClO_4^- units, which a splitting of the ν_a(Cl-O) band at 1000 to 1150 cm^{-1} would potentially indicate.

4.4.1 Microanalysis and Mid-IR Spectroscopy

Table 4.8: Experimental versus calculated microanalysis values for $Fe_2(bipyNO)_5(ClO_4)_4 \cdot 6MeOH$ (Complex4).

Trial number	Experimental values (%)				Calculated values (%)			
	C	H	N	S	C	H	N	S
1	43.43	4.088	9.41	0	43.04	4.128	8.96	0
2	43.61	4.114	9.49	0				
Average	43.52	4.101	9.45	0				
Δ (%)$_{exp\ vs\ calc}$	+0.48	-0.027	+0.49	0				

The experimental microanalysis data of Complex4 agrees well with the calculated values (M_r: 1562.6769 g.mol^{-1}). The calculated carbon and nitrogen percentages are admittedly low. However, numerous alternative, potentially feasible structures* and geometries were considered, each with yet increasingly substantial elemental percentage deviations from the experimental values. The proposed structure as shown in Fig. 4.33 was therefore regarded as the most reasonable approximation.

It has already been remarked upon that the mid-IR spectrum of the complex (Fig. 4.34) was of limited utility insofar as its contribution to the proposed structure was concerned. The ambiguity was a consequence of the three bands in the *ν*(NO) region (ii) in the spectrum of pure BipyNO, all of which appear to shift on coordination. The bands are at 1251 cm^{-1} (•), 1228 cm^{-1} (†), and 1190 cm^{-1} (‡). They shift to 1229 cm^{-1}, 1216 cm^{-1}, and 1182cm^{-1}, respectively, on coordination. Although unassigned conclusively, the first two bands (• and †) are considered to likely be due to the coupled BipyNO *ν*(NO) + *ν*(ring) vibrations [8, 26]. The more intense band labelled (‡) has been assigned as the *ν*(CH) vibration, by comparison to the assignments made by Thornton and Watkins [26] for their series of 2,2'-bipyridine-*N,N'*-oxide

* All feasible ratios of MeOH to BipyNO for five and six coordinate Fe(II) complexes were examined, and each gave percentage values that were irreconcilable with the experimental results.

complexes with metal(II) perchlorates. The negative shift of both (•) and (†) bands with the former showing shouldering is considered to reflect the BipyNO μ- and *N*-coordination modes.

It is conceded that these assignments were made tentatively, and further corroborative evidence is needed.

The other regions of interest are labelled (i) and (iii). The broad band in the former range is due, in 'B', to the ν(OH) vibrations of coordinated and solvent methanol; while that in 'A' has already been assigned in section 3.2 (Fig. 3.6). The complex band in the region labelled (iii) is assigned as a coupled *ν*(NO)/*ν*(ring) vibration by comparison to the assigned PyzNO mid-IR spectrum. It is thought that this band shifts into the far-IR region on coordination, hence its absence in (B).

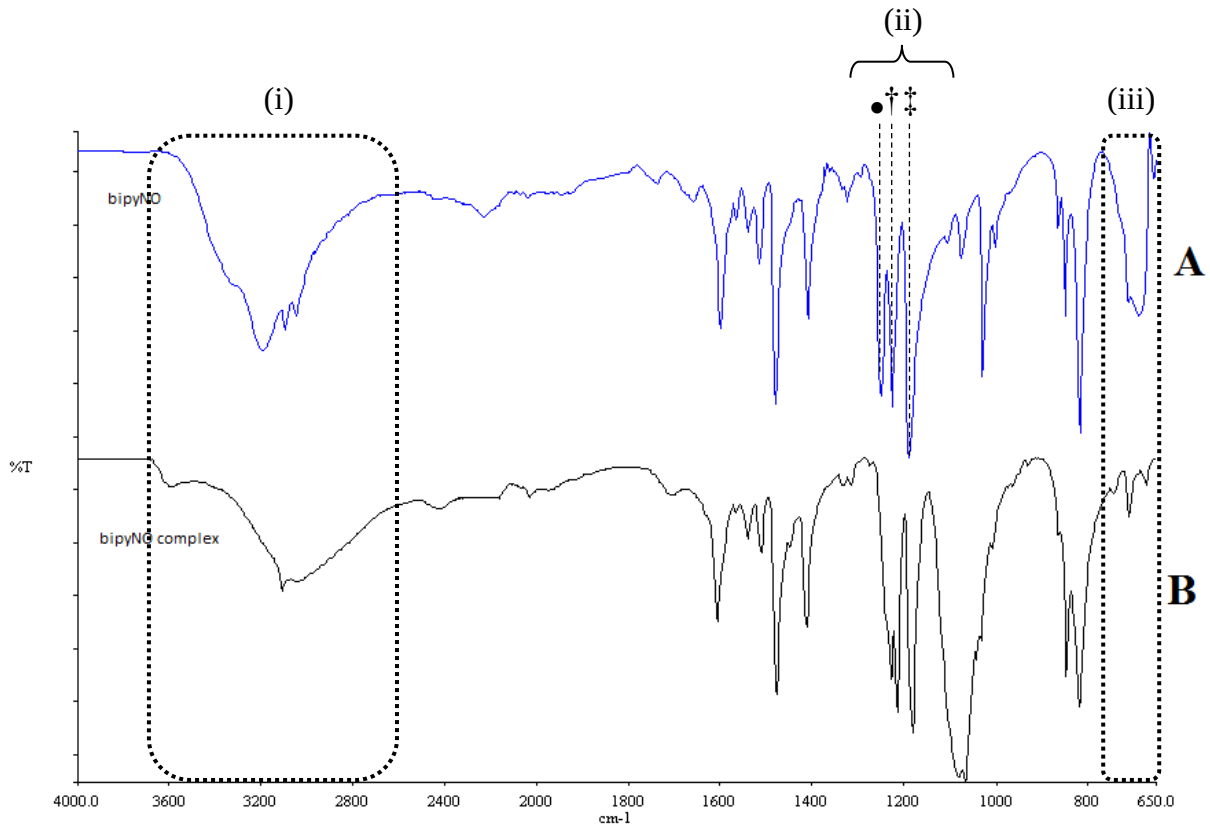

Figure 4.34: Mid-infrared spectra (4000 – 650 cm^{-1}) of BipyNO (A), and $Fe_2(bipyNO)_5(ClO_4)_4 \cdot 6MeOH$ (Complex4) (B). The boxed regions are those in which the significant vibrations occur as discussed previously; and are labelled accordingly (i-iii).

4.4.2 X-ray Photoelectron Spectroscopy

The wide scan XPS spectrum of Complex4 indicates the presence of iron, carbon, nitrogen, oxygen and chlorine, as expected. The spectrum is given in Fig. 4.35 below.

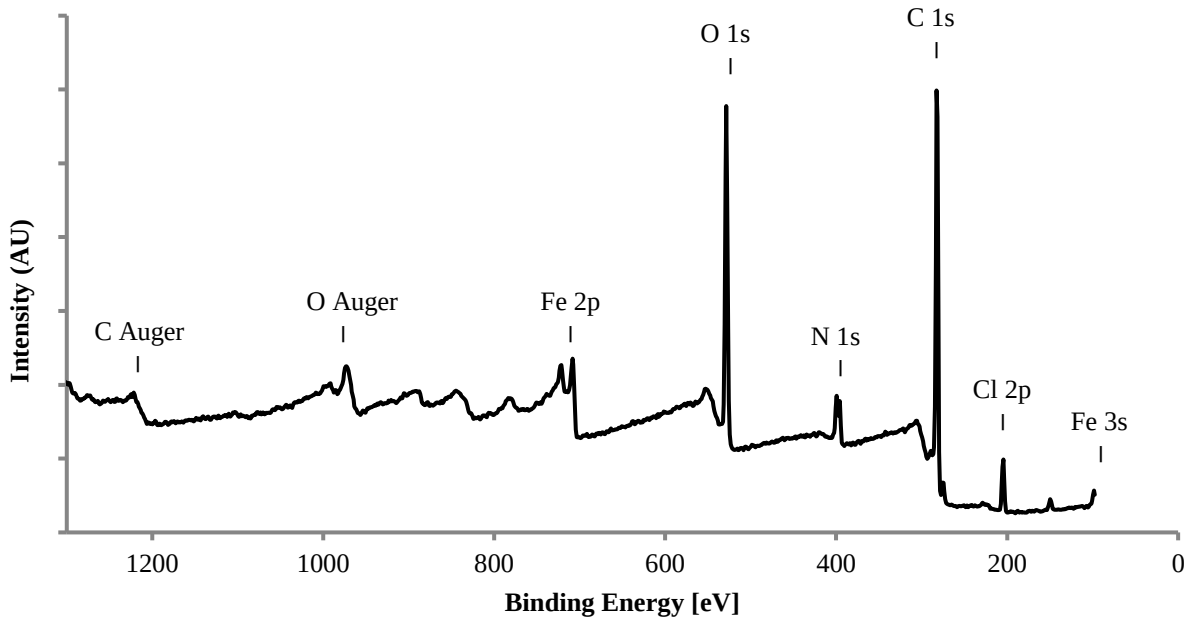

Figure 4.35: Wide scan XPS spectrum of $Fe_2(bipyNO)_5(ClO_4)_4 \cdot 6MeOH$ (Complex4) collected in the range 97.5 eV – 1302.5 eV.

As previously done, the high resolution scans of the C 1s, N 1s and O 1s regions were also collected (Fig. 4.36). Again, deconvolution and theoretical Gaussian-Lorentzian curve fitting were undertaken.

The original high resolution spectrum (no deconvolution) of Fe 2p region is shown separately in Fig. 4.37.

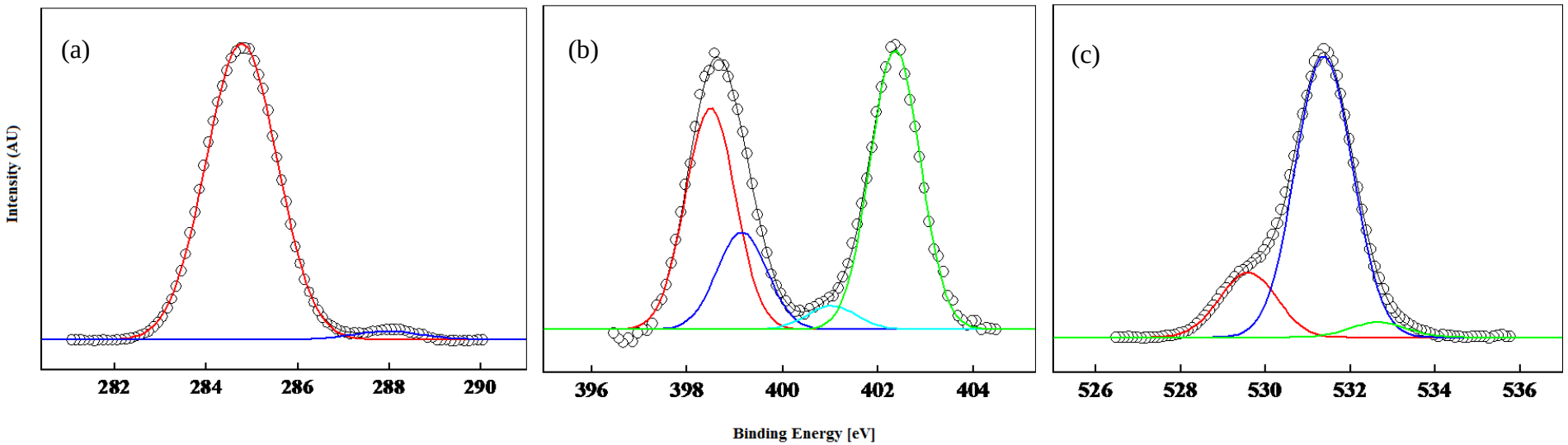

Figure 4.36: Deconvoluted high resolution XPS spectra of $Fe_2(bipyNO)_5(ClO_4)_4{\cdot}6MeOH$ (Complex4) showing the (a) C 1s, (b) N 1s and (c) O 1s regions.

Fig. 4.36 (a) indicates that the carbon detected is in at least two different chemical environments. The peak centred at 288.0 eV is due to the carbon atoms of coordinated methanol, while the peak centred at and 284.8 eV is due to the aromatic carbon atoms of BipyNO. The presence of only one aromatic carbon peak was initially regarded as anomalous with respect to the proposed structure. However, it may suggest that that inherent electron richness of BipyNO, due to its extended π-electron cloud, may offset the differential shift in C 1s BE that would be expected when comparing its monodentate and $\mu_{1,1}$ coordination modes [24, 25]. Thus, the resulting BE's may be essentially 'degenerate' when viewed by XPS.

The carbon atoms of the solvate methanols were not detected as these will likely have been volatilised under the XPS UHV conditions.

Fig. 4.36 (b) (N 1s) shows four peaks. The two peaks of highest intensity (402.4 eV and 398.5 eV) are assigned as due to the nitrogens of μ-BipyNO, while the peaks of lower intensity (401.0 eV and 399.2 eV) are due to those of monodentate BipyNO. The peak at 402.4 eV has been assigned to the nitrogen atom of the N-*O*→Fe moiety, while the one at 398.5 eV corresponds to the nitrogen of the non-coordinated pyridine ring. The peaks at 401.0 eV and 399.2 eV have been respectively assigned to nitrogens of the *N*→Fe and *N*-oxide moieties on the monodentate BipyNO ligands. The relative intensities of the peaks were considered also decisive in interpreting the spectrum.

The O 1s region of the spectrum (Fig. 4.36(c)) shows three peaks centred at 532.8 eV, 531.4 eV and 529.7 eV, respectively. The first peak has been assigned to the oxygen atom of coordinated methanol, while the second and third peaks have been correspondingly assigned to those of μ-BipyNO and monodentate BipyNO [17-22]. The positions and relative intensities of these two peaks provide substantial indication that the *N*-mode is preferred in monodentate BipyNO. The oxygen O 1s electron of μ-BipyNO is expected to have a higher BE than that of *N*→Fe monodentate BipyNO, due to electronic coordination effects. That is, the greater electron density associated with the uncoordinated O-atom of the *N*→Fe mode (monodentate BipyNO), in comparison with the equivalent, doubly coordinated atom of the μ-mode, should reflect in a correspondingly lower O 1s BE of the former [18-22, 27].

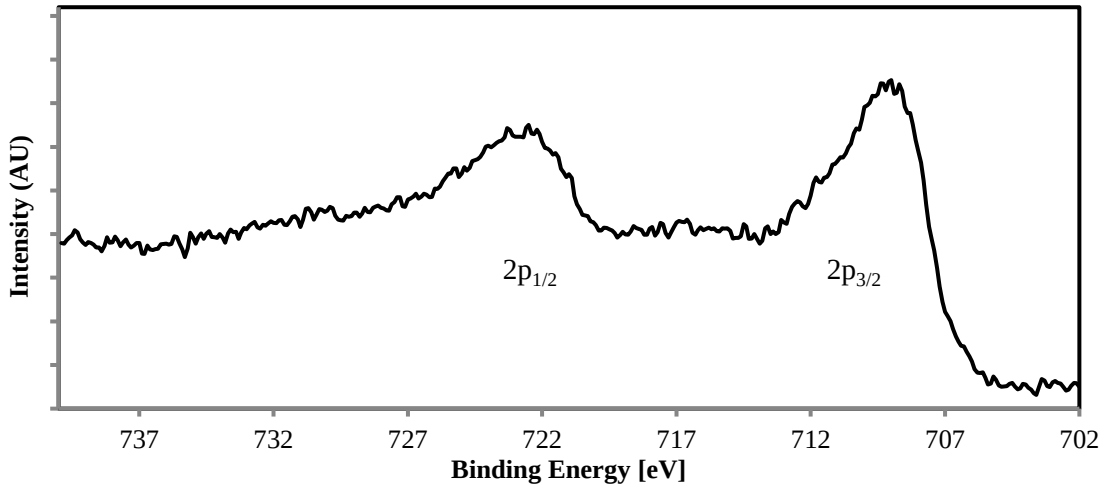

Figure 4.37: High resolution XPS spectrum of the Fe 2p region of $Fe_2(bipyNO)_5(ClO_4)_4 \cdot 6MeOH$ (Complex4).

Fig. 4.37 shows two distinct resonances. The peak centred at 708.9 eV is due to the Fe $2p_{3/2}$ state, while the peak centred at 723.3 eV is due to the $2p_{1/2}$ state. The peaks represent anticipated binding energies for these 2p states of Fe(II) [17, 20, 22, 23, 28].

4.4.3 X-ray Powder Diffraction

The XRPD pattern of Complex4 is shown in Fig. 4.38. As the complex was found to be resistant to atmospheric hydration, as evidenced by TG, DSC data, and mid-IR data; no sample pre-prep was necessary.

Fig 4.38 shows fairly sharp and well defined reflections, indicating significant crystallinity. All quantitative peaks are found in the 16.7 – 28.0 $^{o}2\theta$ range, which contains all of the reflections associated with *N*-Fe and *O*-Fe BipyNO phases, as well as the MeOH-Fe phase; although the latter requires further verification by single crystal XRD or *in situ* temperature-programmed XRPD. This indicates a small to moderately sized unit cell. The peaks are significantly broader relative to those in Fig's. 4.3 and 4.15, which would indicate correspondingly smaller average crystallite sizes. This is in good agreement with the SEM micrographs, which show minute needle-shaped microcrystalline structures (Fig. 4.42). As mentioned, Complex4 did not exhibit any net crystallographic change on standing in an H_2O-saturated atmosphere; other that those due to the effects of preferred orientation, which are irreproducible in different XRPD experiments.

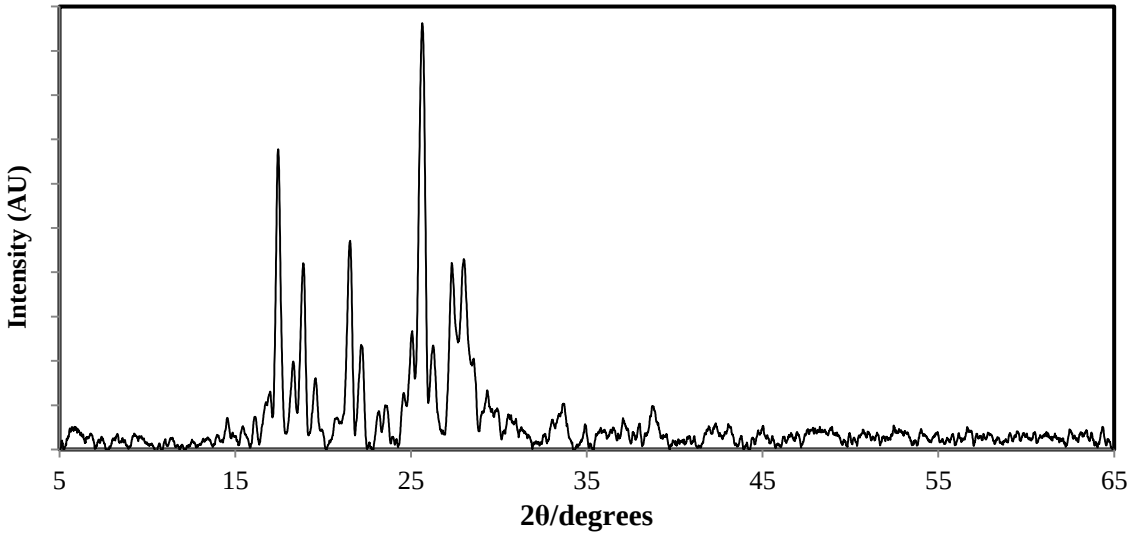

Figure 4.38: X-ray powder diffraction pattern (5° - 65° 2θ) of $Fe_2(bipyNO)_5(ClO_4)_4 \cdot 6MeOH$ (Complex4).

Table 4.9: 2θ versus *d*-spacing values for $Fe_2(bipyNO)_5(ClO_4)_4 \cdot 6MeOH$ (Complex4).

$Fe_2(bipyNO)_5(ClO_4)_4 \cdot 6MeOH$	
2θ (°)	***d*-Spacing (Å)**
16.714	5.300
17.414	5.088
18.834	4.708
19.016	4.663
19.506	4.547
21.482	4.133
22.125	4.014
22.345	3.975
23.468	3.788
24.475	3.634
24.974	3.563
25.607	3.476
25.885	3.439
27.296	3.265
27.957	3.189

4.4.4 Differential Scanning Calorimetry, Evolved Gas Analysis and Thermogravimetry

The DSC thermogram of Complex4 (Fig. 4.39) shows a weak broad endotherm spanning the 30 – 100 °C temperature range reflecting the loss of MeOH solvate, as is also evidenced by the EGA stack plot obtained from TG-FTIR analysis (Fig. 4.40).

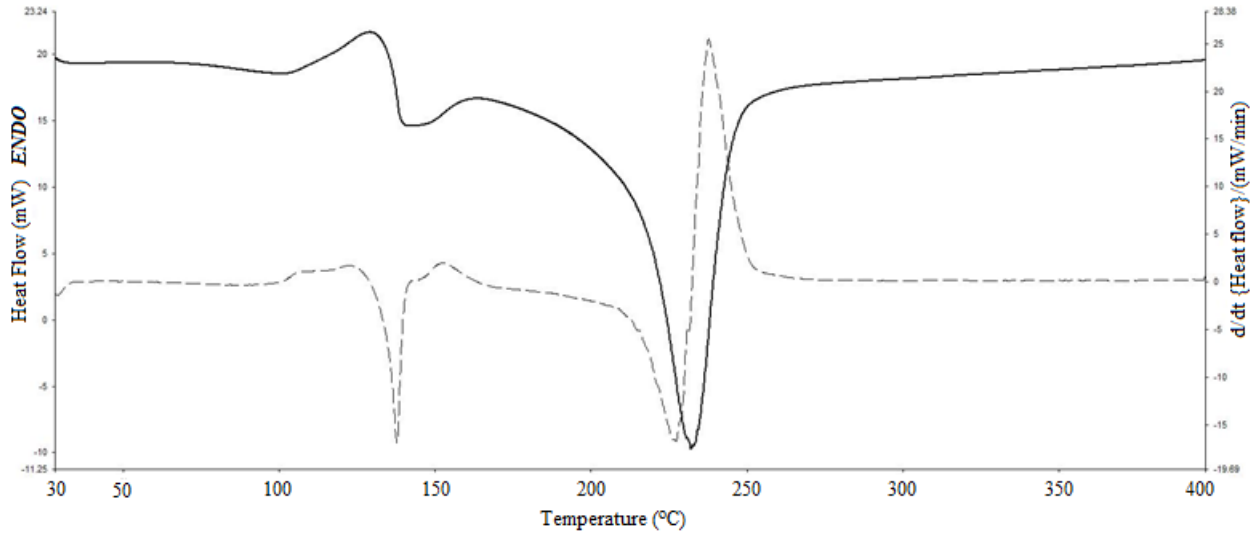

Figure 4.39: DSC thermogram (temperature range: 30 – 400 °C, heating rate: 10 °C.min^{-1}) of $Fe_2(bipyNO)_5(ClO_4)_4 \cdot 6MeOH$ (Complex4).

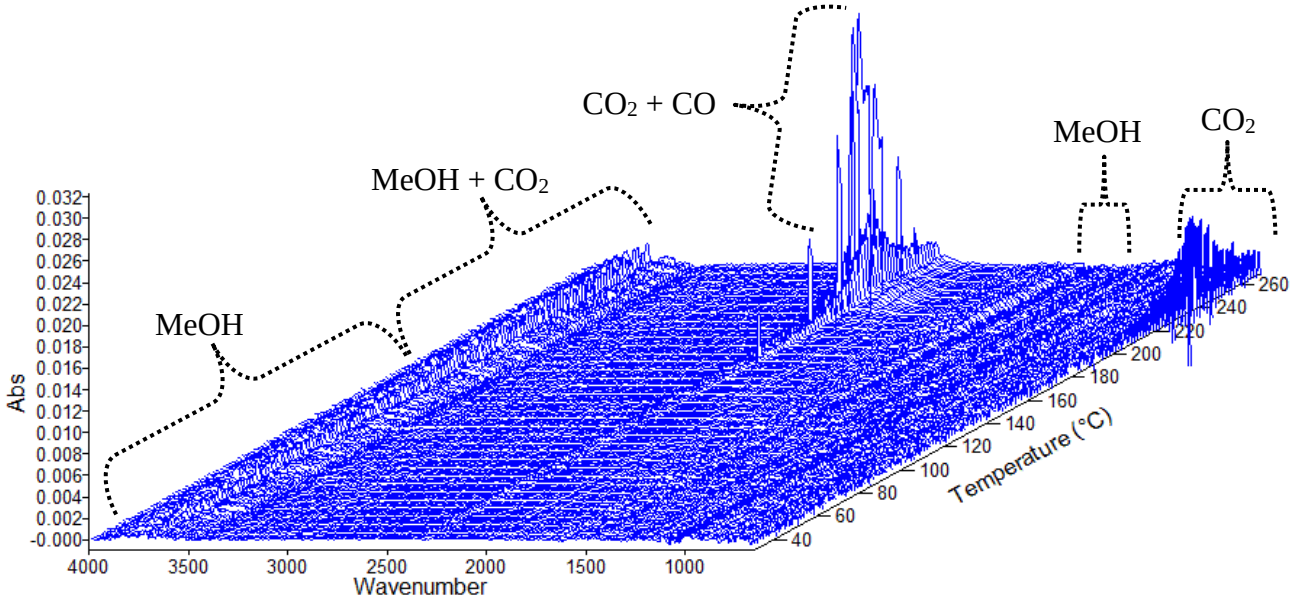

Figure 4.40: EGA stack plot of $Fe_2(bipyNO)_5(ClO_4)_4 \cdot 6MeOH$ (Complex4) (30-270 °C).

TG (Fig. 4.41) shows a weight loss of ~ 4.4 % in the 30 – 95 °C range*, which corresponds to the loss of 2 MeOH units per formula unit (theoretical: 4.10 %). Concurrently, Fig. 4.40 shows the associated methanol ν_a(OH) + ν_s(OH) bands between 3700 – 3300 cm^{-1}, as well as some activity around 1500 cm^{-1} corresponding to the ν(CO) vibration.

The DSC shows an overlapping endotherm and exotherm above 100 °C, with the loss of coordinated MeOH. The strong exotherm above 135 °C occurs after the loss of 3.5 coordinated MeOH's (when compared to the TG), possibly reflecting a phase change. The TG shows a weight loss of 7.0 % in the 100 – 135 °C range due loss of the 3.5 MeOH units (theoretical: 7.18 %).

Above 150 °C the last of the coordinated methanol is lost (shown by the corresponding endotherm in the DSC), which triggers the decomposition of the complex. The decomposition is reflected by the strong exotherm (DSC) and the production of CO and CO_2, as seen on the EGA. DSC and TG show this process to continue until 250 °C, while the latter measured an accompanying weight loss of 35.9 %.

The remaining mass of 52.7 % is a carbon/FeO/Fe_2O_3 residue. The carbon component is gradually, but incompletely oxidized by 900 °C.

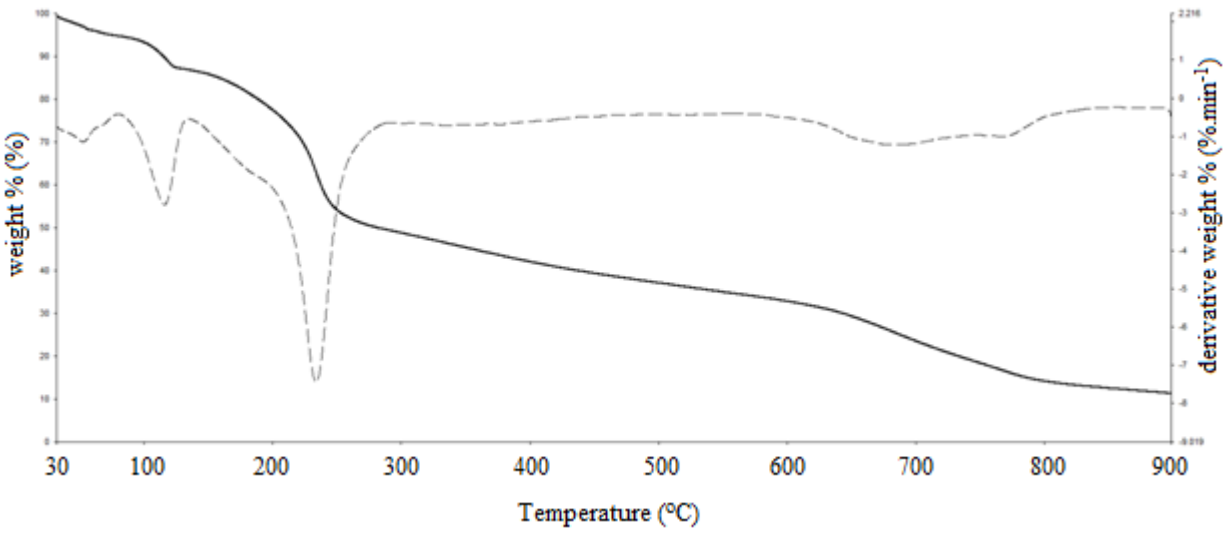

Figure 4.41: TG thermogram (heating rate: 10 °C.min^{-1}) of $Fe_2(bipyNO)_5(ClO_4)_4 \cdot 6MeOH$ (Complex4).

* 3.6 % weight loss at 30 – 55 °C (1.75 MeOHs; theoretical: 3.59) and 0.8 % weight loss at 55 – 95 °C (0.25 MeOHs; theoretical: 0.51 %)

4.4.5 Scanning Electron Microscopy

The SEM micrographs of Complex4 show complex's microcrystalline consistency. Attempts to obtain micrographs at magnifications greater than that in Fig. 4.42 (iv) were made, however, the crystals began to charge, and a significant loss in resolution resulted. For this reason, unlike Complex1, the crystal system to which Complex4 belongs could not be determined. It is however clear that the complex generates elongated needle-shaped crystalline structures. The average diameter of the crystals was estimated at ~ 12.5 μm. The micrographs are shown at increasing magnification from left to right in Fig. 4.42.

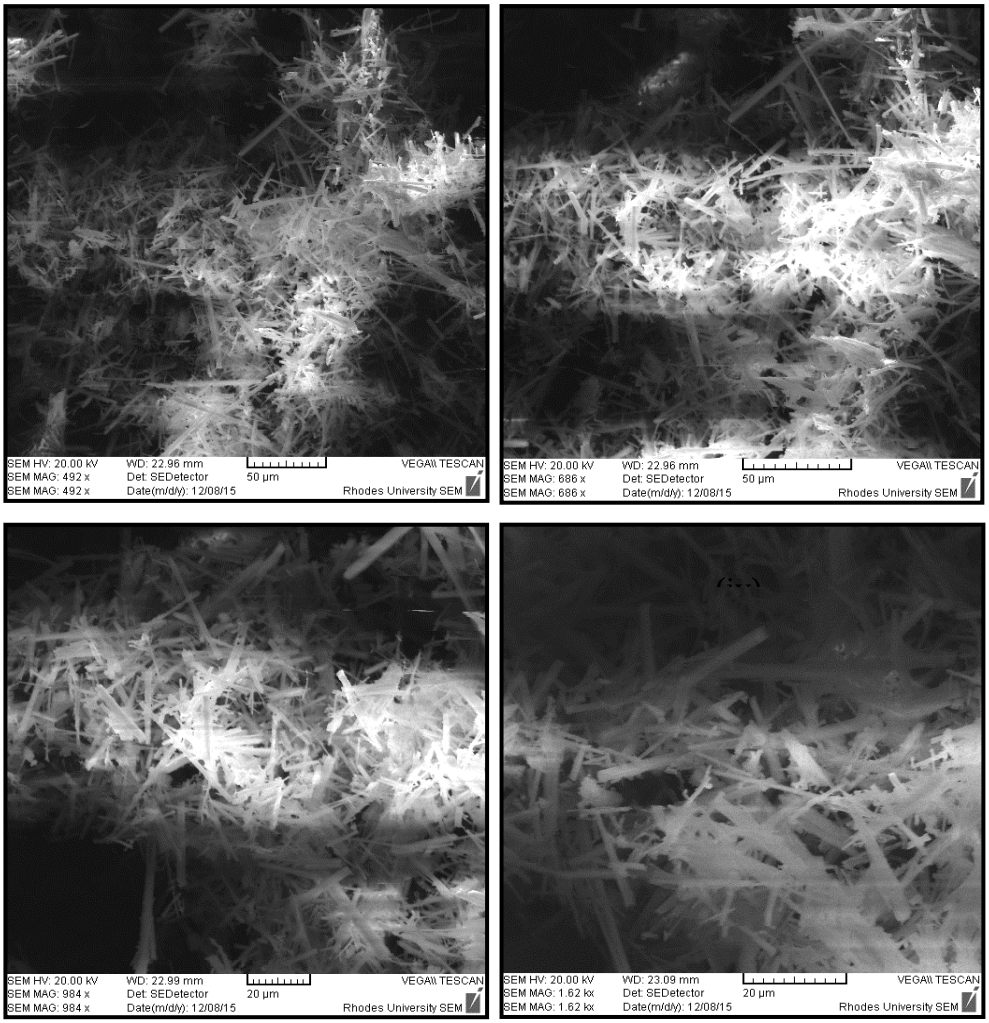

Figure 4.42: SEM micrographs of $Fe_2(bipyNO)_5(ClO_4)_4{\cdot}6MeOH$ (Complex4) needle-like crystals at increasing magnification: (i) = 200x , (ii) = 280x, (iii) = 400x, and (iv) = 650x.

4.4.6 Electron Paramagnetic Resonance Spectroscopy

The EPR spectrum of Complex4 was recorded at 77 K, and shows pronounced resonance features, in spite of there being now atmospheric exposure at this stage. This would ostensibly indicate that the complex forms its HS state at the moment synthesis. It was considered that the coordination of MeOH may be the factor which resulted in the failure to generate a LS configured BipyNO complex. However, BipyNO, being a stronger field ligand in comparison with PyzNO, was expected to counteract the effects of MeOH-induced CFSE (Δ_o) diminution. That is, the increased interelectronic repulsion in the coordination sphere due to donation from the extended pi-cloud was expected to sufficiently destabilize the highest occupied molecular orbital* to cause the HS→LS transition [29]. Although this description presumes the sequential binding of MeOH and BipyNO, a LS species was expected irrespective of the order of coordination. It was therefore considered that L→M π-bonding might be in effect, so that the pairing energy of a LS complex would be considerably greater than the resulting Δ_o [29]. The electron rich π-system of the BipyNO (*via* either *N*- or *O*- modes) is expected to be amenable to this sort of bonding [25, 30]. Fig. 4.43 shows the EPR spectrum of the complex.

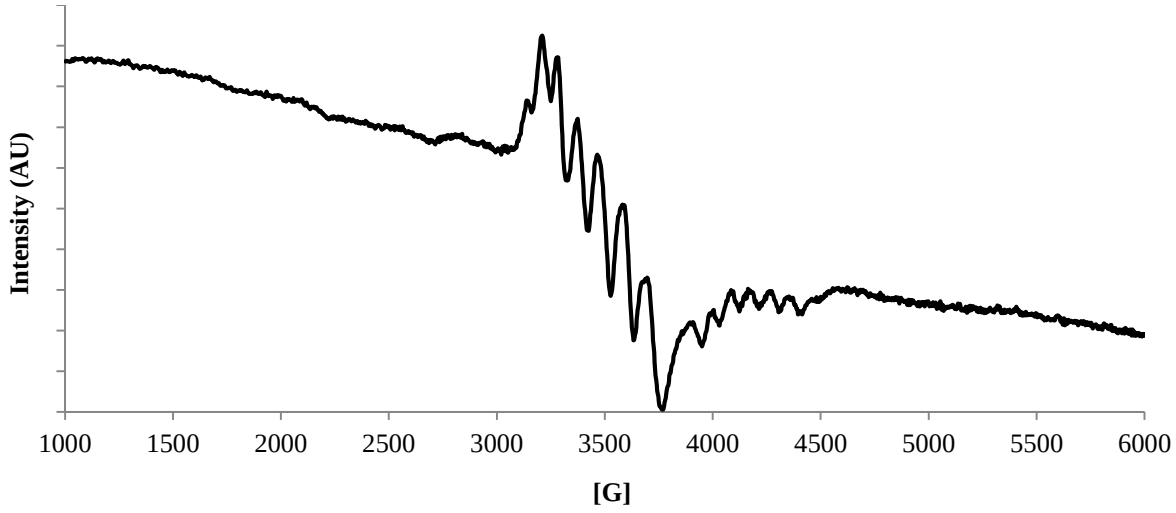

Figure 4.43: EPR spectrum of $Fe_2(bipyNO)_5(ClO_4)_4 \cdot 6MeOH$ (Complex4); recorded at77 K (liquid N_2 cold-finger dewar).

* The HOMO should be the d_x^2-$_y^2$ orbital in the case of a pseudo square-based pyramidal binuclear HS Fe(II) structure.

The major peak in the spectrum has a line width of ~ 550 G, and is split into thirteen peaks of unequal spacing; by a combination of spin-orbit coupling and hyperfine interactions. As was the case with Complex1 complex, simulation studies are yet be undertaken to evaluate the corresponding g-parameters. The electron g factor (g_e) was approximated at 1.9998 using an experimental centre field of 3491 G; (using equation 1.2; section 4.1.5).

As previously noted, Complex4 showed no measurable susceptibility to atmospheric hydration. DSC, TGA, EGA and mid-IR showed no measureable differences between the original and the atmosphere-exposed complexes. This was found to be true even when the sample was put into a water vapour saturated vessel. Additionally, the complex was found to be insoluble in water; in contrast to all the other complexes, which exhibit strong water solubility. Therefore, the discussion of the characterization of the water-exposed BipyNO complex, in the manner shown for the other complexes, will be omitted to avoid an overlap with section 4.4.

References

[1] **Speca, A.N.; Pytlewski, L.L.; Karayannis, N.M**. Transition metal perchlorate complexes with pyrazine-*N*-oxide. *J. Inorg. Nucl. Chem*. **35** (1973), 3113-3117.

[2] **Speca, A.N.; Pytlewski, L.L.; Karayannis, N.M**. Pyrazine-*N*-oxide complexes with 3d metal chlorides. *J. Inorg. Nucl. Chem*. **35** (1973), 4029-4035.

[3] **Nakamoto, K**. *Infrared and Raman Spectra of Inorganic and coordination compounds*. 6th ed. John Wiley and Sons, Inc., New Jersey, USA (2009).

[4] **Nyquist, R. A. and Kagel, R. O**. *Handbook of Infrared and Raman Spectra of Inorganic Compounds and Organic Salts*, vol. 4. Academic Press, Inc., Chestnut Hill, Massachusetts, USA (1997).

[5] **Grau, M.; England, J. de Rosales, R. T. M.; Rzepa, H. S.; White, A. J. P.; Britovsek, G. J. P.** Coordination equilibria between seven- and five-coordinate iron(II) complexes. *Inorg. Chem.*, **52** (2013), 11867–11872.

[6] **Huheey, J. E.** *Inorganic Chemistry: Principles of Structure and Reactivity*. 2nd ed. Harper and Row, New York, USA (1978).

[7] **Nordlander, E.; Whalen, A. M.; Prestopino, F**. Iron 1993. *Coord. Chem. Rev*. **146** (1995), 229-241.

[8] **Thornton, D. A. and Watkins, G. M.** An assessment of the assignment of characteristic N-O vibrations in aromatic *N*-oxides. *Spectrosc. Lett*. **25** (1992), 1023-1031.

[9] **Banwell, C.N.** *Fundamentals of Molecular Spectroscopy*. 2nd ed. McGraw-Hill Book Company (UK) Ltd., Maidenhead, Berkshire, England (1972).

[10] **Lamprecht, E.** (2008) *Thermal, spectroscopic and X-ray diffraction studies of copper(II) 1,2,4,5,-benzenetetracarboxylates and copper(II) oxalate: a study of metal-organic frameworks.* Doctoral thesis. Grahamstown: Rhodes University.

[11] *Powder Diffraction File: Alphabetical Index Inorganic Phases*. JCPDS, International Centre for Diffraction Data, Swarthmore, Philadelphia, USA (1989).

[12] **Weil, J. A. and Bolton, J. R.** *Electron Paramagnetic Resonance: Elementary Theory and Practical Applications*. 2nd ed., John Wiley & Sons Ltd (2006).

[13] **Harriman, J. E. and Loebl, E. M.** *Theoretical Foundations of Electron Spin Resonance*. Phys. Chem.: A Series of Monographs, **37** (1978).

[14] **Krzystek. J.; Smirnov, D.; Schlegel, C.; van Slageren, J.; Telser, J**. High-frequency and –field EPR and FDMRS study of the $[Fe(H_2O)_6]^{2+}$ ion in ferrous fluorosilicate. *J. Mag. Res*. **213** (2011), 158-159.

[15] **Krzystek. J.; Ozarowski, A.; Telser, J.; Crans, D. C.** High frequency and –field electron paramagnetic resonance of vanadium(IV, III and II) complexes. *Coord. Chem. Rev*. **301-302** (2015), 124-127.

[16] **Krzystek. J.; Ozarowski, A.; Telser, J.** Multi-frequency, high-field EPR as a powerful tool to accurately determine zero-field splitting in high-spin transition metal coordination complexes. *Coord. Chem. Rev*. **250** (2006), 2309-2319.

[17] **Huo, S-J; He, J-M; Chen, L-H, Fang, J-H**. Adsorption configuration of sodium 2-quinoxalinecarboxylate on iron substrate: Investigation by in situ SERS, XPS and theoretical calculation. *Spectrochim. Acta Pt. A*: *Molecular and Biomolecular Spectroscopy*. **156** (2016), 124-127.

[18] **Bouchet-Fabre, B.; Zellama, K.; Godet, C.; Ballutaud, D.; Mine´a, T**. Comparative study of the structure of α-CN_x and α-CN_x:H films using NEXAFS, XPS and FT-IR analysis. *Thin Solid Films*. **482** (2005), 161-162.

[19] **Georgiou, P.; Walton, J.; Simitzis, J**. Surface modification of pyrolyzed carbon fibres by cyclic voltammetry and their characterization with XPS and dye adsorption. *Electrochim. Acta*. **55** (2010), 1212-1214.

[20] **Negro, E.; Monteverde Videla, A. H. A.; Baglio, V.; Aricò, A. S.; Specchia, S.; Kopera, G. J. M**. Fe–N supported on graphitic carbon nano-networks grown from cobalt as oxygen reduction catalysts for low-temperature fuel cells. *Appl. Cat. B: Environmental*, (**80**) 2015, 166-167.

[21] **Hueso, J.L.; Espinós, J.P.; Caballero, A.; Cotrino, J.; González-Elipe, A.R**. XPS investigation of the reaction of carbon with NO, O_2, N_2 and H_2O plasmas. *Carbon*. **45** (2007), 91-94.

[22] **Graat, P.C.J.; Somers, M.A.J.; Mittemeijer, E.J**. The initial oxidation of ε-Fe_2N_{1-x}: an XPS investigation. *Appl. Surf. Science*. **136** (1998), 242-254.

[23] **Ivanova, T.M.; Kochur, A.G.; Maslakov, K.I.; Kiskin, M.A.; Savilov, S.V.; Lunin, V.V.; Novotortsev, V.M.; Eremenko, I.L**. XPS study of the electron structure of heterometallic trinuclear complexes $Fe_2M(\mu_3\text{-}O)(\mu\text{-}Piv)_6(HPiv)_3$ (M= Mn, Co, Ni). *Journal of Electron Spectroscopy and Related Phenomena*. **205 (**2015), 2-4.

[24] **Kwan, Y. C. G.; Ng, G. M.; Huan, C. H. A**. Identification of functional groups and determination of carboxyl formation temperature in graphene oxide using the XPS O 1s spectrum. *Thin Solid Films*. **590** (2015), 43-46.

[25] **Eicher, T.; Hauptmann, S.; Speicher, A.** *The Chemistry of Heterocycles: Structures, Reactions, Synthesis, and applications*. 3rd ed. (rev), Wiley-VCH, Weinheim, Germany (2013).

[26] **Thornton, D. A.; Watkins, G. M.** The infrared spectra (4000 – 50 cm^{-1}) of complexes of 2,2'-bipyridine-*N*,*N*'-dioxide and its perdeuterated analogue with metal(II) perchlorates of the first transition series. *J. Coord. Chem.* **25** (1992), 317-321.

[27] **Lei, J.; Rudenja, S.; Magtoto, N., Kelber, J.A**. Cu electrodeposition on Ru(0001): Perchlorate dissociation and its effects on Cu deposition. *Thin Solid Films*. **497** (2006), 125-127.

[28] **Chakravarty, S.; Kumar, N.; Panda, K.; Ravindran, T.R.; Panigrahi, B.K.; Dash, S.; Tyagi, A.K.; Amarendra, G**. The influence of nitrogen concentration on microstructure and ultra-low friction behaviour of Fe–N thin films. *Tribology International*. **64** (2014), 74-77.

[29] **Lever, A B. P**. *Inorganic Electronic Spectroscopy*, 2nd ed., Elsevier, Amsterdam, Netherlands (1984).

[30] **Royer, J** (Ed.). *Asymmetric Synthesis of Nitrogen Heterocycle*s. Wiley-VCH, Weinheim, Germany (2009).

.

Chapter 5

Solvent Studies

When stored over a desiccant, Complex1 and Complex2 retain their red colour indefinitely. However, when allowed exposure to an environment in which even trace water vapour is present, they readily undergo a rapid colour transformation to produce a yellow species (see Appendix) [1]. An intermediate orange species is transiently produced during the process. On heating, the yellow materials again turns orange at ca. 60 - 65 ^{o}C followed by a complete reversion to the blood red solid at 85 - 100 ^{o}C.

With Complex2, hydration was observed to be accompanied by the surface appearance of white crystalline needles, which disappeared over the course of periods exceeding two days of atmospheric exposure. These crystals have been concluded to be PyzNO, liberated by hydrolysis, which then subsequently sublimed. This agrees with crystal structure of Complex6 (Fig.'s 5.8 and 5.9), which shows no free PyzNO.

Given the uncertainty in the structural nature of Complex1, in the case of a monomeric form, the coordination of water at the sixth site of an initially five-coordinate complex produces a pseudo-octahedral species (the short-lived orange species that occurs on hydration). Further exposure to water then results in the hydrolysis of the trans *O*→Fe bond to generate the di-aqua-substituted complex, $[Fe(pyzNO\text{-}\kappa N)_4(H_2O)_2](ClO_4)_2$ (ignoring hydrate waters).

Given a dimeric structure, the successive substitution of both μ-PyzNO ligands (*via* a dimeric intermediate with one remaining μ-PyzNO) produces two monomeric complexes with the formula given above. In effect, two waters replace each μ-PyzNO. On this theme, the replacement of the first μ-PyzNO gives the orange intermediate, with the replacement of the second producing the final yellow product. A mechanism whereby one μ-*O*-Fe bond with respect to each ligand is hydrolysed in the first step, producing two monomeric intermediates, with the other (now axial, former μ-) PyzNO being replaced in the second step, is also possible.

In either case, the coordinating water induces increased Fe-PyzNO bond lengths as a result of the increased electron density in the coordination sphere. The net stabilization of the e_g* molecular orbital, resulting from the saturation of complex by a relatively weak field ligand,

would effectively diminish the magnitude of the CFSE (Δ_o), thereby stimulating an electronic rearrangement to produce the high spin state.

The polymeric Complex2 was proposed to undergo hydration *via* a route that involved the initial hydrolysis of the Fe-*O* bond of μ-PyzNO. The result would be the formation of mono-aqua substituted mononuclear intermediate, followed by a second PyzNO→H_2O substitution step to produce the final $[Fe(pyzNO\text{-}\kappa N)_4(H_2O)_2](ClO_4)_2{\cdot}2H_2O$ product.

It was proposed, considering the polymeric structure of Complex2, that water dissociates such a supramolecule into discrete Fe(II) centres [2]. The reduced π-electron delocalisation (now confined to localised monomeric structures) would then be accompanied by increased inter-electronic repulsion in ML σ hybrid orbitals, leading to increased M-L bond lengths. The reduced Δ_o would facilitate LS→HS SCO by a combination of two interactions, namely: stabilisation of the t_{2g} orbital (reduced π-delocalisation producing greater M-L inter-electronic repulsion), and stabilization of the e_g* orbital (increased M-L bond lengths).

Figure 5.1 applies to both square pyramidal (possibly Complex1) and tetragonally distorted pseudo-octahedral (Complex2 and possibly Complex1) geometries (C_4v and D_4h symmetries). However, the model will invariably be complicated by mixed PyzNO *N*- and *O*-coordination, which mid-IR (Complex1 and Complex2), XPS and crystal structure data (Complex2) indicate.

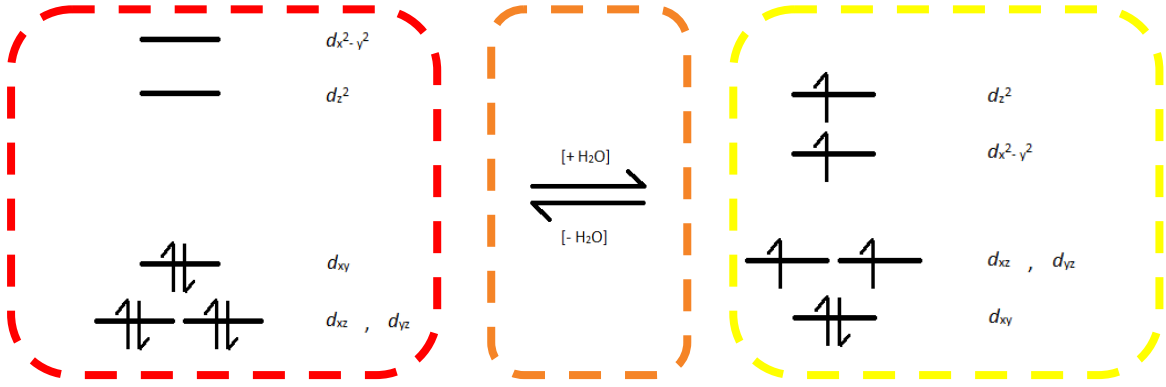

Figure 5.1: Proposed *d* orbital energy diagrams of $Fe_n(\mu_{1,1}\text{-}pyzNO)_{2n-2}(pyzNO)_{3n+2}(ClO_4)_{2n}$ (n = {1, 2}) (Complex1) and $\{Fe(\mu\text{-}pyzNO\text{-}\kappa N,\kappa O)_{n-1}(pyzNO\text{-}\kappa N)_2(pyzNO\text{-}\kappa O)_2\}_n(ClO_4)_{2n}$ (Complex2) depicting theoretical orbital reorganization during hydration and dehydration.

5.1 Characterisation of the Hydrated Complexes

5.1.1 $Fe_n(\mu_{1,1}\text{-pyzNO})_{2n-2}(pyzNO)_{3n+2}(ClO_4)_{2n}$ (n = {1, 2}) + $3H_2O \rightarrow$ $Fe(pyzNO)_5(ClO_4)_2(H_2O)_3$ (Complex1 → Complex5)

5.1.1.1 Microanalysis and Time-dependent *in situ* Mid-IR Hydration Studies

Table 5.1: Experimental versus calculated microanalysis for hydrated $Fe_n(\mu_{1,1}\text{-pyzNO})_{2n-2}(pyzNO)_{3n+2}(ClO_4)_{2n}$ (n = {1, 2}) (Complex5).

Trial number	Experimental values (%)				Calculated values (%)			
	C	H	N	S	C	H	N	S
1	30.28	3.233	17.70	0.092	30.44	3.320	17.75	0
2	30.06	3.289	17.82	0.042				
Average	30.17	3.261	17.76	0.067*				
Δ (%)$_{exp\ vs\ calc}$	-0.27	+0.059	+0.01	+0.067				

The experimental elemental analysis data is consistent with the calculated values for a $Fe(pyzNO)_5(ClO_4)_2(H_2O)_3$ species (M_r: 789.234 g.mol^{-1}). However, whether 1 or 2 waters are coordinated, whilst the remaining water(s) is a solvate unit, requires experimental verification. As previously noted, it is proposed that a di-aqua-substituted complex results, *via* a mono-aqua-substituted intermediate. Moreover, the mid-IR spectra of Complex5 and Complex6 are similar to the extent that they can be virtually superimposed (see Fig's 5.3(K) and 5.10(I)), which suggests that they may be the same compound. The discrepancies in their microanalyses correspond to a difference of one water molecule per formula unit. The microcrystalline nature of Complex1, and hence that of its hydration product, Complex5, has made crystallographic confirmation of this as yet unfeasible. Therefore, the main possibilities that have been considered as potential candidates for the hydrated structure are shown in Fig. 5.2; with 5.2B being favoured as the more likely product.

* The detected sulphur is due to the contamination of the microanalysis column by the previous analyses of compounds containing this analyte, which is difficult to subsequently remove completely despite the purging procedure the takes place between successive runs. However, the trace amounts thereof that are detected are not deemed to significantly affect current results.

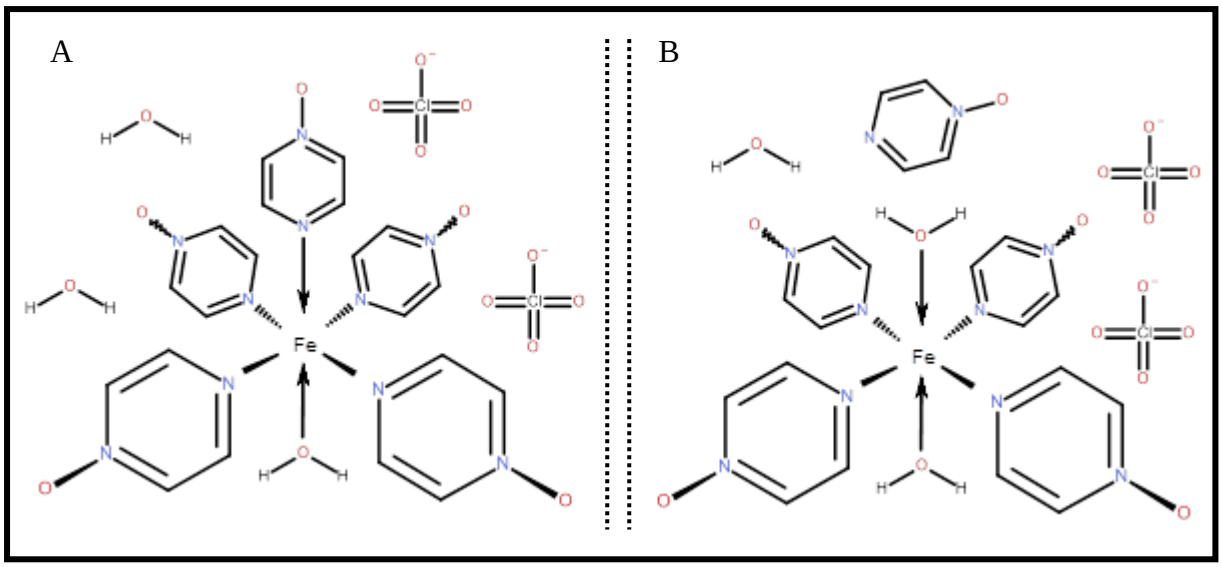

Figure 5.2: Representation of possible structures for the hydrated complex, $Fe(pyzNO)_5(ClO_4)_2(H_2O)_3$ (Complex5).

The *in situ* time-dependent mid-IR hydration profile of the Complex1 (to produce Complex5) is shown in Fig. 5.3. It shows the various vibrational changes that occur to the complex as a function of the time for which it is exposed to the atmosphere. As the crystals have a naturally powdery macroscopic consistency, milling prior to analysis was not necessary.

The first major discernible change is the appearance of the broad and medium strong band at 3600 - 2800 cm^{-1} that contains the ν_a(OH) and ν_s(OH) vibrations of water, and is characteristic of hydrogen bonding [1, 3]. More significantly though, changes in the ν(NO) region become apparent equally rapidly, indicating a direct interaction of adsorbed H_2O with coordinated PyzNO. The emergent band at 1285 cm^{-1} between 0 and 10 min of atmospheric exposure becomes very intense between 10 and 20 min, virtually overshadowing the coupled ν(NO) + ν(ring) bands (1303 and 1248 cm^{-1}) of the original complex. The coupled ν(NO) + ν(ring) vibration of free PyzNO is at 1309 cm^{-1}. That the emergent band is at a lower frequency than that of pure (anhydrous) PyzNO is ascribed to extensive hydrogen bonding of coordinated and solvate waters with the oxygen of the free *N*-oxide moiety [4, 5]. The band's emergence is thus considered consistent with the liberation of PyzNO by hydrolysis.

The coupled ν(NO) + ν(ring) at 1248 cm^{-1}, assigned to *O*-coordinated PyzNO, experiences a significant loss in intensity, signifying the preferential cleavage of *O*-Fe bonds, while the coupled ν(NO) + ν(ring) associated with *N*→Fe bonding (1303 cm^{-1}) becomes increasingly intense. The latter would ostensibly suggest an increase in the number of *N*→Fe bonds, perhaps

by an underlying water-mediated rearrangement mechanism. This and the aforementioned 'emergent band' appear to eventually coalesce between 60 and 70 minutes of atmospheric exposure, the former then essentially constituting a shoulder at this point.

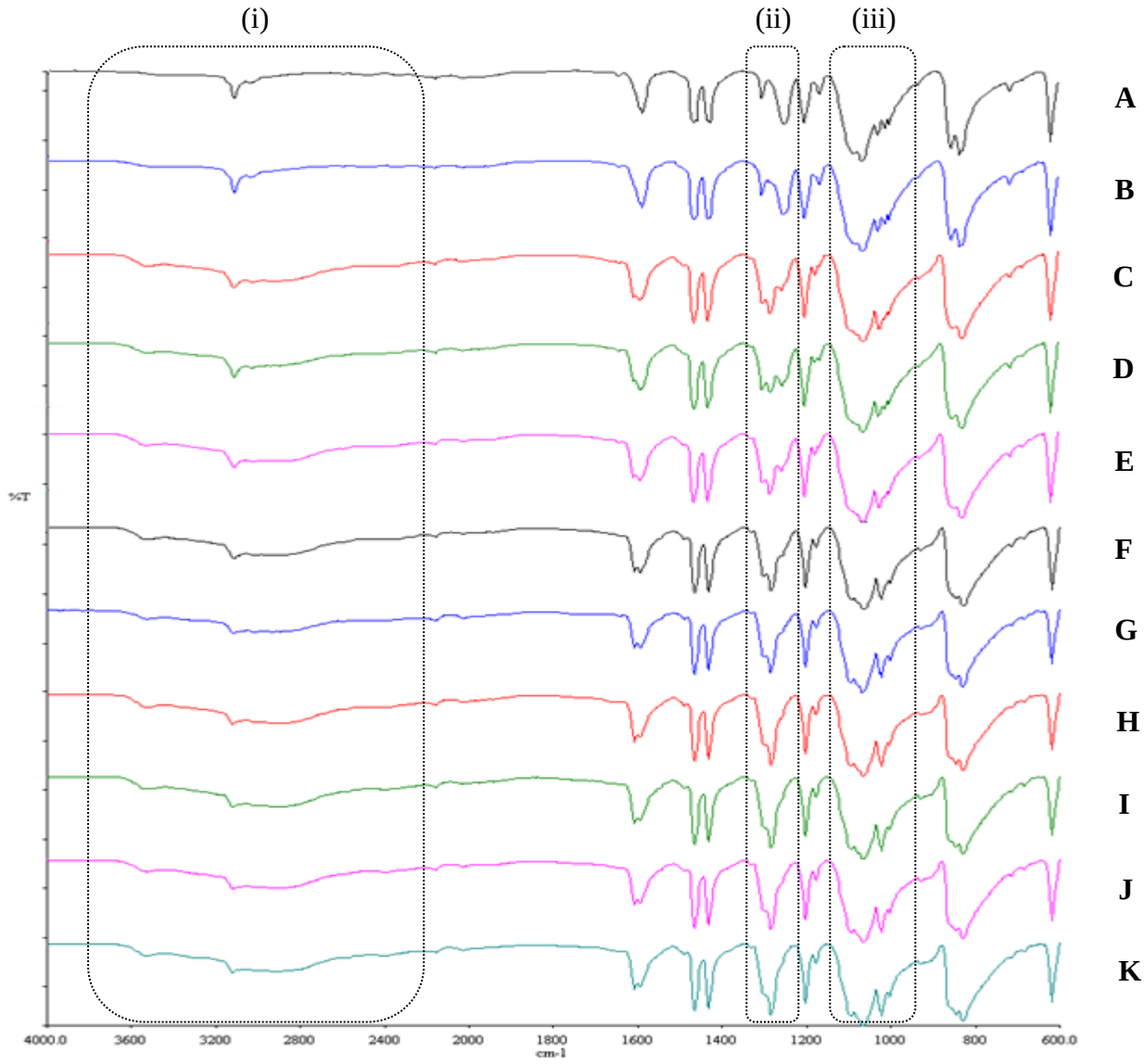

Figure 5.3. Mid-IR (4000 cm^{-1} – 600 cm^{-1}) spectra for the time-dependent *in situ* hydration profile of $Fe_n(\mu_{1,1}\text{-pyzNO})_{2n-2}(pyzNO)_{3n+2}(ClO_4)_{2n}$ (Complex1) (n = {1, 2}). A – 0 min, B – 10 min, C – 20 min, D – 30 min, E – 40 min, F – 50 min, G – 60 min, H – 70 min, I – 80 min, J – 90 min, K – 100 min. Boxed regions are (i) H_2O – $\nu_a(OH) + \nu_s(OH)$, (ii) PyzNO – coupled $\nu(NO) + \nu(ring)$, and (iii) ClO_4^- - $\nu_a(OCl)$ and PyzNO - $\nu(ring)$ vibrations.

The ClO_4^- ion (T_d symmetry) has three characteristic mid-IR bands, *viz.* a very strong broad asymmetric stretch ($\nu_a ClO_4^-$) centred at 1100 cm^{-1}; a weak (IR-forbidden) symmetric stretch ($\nu_s ClO_4^-$) at ca. 930 cm^{-1}; and a strong bend (δClO_4^-) at ~ 635 cm^{-1} [1, 3].

The weak $\nu_s ClO_4^-$ is not readily discernible, being largely overshadowed by a combination of the coupled ring breathing/ν(NO) mode of PyzNO in the region of 1010 cm^{-1}, and the weak unassigned shoulder at 978 cm^{-1} [1]. The distinct hydration-dependent sensitivity (intensity and number) of the ring breathing vibration is ascribed to the liberation of PyzNO *via* *O*→Fe hydrolysis.

The broadness and shouldering observed for the vsbr ν_a vibration is attributable to three features, namely: the triply degenerate F_2 vibration, to ClO_4^- being disordered, and to the relative natural abundance (24%) of the ^{37}Cl isotope [3, 4, 6-9]. The ν_a band splits into two largely overlapping bands in both the hydrated and the anhydrous variants. These have been assigned at 1075 cm^{-1} and 1074 cm^{-1} for the hydrated and anhydrous species, respectively, with shoulders at ~ 1090 cm^{-1} for both variants. The shoulders are normally ascribed to the reduction of ClO_4^- symmetry from T_d to C_3v due to the crystalline packing of the solid [3]. Although ClO_4^- coordination was considered as a potential source of this behaviour, the presence of this species as both a free counterion (T_d) and coordinated ligand (C_3v) would distinctly split the asymmetric stretch into two non-degenerate terms, giving two resultant bands. Monodentate perchlorate typically exhibits two distinct and very strong bands between 1200 and 1000 cm^{-1} [4]. Given the subtlety of the *splitting* seen in Fig. 5.3, this possibility was ruled out, particularly considering that there is no change in this region as a time dependent function of the degree of hydration. The coalescence of these bands, due to the displacement of weakly coordinated ClO_4^- by H_2O, would be expected to be the most discernible feature in consecutive IR spectra.

Fig 5.3 also shows that, although the 'emergent' bands ascribed here to free and *N*-coordinated PyzNO appear to continue to merge between 60 and 80 min, there are no additional quantitative changes occur at exposure times beyond 70 min. The hydration process is therefore presumed to be complete at that stage. An IR spectrum was collected again after a 5 h of atmospheric exposure, and was found to be identical with IR spectra collected after ≥70 min of hydration.

5.1.1.2 X-ray Powder Diffraction

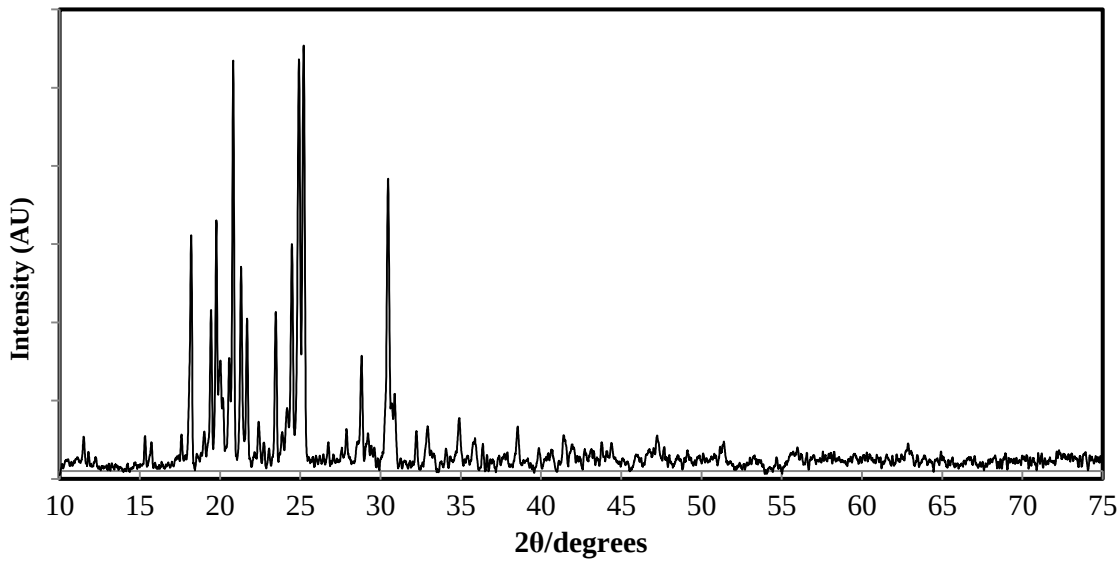

Figure 5.4: XRPD pattern of the $Fe(pyzNO)_5(ClO_4)_2(H_2O)_3$ complex (Complex5).

Table 5.2: 2θ versus *d*-spacing values for $Fe(pyzNO)_5(ClO_4)_2(H_2O)_3$ (Complex5).

$\{Fe(pyzNO)_5(ClO_4)_2(H_2O)_3\}$	
2θ (º)	***d*-Spacing (Å)**
18.193	4.872
19.431	4.564
19.766	4.488
20.016	4.432
20.179	4.397
20.572	4.313
20.812	4.265
21.306	4.167
21.685	4.095
23.465	3.788
24.832	3.583
25.206	3.502
28.813	3.096
30.436	2.934

The XRPD pattern of Complex5 is shown in Fig 5.4, with the first ten reflections of quantitative intensity and their corresponding *d*-spacing values tabulated in table 5.2.

Fig. 5.4 reflects the hydration-induced transformation of the structure of Complex1; showing the appearance of new reflections associated with the newly generated phases. The peaks in Fig. 4.3 at 19.507, 20.064, 20.774, 21.129, 21.886, 23.354 and 24.256 $^{o}2\theta$, although subtly shifted, are retained on hydration, but with intensity variations, and are thus possibly attributable to reflections associated with *N*→Fe PyzNO coordination. The corresponding peaks are at 19.766, 20.016, 20.812, 21.306, 21.685, 23.465 and 24.832 $^{o}2\theta$ in Fig. 5.4. The new peaks at 18.193, 28.813 and 30.043 $^{o}2\theta$ potentially signal the generation of the H_2O *O*→Fe phase, as partly evidenced by comparison with Fig. 5.14, but are possibly due to free PyzNO or solvate H_2O.

5.1.1.3 Differential Scanning Calorimetry and Thermogravimetry

Figure 5.5 shows a convoluted endotherm at 70 – 95 ^{o}C, which comprises two overlapping *sub-endotherms*, as evidenced by the first derivative. This endotherm is due to the loss of water, initially held in two different environments within the lattice. The temperature range in which this two-step endotherm occurs suggests the loss of two solvate waters. As microanalytical data pointed towards a total of three waters per formula unit, DSC therefore suggests that the complex has the structure shown in Fig. 5.2 A. The first endotherm, centred at 75 ^{o}C, is ascribed to the loss of the first solvate water, while the second, stronger endotherm, centred at 85 ^{o}C, is due to the loss of the second solvate water.

The first (partial) PyzNO thermolysis step occurs in the 170 – 190 ^{o}C range, followed after by the decomposition of the remaining PyzNO-Fe-ClO_4 species at 200 ^{o}C.

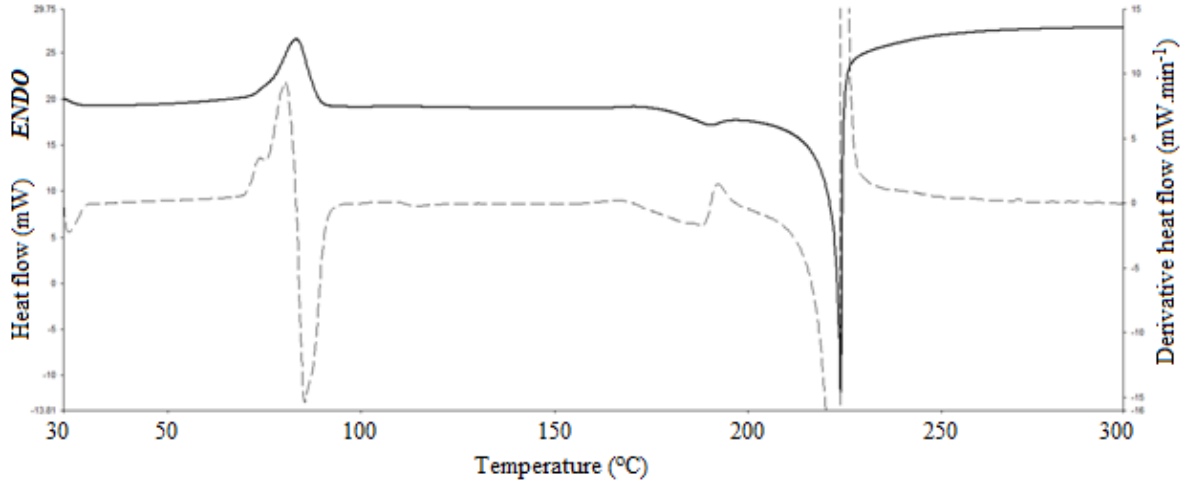

Figure 5.5: DSC thermogram (10 ^{o}C.min^{-1}) of the $Fe(pyzNO)_5(ClO_4)_2(H_2O)_3$ complex (Complex5).

The major difficulty came in the alignment of the DSC data with the corresponding TG thermogram. The latter shows six distinct weight loss steps, which is inconsistent with the DSC profile. Three of these weight losses occur in the 100 – 170 ^{o}C range, in which DSC shows no major enthalpy change. A very small endotherm is seen between 105 and 120 ^{o}C, which is more discernible on inspection of the first derivation. A weight loss of 6.0 % occurs between 30 and 90 ^{o}C (1), which corresponds to the loss of 2.5 waters per formula unit (theoretical: 5.71 %). A further 3.5 % weight loss occurs in the 105 – 120 ^{o}C range (2), followed by a three-step mass loss (3-5) before explosive decomposition at 204 ^{o}C. Weight losses of 5.3 % (120 – 147 ^{o}C), 7.8 % (150 – 170 ^{o}C), and 4.9 % (170 – 190 ^{o}C) were found.

Complete decomposition of the remaining PyzNO-Fe-ClO_4 species occurs at 204 ^{o}C, leaving a carbon/FeO/Fe_2O_3 residue mixture.

Attempts to rationalise the weight percent loss in terms of individual components was not possible*. Each thermogram was recorded in triplicate, each time with no significant change in their constituent features as seen in Fig's. 5.5 and 5.6.

The complicated decomposition may be the result of the oxidation of the iron centre [9]. This warrants further investigation that is beyond the scope of this work.

* 2.5 H_2O = 5.7%; 3 H_2O = 6.8%; 0.5 H_2O = 1.1%; 1 PyzNO = 11.7%, 1 Pyz = 9.6%.

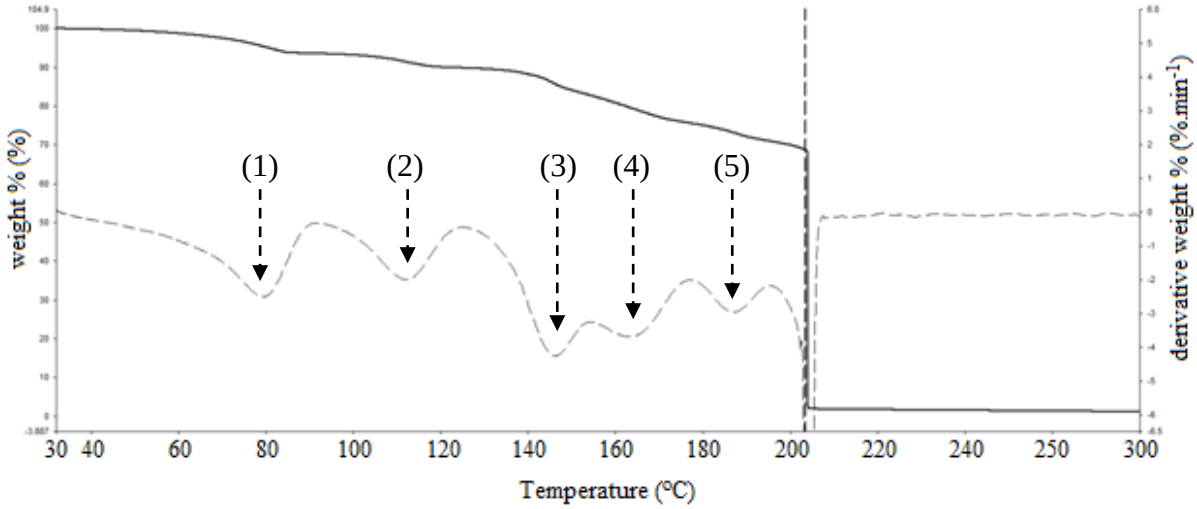

Figure 5.6: TGA thermogram (10 $^{o}C.min^{-1}$) of the $Fe(pyzNO)_5(ClO_4)_2(H_2O)_3$ complex (Complex5).

5.1.1.4 Scanning Electron Microscopy

Distinct changes in the surface morphological features occur to Complex1 on hydration, as seen in the SEM micrograph of Complex5 shown in Fig. 5.7.

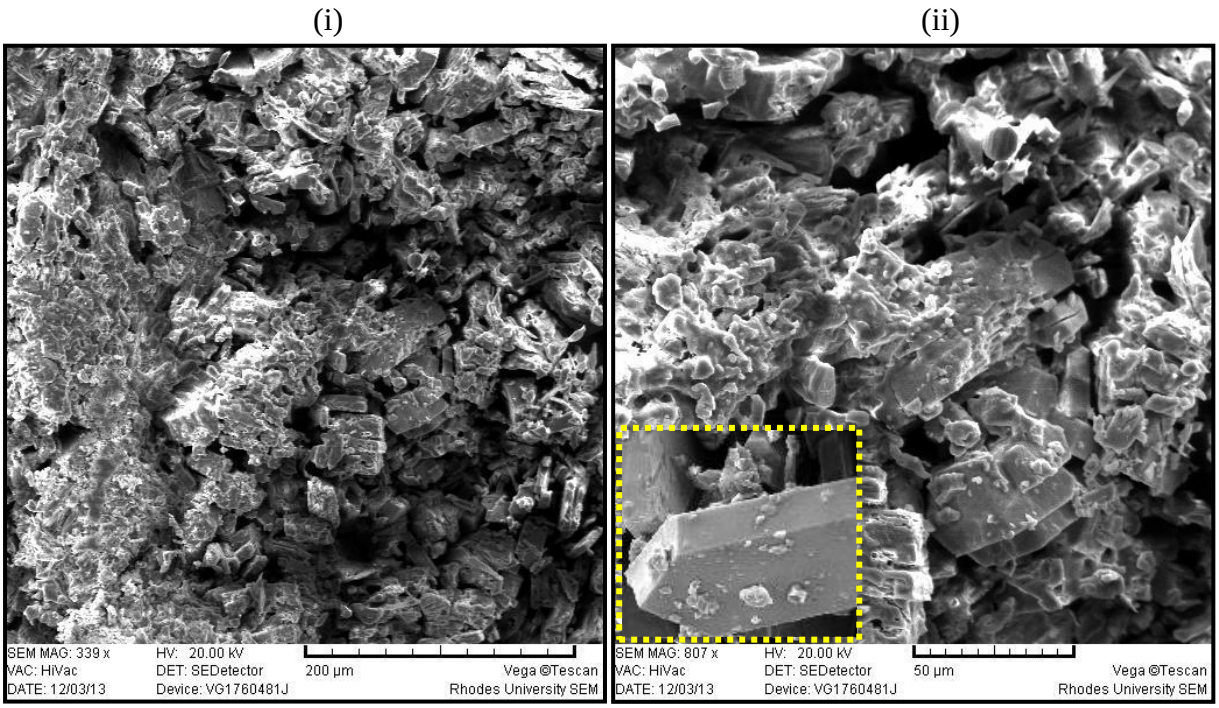

Figure 5.7: SEM micrograph of $Fe(pyzNO)_5(ClO_4)_2(H_2O)_3$ (Complex5) at 170x magnification (i), and at 500x magnification (ii) (boxed in yellow is an insert of a micrograph of the anhydrous complex for comparison).

There appears to be a significant loss of crystallinity, with the ordered surface planes seen in Fig. 4.6 being ostensibly lost. This is reflected in the peak broadening seen in the XRPD pattern seen in Fig. 5.4. The penetration of the lattice by water appears to be accompanied by a significant disruption of the ordering of atoms, which in turn manifests as the breaking up of crystallites.

5.1.2 $\{Fe(\mu\text{-}pyzNO\text{-}\kappa N,\kappa O)_{n-1}(pyzNO\text{-}\kappa N)_2(pyzNO\text{-}\kappa O)_2\}_n(ClO_4)_{2n} + 4\ H_2O \rightarrow [Fe(pyzNO\text{-}\kappa N)_4(H_2O)_2](ClO_4)_2{\cdot}2H_2O$ (Complex2 → Complex6)

The crystal structure of the hydrated variant of Complex2, Complex6, was solved by single crystal X-ray crystallography.

5.1.2.1 X-ray Single Crystal Diffraction

Structurally, Complex6 is a three-dimensional complex framework with $P2_1/c$ symmetry, which comprises octameric clusters of discrete $[Fe(pyzNO)_4(H_2O)_2]^{2+}$ cations. The latter are linked together *via* intermolecular hydrogen bonding (coordinated H_2O and *N*-oxide oxygen), as well as the electrostatic attraction of their constituent nuclei for the perchlorate counterion. The latter, as also seen in the crystal structure of the anhydrous polymeric precursor (Complex2), is intermediate between successive neighbouring nuclei; with an average Fe···Cl inter-/intramolecular proximity or spacial separation of 5.1439(5) Å.

As previously mentioned, the crystal structure of Complex6 shows no free PyzNO, which would otherwise by expected upon liberation of the latter by hydrolysis. The appearance of white crystal needles on the surface of Complex2 during hydration, following by their gradual sublimation, is thought to be the manner in which PyzNO is lost by the complex. This implies an irreversibility of the process, and only partial restoration of the original structure is expected to be possible by the heat-mediated solid state dehydration of Complex6.

The crystal structure of Complex6 is shown in Fig's. 5.8 and 5.9.

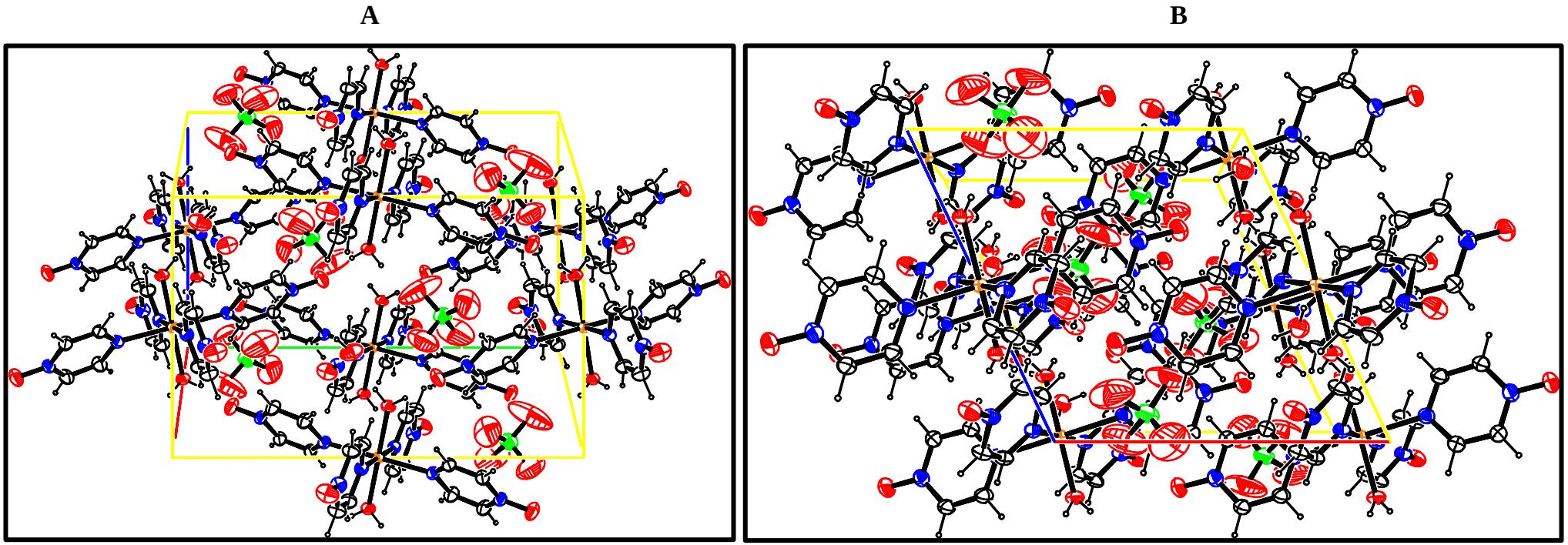

Figure 5.8: The crystal structure (A: Normal to (100); B: Normal to (010)) of $[Fe(pyzNO\text{-}\kappa N)_4(H_2O)_2](ClO_4)_2{\cdot}2H_2O$ (Complex6). Colour coding: yellow box = unit cell; Atoms: yellow = Fe, black = C, blue = N, red = O, green = Cl.

Most noticeable in the structure is the absence of PyzNO *O*-coordination. Accompanying the μ-PyzNO→H_2O substitution step(s) is a rearrangement reaction in which the two equatorial *O*→Fe metal-ligand bonds are replaced by *N*→Fe moieties.

There is a ~ 1.4889 Å increase in the average spacial separation of Fe and Cl atoms on hydration of Complex2. This is suspected to be a consequence of the net diminution of the positive charge density of associated Fe(II) atoms upon the LS→HS transition. That is, the enhanced electron delocalisation towards the ligands, *via* the occupation of the e_g* orbital set, effectively reduces the electrostatic attraction of each Fe(II) atom to its perchlorate counterion.

The macroscopic structural rigidity of Complex6 most likely derives principally from the intermolecular H-bonding and dipole-dipole attraction introduced by coordinated and solvate water moieties. Although as yet unconfirmed by NMR - which was attempted but was unsuccessful due to the effects of signal broadening associated with the solution state ^{1}H NMR of strongly paramagnetic species - or modelling studies, extensive H-bonding is suspected as all O-H contact distances are in the 1.760 – 2.920 Å range [10].

The π-π stacking component of Complex2 is significantly diminished on hydration, as evidenced by Fig's. 5.8 A and B. However, as Fig. 5.9 A shows, there is a substantial degree of ordered parallel overlap between the constituent PyzNO moieties of neighbouring nuclei in the 001 direction. This suggests that, although markedly reduced, there is still a substantial degree of aromatic π-π attraction which contributes to the complex's intermolecular inflexibility. An enhanced view of the crystal structure showing the configuration of an arbitrary Fe(II) centre within the lattice is shown in Fig. 5.10 B.

Each Fe centre is a tetragonally distorted octahedron with respective axial (H_2O: Fe-*O*) and equatorial (PyzNO: Fe-*N*) bond lengths of 2.0479(13) Å, and 2.259(3) Å for Fe(1)-N(11) and 2.217(2) Å for Fe(1)-N(21). The subtle mutual discrepancy (~0.042 Å) in the equatorial bond length values is assumed to be a consequence of steric interaction between coordinated H_2O (O and H atoms), and PyzNO (H atoms) situated in the 'xz' (or 'yz') plane.

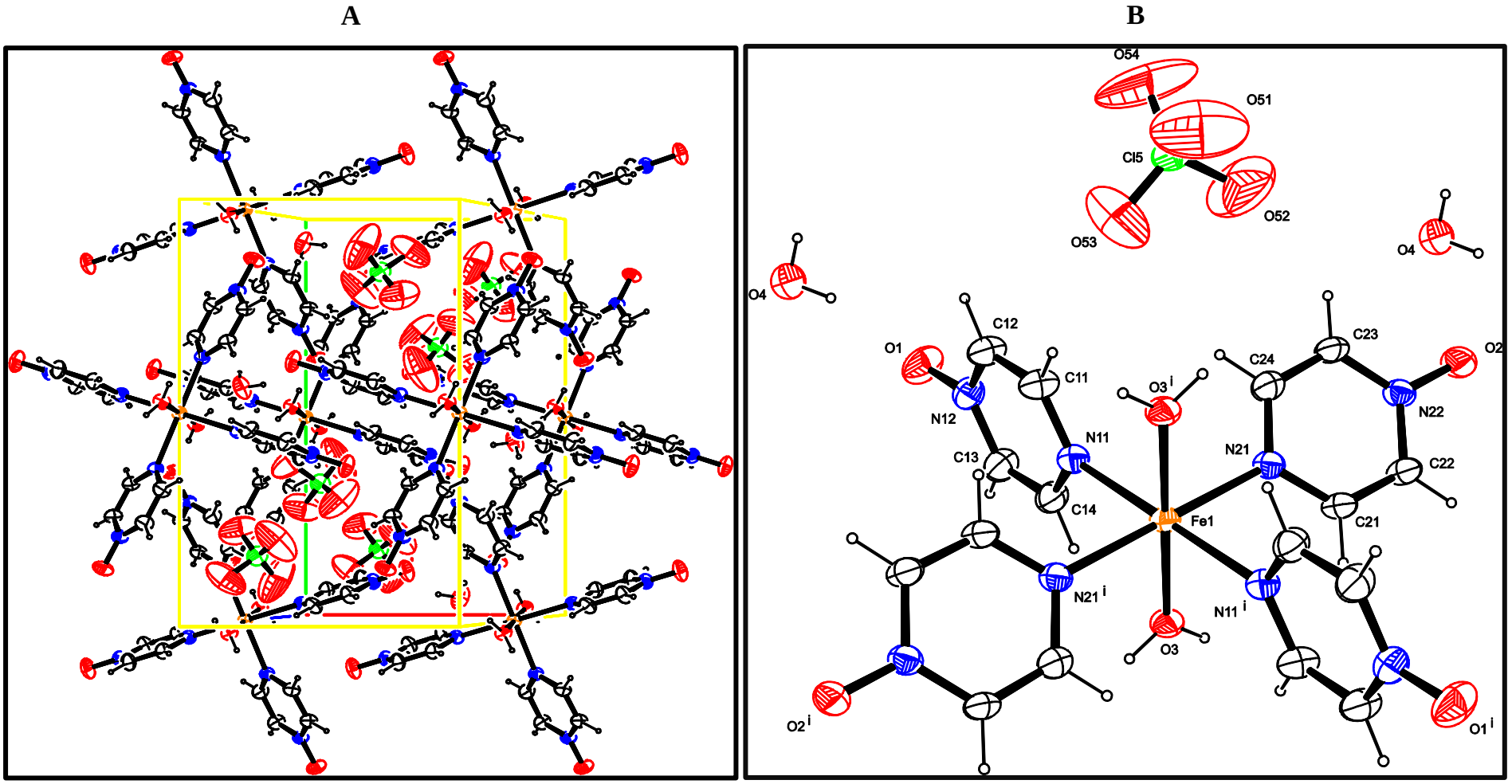

Figure 5.9: The crystal structure (A: Normal to (001); B: enhanced view of one Fe centre) of $[Fe(pyzNO\text{-}\kappa N)_4(H_2O)_2](ClO_4)_2{\cdot}2H_2O$ (Complex6), with B showing atomic numbering in the basic repeating unit. Colour coding: yellow box = unit cell, Atoms: yellow = Fe, black = C, blue = N, red = O, green = Cl.

The crystal structure of this hydrated form, produced from the initially polymeric Complex2, confirms the hypothesis that the incoming water hydrolyses the Fe-*O* bonds of coordinated PyzNO. Moreover, only *N*-coordinated PyzNO remains in the coordination sphere. This is unsurprising as *N*-coordination is theoretically more compatible with the soft Fe(II) centre from both 'molecular orbital theory' and 'hard and soft acid-base theory' viewpoints. The dative covalent bond associated with the harder *O*-atom of PyzNO is therefore expected to undergo hydrolysis before its Fe-*N* counterpart. As predicted, a di-aqua-substituted complex is the end product of hydration.

Although only one is shown in Fig 5.9 B, there is an additional perchlorate counterion per formula unit. The resulting complex has the formula: $[Fe(pyzNO\text{-}\kappa N)_4(H_2O)_2](ClO_4)_2{\cdot}2H_2O$. Additionally, microanalysis shows that the PyzNO liberated by hydrolysis remains in the sample. It is thought to have gradually sublimed during the week of atmospheric exposure, hence the failure to detect the free ligand crystallographically. The microanalysis results are consistent with a $[Fe(pyzNO\text{-}\kappa N)_4(H_2O)_2](ClO_4)_2{\cdot}2H_2O$ structure.

The crystal data of Complex6 is given in table 5.3.

Table 5.3: Crystal data of the $[Fe(pyzNO\text{-}\kappa N)_4(H_2O)_2](ClO_4)_2{\cdot}2H_2O$ complex (Compex6).

Property	**$[Fe(pyzNO\text{-}\kappa N)_4(H_2O)_2](ClO_4)_2{\cdot}2H_2O$**
Crystal system	Monoclinic
Space group	$P2_1/c$
a (Å)	9.6665(3)
b (Å)	15.6835(4)
c (Å)	9.9486(3)
α (°)	90
β (°)	115.350(1)
γ (°)	90
Volume ($Å^3$)	1363.02(7)
$Density_{calc}$ ($g.cm^{-1}$)	1.733

It is noted that for a solid state phase change of the sort described to occur, and still produce crystals of suitable quality for diffraction studies, there must be no fracturing of the existing crystal. That is to say, there must exist only small differences in unit cell parameters. The alternative is for there to be some templating for crystal growth. That suitable crystals grew in the solid state suggests that Complex6 (di-aqua hydrate) is an irreversible product resulting from possible templating, which occurs *via* a mono-aqua-substituted (orange) intermediate.

In terms of the above, three parameters of interest are highlighted in table 5.4. There are two sides that are of similar length, and the cell volume of the Complex6 is double (to a difference of only 8Å) that of Complex2. This raises the possibility of the subsequent hydrolysis of the intermediate yellow-orange hydrate $[Fe(PyzNO\text{-}\kappa N)_5(H_2O)](ClO_4)_2{\cdot}3H_2O$ to Complex6 with the displacement of a PyzNO ligand, and an accompanying change in angle of $\alpha_{(red)} = 100.368°$ to $\beta_{(yellow)} = 115.31°$, through plasticity of the crystal.

Table 5.4: Summary of the changes in crystal parameters due to the Complex2 → Compex6 transformation.

h, k, l		Complex2 ($P\bar{1}$)	Complex6 ($P2_1/c$)
(100)	a	8.1003	**9.6665**
(010)	b	**9.5432**	15.6835
(001)	c	**10.0862**	**9.9486**
	α	100.368	90
	β	103.900	115.31
	γ	109.009	90
	Vol ($Å^3$)	**687.71**	**1363.02**
	Density	1.778	1.738

The crystal system and space group also change from triclinic to monoclinic, and from $P\bar{1}$ to $P2_1/c$, respectively. An increase in density had been expected due to increased H-bonding. However, the measured decrease is the result of a 675.32 $Å^3$ volumetric increase that is accompanied by a 24.03 $gmol^{-1}$ mass decrease due to $PyzNO \rightarrow 2H_2O$ substitution, and the further addition of 2 solvate units.

The average axial Fe-*N* bond length in Complex2 (LS) was found to be 2.1767 Å, whereas the average value for $[Fe(pyzNO\text{-}\kappa N)_4(H_2O)_2](ClO_4)_2{\cdot}2H_2O$ (HS) was found to be 2.2380 Å. This represents a 0.0613 Å increase on hydration, which is a synergistic result of PyzNO→H_2O substitution, and the LS→HS transition.

5.1.2.2 Microanalysis and *in situ* Time-dependent Mid-IR hydration Studies

Table 5.5: Experimental versus calculated microanalysis for $[Fe(pyzNO\text{-}\kappa N)_4(H_2O)_2](ClO_4)_2{\cdot}2H_2O$ (Complex6).

Trial number	Experimental values (%)				Calculated values (%)			
	C	H	N	S	C	H	N	S
1	29.78	3.477	17.26	0.073	29.76	3.496	17.35	0.000
2	29.97	3.401	17.30	0.000				
Average	29.88	3.439	17.28	0.073				
$\Delta\ (\%)_{exp\ vs\ calc}$	0.12	-0.057	-0.08	+0.073				

The experimental microanalytical data for Complex6 indicate one additional free ('solvate') PyzNO per formula unit (M_r: 807.246 g.mol^{-1}). That is, the calculated values in table 5.5 were done so for a $[Fe(pyzNO\text{-}\kappa N)_4(H_2O)_2](ClO_4)_2{\cdot}2H_2O{\cdot}$PyzNO structure, as these were found to have the closest match with experimental data.

This is consistent with the expectation that Complex2 should produce one free PyzNO per formula unit upon hydrolysis of all bridging M-L bonds (plus 1 PyzNO from terminal nuclei). The crystal structure of Complex6 (Fig's. 5.8 and 5.9) was solved by single crystal XRD after its exposure to the atmosphere for 1 week to ensure complete hydration. As the crystal structure showed no indication of disordered or uncoordinated PyzNO, the latter was presumed to have been lost due to sublimation from the open sample vessel during this period. This is therefore the suggested cause of the discrepancy in the M_r value found by microanalysis and the value of 711.18 g.mol^{-1} found by XRD (ΔM_r: 96.066 g.mol^{-1}; M_r for PyzNO: 96.0887 g.mol^{-1}).

As previously noted, the microanalyses of Complex5 and Complex6 show a difference in their respective masses of 18.012 g.mol^{-1}, which corresponds to one water per formula unit.

As with the time-dependent hydration profile of Complex1, Fig. 5.10 first shows the appearance of a broad and medium strong band at 2800 - 3600 cm^{-1} due the ν_a(OH) and ν_s(OH) vibrations of adsorbed water. Between 30 and 40 minutes, the ν(NO) band of μ-PyzNO (1241 cm^{-1}) begins to diminish in intensity due to the hydrolysis of the its O→Fe bond. This band has altogether disappeared after 60 min; signifying the complete monomerization of the complex. .

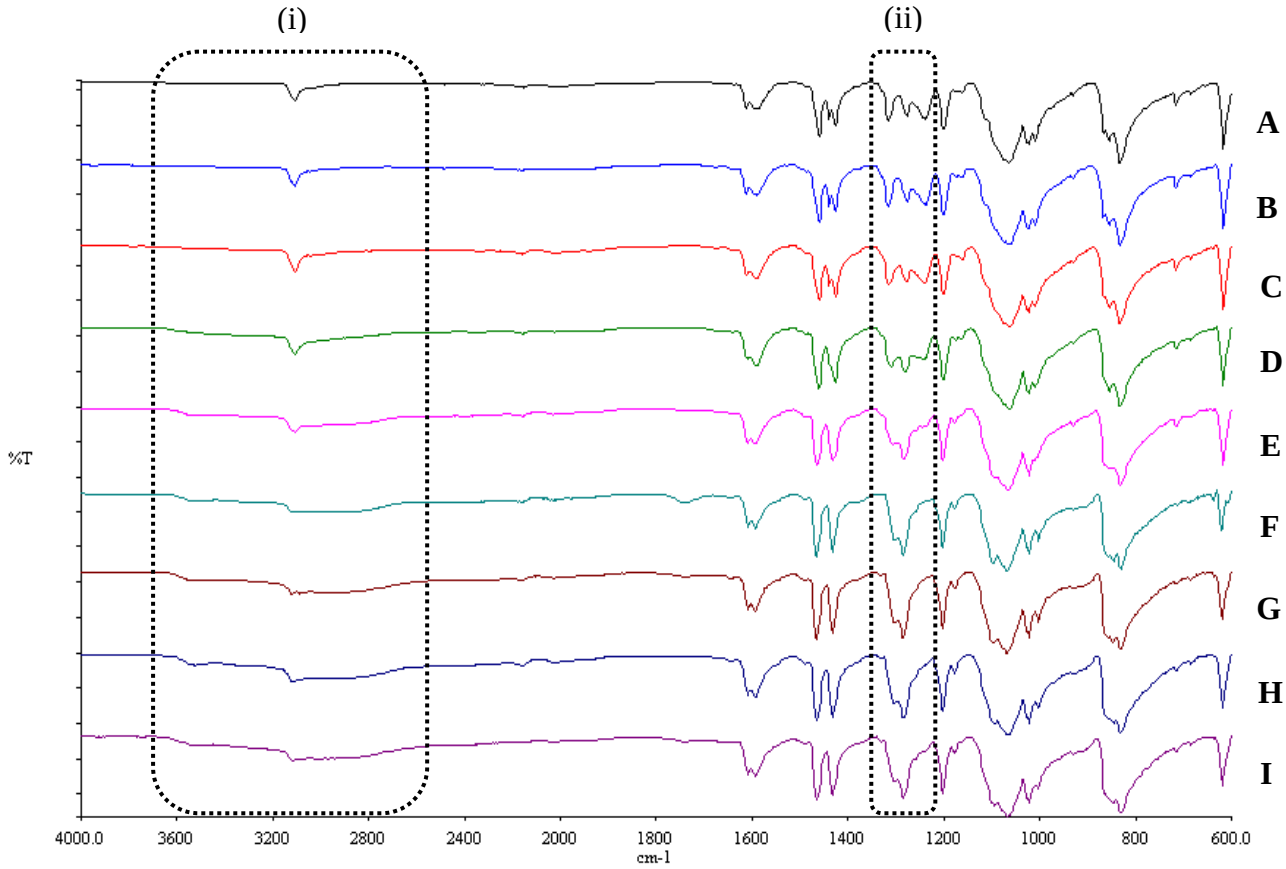

5.10: Mid-IR spectra for the time-dependent hydration profile (atmospheric exposure) of {Fe(μ-pyzNO-κ*N*,κ*O*)$_{n-1}$(pyzNO-κ*N*)$_2$(pyzNO-κ*O*)$_2$}$_n$(ClO$_4$)$_{2n}$ (Complex2). A – 10 min, B – 20 min, C – 30 min, D – 40 min, E – 50 min, F – 60 min, G – 70 min, H – 80 min, I – 90 min. Boxed regions are (i) H_2O - ν_s(OH) + α(OH), and (ii) PyzNO - ν(NO) + ν(ring).

The band due to the *O*-mode of bonded PyzNO shifts from 1279 cm^{-1} to 1296 cm^{-1} after 40 min, which occurs as its Fe-*O* bond is also cleaved to produce free ligand. The band due to the -*N*-mode of coordination (1317 cm^{-1}) remains unchanged, indicating no perceivable Fe-*N* hydrolysis. No discernible change is seen after 70 min, suggesting the completion of the hydration process.

5.1.2.3 X-ray Photoelectron Spectroscopy

As with its anhydrous precursor, the wide scan XPS spectrum of Complex6 confirms the presence of iron, carbon, nitrogen, oxygen and chlorine. The spectrum is given in Fig. 5.11 below.

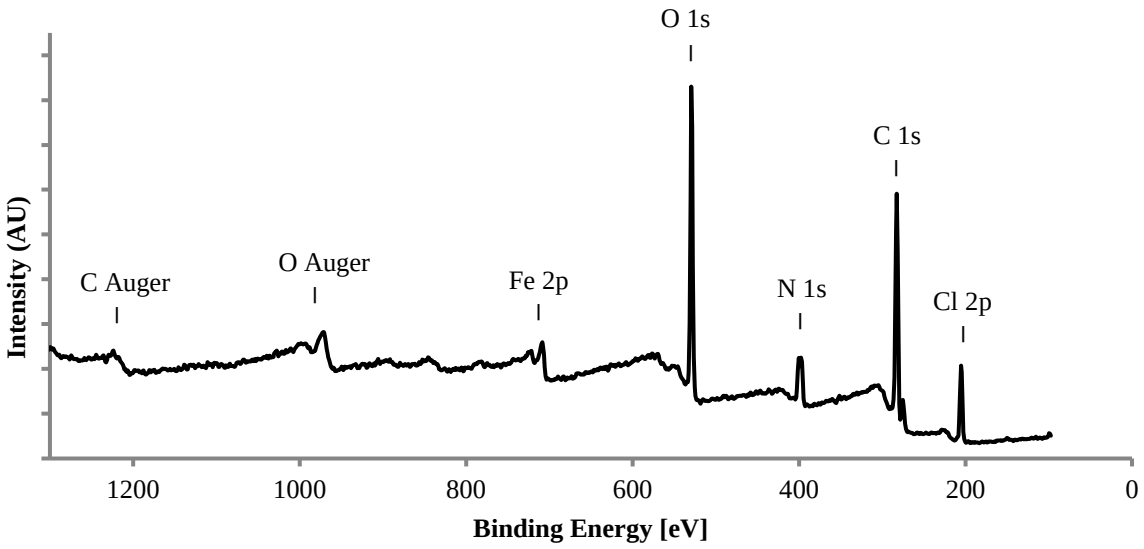

Figure 5.11: Wide scan XPS spectrum of $[Fe(pyzNO\text{-}\kappa N)_4(H_2O)_2](ClO_4)_2{\cdot}2H_2O$ (Complex6) collected in the range 97.5 eV – 1302.5 eV.

High resolution scans of the C 1s, N 1s, O 1s and Fe 2p regions were also collected as with the anhydrous complex, whilst employing the appropriate deconvolution and theoretical Gaussian-Lorentzian curve fitting where appropriate.

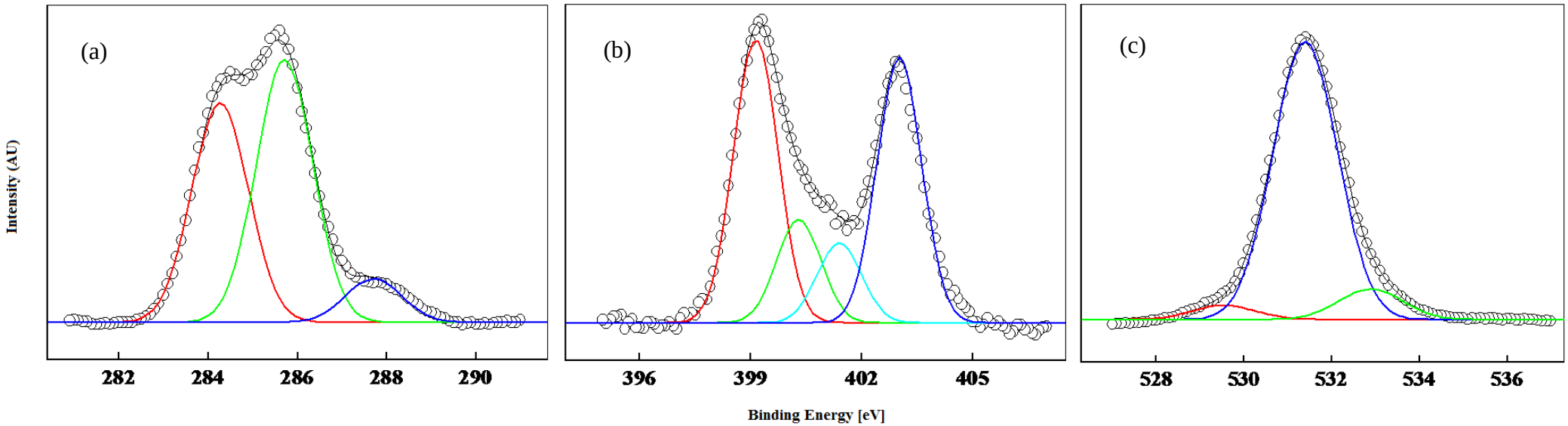

Figure 5.12: Deconvoluted high resolution XPS spectra of [Fe(pyzNO-κ*N*)$_4$(H$_2$O)$_2$](ClO$_4$)$_2$·2H$_2$O (Complex6) showing the (a) C 1s, (b) N 1s and (c) O 1s regions.

The XPS spectrum of the C 1s region of Complex6 is discussed in comparison with its anhydrous precursor (Complex2; Fig. 4.13(a)). The spectrum shows the appearance of a peak at 284.2 eV, which replaces the peak in Fig. 4.13(a) which was assigned to μ-PyzNO (289.0 eV). The former has been assigned to the aromatic carbons of free PyzNO (formerly *O*-coordinated and μ-PyzNO). The peak assigned to *N*-coordinated PyzNO shifts from 285.0 eV to 286.0 eV on hydration. This indicates that the axial coordination of water results in further electron withdrawal from *N*-bonded PyzNO. The relative hardness of water in comparison with PyzNO, in combination with the resulting exclusive *N*-coordination of PyzNO in Complex6, is a good basis to account for this shift [11-13].

Lastly, the peak assigned to *O*-coordinated PyzNO in the precursor (286.5 eV) is absent. There is, however another new peak centred at 287.8 eV. The origin of this peak is ambiguous. It could either be due to some residual *O*-bonded PyzNO (incomplete hydrolysis[*]), or due to the aromatic carbons of *N*-bonded PyzNO in a few square-based pyramidal nuclei (incomplete H_2O addition). In both cases, the aromatic carbons would have their own characteristic 1s peak, but with a comparatively higher BE and lower intensity. Extended exposure to a more humid atmosphere may aid to definitively make the assignment, albeit at the risk of complete dissolution.

The N 1s region revealed four overlapping peaks centred at 403.1 eV, 401.3 eV, 400.3 eV and 399.2 eV, respectively. The first peak is assigned to ring nitrogen atom of the *N*→Fe moiety, and is positively shifted (+2.6 eV) due to the increased electron withdrawing effects accompanying hydration (discussed above). The associated Fe(II) nuclei have only *N*-coordinated PyzNO. The two peaks at 401.3 and 400.3 eV are assigned to the nitrogen atoms at positions 2 and 5 of free PyzNO, respectively. The last peak is assigned to the ring nitrogen atom at position 2 (N-O moiety) of the *N*-coordinated PyzNO.

The O 1s region reveals three overlapping peaks centred at 533.0 eV, 531.4 eV and 529.5 eV. The intense middle peak is due to *N*-coordinated PyzNO, and is only slightly negatively shifted (-0.5 eV) relative to that of Complex2. The shift is due to the structural and electronic

[*]'Incomplete hydrolysis' refers to the orange mono-aqua-substituted complex. This would explain the positive shift in BE from 286.5 eV to 287.8 eV, which is due to the increased electron-withdrawal from axial *O*-coordinated PyzNO due to *trans*-coordination water.

reorganization of the coordination sphere on hydration, which subtly changes the O 1s electron binding energy. The μ-PyzNO peak (534.5 eV) disappears as expected. The peak at 533.0 eV is assigned to the oxygen atom of coordinated water*. Lastly, the peak at 529.5 eV is ascribed to the oxygen of free PyzNO.

As previously mentioned, an increase in scan width is suspected to be required in order to detect the oxygen of the ClO_4^- counterion.

The spectrum of the Fe 2p region of the spectrum is given below.

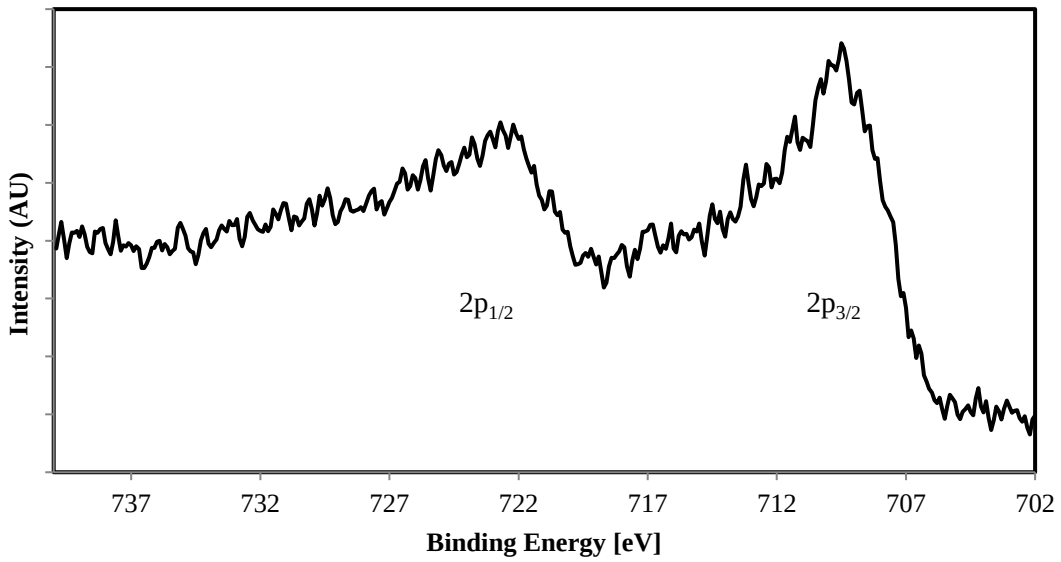

Figure 5.13: High resolution XPS spectrum of the Fe 2p region of $[Fe(pyzNO\text{-}\kappa N)_4(H_2O)_2](ClO_4)_2{\cdot}2H_2O$ (Complex6).

The Fe 2p region shows two peaks centred at 709.5 eV, and 722.8 eV. These peaks are attributed to resonances associated with Fe $2p_{3/2}$ and Fe $2p_{1/2}$ states respectively [13, 14]. Both peaks are shifted relative to those in the Fe 2p region of the anhydrous complex. This is a reflection of the global *increase* in ligand electronegativity by average field approximation, due to the bi-substitution of PyzNO from the complex by water.

* Two water peaks (coordinated and solvate units) were expected. However, the UHV conditions of the XPS sample chamber are suspected to have volatilized the solvate component, transferring it from the sample to the purge stream.

5.1.2.4 X-ray Powder Diffraction

The XRPD pattern of Complex6 shows significant differences with that of its anhydrous species (Fig. 4.15), indicating the definite formation of a new phase on hydration. However, many of the peaks corresponding to (100) family of reflections are preserved, indicating at least partial retention of the original structure (*N*-Fe phase). The disappearance of reflections at 39.4 $^{o}2\theta$, and 52 – 59 $^{o}2\theta$ signifies the loss of the *O*-Fe phase associated with PyzNO, while the new peaks (notably: 37.6 and 41.9 $^{o}2\theta$) are due to the addition of water.

There is a small measure of peak broadening observed, which is consistent with a corresponding reduction in crystallite size. This was expected as the influx of water into the lattice results in some degree of crystal fracturing. All peaks of quantitative intensity are concentrated in the 15 – 49 $^{o}2\theta$, barring the satellite peak at 58.362 $^{o}2\theta$, in comparison to those of Complex2 (15 – 71 $^{o}2\theta$). This is indicative of larger unit cell, which is corroborated by single crystal diffractometry data. Fig. 5.14 also shows fewer reflections, which may indicate some degree of loss of crystallinity.

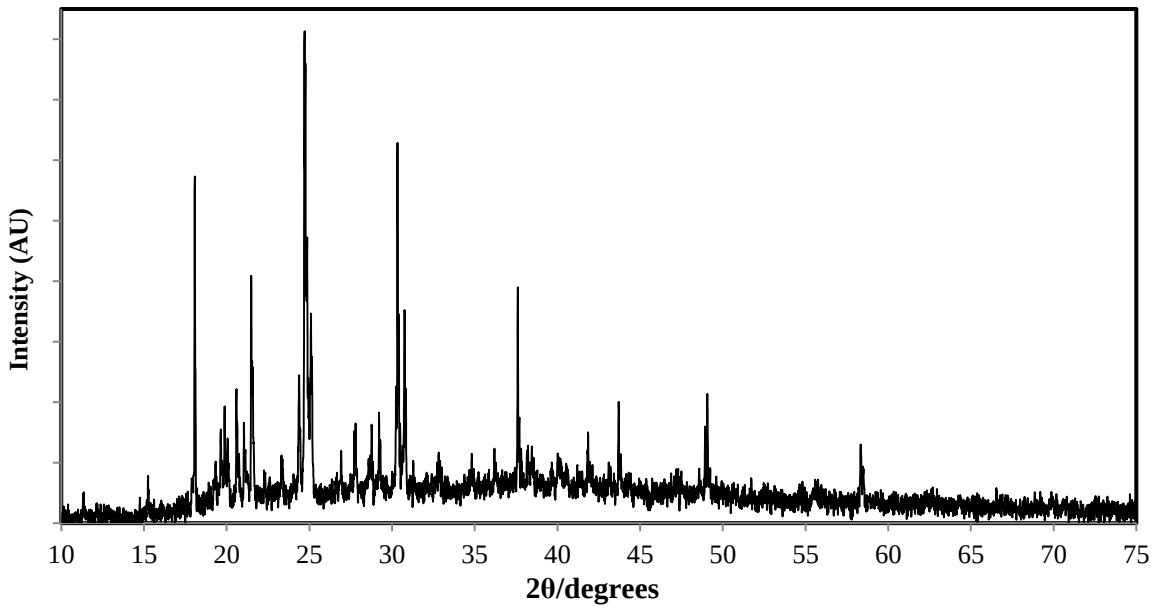

Figure 5.14: XRPD pattern of $[Fe(pyzNO\text{-}\kappa N)_4(H_2O)_2](ClO_4)_2{\cdot}2H_2O$ complex (Complex6).

5.1.2.5 Differential Scanning Calorimetry, Evolved Gas Analysis and Thermogravimetry

The DSC thermogram of Complex6 (Fig. 5.15) looks almost the same as that of Complex5. This indicates that the complexes are characterised by a great degree of structural similarity. This interpretation was bolstered by the congruence of the former's crystal structure with the (CHNS- and Mid-IR-based) proposed structures of the two complexes. The two-part endotherm (derivative curve) in the 66 – 100 ^{o}C temperature range is due to the loss of the 1.5 solvate waters. The first *sub-endotherm* (centred at 72 ^{o}C) is due to the loss of one solvate water, while the second *sub-endotherm* (centred at 90 ^{o}C) is due to the loss of another half a solvate. TG and EGA suggests the accompanying sublimation of free PyzNO, but this is not clearly seen in Fig 5.15 due to the 'non-energetic' nature of the process, with PyzNO known to readily sublime even at room temperature.

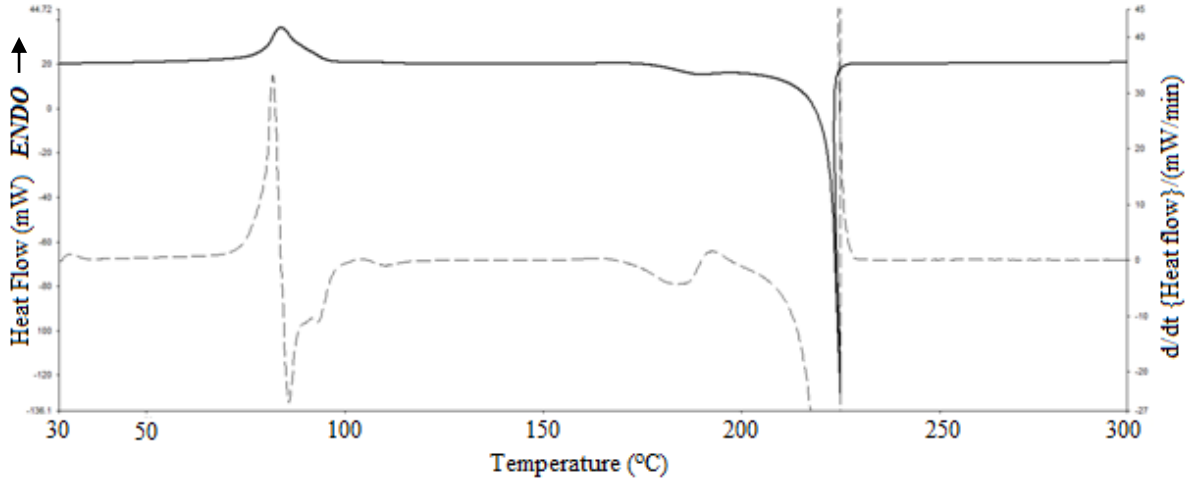

Figure 5.15: DSC thermogram (10 ^{o}C.min^{-1}) of the [Fe(pyzNO-κ*N*)$_4$(H$_2$O)$_2$](ClO$_4$)$_2$·2H$_2$O complex (Complex6).

TGA (Fig. 5.17) shows a total weight loss of 9.1 % between 60 and 110 ^{o}C (1) due to the loss of 1.5 solvate waters (theoretical: 3.16 %), and the concurrent loss of half a PyzNO per formula unit (theoretical: 5.62 %) by sublimation. This is evidenced by EGA in Fig. 5.16 which shows activity at 4000 – 3400 cm^{-1} (ν_a(OH) and ν_s(OH)), at ~1400 cm^{-1} (coupled ν(NO) + ν(ring) or ν(CH)), and at ~1000 cm^{-1} (ν(ring)). A second weight loss of 1.2 % occurs at 110 – 135 ^{o}C, and is due to the loss of the remaining 0.5 solvate waters per formula unit (theoretical: 1.05 %). A third mass loss step is seen between 150 and 170 ^{o}C (2.3 %), and is ascribed to the

volatilization of one coordinated water molecule (theoretical: 2.11 %). The fourth and final mass loss step before complete decomposition of the complex occurs at 170 – 210 °C, with EGA showing the concomitant immergence of significant activity at 3100 – 3050 cm^{-1} and 2500 cm^{-1}. This activity has been assigned to the loss of the remaining (one) free PyzNO per formula unit both as PyzNO and CO_2 (ν(CH) and ν(CO), respectively), along with the last coordinated H_2O moiety, for a total weight reduction of 13.7 % (theoretical: 13.34 %).

While the infrared activity 3100 – 3050 cm^{-1} ceases at 200 °C, the activity at 2500 cm^{-1} gets progressively stronger until the complex's decomposition. This suggests the detection of both intact PyzNO, and its main decomposition product CO_2, until PyzNO begins to fully decompose after 200 °C.

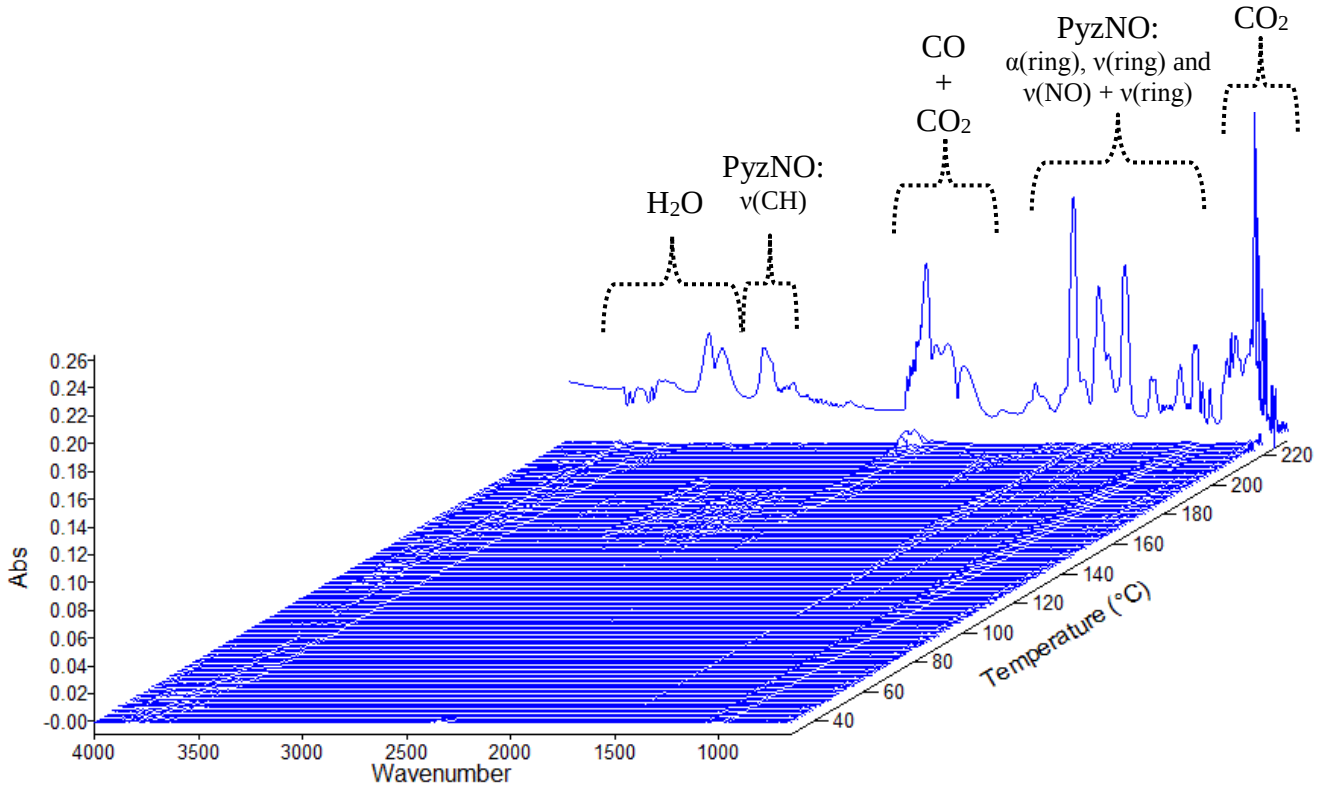

Figure 5.16: EGA stack plot of $[Fe(pyzNO\text{-}\kappa N)_4(H_2O)_2](ClO_4)_2{\cdot}2H_2O$ (Complex6) (30-230 °C).

The complete loss of water as well as free PyzNO induces ClO_4^- thermal decomposition at 225 °C. The shockwave of rapid gas expansion due the explosive thermolysis reaction produces the sudden displacement of the EGA background (as previously noted) at this temperature. As evidenced by the EGA at decomposition, significant PyzNO is ejected from the sample

(coordination sphere) without undergoing prior oxidation to CO or CO_2. Strong bands which have been assigned to intact PyzNO, as shown in Fig. 5.16, are seen.

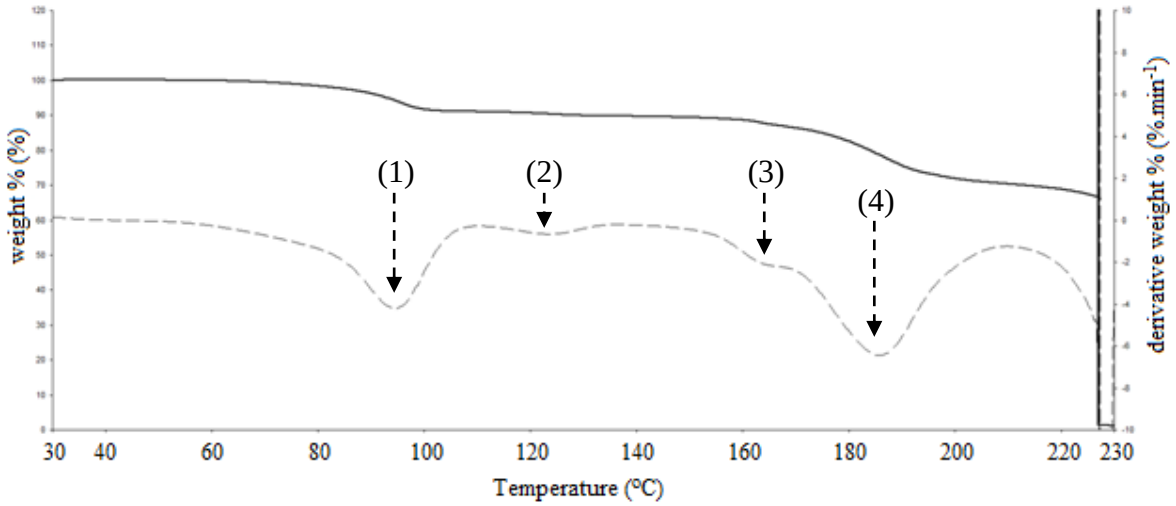

Figure 5.17: TGA thermogram (10 $^{o}C.min^{-1}$) of the $[Fe(pyzNO\text{-}\kappa N)_4(H_2O)_2](ClO_4)_2{\cdot}2H_2O$ complex (Complex6).

5.1.2.6 Scanning Electron Microscopy

The SEM micrographs of Complex6 in Fig. 5.18 show the hydration-associated change in crystalline structure. The individual crystallites appear broken up in comparison with Fig. 4.19. This is the *macroscopic* result of the incorporation of water into the lattice, accompanied by the liberation of *O*-coordinated and μ-PyzNO. This agrees with the XRPD data, as discussed previously. The striations seen in Fig. 5.18 (ii) are microscopic fissures generated by the expansion of the unit cell on hydration. However, the new crystal system (monoclinic) into which the complex transforms isn't readily discernible in the crystallite fragments.

(i) (ii)

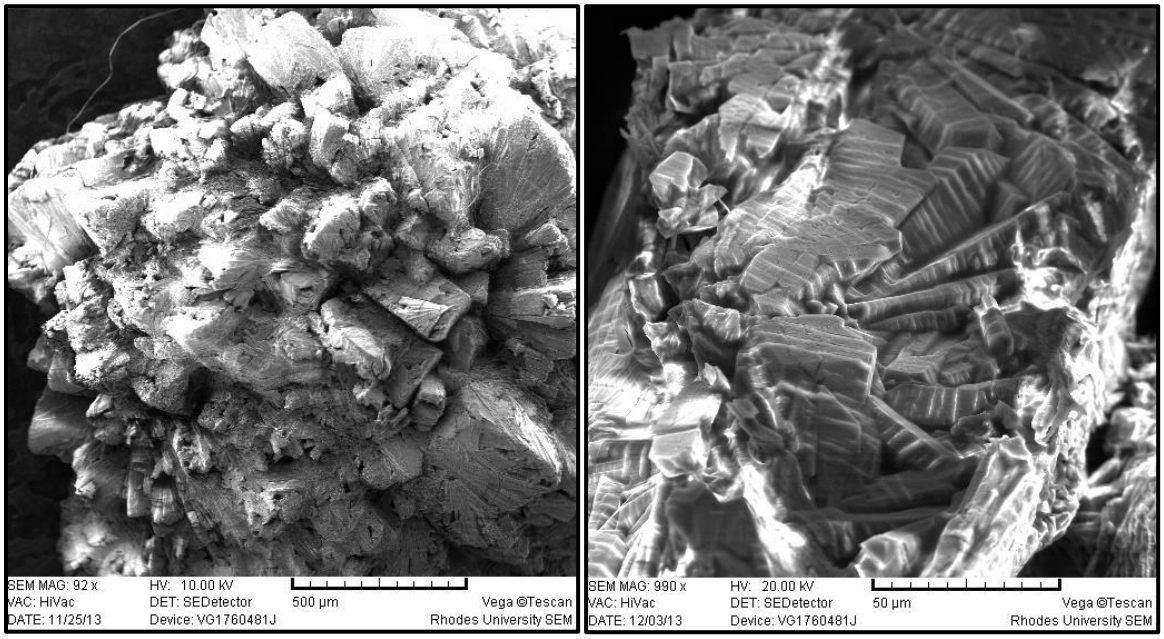

Figure 5.18: SEM micrograph of $[Fe(pyzNO\text{-}\kappa N)_4(H_2O)_2](ClO_4)_2{\cdot}2H_2O$ (Complex6) at 44x magnification (i), and at 480x magnification (ii).

5.2 Further Solvation Studies of $\{Fe(\mu\text{-}pyzNO\text{-}\kappa N,\kappa O)_{n-1}(pyzNO\text{-}\kappa N)_2(pyzNO\text{-}\kappa O)_2\}_n(ClO_4)_{2n}$ (Complex2)

Complex2 was exposed to atmospheres saturated with the vapours of a variety of other solvents, in order to determine whether or not the hydration mediated changes discussed in section 5.1.2 would occur. The solvents were distilled where necessary and subsequently stored over 3 Å molecular sieves. Formaldehyde and acetaldehyde could not be distilled as these are aqueous solutions*. Caution (limited exposure times of 2 – 5 min) was therefore employed in these trails in order to circumvent or minimize the impact of water in subsequent analyses.

Where there was significant solvent uptake by Complex2, a tabulated summary of the thermoanalytical behaviour of the sample has been included. However, owing to software limitations associated with the absence of an appropriate baseline, some of the associated ΔH values were unable to be calculated.

*It was not possible to distill pure forms of these solvents from their aq. solutions, since they are gaseous at room temperature – formaldehyde & acetaldehyde have respective boiling points of -21°C & -19 °C [9].

5.2.1 Cyclohexane

Fig. 5.19 (i) of Complex2-cyclohexane shows no strong solvent uptake by the complex. There is a small endotherm seen between 30 and 37 ^{o}C, which is due to the evaporation of weakly adsorbed solvent. No other especially energetic thermal events can be seen for the cyclohexane exposed complex until the onset of decomposition at 180 ^{o}C, per the DSC 30 - 300 ^{o}C profile*. However, a gradual baseline incline in the 30 – 140 ^{o}C thermal profile is noted; which is thought to be due the gradual desorption of trace amounts of solvent. 5.19 (ii) shows a weight reduction of 3.23 % in the 37 – 140 ^{o}C temperature range.

Ring π-π and induced dipole interactions would likely be the principal modes of physical adsorption of the solvent by coordinated PyzNO (surface and crystal defects). However, Fig. 5.19 (iii) shows no detection of cyclohexane in the TG exhaust stream, other than in the 30 – 32 ^{o}C range (weak band at 1510 cm^{-1} and medium weak band at 2930 cm^{-1}), as the concentration is below the instrument's lower detection limit.

The XRPD pattern of Complex2-cyclohexane (Fig. 5.19 (iv)) is consistent with the above description, indicating some change from the original structure. The crystallinity of the complex is retained as evidenced by the sharp and well resolved reflections

* The full DSC thermograms (30 – 300 ^{o}C) are included in the Appendix.

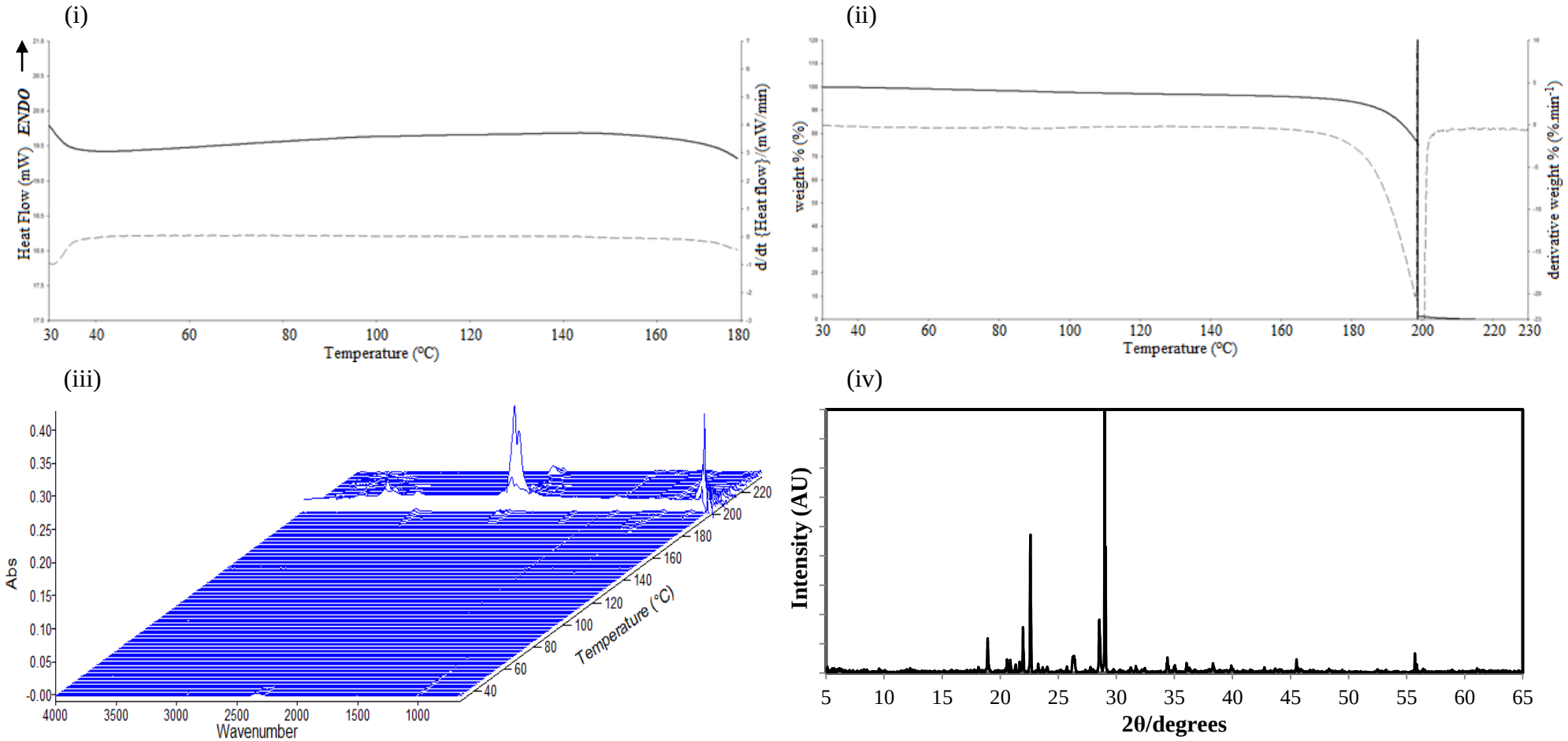

Figure 5.19: The (i) 30 – 180 ºC DSC thermogram, (ii) 30 – 230 ºC TG thermogram, (iii) EGA stack plot and (iv) XRPD pattern of $\{Fe(\mu\text{-pyzNO-}\kappa N,\kappa O)_{n-1}(pyzNO\text{-}\kappa N)_2(pyzNO\text{-}\kappa O)_2\}_n(ClO_4)_{2n}$ (Complex2) exposed to cyclohexane vapour.

5.2.2 Toluene

No distinct thermal events can be seen for the toluene exposed complex in this temperature range until the onset of decomposition at approximately 188 ^{o}C. This indicates that Complex2 does not exhibit any especially energetic solvation-desolvation behaviour with this solvent. However, the baseline does bear a gradual incline, with an average slope of $\sim$ 0.08 mW.min^{-1} at 30 – 100 ^{o}C, after which it begins to level out. Fig. 5.20 (ii) shows a 0.026 % weight reduction in this temperature range. This evidences that there is no solvent uptake, but merely surface physical adsorption; perhaps mediated by π-π interactions with coordinated PyzNO.

Fig. 5.20 (iii) corroborates this interpretation, as the IR regions at 1200 – 1000 cm^{-1} and 800 – 650 cm^{-1} show very minor activity. This activity is ascribable to the medium strong sharp band 1075 cm^{-1} (in-plane δ(CH)), and the strong and sharp band at 735 cm^{-1} (out-of-plane δ(CH)) in the toluene IR fingerprint region, respectively [15]. The 1500 – 1600 cm^{-1} region is also active, which may be due to the strong sharp aromatic ν(C-C) vibration (1506 cm^{-1}). The absence of the bands centered around 3000 cm^{-1}, due to the aromatic and alkyl ν(CH) bands are likely due to the low concentration of adsorbed solvent.

Fig. 5.20 (iv) also agrees with the above description, showing only minor changes with respect to Fig. 4.15, and what has been ascribed to the effects of preferred orientation, as well as due to surface solvent adsorption.

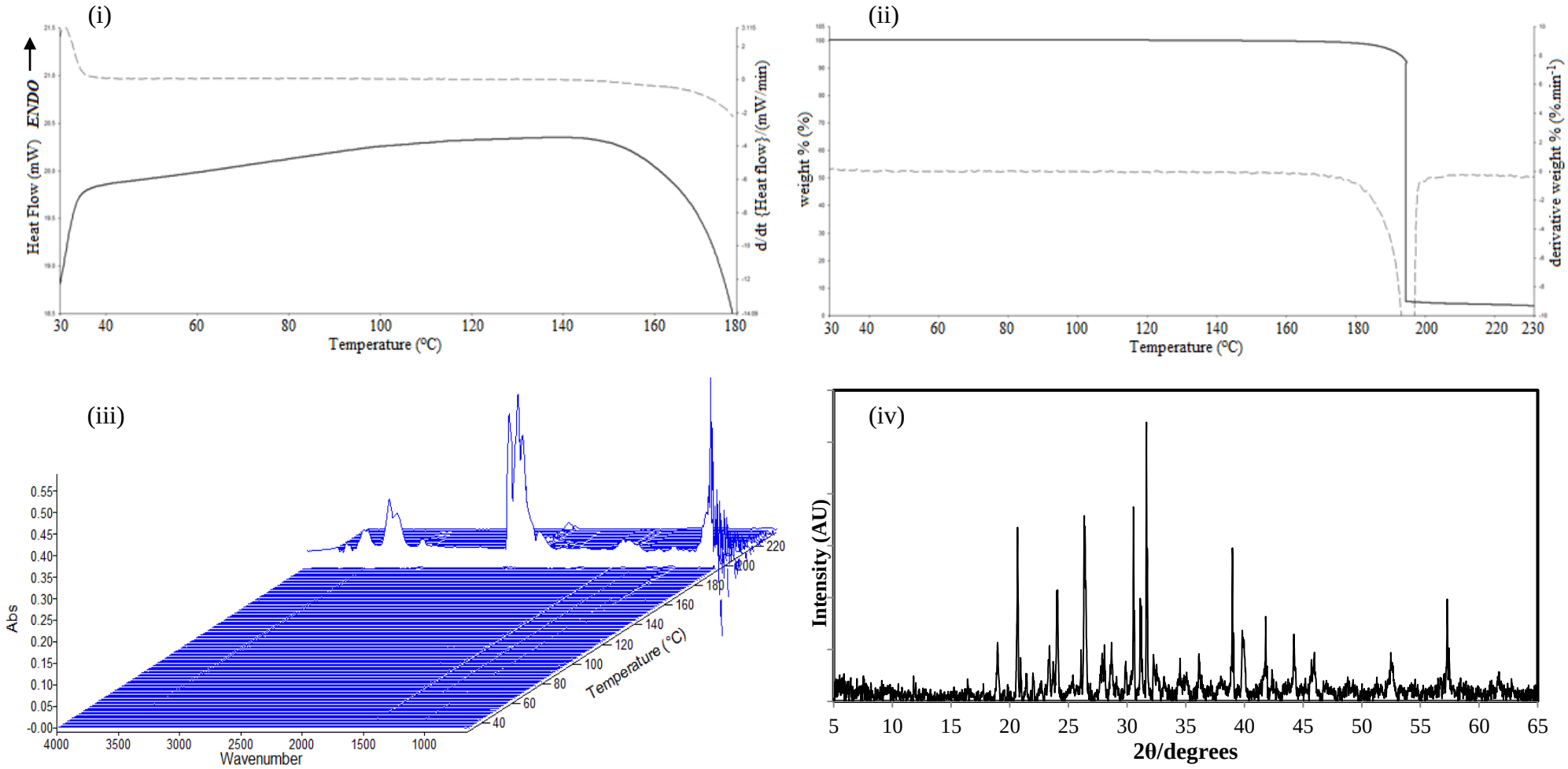

Figure 5.20: The (i) 30 – 180 °C DSC thermogram, (ii) 30 – 230 °C TG thermogram, (iii) EGA stack plot, and (iv) XRPD pattern of $\{Fe(\mu\text{-pyzNO-}\kappa N,\kappa O)_{n-1}(pyzNO\text{-}\kappa N)_2(pyzNO\text{-}\kappa O)_2\}_n(ClO_4)_{2n}$ (Complex2) exposed to toluene vapour.

5.2.3 Diethyl ether

Figure 5.21 (i) of Complex2-diethyl ether shows a small endotherm in the 30 – 57 ^{o}C range, which is due to desorption of trace amounts of weakly surface-held solvent [16]. Fig. 5.21 (iii), however, shows no corresponding activity due to the low concentration in the TG exhaust stream. In particular, the absence of the otherwise very strong diethyl ether *v*(CO) vibration at around 1100 cm^{-1} [15] confirms that there is only a very small solvent-complex interaction, which is limited to the crystalline surface.

DSC shows H_2O condensation (100 ^{o}C) in the crimped sample pan, possibly due to ether evaporation during preparation. It is not seen in the TG (Fig. 5.21 (ii)) as this uses a sample pan which is open to the purge gas.

TG shows no mass loss prior to decomposition, which is consistent with only minor solvent-complex surface interaction.

Fig. 5.21 (iv) shows the retention of crystallinity, but with all major reflections concentrated between 18 and 31 $^{o}2\theta$, indicating a net reduction in unit cell size.

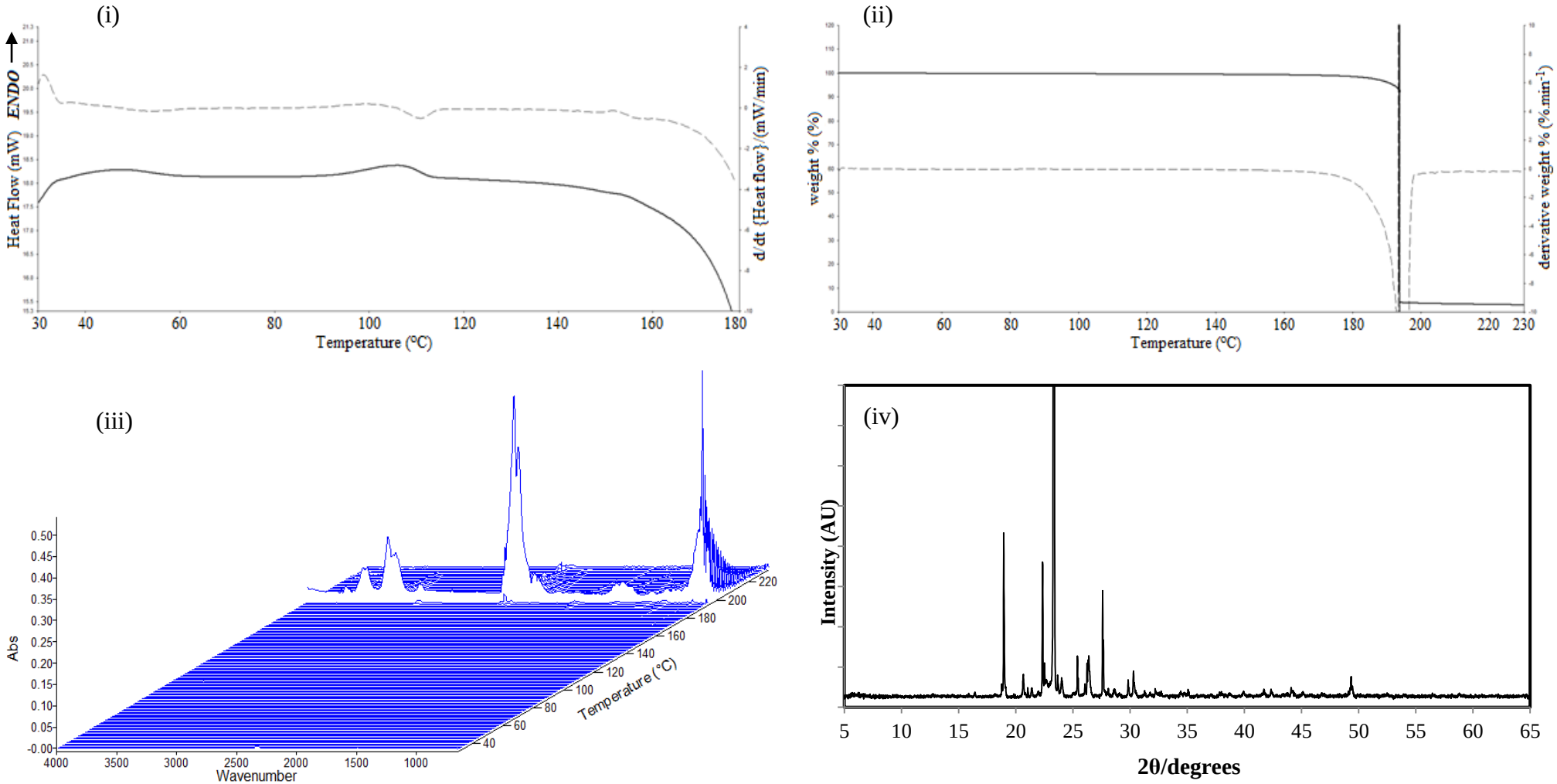

Figure 5.21: The (i) 30 – 180 °C DSC thermogram, (ii) 30 – 230 °C TG thermogram, (iii) EGA stack plot, and (iv) XRPD pattern of $\{Fe(\mu\text{-pyzNO-}\kappa N,\kappa O)_{n-1}(pyzNO\text{-}\kappa N)_2(pyzNO\text{-}\kappa O)_2\}_n(ClO_4)_{2n}$ (Complex2) exposed to diethyl ether vapour.

5.2.4 Tetrahydrofuran

The complex does not exhibit any distinct thermal solvation-desolvation behaviour with THF. The gradual baseline incline seen in Fig. 5.22 (i) is likely due to the slow desorption of trace solvent adsorbed on the crystalline surface.

Fig. 5.22 (ii) shows only a very small and gradual weight decline of 0.2 % between 30 and 120 ^{o}C.

Fig. 5.22 (iii) shows minute activity centred at 1500 cm^{-1} and 3750 cm^{-1}, which although unassigned, may be due to trace water detection. The water may have been acquired through atmospheric exposure during sample transfer to into the thermal instrumentation; however, DSC is not seen to confirm this.

The absence of the very strong pair of overlapping ν_a(CH) and ν_s(CH) vibrations centred at ca. 2990 and 2850 cm^{-1}, respectively, as well as the strong and sharp ν(CO) vibrations at 1100 and 900 cm^{-1} [15] in Fig 5.22 (iii) corroborates the lack of significant solvent uptake.

Fig. 5.23 (iv) indicates very little change from the XRPD pattern of the original material, other than intensity variations due to the irreproducible effects of preferred orientation. This again indicates the resistance of Complex2 to THF exposure.

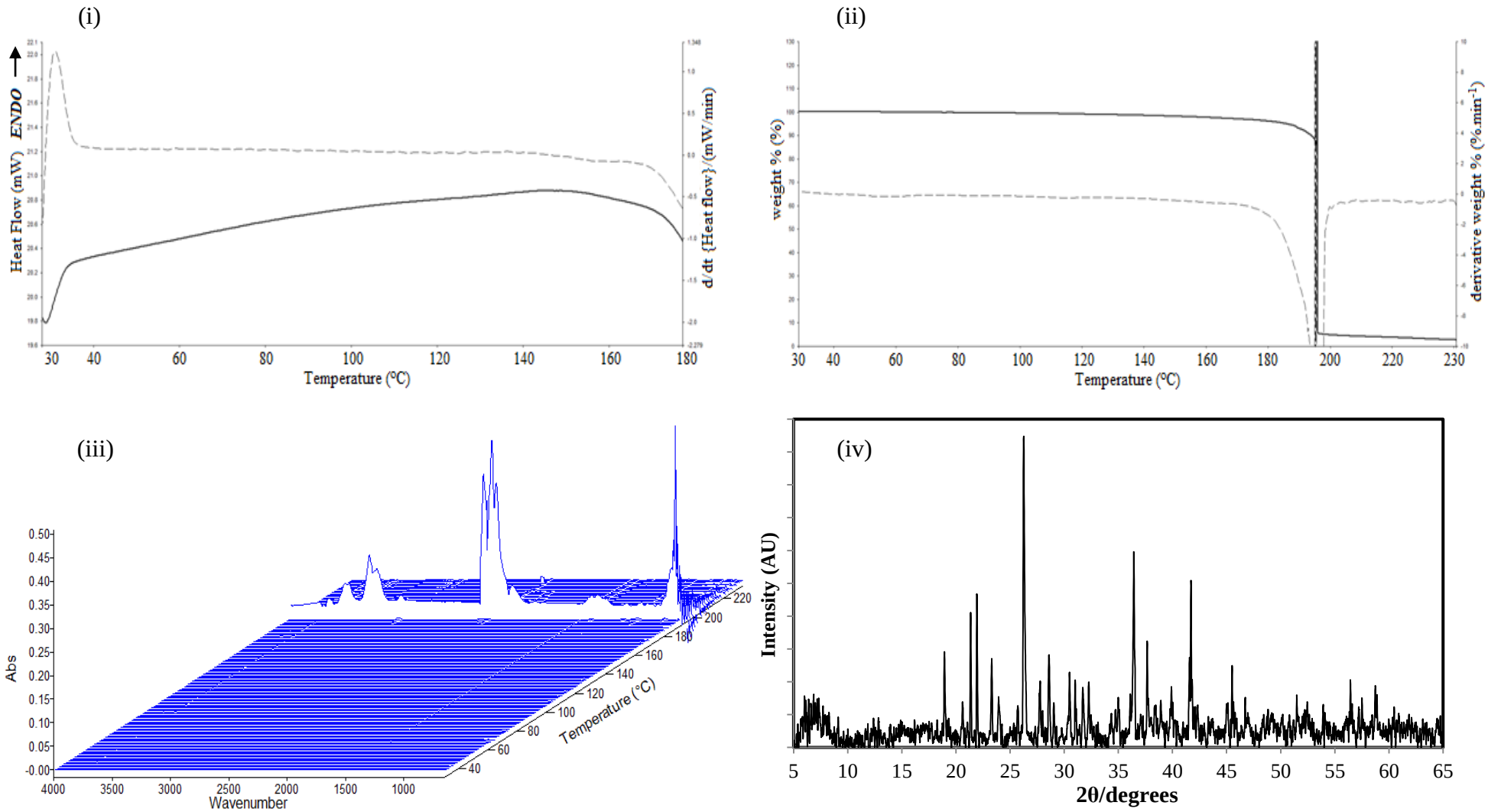

Figure 5.22: The (i) 30 – 180 °C DSC thermogram, (ii) 30 – 230 °C TG thermogram, (iii) EGA stack plot, and (iv) XRPD pattern of $\{Fe(\mu\text{-pyzNO-}\kappa N,\kappa O)_{n-1}(pyzNO\text{-}\kappa N)_2(pyzNO\text{-}\kappa O)_2\}_n(ClO_4)_{2n}$ (Complex2) exposed to tetrahydrofuran vapour.

5.2.5 Chloroform

Complex2 shows very similar behaviour with chloroform exposure as in the diethyl ether trial. Figure 5.23 (i) shows a very low energy *two-step* desorption of loosely held solvent is seen in the 30 – 78 ^{o}C temperature range, by way of a gradual baseline incline [16]. There is a slight point of inflection on the primary curve at ~ 42 ^{o}C, which represents the temperature at which the two overlapping *sub-endotherms* merge. The temperatures of their respective height maxima cannot be accurately determined due to their overwhelmingly weak and broad nature.

Fig. 5.23 (iii) shows no detection of chloroform as the concentration thereof is likely below the detection limits of the IR-spectrometer.

As in with Complex2-diethyl ether, DSC shows H_2O desorption at 100 ^{o}C (condensate) in the crimped sample pan, likely due to $CHCl_3$ evaporation during preparation. Again, this is not seen in the TG (Fig. 5.23 (ii)) as this uses a sample pan which is open to the purge gas.

Fig. 5.23 (iv) does not indicate any substantial changes from the original material.

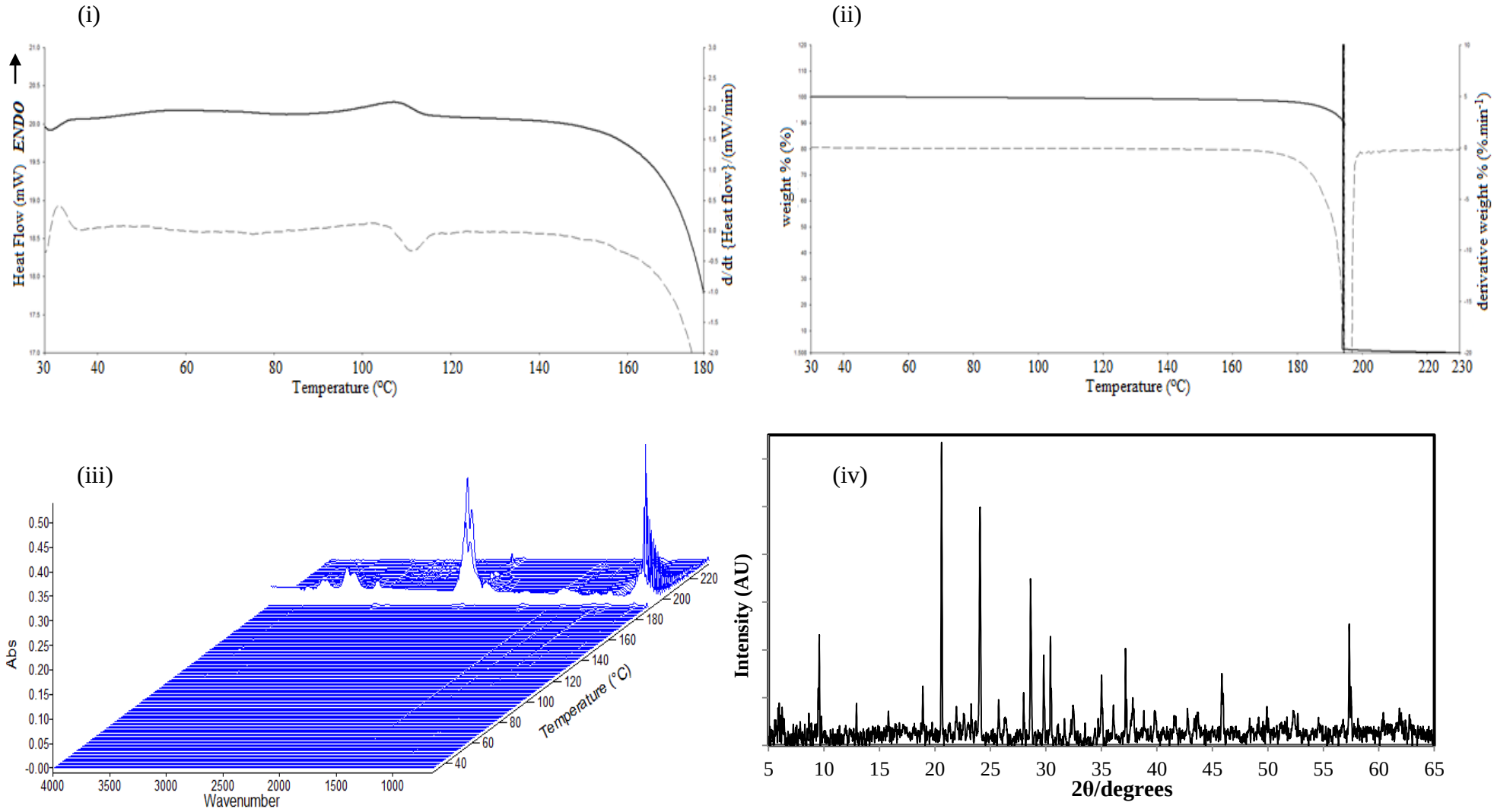

Figure 5.23: The (i) 30 – 180 °C DSC thermogram, (ii) 30 – 230 °C TG thermogram, (iii) EGA stack plot, and (iv) XRPD pattern of $\{Fe(\mu\text{-pyzNO-}\kappa N,\kappa O)_{n-1}(pyzNO\text{-}\kappa N)_2(pyzNO\text{-}\kappa O)_2\}_n(ClO_4)_{2n}$ exposed to chloroform vapour.

5.2.6 *p*-dioxane

Complex2 showed strong *p*-dioxane uptake. Fig. 5.24 (i) shows a broad endotherm at 30 – 67 ^{o}C (1) due to the evaporation of excess weakly surface-held solvent, as evidenced by Fig. 5.24 (iii). The latter shows the ν(CH) vibrations of *p*-dioxane at 3000 – 2800 cm^{-1}, and its ν(CO) vibrations at 1170 and 960 cm^{-1} [15]. Fig. 5.24 (ii) shows a parallel weight reduction of 5.9 %. It also shows a 4.8 % weight loss even before the onset of the experiment*.

An intense, three-part endotherm is then seen in the 65 - 118 ^{o}C range, with height maxima at 81, and 110 and 85 ^{o}C, respectively. TG shows a combined weight loss of 10.6 % at 68 – 118 ^{o}C (2). This is due to the loss of 1.5 solvate *p*-dioxane molecules per formula unit (theoretical: 11.05 %). EGA shows only the continued detection of *p*-dioxane.

The third weight loss, at 150 – 170 ^{o}C (3) (3.9 %) corresponds to the loss of 0.5 *p*-dioxane moieties per formula unit (theoretical: 3.68). The final 13.3 % weight loss at 170 – 203 ^{o}C (4) is due to the loss of approximately 1.5 PyzNOs per formula unit (theoretical: 12.63 %), as evidenced by its detection in the EGA stack plot. EGA indicates partial PyzNO decomposition, as seen by the appearance of bands previously assigned to ν(CO) of CO_2, and the ν(CH), ν(ring) and coupled ν(NO) + ν(ring) vibrations of PyzNO. Mass loss (4) then triggers the explosive decomposition of ClO_4^-.

Fig. 5.24 (iv) shows a virtually complete loss of crystallinity, and the accompanying loss of all quantitative reflections prior to solvent exposure. There are as many as six broad amorphous reflections, which indicate the immergence of an entirely new phase.

Table 5.6: Summary of thermoanalytical profile of Complex2-*p*-dioxane

Event number	Event	ΔTemp. (range/^{o}C)	Moles of dioxane/Fe	ΔH (J.g^{-1})
(1)	Dioxane loss	30 – 67	–	–
(2)	Dioxane loss	65 – 118	1.5	91.99
(3)	Phase change	150 – 170	0.5	–
(4)	Phase change	170 – 203	1.5 PyzNO	–

*This occurred between the time at which the loaded mass was recorded and the time at which the instrument began the heating profile. The lag is due to an inherent system delay as the program software configures the instrument after the parameters have been set, but prior to the actual analysis.

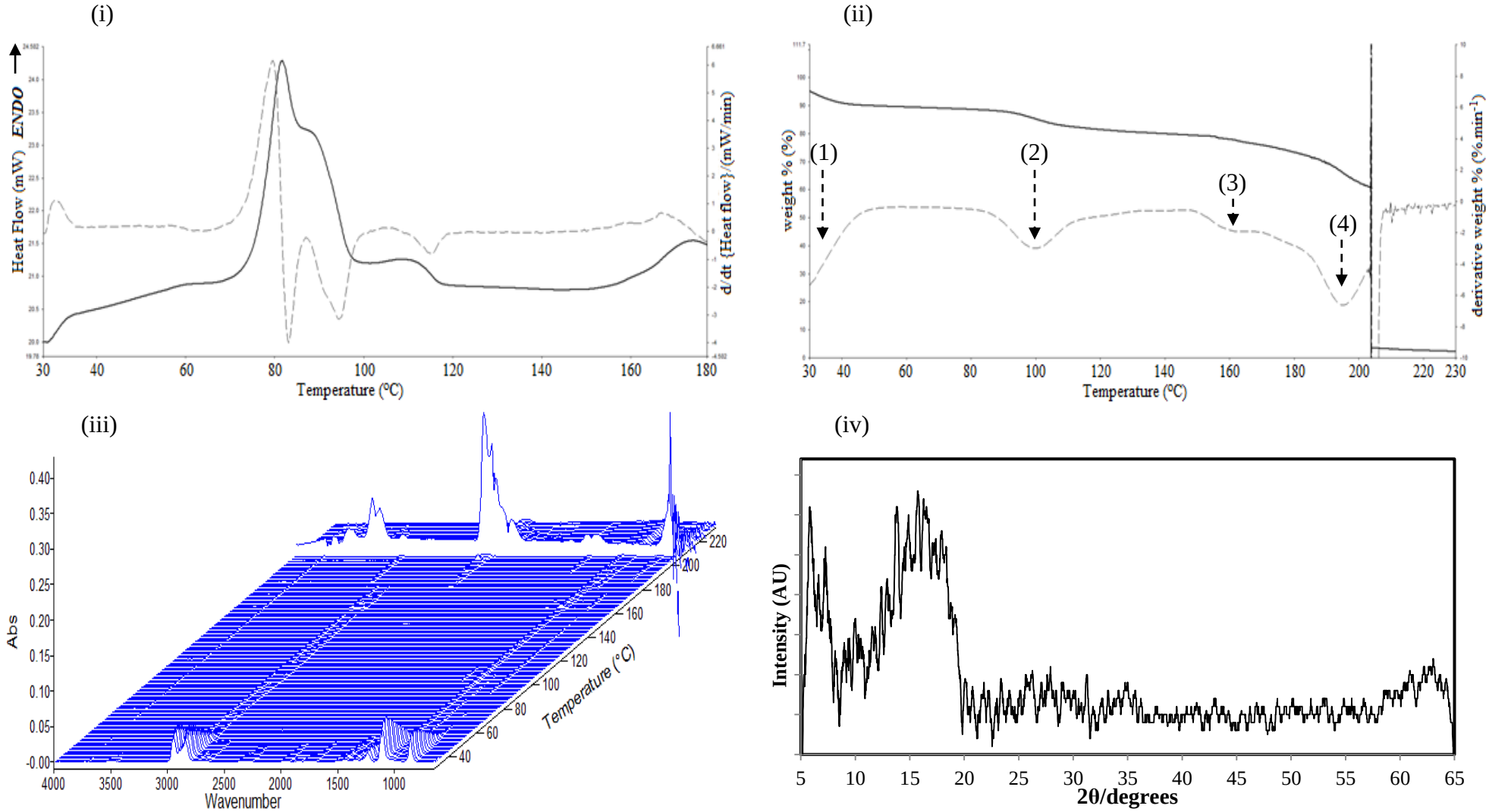

Figure 5.24: The (i) 30 – 180 ºC DSC thermogram, (ii) 30 – 230 ºC TG thermogram, (iii) EGA stack plot, and (iv) XRPD pattern of $\{Fe(\mu\text{-pyzNO-}\kappa N,\kappa O)_{n-1}(pyzNO\text{-}\kappa N)_2(pyzNO\text{-}\kappa O)_2\}_n(ClO_4)_{2n}$ (Complex2) exposed to *p*-dioxane vapour.

5.2.7 Acetone

Complex2 exhibited significant acetone uptake. TG in Fig. 5.25 (ii) shows a 12.2 % weight loss due to the evaporation of very weakly adsorbed solvent prior to heating (see section 5.2.5 footnote). This corresponds to the loss of 2 acetone molecules per formula unit (theoretical: 12.43 %).

The remaining adsorbed acetone is volatilised in a single mass loss step with an associated weight decrease of 9.1 % between 30 and 40 ^{o}C, as evidenced by Fig. 5.25 (i) and (ii). This corresponds to 1.5 acetones per formula unit (theoretical: 9.33 %).

The EGA in Fig. 5.25 (iii) shows the corresponding ν_a(CH), ν_s(CH), ν(C=O), δ_a(CH_3) and δ_s(CH_3) vibrations at 3500, 3000, 1738, 1450 and 1250 cm^{-1}, respectively [15]. The apparent continued detection of acetone beyond 45 ^{o}C is ascribed to residual solvent vapour in the exhaust stream and in the infrared spectrometer after its substantial initial evolution from the sample.

Fig. 5.25 (iv) shows no discernible disruption of the crystalline nature of the complex. It does however show an emergent reflection at 9.586 $^{o}2\theta$, which possibly suggests a net expansion of the unit cell. In general, the complex appears largely unaffected (irreversibly) by acetone exposure.

Table 5.7: Summary of thermoanalytical profile of Complex2-*p*-acetone

Event number	Event	ΔTemp. (range/^{o}C)	Moles of acetone/Fe	ΔH ($J.g^{-1}$)
(1)	Acetone loss	30	2	–
(2)	Acetone loss	30 – 40	1.5	–

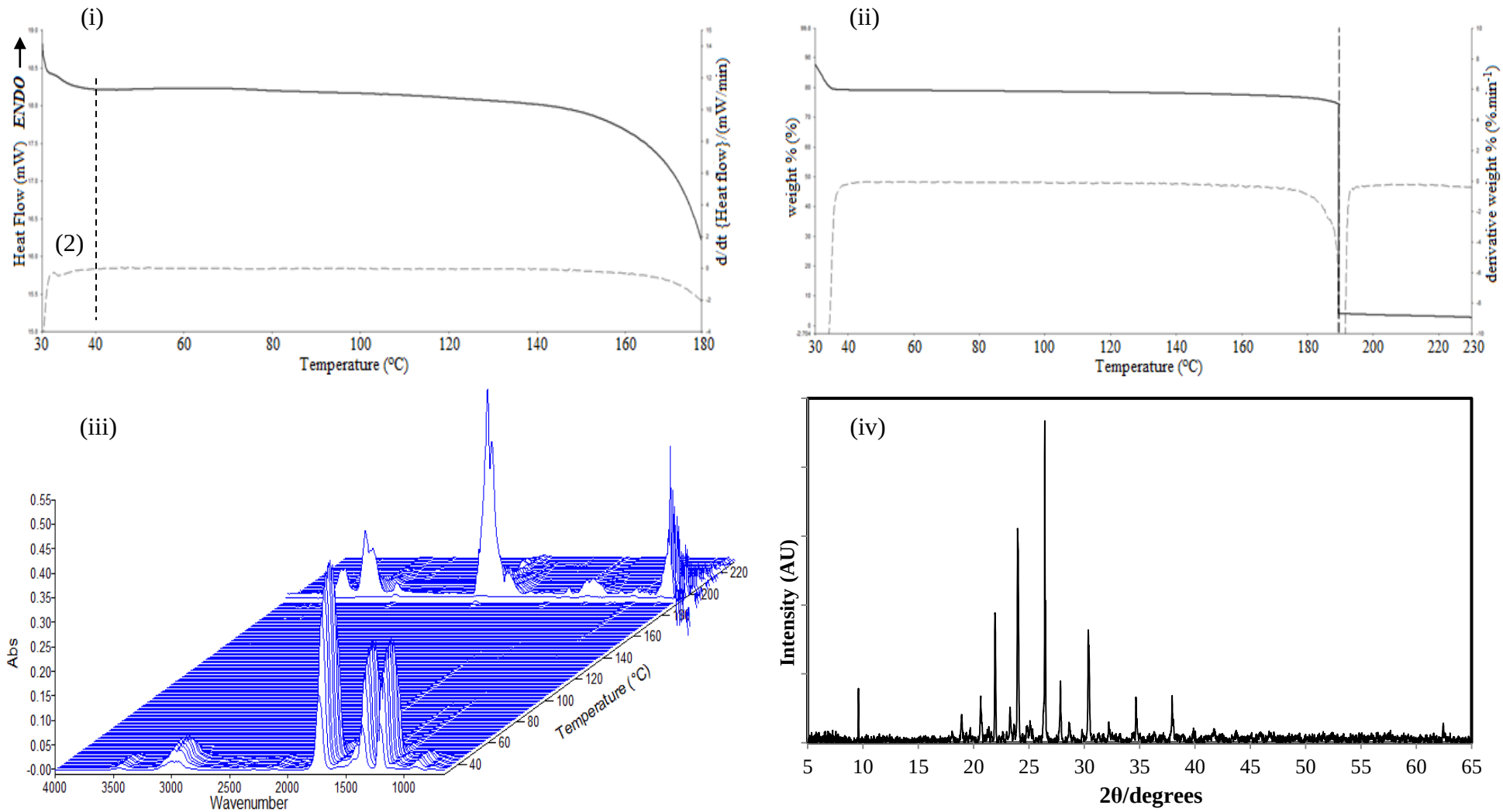

Figure 5.25: The (i) 30 – 180 °C DSC thermogram, (ii) 30 – 230 °C TG thermogram, (iii) EGA stack plot, and (iv) XRPD pattern of $\{Fe(\mu\text{-pyzNO-}\kappa N,\kappa O)_{n-1}(pyzNO\text{-}\kappa N)_2(pyzNO\text{-}\kappa O)_2\}_n(ClO_4)_{2n}$ (Complex2) exposed to acetone vapour.

5.2.8 Methanol

Fig. 5.26 (i) indicates significant interaction of methanol with Complex2, by comparison with Fig. 4.16. DSC shows the endothermic mass loss of methanol in two steps ((1) and (2)) before 87 ^{o}C. This is seen in the EGA in Fig. 5.26 (iii) through the presence of the *ν*(CH) and δ(C-OH) bands at 3000 and 1000 cm^{-1}, respectively [15, 17].

The TG thermogram in Fig. 5.26 (ii) shows a combined weight loss of 6.9 % between 30 and 87 ^{o}C, which corresponds to the loss of 1.75 methanols per formula unit (theoretical: 7.09 %). DSC steps (1) and (2) have corresponding TG mass losses of 6.0 and 0.9 %, indicating associated losses of 1.5 and 0.25 methanols, respectively (theoretical: 6.08 and 1.03).

Endotherms are seen in the 89 – 117 ^{o}C (3) and 141 – 170 ^{o}C (4) temperature ranges, without any measurable corresponding mass changes on the TG thermogram, which suggests associated phase changes instead, before explosive decomposition.

The partial dissolution of Complex2 with loss of crystallinity in a MeOH atmosphere is indicated by the XRPD in Fig 5.26 (iv).

Table 5.8: Summary of thermoanalytical profile of Complex2-methanol

Event number	Event	ΔTemp. (range/^{o}C)	Moles of MeOH/Fe	Δ*H* (J.g^{-1})
(1)	MeOH loss	30 – 59	1.5	–
(2)	MeOH loss	60 – 88	0.25	57.1
(3)	Phase change	89 – 117	–	ca. 10
(4)	Phase change	141 – 170	–	–

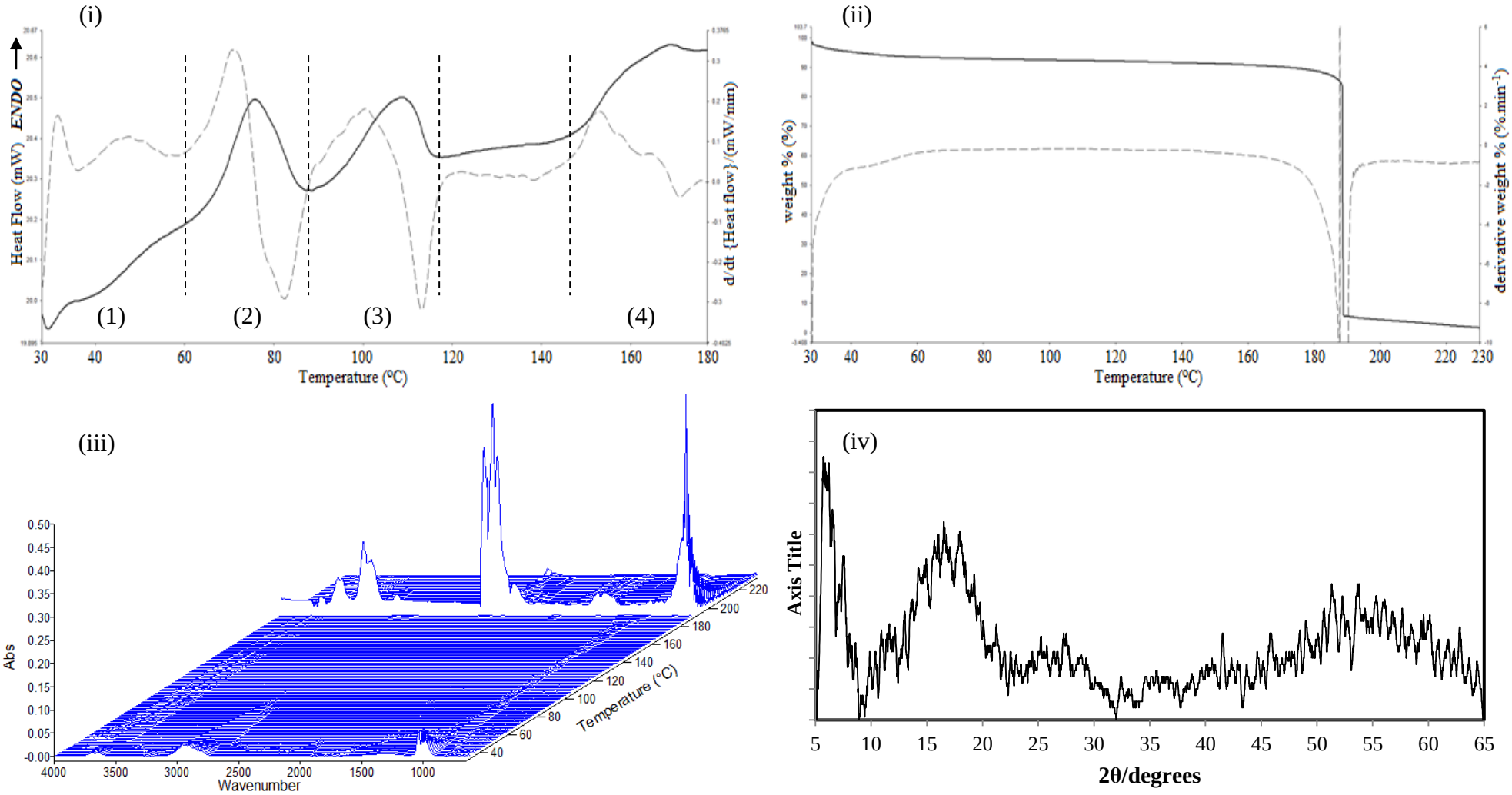

Figure 5.26: The (i) 30 – 180 °C DSC thermogram, (ii) 30 – 230 °C TG thermogram, (iii) EGA stack plot, and (iv) XRPD pattern of $\{Fe(\mu\text{-pyzNO-}\kappa N,\kappa O)_{n-1}(pyzNO\text{-}\kappa N)_2(pyzNO\text{-}\kappa O)_2\}_n(ClO_4)_{2n}$ (Complex2) exposed to methanol vapour.

5.2.9 Ethanol

The thermoanalytical study of Complex2-ethanol indicates measurable solvent uptake. DSC in Fig. 5.27 (i) shows the endothermic loss of ethanol occurring in two steps.

The first endotherm is truncated, as it begins before the start of the heating profile, returning to the baseline at 32 ^{o}C. Unsurprisingly, TG (Fig. 5.27 (ii)) indicated a weight loss of 5.6 % before heating commenced. This corresponds to the loss of one ethanol molecule per formula unit (theoretical: 5.71 %), due to desorption of weakly held solvent from the crystal surface.

TG shows a further weight decline of 3.3 % before 45 ^{o}C, which corresponds to the loss of 0.5 ethanols per formula unit (theoretical: 2.86). This is evidenced by the strong EGA detection (Fig. 5.27 (iii)) of the ethanol ν(CH), $\delta(CH_3)$ and ν(C-OH) vibrations at 3100 – 2900 cm^{-1}, 1500 – 1400 cm^{-1} and 1100 – 1000 cm^{-1}, respectively [15]. DSC shows a very weak endotherm in this range, which requires some examination of the first derivative curve to observe.

DSC then shows a two-step endotherm at 84 – 116 ^{o}C, which occurs without a corresponding TG mass loss, indicating a possible phase change in this range.

Fig. 5.27 (iv) shows very little loss in crystallinity, which is unsurprising given the relatively weak solvent-complex interaction indicated by DSC.

Table 5.9: Summary of thermoanalytical profile of Complex2-ethanol

Event number	Event	ΔTemp. (range/^{o}C)	Moles of EtOH/Fe	ΔH (J.g^{-1})
(1)	EtOH loss	below 30 – 32	1	–
(2)	EtOH loss	32 – 45	0.5	–
(3)	Phase change	84 – 116	–	7.4

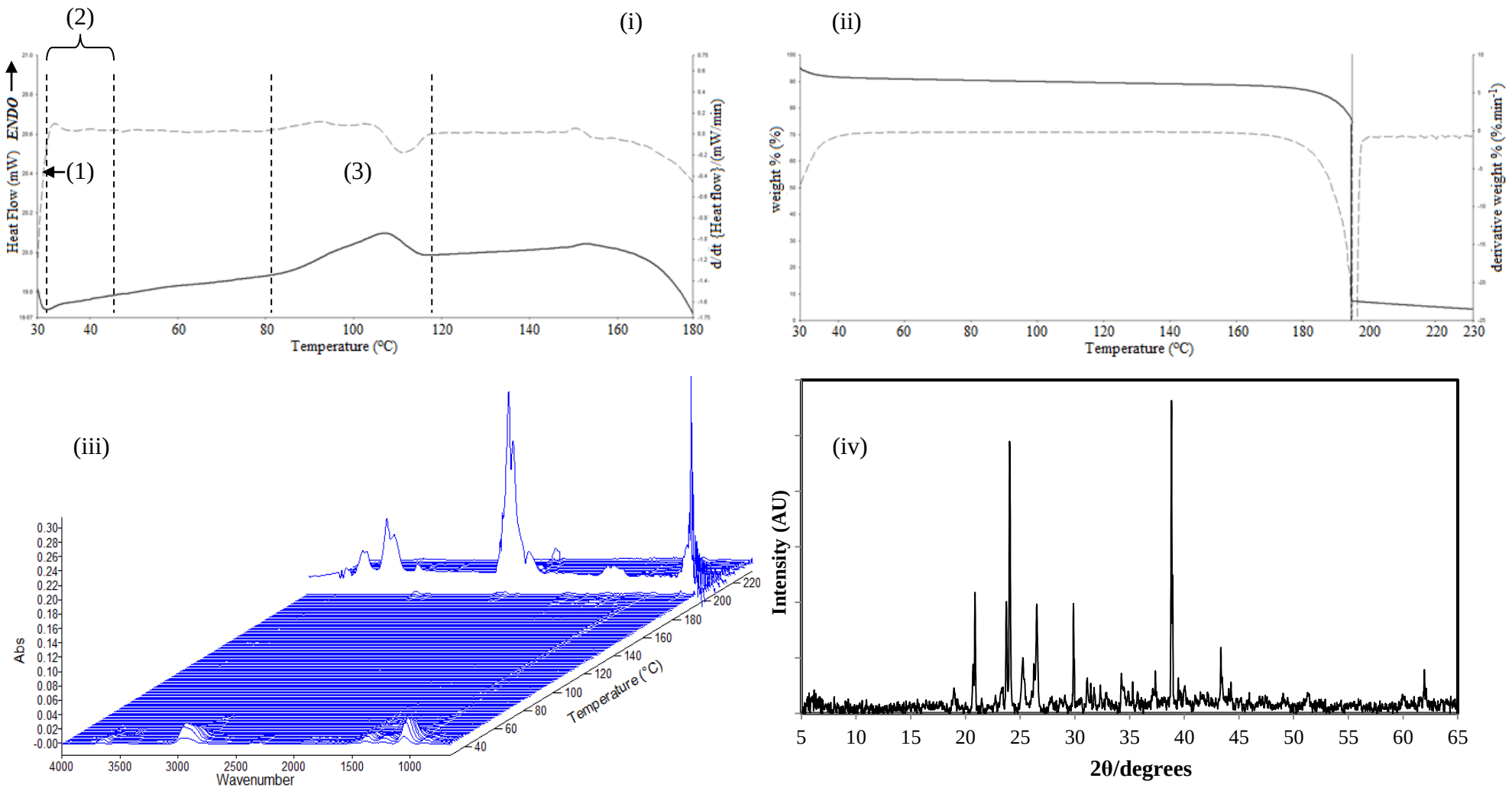

Figure 5.27: The (i) 30 – 180 °C DSC thermogram, (ii) 30 – 230 °C TG thermogram, (iii) EGA stack plot, and (iv) XRPD pattern of $\{Fe(\mu\text{-pyzNO-}\kappa N,\kappa O)_{n-1}(pyzNO\text{-}\kappa N)_2(pyzNO\text{-}\kappa O)_2\}_n(ClO_4)_{2n}$ (Complex2) exposed to ethanol vapour.

5.2.10 Acetaldehyde

Fig's. 5.28 (i) and (ii) indicate a significant interaction of acetaldehyde with Complex2 by comparison with Fig's. 4.16 and 4.18, respectively. DSC and TG show the slow loss of acetaldehyde (MeCHO) with three small endotherms before 104 ^{o}C.

The TG weight loss of 7.5 % at 30 – 59 ^{o}C corresponds to loss of 1.5 MeCHO molecules per formula unit (theoretical: 7.64 %). This mass loss likely occurs from the surface of the material. A further 5.0 % weight loss is seen in the 61 – 89 ^{o}C range, which is due to the loss of 1 MeCHO per formula unit (theoretical: 5.09 %). A third mass loss step is seen at 89 – 103 ^{o}C with an associated weight reduction of 2.7 %. 0.5 MeCHO moieties per formula unit are lost in this step (theoretical: 2.54 %).

EGA in Fig. 5.28 (iii) shows the associated ν(CH) bands at 3000 – 2770 cm^{-1}, and the coupled $\delta(CH_3)/\delta(HC=O)$ vibrations at ca. 1750 and 1000 cm^{-1} [15] in the 30 – 105 ^{o}C range.

The strong endotherm above 103 ^{o}C suggests a massless phase change (no TG mass loss), followed by the explosive decomposition of the complex.

Fig. 5.28 (iv) shows the loss of crystallinity which is associated with extended exposure of the complex in an acetaldehyde atmosphere, due the effects of partial dissolution and the underlying phase change.

Table 5.10: Summary of thermoanalytical profile of Complex2-acetaldehyde

Event number	Event	ΔTemp. (range/^{o}C)	Moles of MeCHO/Fe	ΔH (J.g^{-1})
(1)	MeCHO loss	30 – 59	1.5	21.2
(2)	MeCHO loss	61 – 89	1	18.9
(3)	MeCHO loss	89 – 102	0.5	–
(4)	Phase change	103 – 148	–	266.7

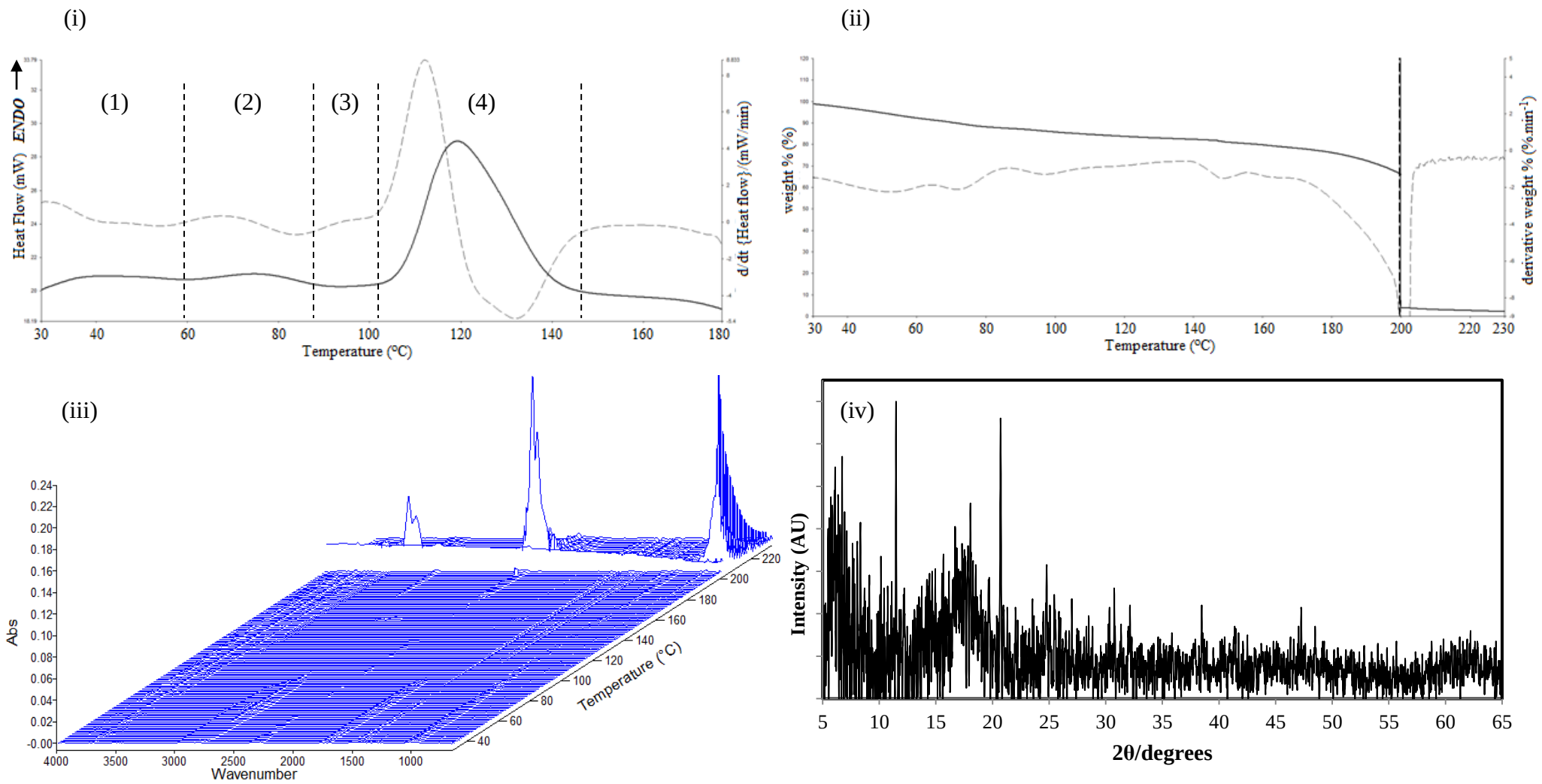

Figure 5.28: The (i) 30 – 180 °C DSC thermogram, (ii) 30 – 230 °C TG thermogram, (iii) EGA stack plot, and (iv) XRPD pattern of $\{Fe(\mu\text{-pyzNO-}\kappa N,\kappa O)_{n-1}(pyzNO\text{-}\kappa N)_2(pyzNO\text{-}\kappa O)_2\}_n(ClO_4)_{2n}$ (Complex2) exposed to acetaldehyde vapour.

5.2.11 Formaldehyde

Complex2 shows similar behaviour with formaldehyde (H_2CO) exposure as in the acetaldehyde trial. This is unsurprising as the two solvents are isoelectronic and have very closely related structures.

DSC (Fig. 5.29 (i)) shows a weak endotherm at 30 - 61 ^oC due to desorption of solvent initially held on the crystal surface, while TG (Fig. 5.29 (ii)) shows an associated weight loss of 7.1 %. This is due to the loss of 2 H_2CO molecules per formula unit (theoretical: 6.94).

TG shows a further mass loss of 7.9 % before 110 ^oC, which corresponds to the loss of 2.25 H_2CO molecules per formula unit (theoretical: 7.81 %). DSC shows that this occurs in two distinct steps, with the major endotherm lying in at 63 – 92 ^oC. Although TG is unable to distinguish the two steps, showing only one mass loss, the second step lies in the 92 – 110 ^oC range.

Fig. 5.29 (iii) shows the H_2CO ν(CH) bands 3130 – 2610 cm^{-1}, the ν(C=O) band at ca. 1700 cm^{-1}, and the δ(HCH) band at ca. 1000 cm^{-1} [15].

A four-step massless phase change is seen in the 110 – 148 ^oC range as evidenced by the lack of a distinct mass loss event in the TG thermogram. This event is followed by the explosive thermolysis of the complex in the usual way.

Fig. 5.29 (iv) (like Fig. 5.28 (iv)) shows a loss of crystallinity when Complex2 is kept in a formaldehyde atmosphere. This is ascribed to the effects of partial dissolution and the underlying phase change.

Table 5.11: Summary of thermoanalytical profile of Complex2-formaldehyde

Event number	Event	ΔTemp. (range/^oC)	Moles of H_2CO/Fe	ΔH ($J.g^{-1}$)
(1)	H_2CO loss	30 – 62	2	23.0
(2) + (3)	H_2CO loss	63 – 110	2.25	26.1
(4)	Phase change	110 – 148	–	239.4

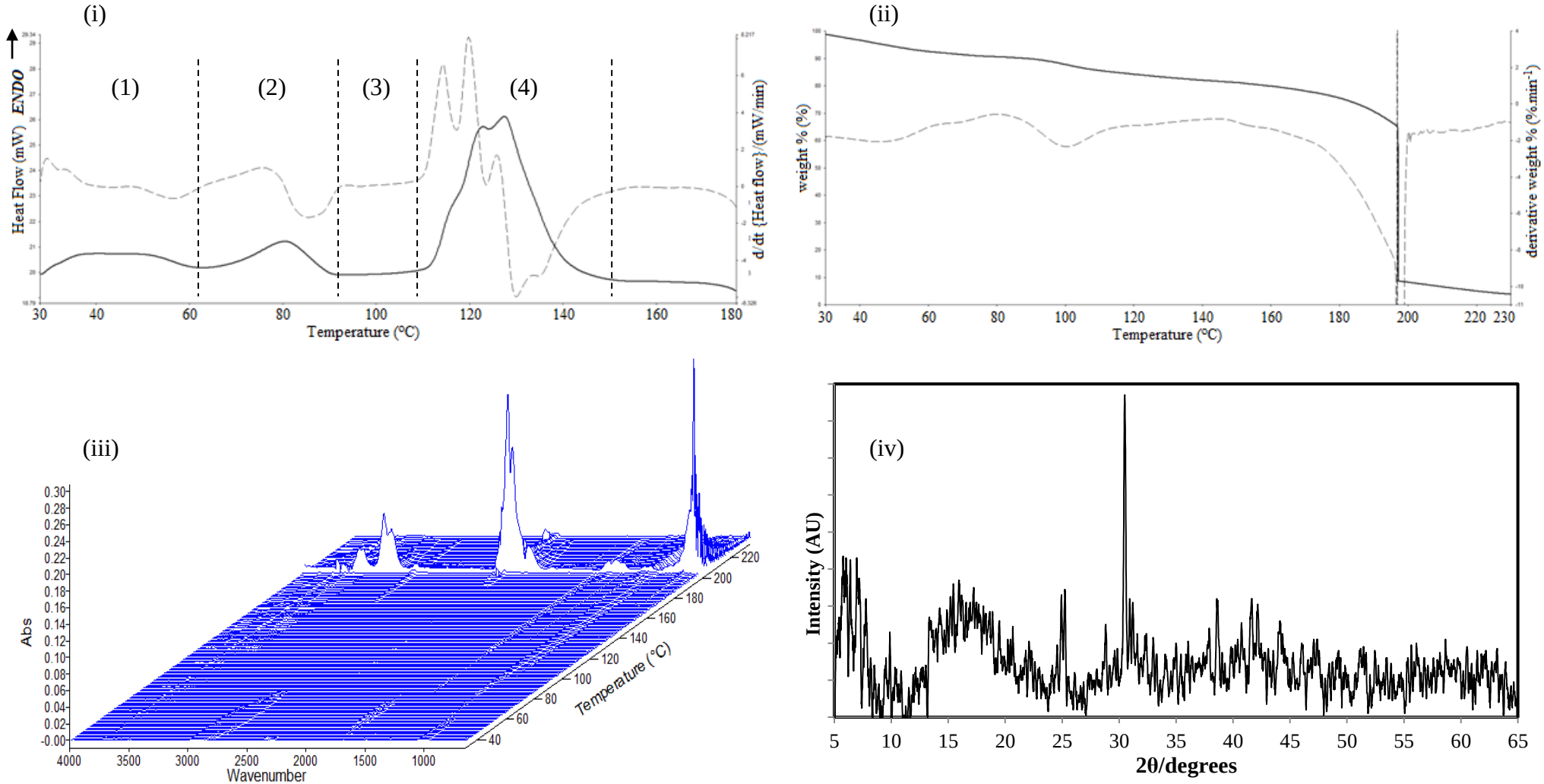

Figure 5.29: The (i) 30 – 180 °C DSC thermogram, (ii) 30 – 230 °C TG thermogram, (iii) EGA stack plot, and (iv) XRPD pattern of $\{Fe(\mu\text{-pyzNO-}\kappa N,\kappa O)_{n-1}(pyzNO\text{-}\kappa N)_2(pyzNO\text{-}\kappa O)_2\}_n(ClO_4)_{2n}$ (Complex2) exposed to formaldehyde vapour.

As evidenced by X-ray crystallography studies, there was a definite substitution of the bonded PyzNO by water to produce the $[Fe(pyzNO)_4(H_2O)_2](ClO_4)_2.2H_2O$ complex (Complex6) from its precursor, Complex2. However, the studies also showed that there were uncoordinated solvate waters trapped in the lattice by intermolecular interactions. The two solvate waters per formula unit may act in synergy with coordinated waters, *via* a manner similar to that depicted in Fig. 1.14, to further enhance the observed spectral and magnetic changes. That is, the interaction of hydrate waters with *O*-atoms of the remaining *N*-coordinated PyzNOs; *via* hydrogen-bonding, etc., may serve to further stabilize the e_g* orbital by allowing further delocalisation of *d*-electron density. Consequently, the colour change on hydration ultimately becomes more pronounced (greater red↔yellow contrast) than may otherwise have been the case.

Some evidence of this was provided by the above comparative solvent studies of the complex. Even in the case where a red → yellow colour change was seen to occur on solvent exposure, none of the colour changes were as substantial as that seen on hydration. In some instances – most notably the samples exposed to the aldehydes – the IR spectra seemed virtually identical to that of Complex6. However, the colours were visibly different (Complex6– yellow, Complex2-aldehydes – dark yellow).

The differences in the resulting H-bonding; with that due to water being the most significant (stable), is the ostensible cause for these discrepancies.

5.3 EPR Solvent Studies of $\{Fe(\mu\text{-pyzNO-}\kappa N,\kappa O)_{n-1}(pyzNO\text{-}\kappa N)_2(pyzNO\text{-}\kappa O)_2\}_n(ClO_4)_{2n}$

An EPR study of Complex2 exposed to the solvents discussed in section 5.2 was undertaken, but with several additions included. The additional test solvents are acetonitrile, formamide, *N*,*N*'-dimethylformamide (DMF), and dimethylsulphoxide (DMSO). The thermoanalytical studies of Complex2 after exposure to these solvents were also performed, and are included in the appendix. However, a full analysis in the format employed in section 5.2 was not possible, as the corresponding XRPD patterns could not be collected. The reason for this was that exposure to all of these solvent resulted in the rapid dissolution of the complex. Thus, only DSC, TG and EGA results were obtained.

The ordering of the solvents in the EPR spectra, although not ideal, was necessary. In section 5.2, an effort was made to employ an order of increasing solvent polarity. However, the marked differences in the EPR spectra in consecutive solvents on employing this rationale produced scaling difficulties when they were combined. They were thus grouped in terms of their spectral similarities, so as to avoid the 'scale-induced' suppression of meaningful features thereof.

A solid state EPR analysis was performed. This was done in order to ensure that all samples were amenable to the study, including those that were insoluble. Solvent exposure was generally permitted for 48 h, with the exception of Fig's. 5.30 (B: (c)), 5.30 (C: (a) and (b)), and 5.30 (D: (a) – (c)); in which exposure was limited to 2 hours in order to avoid complete dissolution of the complex. The non-polar to moderately polar solvents are grouped in Fig. 5.30, while their highly polar counterparts are in Fig. 5.31.

It was found that it was the more polar solvents that induced some measurable paramagnetic behaviour within the complex, while a solvent-induced immergence of the Zeeman Effect was suspected in others; owing to the absence signals associated with the hyperfine coupling of paramagnetic centres [18, 19]. Generally, though, the more polar the solvent, the more pronounced, ostensibly, would be these resulting effects. There were found to be a few exceptions, however this analysis was found to be valid, by and large. Fig. 5.30 shows that the complex was wholly unresponsive in terms of the LS→HS transition on its exposure to some solvents; including cyclohexane, toluene, chloroform, THF and acetonitrile. The first four results were deemed unsurprising due to the low to negligible solvent-complex interaction seen in section 5.2 for these solvents.

Acetonitrile, on the other hand, might be expected to produce some measurable HS activity. The proposed reason for this being that the solvent substituted for PyzNO in the coordination sphere with a greater f parameter than H_2O (but less than 2,2'-bipyridine or 1,10-phenanthroline) [20]. Therefore, it perhaps induced a strong ligand field to the extent that the Δ_o consequently generated was too high to produce a HS state. It is conceivable that Δ_o may in this instance be even larger than in the original complex, perhaps by a M→L π-backbonding mechanism.

Diethyl ether was seen to produce a minor 'peak' as seen in Fig. 5.30 (A). The low intensity of this peak made its assignment as such rather tentative. It may just be a minor

baseline fluctuation, indicating no solvent-induced SCO in this instance, or it might be the presence of a radical impurity [21].

Methanol, ethanol and acetone were seen to induce significant changes in the magnetic properties of the original complex. The result for the lattermost solvent was surprising, as Fig. 5.25 (i) shows very little evidence of solvent uptake, other than the activity seen at 30 – 40 ^{o}C due to surface adsorption. The freezing of the solvent in the lattice at 77 K is the likely manner in which it was retained by the complex. The net stabilization of the e_g set of orbitals by a dipole-dipole interaction mediated mechanism may therefore be means by which a HS spin state was generated. This is however likely to have occur only in surface-localised nuclei, hence the comparatively low intensity of the resonance.

It was initially suspected that formaldehyde, acetaldehyde and *p*-dioxane produce paramagnetic resonance in the complex. Their potential coordination was suspected to induce the LS→HS transition, as suggested by the red→yellow colour change seen after the exposure of Complex2 to these solvent atmospheres. However, the associated EPR spectra could not be definitively interpreted to confirm this transition. The resonance seen in Fig. 5.30 D is suspected to be potentially ascribable to the Zeeman Effect in a simple paramagnetic species, rather than an S=2 ion. Although the species potentially exhibiting this effect in the applied field are as yet a subject of speculation, among them may be a PyzNO radical generated by the heterolytic cleavage of the *O*→Fe bond, given that PyzNO→solvent substitution is indeed occurring on solvent exposure.

Owing to the similarity in the mid-IR spectra of the complexes resulting from exposure to the aforementioned solvents with that of Complex6, very similar complexes are suspected to have been generated. Confirmation by single crystal XRD was however not possible due to lattice effects of partial dissolution. Extensive associated UV/Vis analyses have unfortunately been reserved for future work due to time constraints.

The respective g_e values for the Complex2-formaldehyde, Complex2-acetaldehyde, and Complex2-*p*-dioxane were approximated as 2.0271, 2.0142 and 2.0183 (eqn. 1.2). B_o values of 3441 G, 3466 G and 3459 G were used, respectively. As previously mentioned, these signals are suspected to potentially be due to action of the Zeeman Effect of a simple (monovalent) ion

or radical, and not a confirmation necessarily of paramagnetic Fe(II). In contrast with the EPR spectrum of $[Fe(pyzNO\text{-}\kappa N)_4(H_2O)_2](ClO_4)_2.2H_2O$ (Complex6), the recorded spectra of these species did not bear the usually sort after signals that indicate the hyperfine coupling (lines) of the constituent nuclei of strongly paramagnetic samples. On this basis, it is concluded that the red→yellow colour change is in these cases due exclusively to solvatochromic effects and not the LS→HS transition. As discussed in chapter 1, solvent-induced dipole-dipole stabilization of MLCT* states has been observed to produce comparatively substantial colour changes.

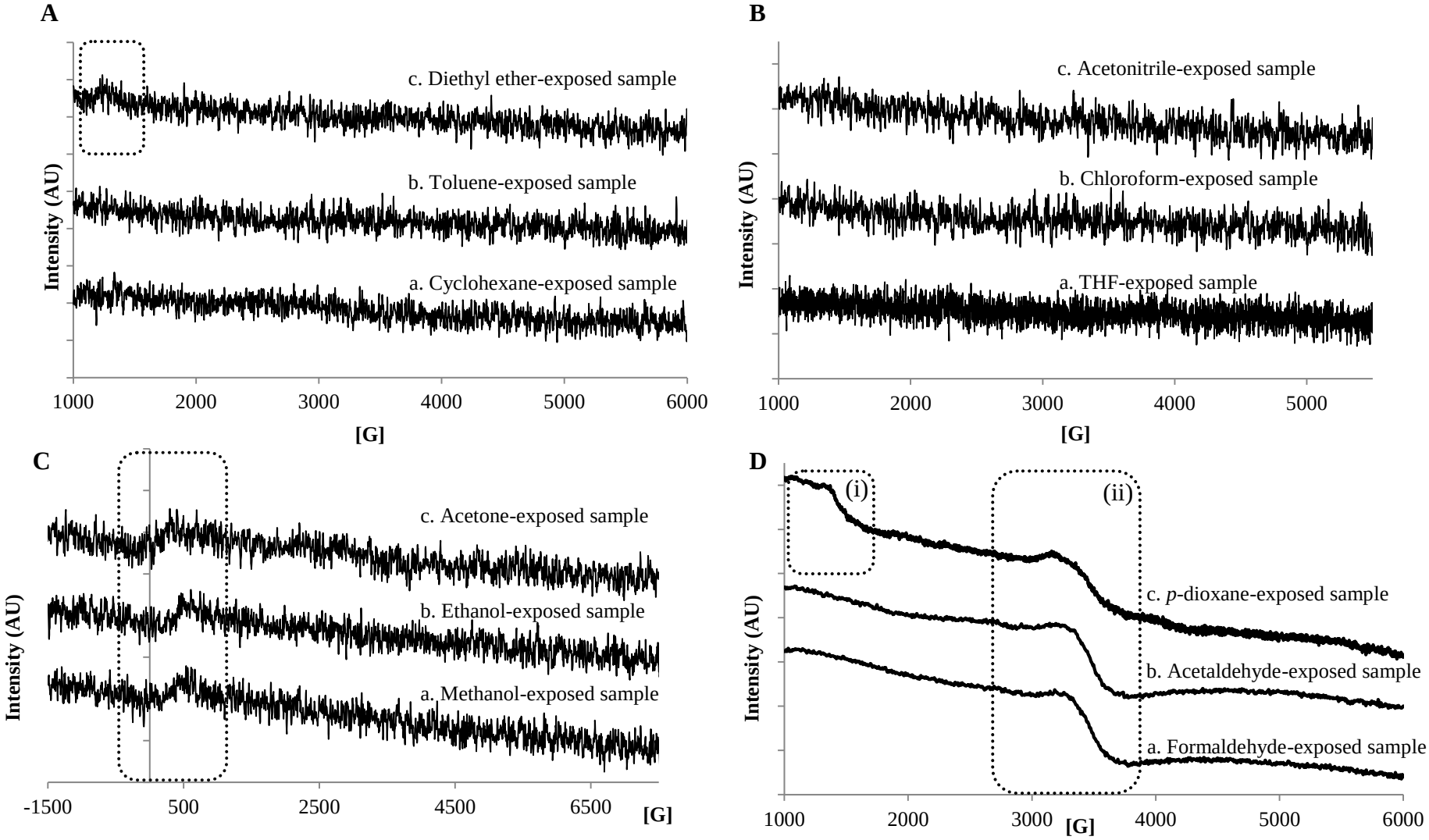

Figure 5.30: EPR spectra of $\{Fe(\mu\text{-pyzNO-}\kappa N,\kappa O)_{n-1}(pyzNO\text{-}\kappa N)_2(pyzNO\text{-}\kappa O)_2\}_n(ClO_4)_{2n}$ (Complex2) after exposure to the vapour-saturated atmospheres (A - D) of varying solvents. Where applicable, the regions of interest are highlighted for discussion. Non-polar to moderately polar solvents are shown.

Figure 5.31 shows the EPR spectra of the complex after its exposure to (a) formamide, (b) DMF, and (c) DMSO. The two latter solvents are expected to have coordinated. The lack of observable resonances, however, is ascribable to a net increase in Δ_o, thereby suppressing the LS→HS transition. Lastly, Complex2-formamide shows significant HS behaviour. The spectrum shows two major resonances, (i) and (ii) in Fig. 5.31 (a). The former is split into two, while the latter is split into three; by hyperfine coupling. g_e was approximated at 2.4331 using an experimental centre field of 2869 G (using eqn. 1.2). However, the degree of solvent substitution has yet to be determined. As with the other highly polar solvents, extended exposure to formamide vapour causes complete dissolution of the complex. This makes microanalytical and crystallographic studies especially difficult to conduct.

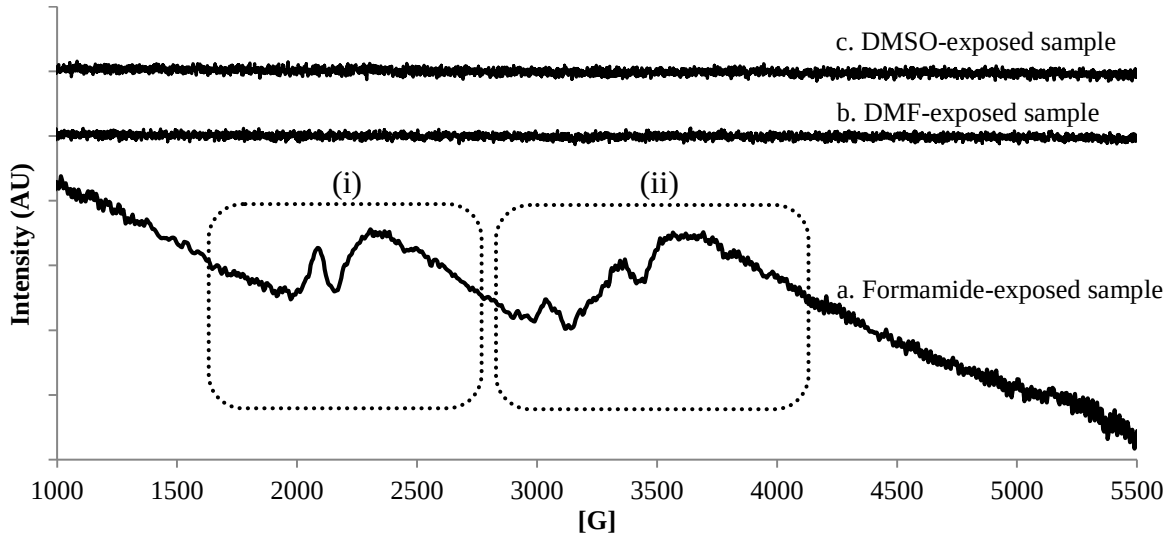

Figure 5.31: EPR spectra of {Fe(μ-pyzNO-κ*N*,κ*O*)$_{n-1}$(pyzNO-κ*N*)$_2$(pyzNO-κ*O*)$_2$}$_n$(ClO$_4$)$_{2n}$ (Complex2) exposed to (a) formamide vapour, (b) DMF vapour, and (c) DMSO vapour. The two major resonances are centered at (i) ~ 2250 G (green box) and (ii) ~ 3450 G (blue box) for Complex2-formamide.

5.4 Comparative Solvent Studies with $Fe(pyzNO)_6(ClO_4)_4 \cdot 3EtOH$ (Complex3): DSC, TGA and FT-IR EGA

Complex3 showed no uptake of cyclohexane, exhibiting only the gradual desorption of solvate EtOH at 30 - 95 ºC (DSC in Fig. 5.32 (i)), as seen in the original untreated material. TG (Fig. 5.32 (ii)) shows an associated weight loss of 5.1 % in this temperature range, corresponding to the loss of 1 EtOH per formula unit (theoretical: 4.75 %). The solvent is not detected by EGA (Fig. 5.32 (iii)) in the TG exhaust stream due the slow rate of gas evolution.

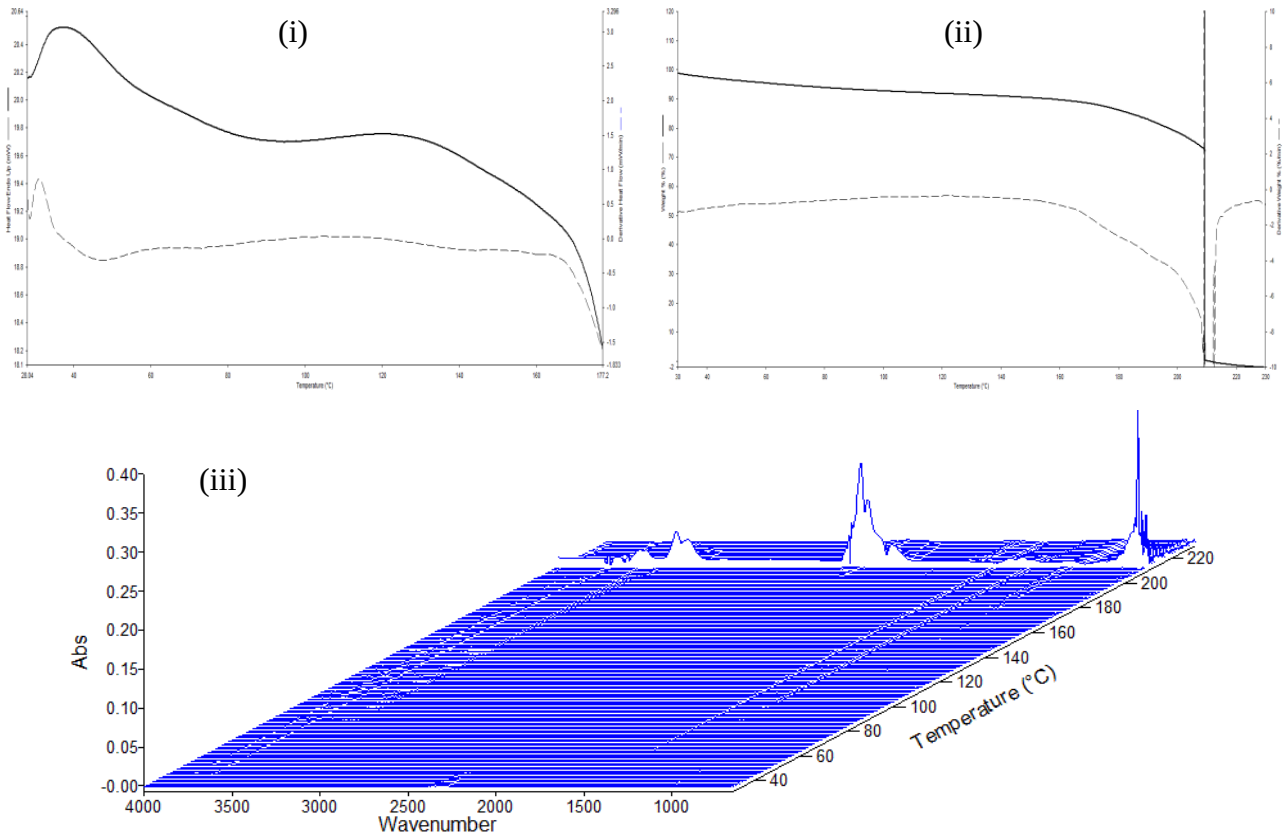

Figure 5.32: The (i) DSC (30 – 180 ºC), (ii) TG thermogram (30 – 200 ºC), and (iii) EGA stack plot of $Fe(pyzNO)_6(ClO_4)_2 \cdot 3EtOH$ exposed to cyclohexane vapour.

Complex3 showed similar behaviour with diethyl ether exposure as in the cyclohexane trial, indicating no significant solvent uptake. Only the gradual loss of solvate ethanol is seen in the 30 – 95 ºC range. Again TG shows the loss of one EtOH per formula unit in this range, with an associated weight decline of 4.9 %; with EGA failing to detect the exceedingly low vapour concentration in the TG purge stream.

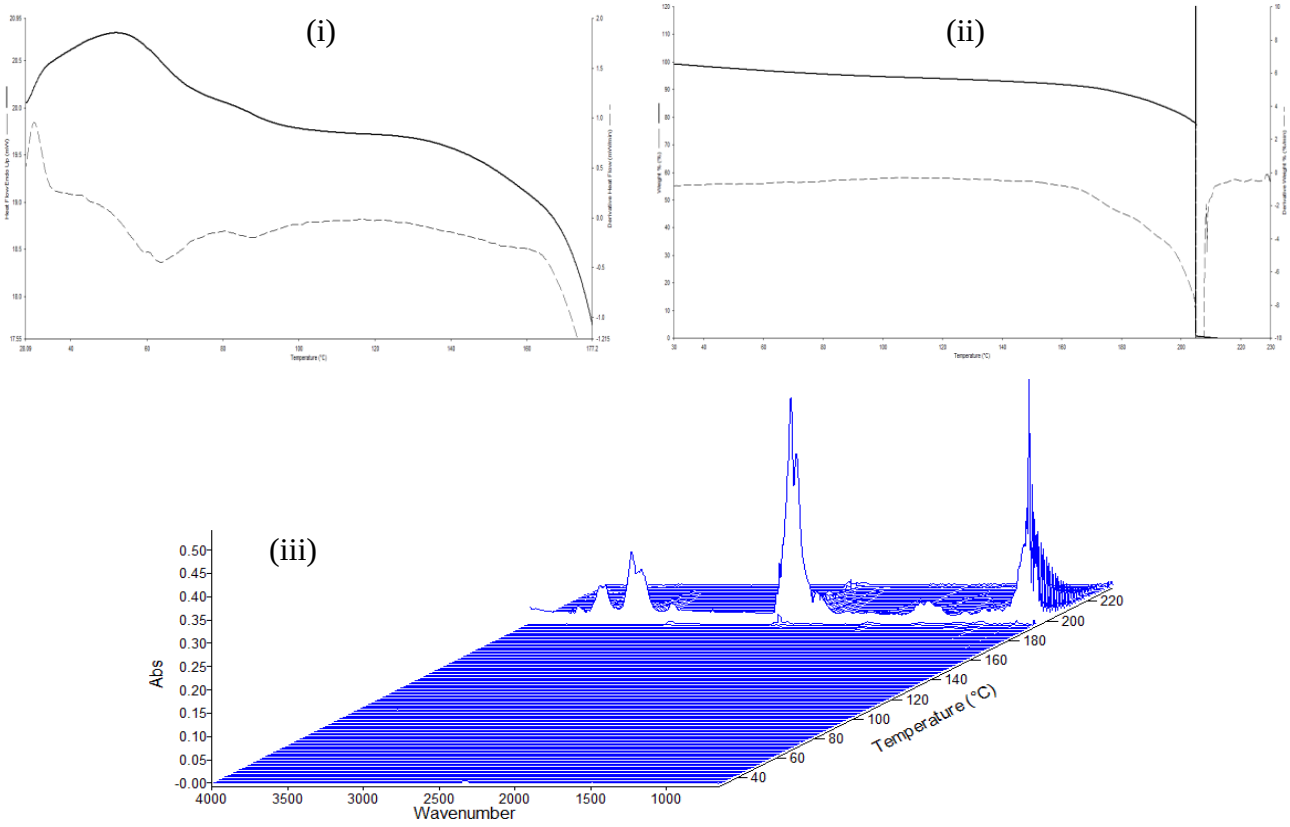

Figure 5.33: The (i) DSC (30 – 180 ºC), (ii) TG thermogram (30 – 200 ºC), and (iii) EGA stack plot of $Fe(pyzNO)_6(ClO_4)_2{\cdot}3EtOH$ exposed to diethyl ether vapour.

The Complex3-THF trial showed similar DSC (Fig. 5.34 (i)) and TG (Fig. 5.34 (ii)) characteristics as the cyclohexane and diethyl ether experiments. The 5.2 % TG weight decline before 95 ºC is ascribed to the loss of 1 solvate EtOH unit. EGA (Fig. 5.34 (iii)) does show some subtle activity, which may be due to some trace detection of the evolved fraction.

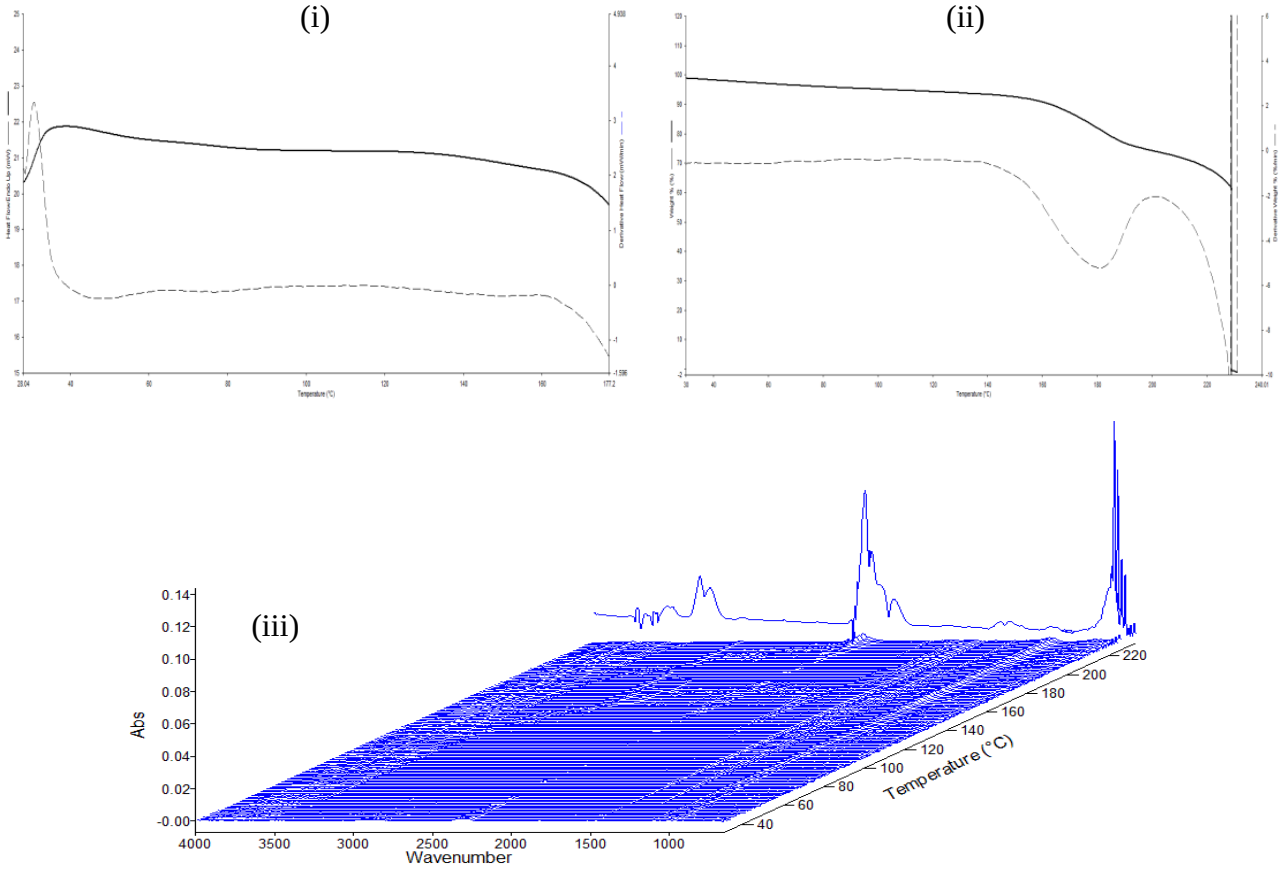

Figure 5.34: The (i) DSC (30 – 180 °C), (ii) TG thermogram (30 – 200 °C), and (iii) EGA stack plot of $Fe(pyzNO)_6(ClO_4)_2 \cdot 3EtOH$ exposed to THF vapour.

Fig. 5.35 (i) indicates a strong solvent-complex interaction with chloroform. The DSC thermogram shows two major mass loss events (37 – 86 °C and 88 – 150 °C) due to the volatilisation of physisorbed solvent. The second event occurs in two steps, as corroborated by TG (88 – 119 °C and 125 – 150 °C) in Fig. 5.35 (ii). The first event coincides with the loss of 1 ethanol solvate moiety. TG shows a 21.0 % weight loss in this step, corresponding to the loss of 2 $CHCl_3$ molecules and 1 solvate ethanol unit (theoretical: 21.27 %).

In Fig. 5.35 (iii), the characteristic medium strong ν(CH) and very strong, broad ν(C-Cl) bands of chloroform were expected at ca. 3000 and 735 cm^{-1}, respectively [15]. However, the very large temperature range of gradual desorption likely produces concentrations in the TG exhaust that are below the FT-IR spectrometer's lower detection limit.

TG shows a 4.51 % weight loss at 88 – 119 °C, and a further 4.5 % weight loss at 125 – 155 °C. Each range has an associated loss of 0.5 chloroform molecules per formula unit (theoretical: 4.46 %), after which explosive decomposition of the complex occurs at 200 °C.

Table 5.12: Summary of thermoanalytical profile of Complex3-chloroform

Event number	Event	ΔTemp. (range/^{o}C)	Moles of $CHCl_3$/Fe	ΔH ($J.g^{-1}$)
(1)	$CHCl_3$ loss	37 – 86	2	38.0
(2) + (3)	$CHCl_3$ loss	88 – 119; 125 – 150	0.5; 0.5	83.1

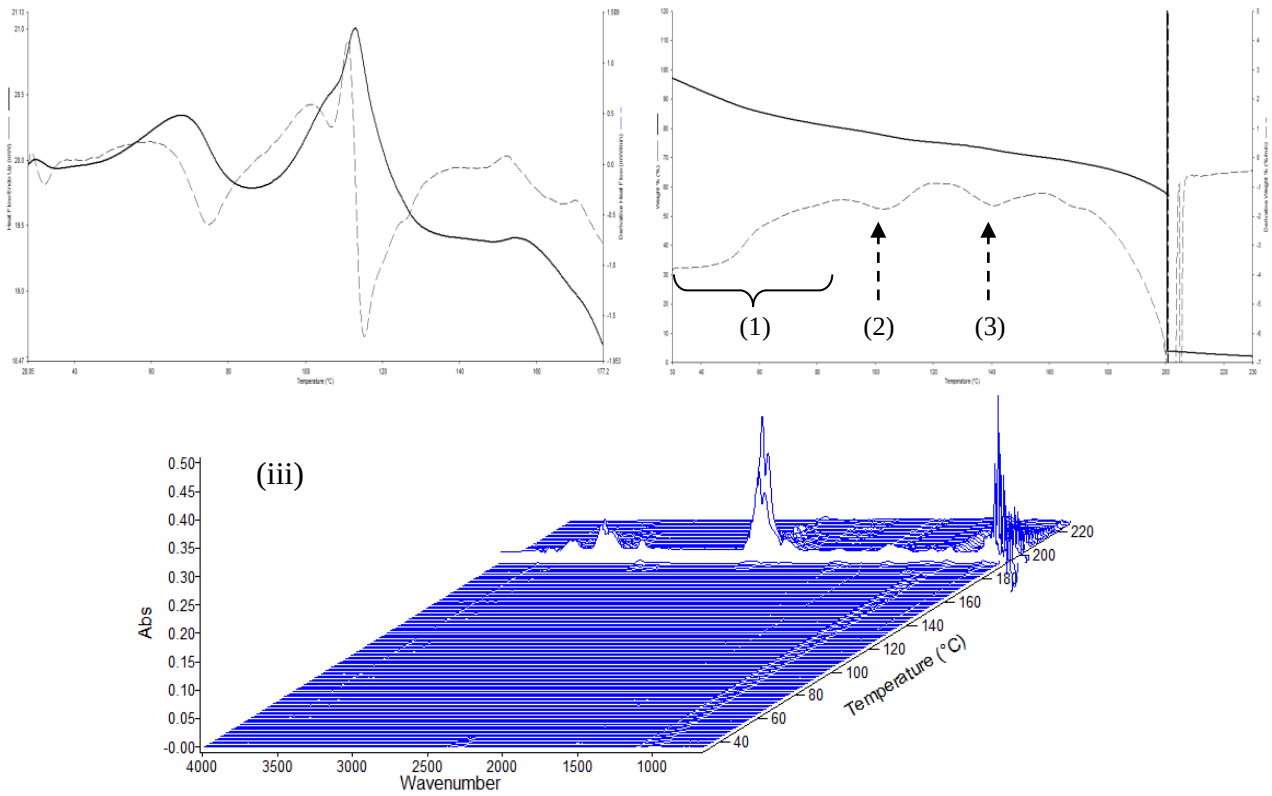

Figure 5.35: The (i) DSC (30 – 180 ^{o}C), (ii) TG thermogram (30 – 200 ^{o}C), and (iii) EGA stack plot of $Fe(pyzNO)_6(ClO_4)_2{\cdot}3EtOH$ exposed to chloroform vapour.

Complex3 shows significant uptake of *p*-dioxane, as evidenced by the multi-stage endothermic loss of bound solvent in Fig's. 5.36 (i) and (ii). A 4.1 % weight loss is seen on the TG before heating commenced as seen with Complex2-*p*-dioxane.

The major DSC endotherms occur at (1) 30 – 48 ^{o}C, (2) 53 – 76 ^{o}C and (3) 77 – 117 ^{o}C, following a series of three small endotherms at (4) 118 – 142 ^{o}C. TG was unable to resolve the stage (3) and (4) into individual mass loss steps, but instead shows one continuous mass loss event (3 + 4).

As stage (1) and (2) both overlap with the characteristic loss of one ethanol solvate at 30 – ca. 80 ^{o}C, the mass loss due to *p*-dioxane in each stage could not be calculated. The number of molecules lost at these individual stages (per formula unit) have thus been combined. TG

weight losses of 5.4 and 7.8 % (total: 13.2 %) were recorded in stages (1) and (2), due to the loss of 1.5 *p*-dioxane molecules and 1 EtOH solvate per formula unit (theoretical: 13.34 %). TG then shows a 6.1 % weight loss at stage (3) due to the loss of 1 *p*-dioxane molecule (theoretical: 6.51 %), followed by a 3.4 % weight loss due to the loss of further 0.5 *p*-dioxanes per Fe centre (theoretical: 3.26 %).

EGA in Fig. 5.36 (iii) shows the detection of *p*-dioxane at 30 – 160 ^{o}C (ν(CH): 3000 – 2800 cm^{-1}; ν(CO): 1170 and 960 cm^{-1}).

The 14.6 % TG weight loss seen at 160 – 211 ^{o}C is ascribed to the thermolysis of 2 PyzNOs per Fe centre (theoretical: 14.37 %) based on EGA (CO_2 ν(C=O): ~2500 cm^{-1}).

Table 5.13: Summary of thermoanalytical profile of Complex3-*p*-dioxane

Event number	Event	ΔTemp. (range/^{o}C)	Moles of *p*-dioxane/Fe	Δ*H* (J.g^{-1})
(1) + (2)	*p*-dioxane loss	30 – 48; 53 – 76	1.5	11.3
(3) + (4)	*p*-dioxane loss	77 – 117; 118 – 142	1; 0.5	49.4; 7.3

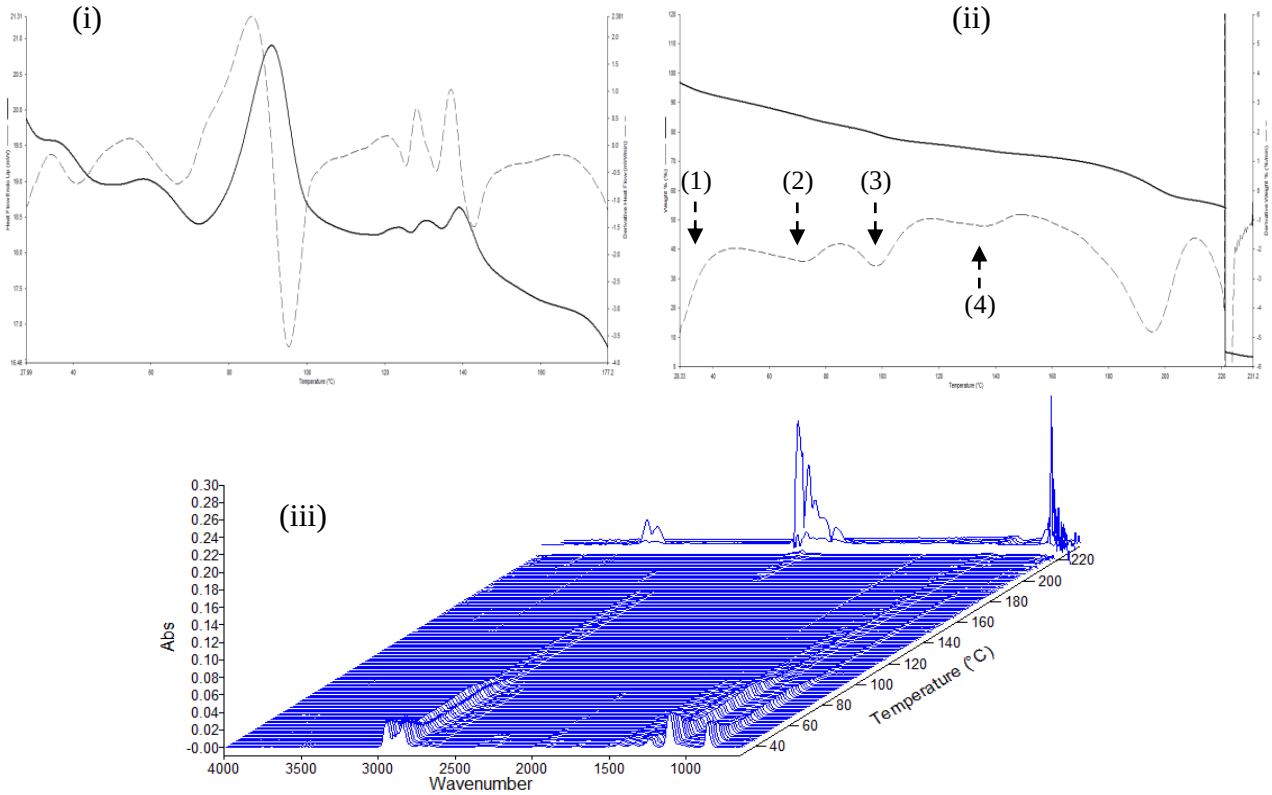

Figure 5.36: The (i) DSC (30 – 180 ^{o}C), (ii) TG thermogram (30 – 200 ^{o}C), and (iii) EGA stack plot of $Fe(pyzNO)_6(ClO_4)_2{\cdot}3EtOH$ exposed to *p*-dioxane vapour.

The DSC profile of Complex3-acetone could not be recorded. The sample was found to strongly adhere to any surface it contacted, making the transfer to the DSC analytical pan unfeasible without significant atmospheric exposure.

TG (Fig. 5.37 (i)) shows the substantial adhesion of the solvent to Complex3. A two-stage loss of adsorbed solvent is seen, which occurs at (1) 28 – 39 °C and (2) 90 – 135 °C, as corroborated by EGA in Fig. 5.37 (ii). Stage (1) involves a weight decrease of 34.1 % due to the loss of 10* acetone molecules per Fe centre (theoretical: 34.45 %). EGA shows the strong detection of acetone, with intense corresponding ν_a(CH), ν_s(CH), ν(C=O), $\delta_a(CH_3)$ and $\delta_s(CH_3)$ bands at 3500, 3000, 1739, 1451 and 1253 cm^{-1}, respectively [15]. Stage (2) sees an 8.4 % weight decrease due to the loss of 2.5 acetone molecules per formula unit (theoretical: 8.61 %), while EGA shows a corresponding increase in the intensity of the acetone bands.

The 7.0 % TG weight loss seen at 154 – 210 °C is ascribed to the decomposition of 1.25 PyzNOs per formula unit, as evidenced by the EGA detection of CO_2 (ν(C=O): ~2500 cm^{-1}).

Table 5.14: Summary of thermoanalytical profile of Complex3-acetone

Event number	Event	ΔTemp. (range/°C)	Moles of acetone /Fe	ΔH ($J.g^{-1}$)
(1)	Acetone loss	28 – 39	10	–
(2)	Acetone loss	90 – 135	2.5	–

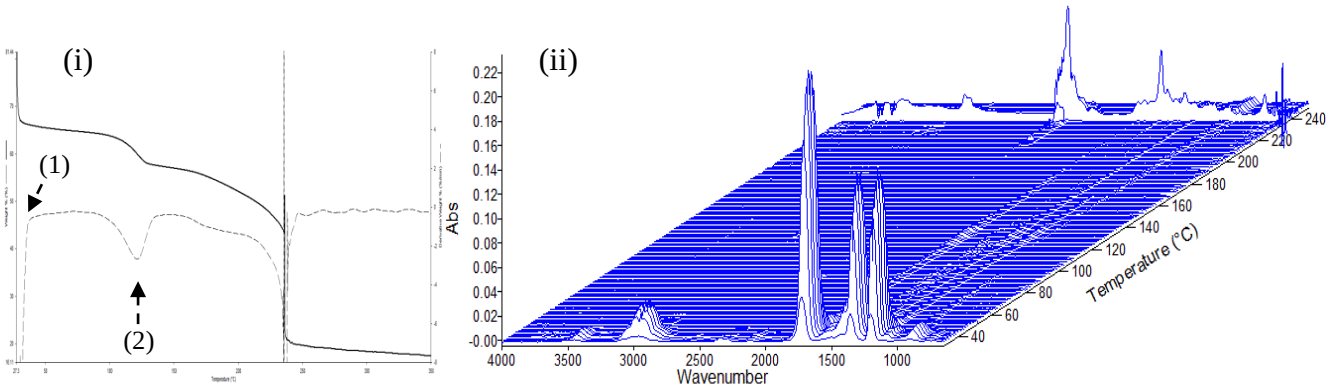

Figure 5.37: (i) The TG thermogram (30 – 200 °C), and (ii) EGA stack plot of $Fe(pyzNO)_6(ClO_4)_2 \cdot 3EtOH$ exposed to acetone vapour.

* The characteristic loss of the one ethanol solvate is centred at ca. 50 °C, so it is thought that its contribution to the mass loss at stage (1) can be largely ignored; though it is conceded that perhaps slightly fewer than 10 acetone molecules are lost in this stage.

Complex3 shows significant uptake of methanol. A two-stage endothermic loss of physisorbed solvent is observed in Fig. 5.38 (i) at (1) 69 – 102 ^{o}C and (2) 109 – 140 ^{o}C, while EGA indicates a 'third' (initial) stage at 30 – 45 ^{o}C. This first stage is due to the evaporation of methanol condensed on the surface of Complex3 (EGA: *v*(CH) and δ(C-OH) at 3000 and 1000 cm^{-1}, respectively [16]). The associated endotherm is suppressed by scaling (especially by the first derivative curve) due to the large endotherm at stage (1) on the DSC thermogram.

The resolution of stage (1) and (2) is not clear on the TG in Fig. 5.38 (ii). A combined weight loss of 15.6 % is recorded at 30 – 140 ^{o}C due the loss of 4 methanol molecules and 1 ethanol solvate per formula unit (theoretical: 15.15 %).

Table 5.15: Summary of thermoanalytical profile of Complex3-methanol

Event number	Event	ΔTemp. (range/^{o}C)	Moles of MeOH/Fe	Δ*H* (J.g^{-1})
(1)	MeOH loss	69 – 102	4 [(1) & (2) comb.]	140.3
(2)	MeOH loss	109 – 140	–	20.4

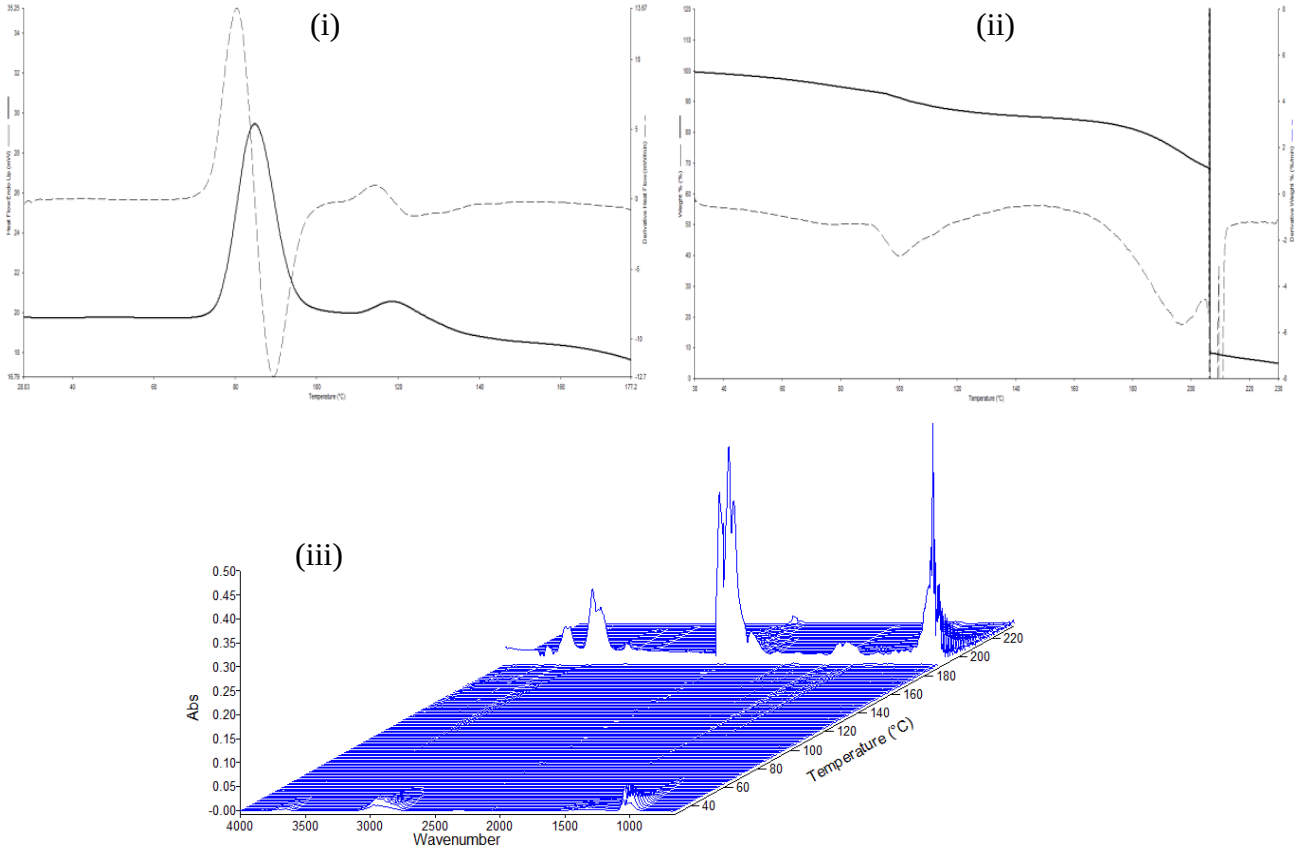

Figure 5.38: The (i) DSC (30 – 180 ^{o}C), (ii) TG thermogram (30 – 200 ^{o}C), and (iii) EGA stack plot of $Fe(pyzNO)_6(ClO_4)_2{\cdot}3EtOH$ exposed to methanol vapour.

The DSC, TGA and EGA results for the Complex3-ethanol trial in Fig. 5.39 (i) – (iii) are consistent with the loss of solvent condensate at (1) 30 – 50 °C, in which TG shows a 12.7 % weight loss (3 EtOHs per Fe centre; theoretical: 12.45 %). EGA shows strong ethanol detection (30 – 60 °C; *ν*(CH), δ(CH_3) and *ν*(C-OH) at 3100 – 2900 cm^{-1}, 1500 – 1400 cm^{-1} and 1100 – 1000 cm^{-1}, respectively [15]). The associated DSC endotherm persists until (2) 95 °C due to the continued loss of the 1 solvate ethanol per formula unit, in the usual way. The massless two-part DSC endotherm that follows at 97 – 141 °C indicates a phase change in this range.

No further activity is seen until thermal decomposition of the complex at 190 °C.

Table 5.16: Summary of thermoanalytical profile of Complex3-ethanol

Event number	Event	ΔTemp. (range/°C)	Moles of EtOH/Fe	Δ*H* ($J.g^{-1}$)
(1) & (2)	EtOH loss	30 – 95	4 [(1) & (2) comb.]	93.0
(3)	Phase change	97 – 141	–	99.2

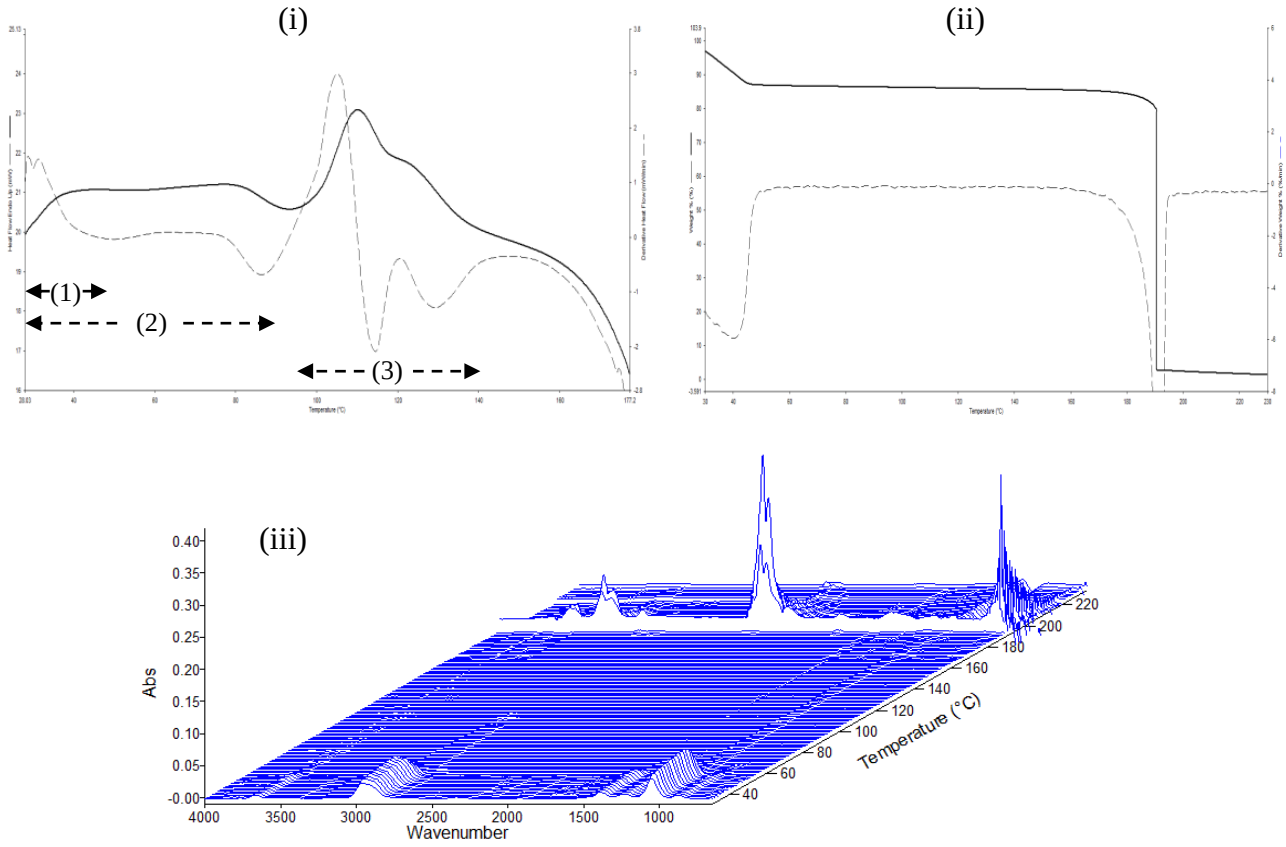

Figure 5.39: The (i) DSC (30 – 180 °C), (ii) TG thermogram (30 – 200 °C), and (iii) EGA stack plot of $Fe(pyzNO)_6(ClO_4)_2{\cdot}3EtOH$ exposed to ethanol vapour.

Complex3 shows the strong uptake of formaldehyde. The DSC endotherm at (1) 30 – 38 ^{o}C (Fig. 5.40 (i)) is due to the loss of surface formaldehyde (H_2CO) condensate (2 per Fe centre; theoretical: 4.58 %), based on the 4.6 % weight loss seen on the TG (Fig. 5.40 (ii)) and EGA (Fig. 5.40 (iii)). One major endotherm is seen at (2) 40 – 125 ^{o}C, which comprises four overlapping *sub-endotherms*. Stage (2) shows a weight decrease of 23.9 % due to the loss of 9 H_2COs per Fe centre, and the usual 1 solvate ethanol moiety (theoretical: 24.15 %). EGA shows the expected detection of H_2CO at 30 – 125 ^{o}C (ν(CH): 3130 – 2610 cm^{-1}; ν(C=O): ~1700 cm^{-1}; δ(HCH): ~1000 cm^{-1} [15]).

The final endothermic 18.5 % mass loss at 158 – 200 ^{o}C is due to the decomposition of 2.5 PyzNOs per formula unit (theoretical: 18.34 %), as evidenced by the EGA detection of CO_2 (ν(C=O): ~2500 cm^{-1}) at this range, followed by the explosive decomposition of the complex.

Table 5.17: Summary of thermoanalytical profile of Complex3-formaldehyde

Event number	Event	ΔTemp. (range/^{o}C)	Moles of H_2CO/Fe	ΔH (J.g^{-1})
(1)	H_2CO loss	30 – 38	2	–
(2)	H_2CO loss	40 – 125	9	167.0

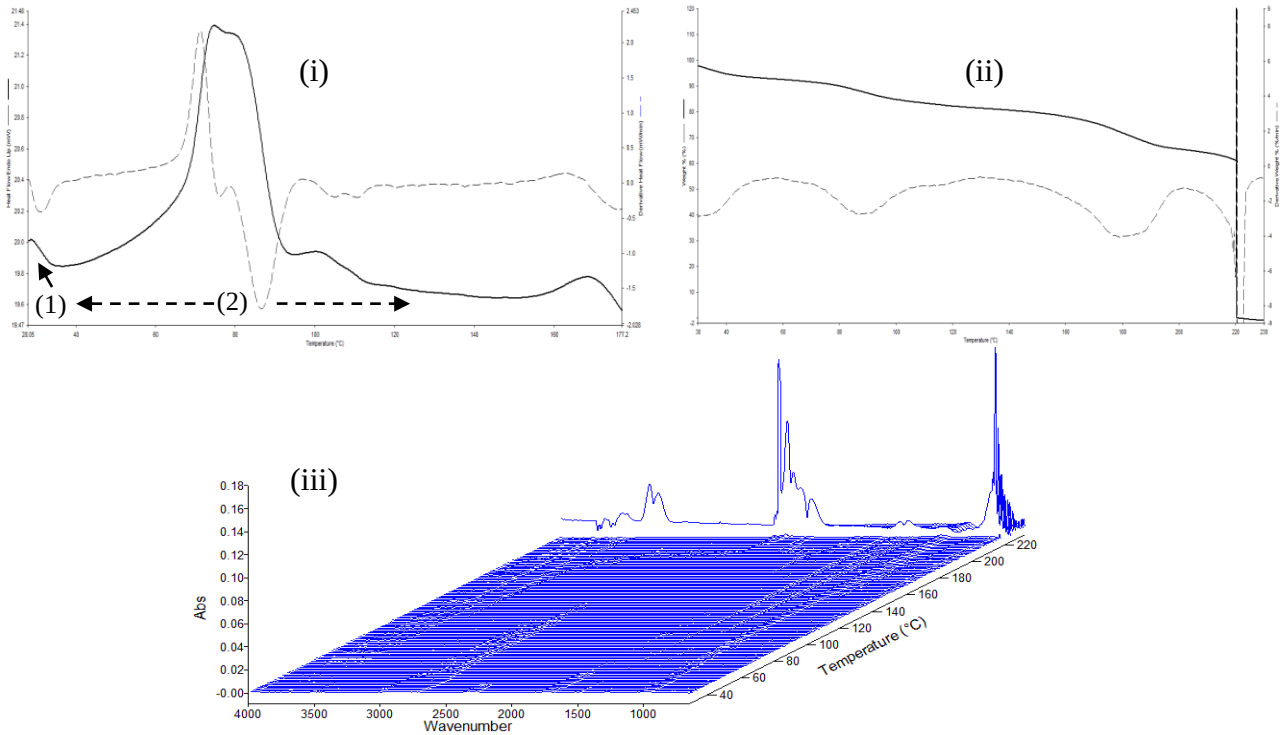

Figure 5.40: The (i) DSC (30 – 180 ^{o}C), (ii) TG thermogram (30 – 200 ^{o}C), and (iii) EGA stack plot of $Fe(pyzNO)_6(ClO_4)_2{\cdot}3EtOH$ exposed to formaldehyde vapour.

As with Complex5, the DSC (Fig. 5.41 (i)) and TG (Fig. 5.41 (ii)) thermograms of Complex3-water did not correspond in the usual way, despite numerous repeat analyses. DSC shows two overlapping endotherms. The first is due to the loss of solvate ethanol (30 – 95 ^{o}C, based on the DSC of the untreated material), and the second is due to the loss of solvate water (ca. 60 – 97 ^{o}C) possibly in two steps. In contrast, TG shows four distinct mass loss events, three of which ((2) – (4)) occur in the 100 – 180 ^{o}C range in which DSC shows no measureable ΔH. The mass losses are however suspected to be due to sublimation of free PyzNO, displaced by water; but EGA (Fig. 5.41 (iii)) is inconclusive. This argument agrees with the 5.2 % weight loss seen in the TG of pure PyzNO (see Appendix Fig. 1.1) at 30 – 110 ^{o}C due to sublimation, while DSC showed only the melting point endotherm with T_{onset} at 111 ^{o}C (Fig. 3.1).

Stage (1) showed a TG recorded weight decrease of 7.7 % which is ascribed to the loss of 2 physisorbed waters and 1 solvate ethanol per formula unit (theoretical: 8.17 %).

Though tentatively, the 4.8 %, 9.1 % and 7.0 % weight losses recorded at stages (2), (3) and (4) have been correspondingly assigned to the sublimation of 0.5, 1 and 0.75 PyzNOs per formula unit (theoretical: 4.78 %, 9.56 % and 7.18 %, respectively).

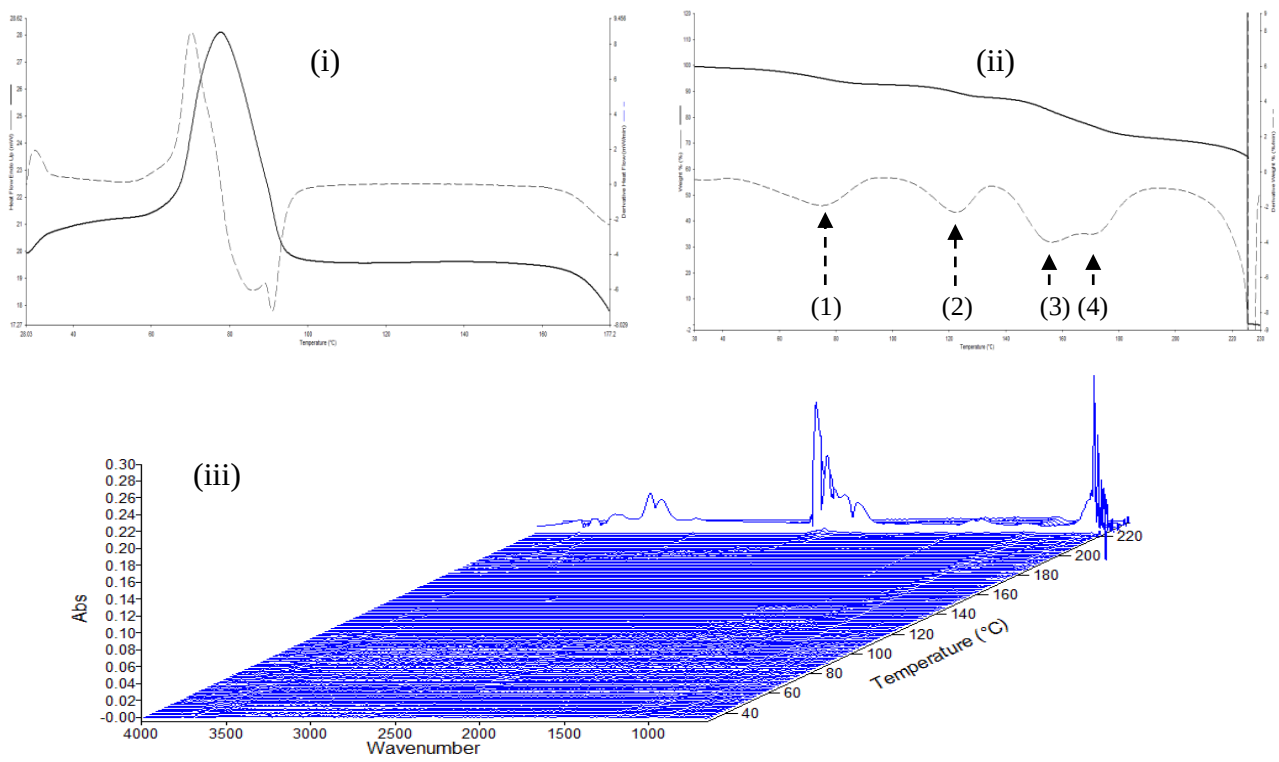

Figure 5.41: The (i) DSC (30 – 180 ^{o}C), (ii) TG thermogram (30 – 200 ^{o}C), and (iii) EGA stack plot of $Fe(pyzNO)_6(ClO_4)_2{\cdot}3EtOH$ exposed to water vapour.

5.5 Comparative Solvent Studies with $Fe_2(bipyNO)_5(ClO_4)_4 \cdot 6MeOH$: DSC, TGA, FT-IR EGA and XRPD

Complex4 shows no significant solvent uptake with cyclohexane, diethyl ether, THF and chloroform exposure (Fig. 5.42). This is evidenced by the near identical nature of the associated DSC thermograms with that of the original material*. Some degree of weak surface adhesion is suspected with cyclohexane, THF and chloroform, as small endotherms are seen which begin before the initiation of the respective heating profile (~28 ^{o}C). These rapidly return to the baseline before 33 ^{o}C in all three cases. The EGA profiles of these samples looked indistinguishable from that of the original untreated material (Fig. 4.38). They have been therefore been omitted to avoid repetitiveness.

Surprisingly, the Complex4-formaldehyde trial also produced results identical to that of the untreated material, thereby indicating no measureable solvent-complex interaction. These results have not been included for brevity.

The TG thermograms show no mass losses other than those described and assigned for the original untreated material (Fig. 4.40), while the XRPD patterns show only peak intensity variations due to the effects of crystallite preferred orientation.

* See Appendix Fig. 2.11 for 30 – 280 ^{o}C DSC thermogram of original untreated material (Complex4).

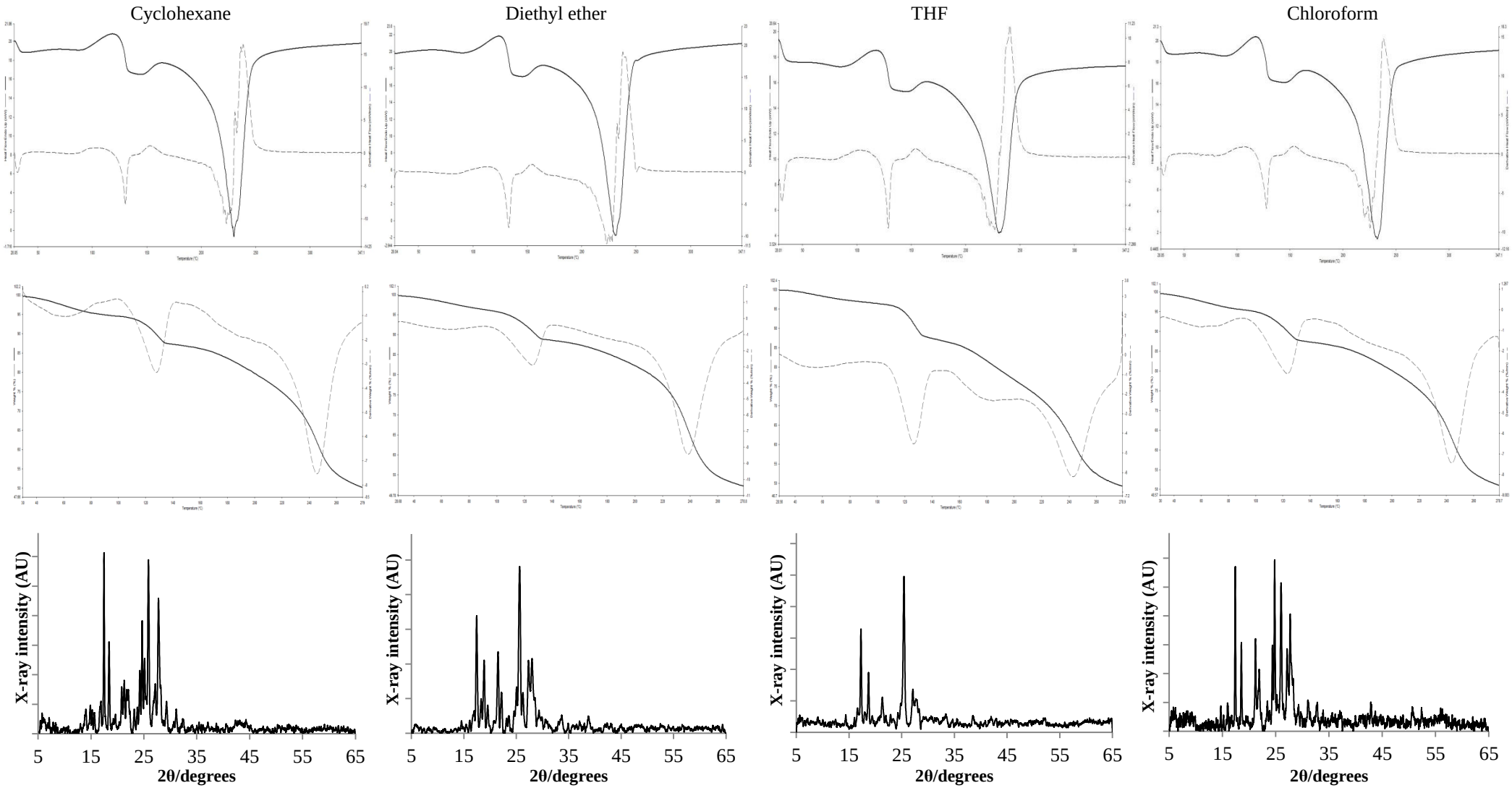

Figure 5.42: The 30 – 350 °C DSCs (top), 30 – 280 °C TGs (middle), and XRPD patterns (bottom) of $Fe_2(bipyNO)_5(ClO_4)_4 \cdot 6MeOH$ after exposure to (from left to right): cyclohexane, diethyl ether, THF and chloroform atmospheres.

DSC analysis of Complex4-*p*-dioxane was unfeasible due to the strong adhesion of the sample to all contacted surfaces, resulting in significant atmospheric exposure.

TG (Fig. 5.43 (i)) shows a 32.2 % weight decrease at (1) 28 – 55 ^{o}C due to the loss of 1.75 methanol solvate moieties and 9.5 *p*-dioxane molecules per formula unit (theoretical: 32.21 %). TG then shows a 10.3 % weight decrease at (2) 55 – 147 ^{o}C due to loss of the final 0.25 MeOH solvates and 3 *p*-dioxanes per Fe centre (theoretical: 9.81 %), after which the thermogram is as for the untreated material (Fig. 5.43 (ii)).

EGA (Fig. 5.43 (ii)) shows the two-step loss of *p*-dioxane at stages (1) and (2), as described above (ν(CH): 3000 – 2800 cm^{-1}; ν_a(CO): 1170 cm^{-1}; ν_s(CO): 960 cm^{-1} [15])

The partial dissolution of Complex4 with loss of crystallinity in a *p*-dioxane atmosphere is indicated by the XRPD in Fig 5.43 (iii).

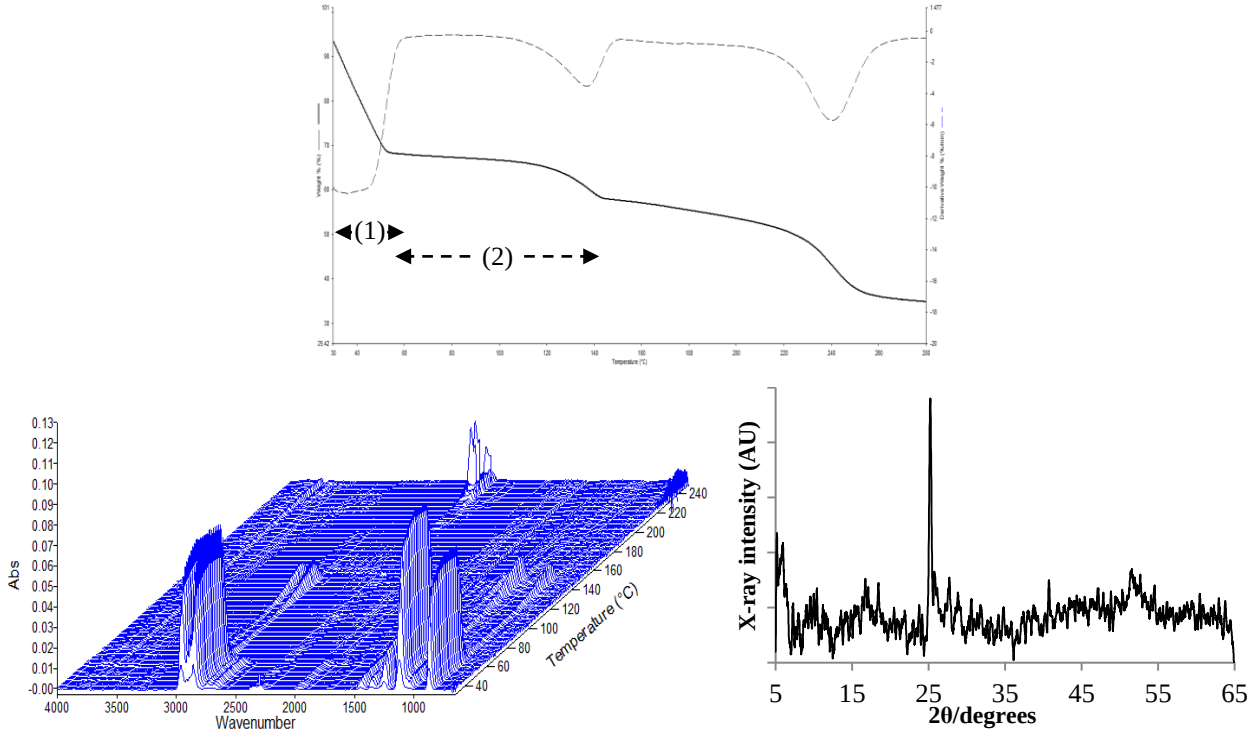

Figure 5.43: The (i) 30 – 280 ^{o}C TG thermogram, (ii) EGA stack plot, (iii) XRPD pattern of $Fe_2(bipyNO)_5(ClO_4)_4$·6MeOH exposed to *p*-dioxane vapour.

DSC analysis of Complex4-acetone was also unable to be conducted as the sample behaved as Complex4-*p*-dioxane on attempts at sample transfer.

TG (Fig. 5.44 (i)) shows a 26.3 % weight decrease at (1) 28 – 32 ^{o}C due to the loss of 10.75 acetone molecules per formula unit (theoretical: 26.34 %). TG then shows weight

decreases of 2.6 % at (2) 32 – 95 ºC and 6.9 % at (3) 95 – 146 ºC due to the consecutive losses of 2 MeOH solvates and 3 acetones per Fe centre (theoretical: 2.70 and 7.35 %), after which the thermogram is as for the untreated material (Fig. 5.43 (ii)).

EGA (Fig. 5.44 (ii)) shows the two-step loss of acetone at stages (1) and (3), as described above (ν_a(CH), ν_s(CH), ν(C=O), δ_a(CH_3) and δ_s(CH_3) at: 3500, 3000, 1738, 1450 and 1250 cm^{-1}, correspondingly [15])

The crystal characteristics of Complex4 appear largely unaffected by acetone exposure, as indicated by the XRPD in Fig 5.44 (iii).

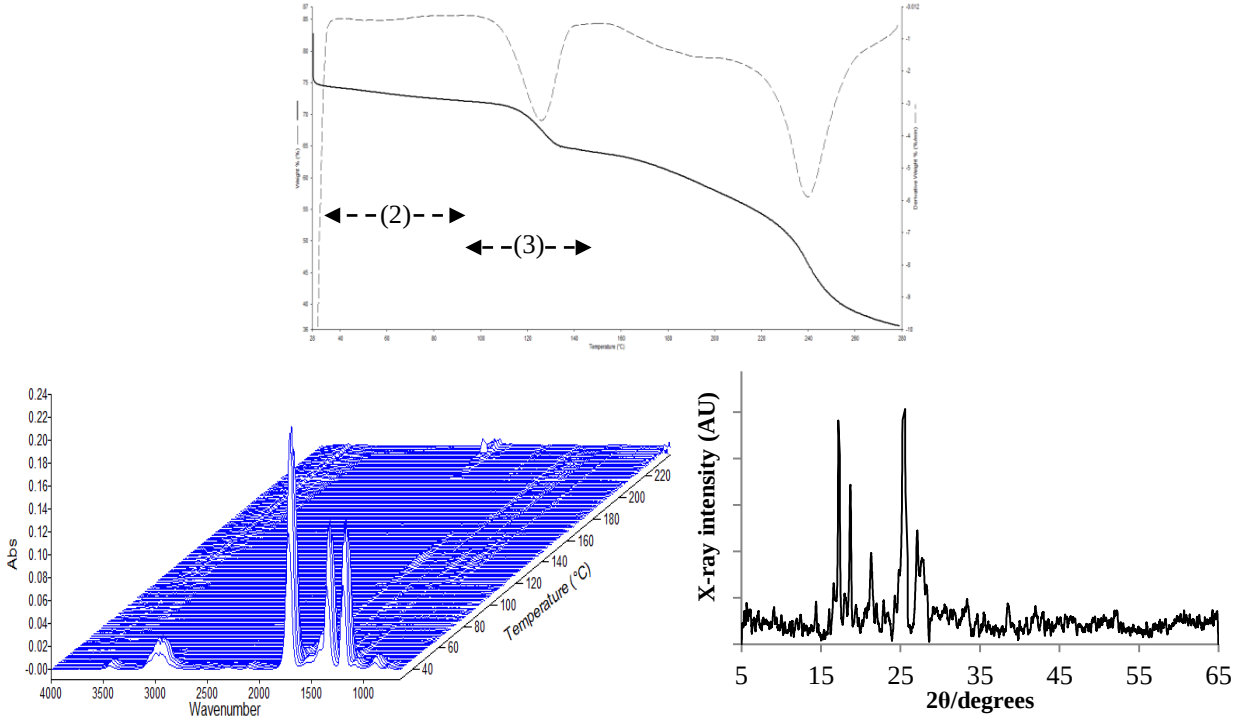

Figure 5.44: The (i) 30 – 280 ºC TG thermogram, (ii) EGA stack plot, (iii) XRPD pattern of $Fe_2(bipyNO)_5(ClO_4)_4 \cdot 6MeOH$ exposed to acetone vapour.

Fig. 5.45 (i), (ii) and (iii) indicate only weak surface adsorption (condensation) of methanol on Complex4, while Fig. 5.45 (iv) shows no crystallographic change on solvent exposure. This result is unsurprising given the two lattice methanols already in the stable formula unit of the original material.

TG (Fig. 5.45 (i)) shows a 6.0 % weight decrease at 28 – 40 ºC due to the loss of the equivalent of 3 methanol molecules per formula unit (theoretical: 5.78 %). The remainder of the thermogram is as for the original untreated material. EGA shows the intense methanol

bands (*v*(OH), *v*(CH), *v*(CO), δ(COH): 3750, 3000, 1450 and 1000 cm^{-1}, respectively [15])) due the high concentration of solvent vapour resulting from rapid evaporation.

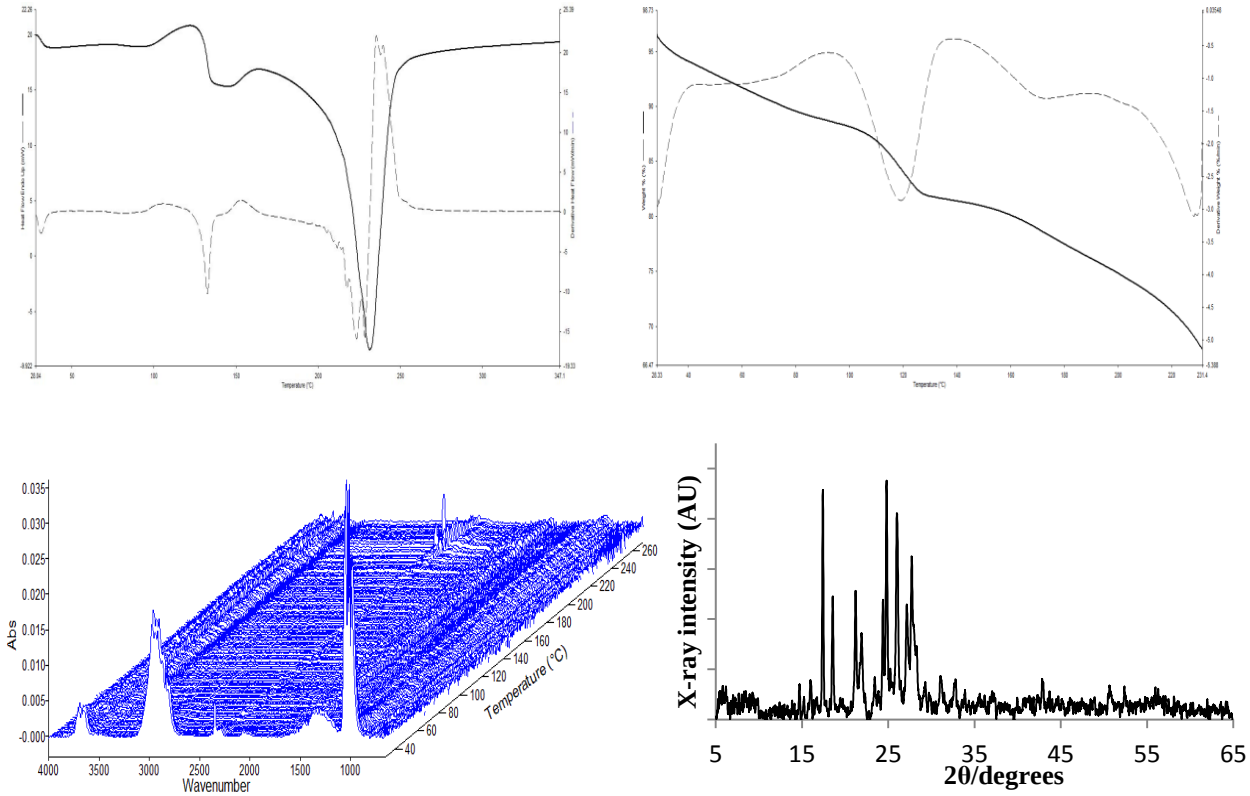

Figure 5.45: The (i) DSC (30 – 350 ºC), (ii) TG thermogram (30 – 280 ºC, (iii) EGA stack plot, (iv) XRPD pattern of $Fe_2(bipyNO)_5(ClO_4)_4{\cdot}6MeOH$ exposed to methanol vapour.

As with Complex4-methanol, Fig. 5.46 (i) – (iii) also indicate only weak surface condensation of ethanol on Complex4, with Fig. 5.46 (iv) showing no crystallographic change as a consequence.

TG (Fig. 5.46 (i)) shows only a 1.0 % weight decrease at 28 – 41 ºC due to the loss of the equivalent of 0.33 ethanol molecules per formula unit (theoretical: 0.97 %). The remainder of the thermogram is as for the original untreated material. EGA shows the ethanol bands (*v*(CH), *v*(CO), δ(COH): 3000, 1400 and 1100 cm^{-1}, respectively [15]) at 30 – 35 ºC.

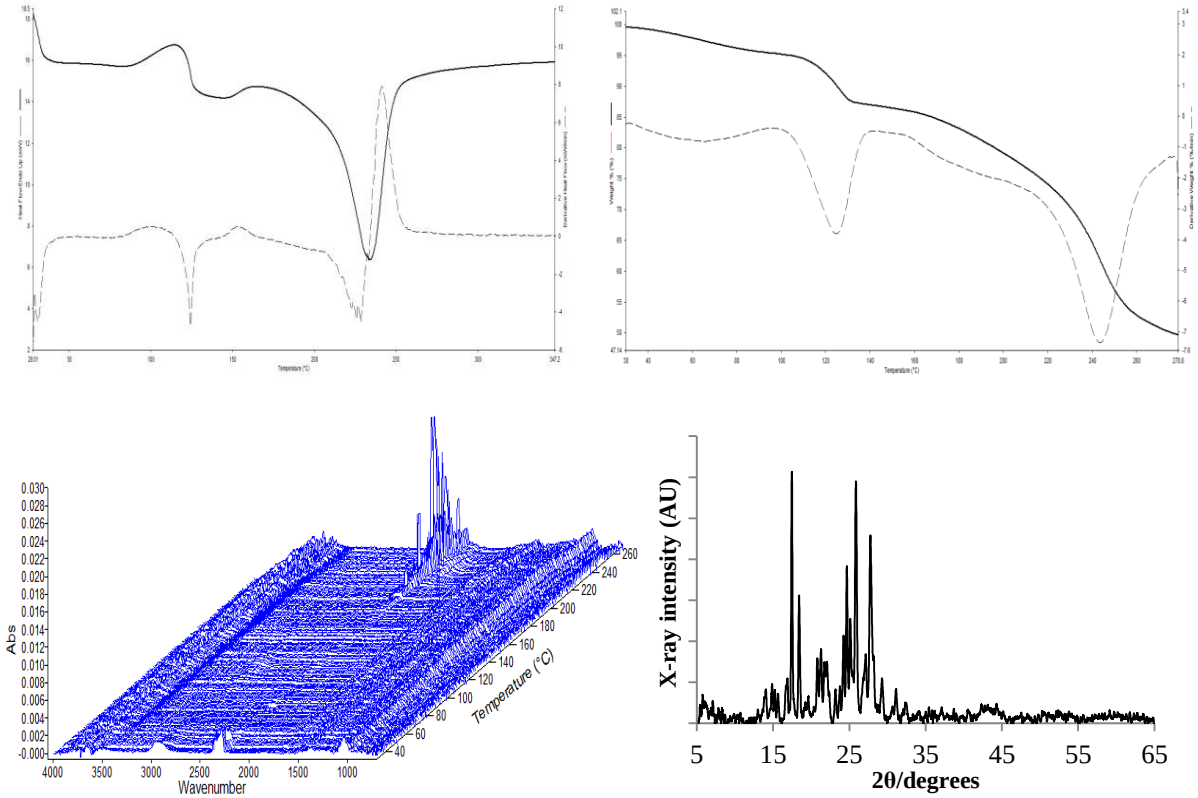

Figure 5.46: The (i) DSC (30 – 350 ºC), (ii) TG thermogram (30 – 280 ºC, (iii) EGA stack plot, (iv) XRPD pattern of $Fe_2(bipyNO)_5(ClO_4)_4 \cdot 6MeOH$ exposed to ethanol vapour.

Complex4 shows the strong uptake of acetaldehyde (MeCHO). EGA Fig 5.47 (iii) indicates a two-stage loss of adsorbed solvent at (1) 30 – 96 ºC and (2) 100 – 140 ºC, with DSC showing intense endotherms in these ranges. Stage (1) sees a 16.8 % TG weight decrease due to the loss of 6 MeCHO molecules and the 2 MeOH solvates per formula unit (theoretical: 16.97 %). Approximately 4.75 of these are lost at 30 – 60 ºC, as indicated by the corresponding 13.7 % TG weight loss (theoretical: 13.71 %). A further 9.2 % weight decrease is seen at stage (2) due to the loss of 3.5 coordinated MeOHs and 1.5 MeCHOs per formula unit (theoretical: 9.21 %) EGA shows the concurrent loss of MeCHO (ν(CH): 3000 – 2770 cm^{-1}; coupled $\delta(CH_3)/\delta(HC=O)$: 1750 and 1000 cm^{-1}) and MeOH (ν(CH): 4000 – 3500 cm^{-1}; ν(CH): 3000 cm^{-1}; ν(CH): 1500 cm^{-1}; δ(C-OH): 1000 cm^{-1}).

The partial dissolution of Complex4 with significant loss of crystallinity upon MeCHO exposure is indicated by the XRPD in Fig 5.47 (iv).

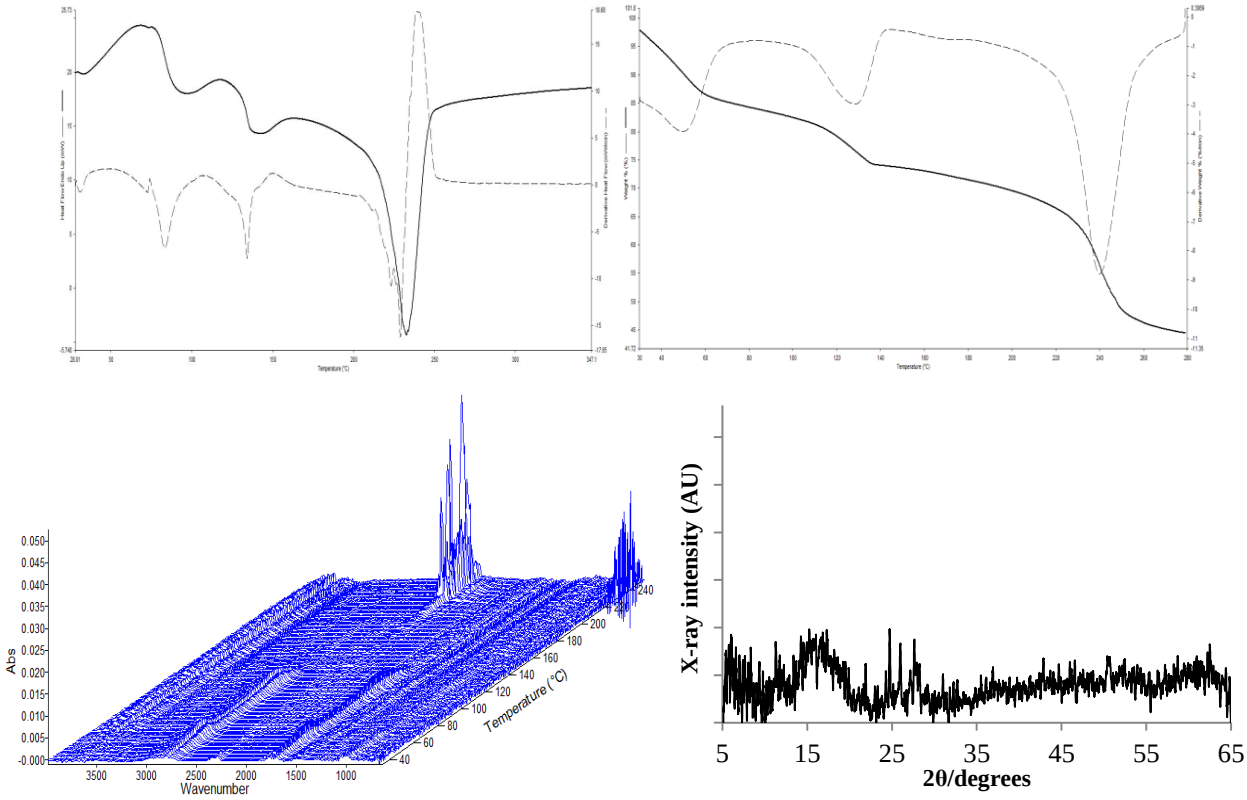

Figure 5.47: The (i) DSC (30 – 350 ºC), (ii) TG thermogram (30 – 280 ºC, (iii) EGA stack plot, (iv) XRPD pattern of $Fe_2(bipyNO)_5(ClO_4)_4 \cdot 6MeOH$ exposed to acetaldehyde vapour.

References

[1] **Watkins, G.M.** (1988) *Ligand Isotope Vibrational Studies of Metal(II) Complexes*. Doctoral thesis. Cape Town: University of Cape Town.

[2] **Twigg, M. V.** Kinetics and thermodynamics of solvolysis of tris(2,2'-bipyridine)iron(II) perchlorate in dimethyl sulfoxide. *Trans. Met. Chem*. **18** (1993), 175-176.

[3] **Nakamoto, K**. *Infrared and Raman Spectra of Inorganic and coordination compounds*. 6th ed. John Wiley and Sons, Inc., New Jersey, USA (2009).

[4] **Thornton, D. A. and Watkins, G. M.** Isotope labelling studies of some aromatic *N*-oxides – Part IV. A full vibrational assignment of the infrared spectra (4000-50 cm^{-1}) of quinoline *N*-oxide dihydrate and its fully deuterated analogue. *Bull. Chim. Soc. Belg*. **100** (1991), 244-245.

[5] **Thornton, D. A. and Watkins, G. M.** An assessment of the assignment of characteristic N-O vibrations in aromatic *N*-oxides. *Spectrosc. Lett*. **25** (1992), 1023-1031.

[6] **Woodward, F.; Gibson, P.J.; Jameson, G.; Landee, C.P.; Turnbull, M.; Willet, R.D**. Two-dimensional Heisenberg antiferromagnets: Syntheses, X-ray structures, and magnetic behavior of $[Cu(pz)_2](ClO_4)_2$, $[Cu(pz)_2](BF_4)_2$, and $[Cu(pz)_2(NO_3)](PF_6)$. *Inorg. Chem.* **46** (2007), 4256-4266.

[7] **Vela, S.; Jornet-Somoza, J.; C.P.; Turnbull, M.M.; Feyerherm, R.; Novoa, J.J.; Deumal, M**. Dividing the spoils: Role of pyrazine ligands and perchlorate counterions in the magnetic properties of bis(pyrazine)diperchloratecopper(II), $[Cu(pz)_2](ClO_4)_2$. *Inorg. Chem.* **52** (2013), 12924-12930.

[8] **Speca, A.N.; Pytlewski, L.L.; Karayannis, N.M**. Transition metal perchlorate complexes with pyrazine-*N*-oxide. *J. Inorg. Nucl. Chem*. **35** (1973), 3113-3125.

[9] **Thornton, D. A. and Watkins, G. M.** The infrared spectra (4000-50 cm^{-1}) of complexes of quinoline *N*-oxide and its perdeuterated analogue with metal(II) perchlorates of the first transition series. *J. Coord. Chem.* **29** (1993), 45-55.

[10] **Leita, B. A.; Moubaraki, B.; Murray, K. S.; Smith, J. K**. Spin-crossover in dimeric hydrogen-bonded iron(II) 2-(pyrazolyl)-pyridine and 2-(imidazolyl)-pyridine complexes. *Polyhedron*. **24** (2004), 2165-2167.

[11] **Georgiou, P.; Walton, J.; Simitzis, J**. Surface modification of pyrolyzed carbon fibres by cyclic voltammetry and their characterization with XPS and dye adsorption. *Electrochim. Acta*. **55** (2010), 1212–1214.

[12] **Hueso, J. L.; Espinós, J. P.; Caballero, A.; Cotrino, J.; González-Elipe, A.R**. XPS investigation of the reaction of carbon with NO, O_2, N_2 and H_2O plasmas. *Carbon*. **45** (2007), 91-94.

[13] **Negro, E.; Monteverde Videla, A. H. A.; Baglio, V.; Aricò, A. S.; Specchia, S.; Kopera, G. J. M**. Fe–N supported on graphitic carbon nano-networks grown from cobalt as oxygen reduction catalysts for low-temperature fuel cells. *Appl. Cat. B: Environmental*, **80** (2015), 166-167.

[14] **Ivanova, T. M.; Kochur, A. G.; Maslakov, K. I.; Kiskin, M. A.; Savilov, S. V.; Lunin, V. V.; Novotortsev, V. M.; Eremenko, I. L**. XPS study of the electron structure of heterometallic trinuclear complexes $Fe_2M(\mu_3\text{-}O)(\mu\text{-}Piv)_6(HPiv)_3$ (M = Mn, Co, Ni). *Journal of Electron Spectroscopy and Related Phenomena*. **205 (**2015), 2-4.

[15] **R. C. Weast** (editor). *Handbook of chemistry and physics*. 51st ed., The Chemical Rubber Co., Cleveland, USA (1971).

[16] **V. Majer and V. Svoboda.** *Enthalpies of vaporization of organic compounds.* 1st ed., Blackwell Scientific Publications, Oxford, England (1985).

[17] **Lamprecht, E.** (2008) *Thermal, spectroscopic and X-ray diffraction studies of copper(II) 1,2,4,5,-benzenetetracarboxylates and copper(II) oxalate: a study of metal-organic frameworks.* Doctoral thesis. Grahamstown: Rhodes University.

[18] **Weil, J. A. and Bolton, J. R.** *Electron Paramagnetic Resonance: Elementary Theory and Practical Applications*. 2nd ed., John Wiley & Sons Ltd, New Jersey, USA (2006).

[19] **Harriman, J. E. and Loebl, E. M.** *Theoretical Foundations of Electron Spin resonance*. Phys. Chem.: A Series of Monographs, **37**, New York, USA (1978).

[20] **Thornton, D. A. and Watkins, G. M.** The infrared spectra (4000-50 cm^{-1}) of complexes of 2,2'-bipyridine, 1,10-phenanthroline and their perdeuterated analogues with metal(II) perchlorates of the first transition series. *J. Coord. Chem.* **25** (1992), 299-314.

[21] **Wang, J. T.; Williams, F**. ESR detection of the dimethyl ether radical cation. *J. Am. Chem. Soc*., **103** (1981), 6994–6996.

Chapter 6

Concluding Remarks and Future Work

Three pyrazine-*N*-oxide (pyzNO) complexes of iron(II) were successfully synthesised and characterised. The complexes $Fe_n(\mu_{1,1}\text{-pyzNO})_{2n-2}(pyzNO)_{3n+2}(ClO_4)_{2n}$ $(n = \{1, 2\})$, $\{Fe(\mu\text{-pyzNO-}\kappa N,\kappa O)_{n-1}(pyzNO\text{-}\kappa N)_2(pyzNO\text{-}\kappa O)_2\}_n(ClO_4)_{2n}$ and $Fe(pyzNO)_6(ClO_4)_2{\cdot}3EtOH$, the latter two of which are being reported for the first time, have been described. A fourth complex, also novel, has been synthesized and characterized, and was proposed to have the formula: $Fe_2(bipyNO)_5(ClO_4)_4{\cdot}6MeOH$.

The crystal structures of the polymeric complex (Complex2), as well as one of its hydrated forms, $[Fe(pyzNO\text{-}\kappa N)_4(H_2O)_2](ClO_4)_2{\cdot}2H_2O$, were solved, and used in part, to infer the structures of the other complexes. The powdery consistency of the latter materials made them incompatible with the available single crystal XRD instrumentation.

The spectral shift ('MeOH/DMP' complexes: red→yellow; 'EtOH/DMP' complex: orange→yellow) on hydration of the PyzNO complexes has been observed, and the accompanying changes to structure and magnetic properties investigated. Mid-IR data, XRD and thermal analyses indicate that the spectral shifts were facilitated primarily by hydrolysis of Fe-*O* bonds in the coordination sphere by the incoming water. Single crystal data has confirmed this for one if the hydrated forms of the polymeric complex.

It would have been ideal to accurately ascribe the ~ 0.059 Å increase in equatorial Fe-*N* bond lengths (on hydration of the polymeric complex) specifically and exclusively to the LS→HS SCO event. However, the complete change in structure, including the loss of bridging and *O*-coordinated PyzNO units that accompanies the coordination of H_2O, is likely to play the decisive role in this regard.

The increase in the Fe-Cl contact distance under the same conditions, though, is thought to be a consequence of this transition. The *addition* of water to the coordination sphere is expected to introduce extensive intermolecular H-bonding given the amenable, crystallographically measured O-H contact distances. Enhanced attractive dipole-dipole behaviour is also expected. These interactions should act to decrease average Fe-Cl spacial separation more so than the

concurrent enhanced electron withdrawal from the Fe(II) ion should offset this effect. However, the (increased) accumulation of electron density about the ligands on hydration is purported to introduce sufficient steric hindrance to the approach of the counterion to the more electrophilic Fe(II) ion. This is the assumed general mechanism by which Fe-Cl interatomic distances are (in this context) increased by the LS→HS crossover.

The systemic ubiquity of HS configured Fe(II) centres in the [Fe(pyzNO-κ*N*)$_4$(H$_2$O)$_2$](ClO$_4$)$_2$·2H$_2$O species is imagined to be a synergistic consequence of intermolecular cooperativity effects, and the porous nature of its crystals. However, BET studies are yet to be undertaken in order to confirm the latter feature; upon the installation of a suitable UPS system on the instrument.

The rapid nature of the hydration-induced spectral and magnetic conversion of the mononuclear complex is ascribable to its relatively high surface area-to-volume ratio, as well as cooperativity phenomena.

In both the polymeric and mononuclear complexes, EPR at 77 K and at 298 K confirmed that a hydration induced SCO event did accompany (or may be responsible for) the observed colour changes.

Limited yields of the associated complexes made bulk magnetic susceptibility measurements (by Gouy balance) unfeasible. However, magnetic characterisation by the semiconducting quantum interference device (SQUID) will form an exciting prospect for future work.

The polymeric complex showed significant uptake of other solvents, among which were *p*-dioxane, and the tested alcohols and aldehydes. Similar colour changes as seen on hydration were also seen in these contexts, with the exception of methanol, in which only a very subtle change to a dark orange colour was seen. Ethanol exposure produced a more pronounced colour change to form an orange species, while exposure to the *p*-dioxane and the aldehydes generated species of varying yellow hue. Of these, the brightest yellow colour was generated from the formaldehyde trails.

Although a crystal structure could not be determined for the Complex2-*p*-dioxane and -aldehyde solvent trials, comparison of the colour changes experienced by the water exposed complex suggested that the transition was mediated by the same underlying mechanism. That

is, the substitution of *O*-coordinated PyzNO by the incoming solvent, to produce a $[Fe(pyzNO)_4(solvent)_2](ClO_4)_2$ complex with a variable number of physisorbed solvate moieties. Mid-IR studies also suggested this, although perhaps not definitively. The Mid-IR spectra of Complex2-*p*-dioxane / formaldehyde / acetaldehyde are virtually superimposable with that of $[Fe(pyzNO\text{-}\kappa N)_4(H_2O)_2](ClO_4)_2{\cdot}2H_2O$. However, as the characteristic mid-IR bands of these solvents, including those in their *fingerprint* regions, coincide with those of $[Fe(pyzNO\text{-}\kappa N)_4(H_2O)_2](ClO_4)_2{\cdot}2H_2O$, that the former were formally coordinated could not be conclusively determined by this technique. Moreover, the electronic effects accompanying coordination were not anticipated to produce sufficiently quantitative shifts in band positions to diagnostically indicate solvent dative covalent bonding, merely by comparison with $[Fe(pyzNO\text{-}\kappa N)_4(H_2O)_2](ClO_4)_2{\cdot}2H_2O$.

Thermal analyses and XRPD data suggested substantial structural changes in the above cases, with only the ethanol-exposed complex largely retaining its crystalline nature. These changes were ascribed to the effects of partial dissolution in these relatively polar media.

Complex2 EPR solvent studies were expected to reveal whether or not the SCO event was limited to water exposure samples, and that in general, all the resulting yellow species were EPR active. However, as discussed in chapter 5.3, the resonances seen in the EPR spectra of some samples, including those from the acetaldehyde, formaldehyde and *p*-dioxane trials, could not be conclusively ascribed to paramagnetic Fe(II). Instead, they could potentially be due to the Zeeman Effect, emergent upon solvent exposure. As mentioned, a potential candidate for this activity may be the odd electron density on a PyzNO radical generated upon heterolytic *O*-Fe bond cleavage in a PyzNO→solvent substitution reaction. The colour changes seen in those instances, on solvent exposure, have been ascribed to solvent-induced bathochromic shifts in UV/Vis maxima (especially MLCT), which are mediated by a combination of solvent substitution and the intermolecular action of the London forces.

The only distinct exception was the EPR spectrum from acetone trial, which, although no colour change at all was observed in the complex on solvent exposure, showed measureable activity. This is as yet an anomalous result pending further investigation.

The preparation of analogous systems for comparison was achieved. Complex4 did not exhibit the spectral features characteristic of the spin crossover event, owing to the insusceptibility of the compound to hydration. The complex's EPR spectrum showed strong

resonance at 77 K. The sample was stored in a desiccator directly after synthesis, making the possibility of the adsorption of significant atmospheric moisture remote. Ostensibly therefore, the complex was generated already in its HS configuration, which made a hydration-induced SCO process unfeasible under the experimental conditions, as evidenced by EPR. Thermal and EG analyses indicated no water uptake at all, and XRPD showed no differences in the diffraction patterns of the original and water exposed samples. Moreover, the only solvent seen to interact strongly with complex was acetaldehyde. It was therefore surmised that the possibility of a solvent-dependent SCO process, in this context, relies strongly upon PyzNO being the primary ligand.

Although it was considered that the coordinated methanol may play a potentially decisive role in the spin state configuration, its preclusion is somewhat challenging considering the choice of solvent system. As the latter was not arbitrarily chosen, but as a result of solubility considerations associated primarily with the metal salt, significant deviation from the protocol in that sense was difficult.

A mixed ligand PyzNO/BipyNO system may be a particularly interesting avenue to pursue, as this may enable the fine-tuning of the LFSE yet closer to the SCO threshold. This prospect has also however been reserved for future work.

The complex obtained from EtOH/DMP, although initially orange; due to the trapping of 3 solvate ethanol units per formula unit (and possible exclusive *O*-mode PyzNO coordination), was found to undergo SCO on hydration as evidenced by EPR. The complex also showed strong interaction with a variety of different solvents, as with the polymeric complex. Thermal and EGA data showed a particularly strong affinity for the polar solvents; although all tested solvents were seen to be taken up, with the exception of THF. A complete EPR solvent study is yet to be undertaken for this complex due to time constraints. However, as with the polymeric species, the analogous colour changes are expected to reflect a similarity in the underlying magnetic properties.

Cobalt(III) perchlorate, being itself a d^6 first row transition metal ion, and having physical properties most closely comparable to iron(II) perchlorate in this context such as redox potentials and chemical reactivity's, etc., is deemed an excellent candidate for a metal salt

analogue in order to generate isostructural complexes against which the iron(II) compounds might be considered.

In closing, the importance of the study of coordination compounds, and especially, in the context of this work, the development of compounds exhibiting analyte-specific transformations in spectral and magnetic properties, whether by the action of SCO or solvatochromism; by technological and academic motivations, is fully acknowledged and appreciated.

Appendix

Part 1

1.1 Additional Characterization of Pyrazine-*N*-oxide:

TGA and FT-IR-EGA

Figures 1.1 and 1.2 show the thermogravimetric behaviour of Pyrazine-*N*-oxide (PyzNO), as well as its concurrent FT-IR evolved gas analysis, respectively. The ligand readily undergoes sublimation as can be clearly seen on the TG thermogram, which shows an approximately exponential mass decline with temperature as a result. Residual PyzNO commences thermolysis at around 160 ^{o}C, as evidenced by the FT-IR detection of the major decomposition product (CO_2; ν_s(C=O) ~ 3000 cm^{-1}) in the TG effluent exhaust. No discernible residue is seen after thermal analysis.

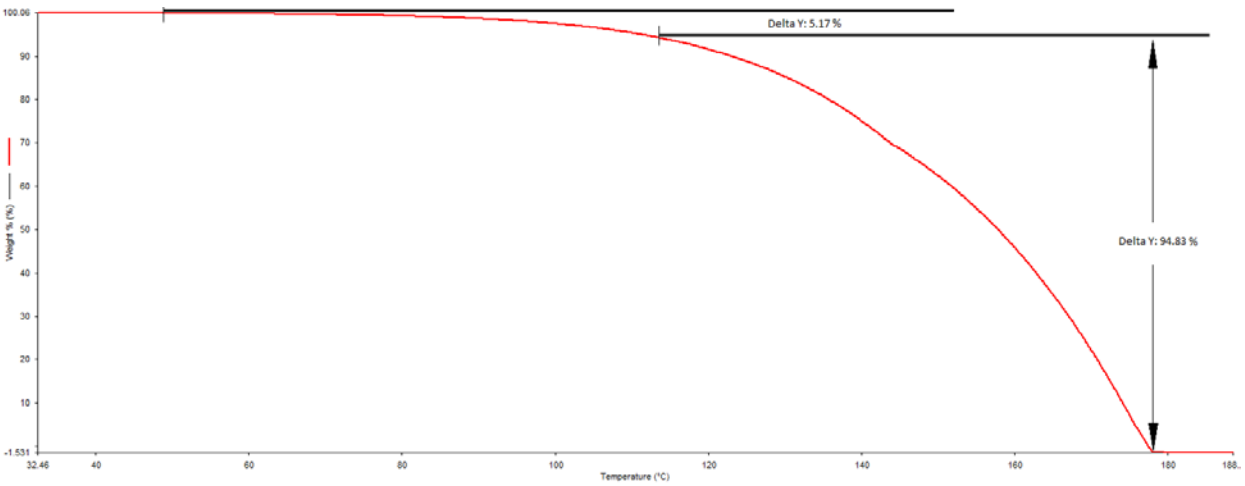

Figure 1.1: TG thermogram (30 – 190 ^{o}C, 10 ^{o}.min^{-1}) of Pyrazine-*N*-oxide

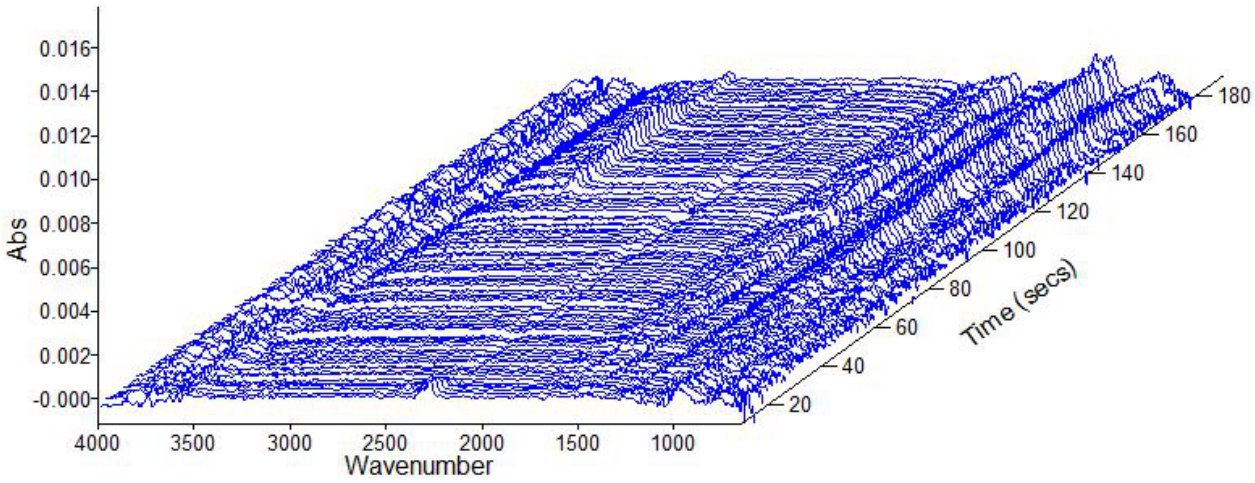

Figure 1.2: TG-IR EGA (30 – 180 ^{o}C, 10 ^{o}.min^{-1}) stack plot of Pyrazine-*N*-oxide

FT-Raman

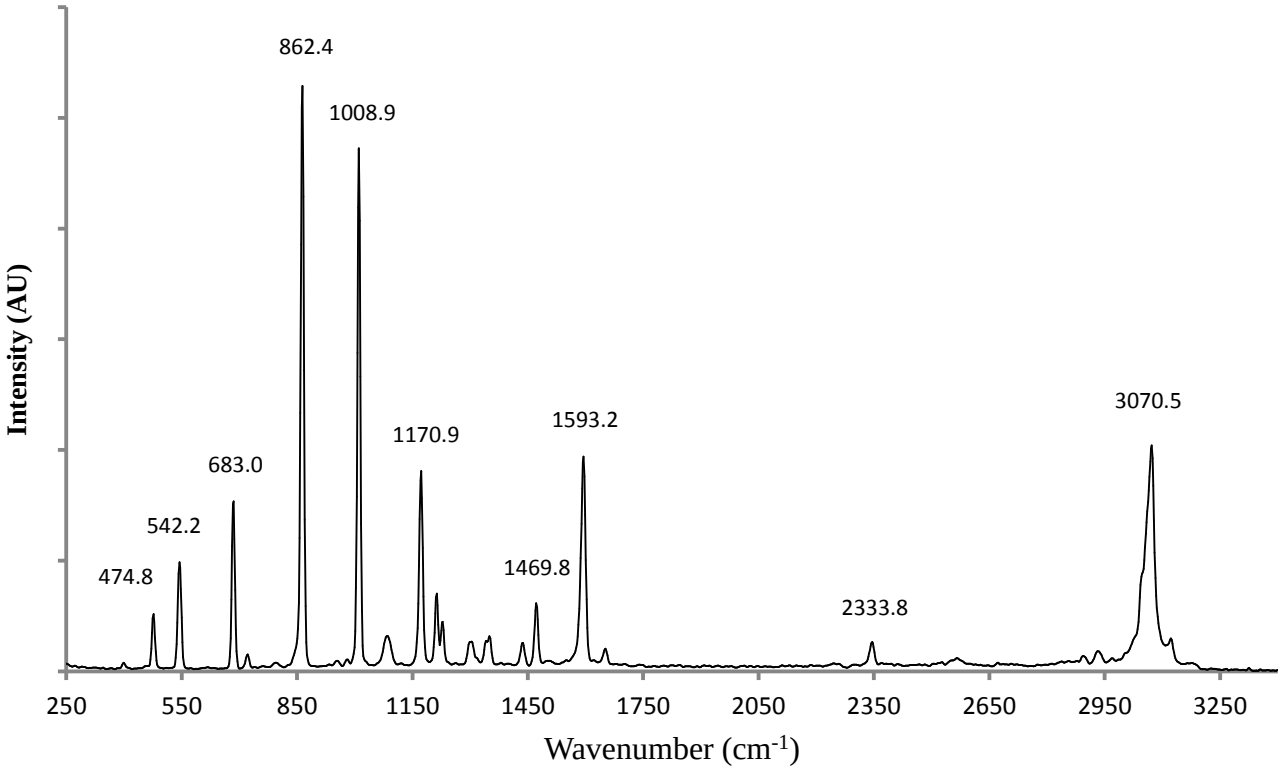

Figure 1.3: FT-Raman spectrum (3400 - 250 cm^{-1}) of Pyrazine-*N*-oxide

The FT-Raman spectrum of the PyzNO product agrees excellently with the literature, and corroborates the assertion that a pure product was obtained [1].

1.2 Additional Characterization of 4,4'-bipyridine-*N*-oxide:

TG-IR-EGA

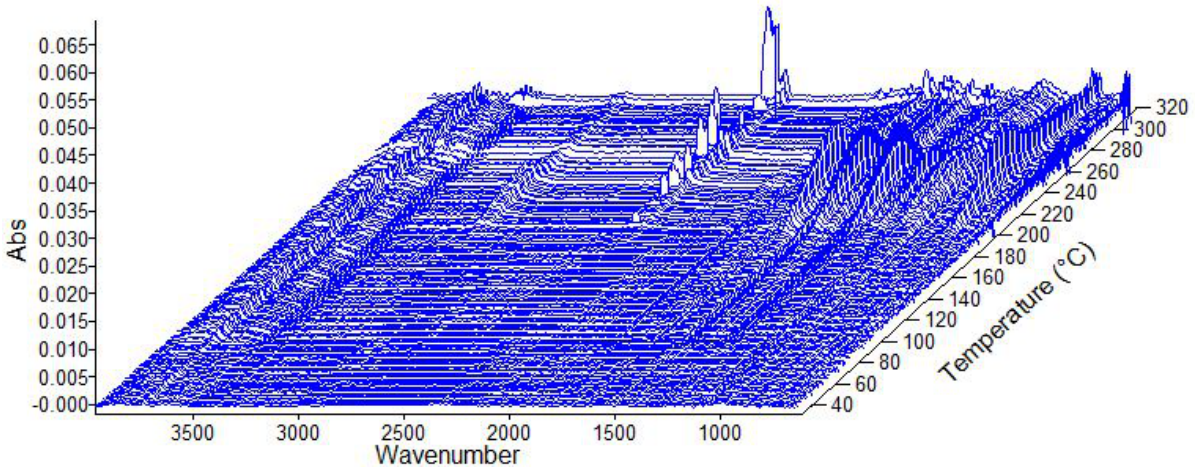

Figure 1.4: TG-IR EGA (30 – 180 ^{o}C, 10 ^{o}.min^{-1}) stack plot of 4,4'-bipyridine-*N*-oxide

Figure 1.4 shows the relative stability of BipyNO until approximately 180 ^{o}C, whereupon it begins to sublime rapidly. Some degree of decomposition is seen to begin at around 200 degrees, as evidenced by the significant emergent activity centered at 2600 cm^{-1} and 3200 cm^{-1}, ostensibly due the evolution of CO and CO_2 gases. As with the thermal analyses of PyzNO, no residue was found subsequently, indicating a high degree of purity of the product. That is, the formation of the $BipyNO_2$ side product was successfully suppressed.

1.3 Synthesis and characterization of pyrazine-*N,N*'-dioxide and 2/3-methylpyrazine-N-oxide

Synthesis of Pyrazine-*N,N*'-dioxide

To 0.9962 g pyrazine (12.4 mmol) was added 7.496 ml glacial acetic acid (127 mmol) and 2.665 ml of 9.333 M H_2O_2 (24.9 mmol). The solution was heated at 90 ^{o}C for 3 hours under reflux. A further 2.665 ml of 9.333 M H_2O_2 (total ratio 4:1 H_2O_2:Pyz) was added and heating continued for a further 5 hours. The solution was cooled and neutralised using Na_2CO_3. The

solvent was reduced to a third by rotary evaporation whereupon the resulting sodium acetate precipitate was filtered off. Extraction into $CHCl_3$ was attempted, albeit with scepticism because of the documented poor solubility of the product in non-polar solvents. Unsurprisingly, the resulting solid product after solvent removal from the organic phase had a mass of 0.0056 g (0.4%). Therefore, the solvent was removed from the aqueous phase and the resulting yellow-brown solid was stirred in 25 ml of hot ethanol. After filtration, the resulting filtrate was reduced to 2ml by rotary evaporation and left overnight in a dark cupboard. The resulting brown crystals of Pyrazine-*N*,*N*-dioxide ($PyzNO_2$) were washed washing with an excess of cold ethanol, dried under suction and recorded (yield: 0.5232 g, 37.5 %). The product was characterised by ^{1}H NMR, DSC and mid-IR spectroscopy.

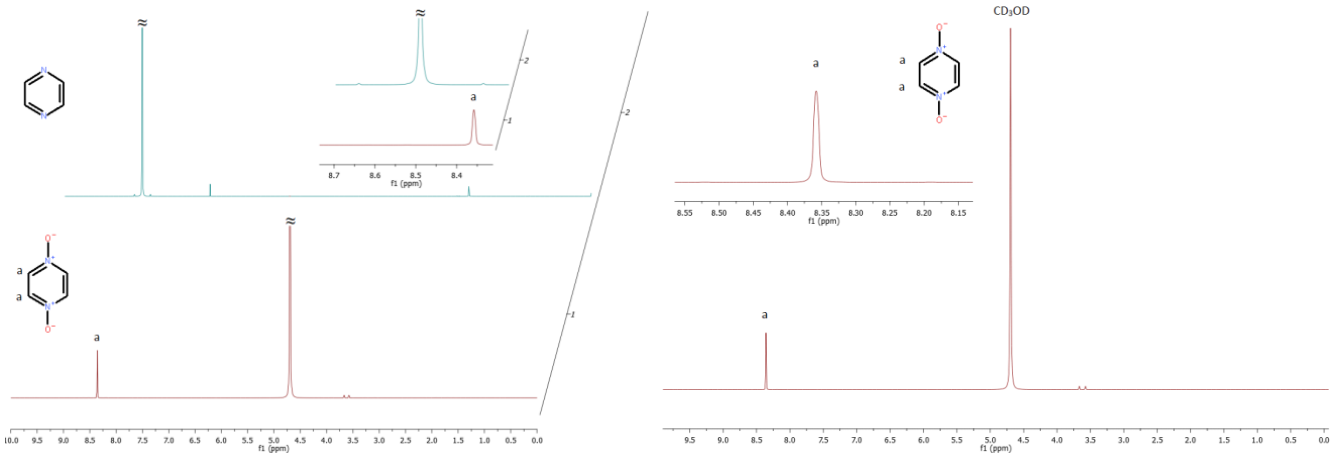

Figure 1.5: On the left are the 600 MHz ^{1}H NMR spectra of pyrazine in $CDCl_3$ (top), and pyrazine-*N*,*N*'-dioxide in CD_3OD (bottom) for comparison. On the right is pyrazine-*N*,*N*'-dioxide alone, in CD_3OD; δ singlet 8.26 ppm (4H). Enhanced views are provided atop each spectrum.

The ^{1}H NMR spectrum of $PyzNO_2$ agrees with what was expected based on theoretical prediction and literature [1]. Watkins elected to employ D_2O as the NMR solvent. The four identical aromatic protons resonate at δ 8.26 ppm to give a singlet. In this case, there are no signals other than the CD_3OD peak present, a point which indicates that a product of good purity was obtained.

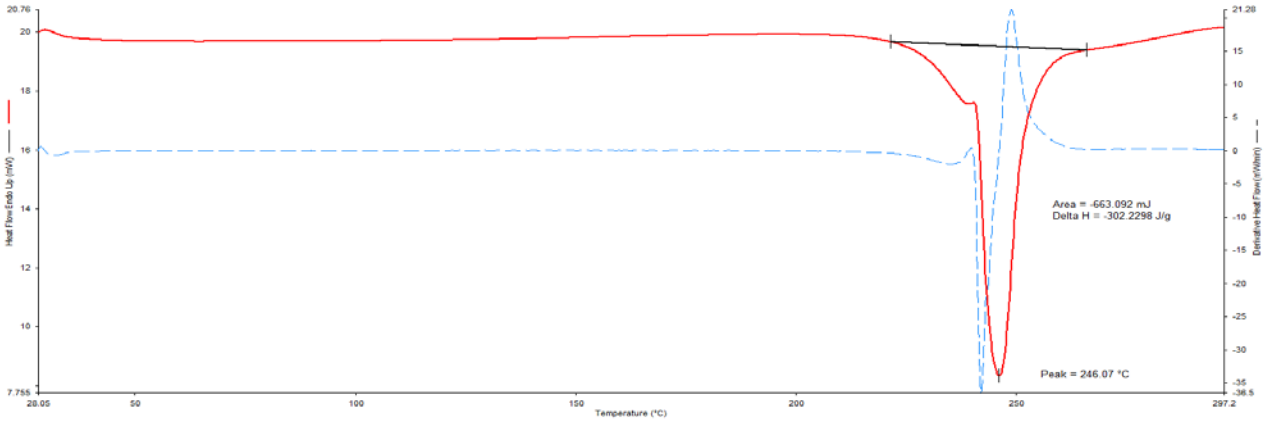

Figure 1.6: DSC thermogram (red; temperature range: 30 – 200 ^{o}C, 10^{o}.min^{-1}) of $PyzNO_2$ product. Decomposition temperature (246 ^{o}C) is shown (ΔH: -33.9 kJ.mol^{-1}; 663.092 mJ). Also shown is the derivative curve (dashed blue).

There has been much disagreement, as Watkins [1] noted, about the melting point of $PyzNO_2$. While Koelsch and Gumprecht [2] originally reported a melting point of 285 – 295 ^{o}C, Klein and Berkowitz [3] found the compound to decompose, rather, at 300 ^{o}C. The decomposition value found by DSC in this current work agrees with the value reported by Popp and Garlough [4] of 250 ^{o}C. In any event, there appears to be a two-step decomposition, the first step is seen as an exotherm centred at 243 ^{o}C, with the final exothermic decomposition step occurring at 246 ^{o}C (ΔH: -33.876 kJ.mol^{-1}).

Attempted synthesis of 2-methylpyrazine-*N*-oxide (MepyzNO)

1 ml of methylpyrazine (Mepyz) (10.83 mmol) was added to 4.475 ml of glacial acetic acid (75.81 mmol) and 1.160 ml of 10.75 M H_2O_2 (21.66 mmol). The solution was heated at 60^{o} C for 2 hours under reflux. In order to evaluate the reaction progress, 10 µL of the reacting solution was removed by Eppindorf pipette, neutralised with Na_2CO_3, and extracted into chloroform. Normal phase TLC (Stationary phase: silica gel 60 F_{254}, Mobile phase: 50/50 EtOH/$CHCl_3$) of the resulting organic phase was conducted against Mepyz precursor. Three distinct spots were visualised under UV light of 254 nm wavelength, the most mobile of which was unreacted Mepyz. The least mobile fraction was methylpyrazine-*N*,*N*'-dioxide ($MepyzNO_2$), while the component with intermediate chromatographic affinity was though be the desired product, MepyzNO. The temperature was adjusted in order to suppress further dioxide formation and allowed to equilibrate at 50^{o} C, whereupon a further 1.160 ml H_2O_2 (total ratio 2:1 H_2O_2:Mepyz) was added and heating continued for a further 5 hours. TLC by

the same method as detailed above revealed no unreacted precursor, however, the dioxide spot had become prominent to the extent that it could not be distinguished from the MepyzNO spot in terms of intensity. The solution was then cooled and the volume reduced to a half (4 ml) by rotary evaporation at 35^{o} C. The solution was neutralised using Na_2CO_3, after which MepyzNO was extracted into chloroform 5 times over using an approximate 1:1 per volume ratio of organic : aqueous phases. The chloroform level was then lowered to 4 ml by rotary evaporation at 30^{o} C. The resulting pale brown liquid was loaded onto a preparative TLC plate of the same composition as the analytical variant used above, for a maximum load width of 1 cm. The same eluting solvent system was also employed.

UV light exposure revealed good separation of the mono-*N*-oxide and di-*N*-oxide components. The former, silica-embedded fraction was removed and stirred in 40 ml of warm EtOH for 1 h. It was then filtered and washed and with 10 ml of EtOH. The resulting filtrate volume was reduced to 5 ml by rotary evaporation and checked by analytical TLC for purity. TLC showed only one distinct spot.

After removal of the chloroform by rotary evaporation at 30^{o} C, the resulting pale red liquid was allowed to cool to room temperature. A white precipitate began to form in the liquid within several minutes. Residual solvent was allowed to evaporate by gently blowing dry air over the sample overnight. This afforded what appeared to be a composite mixture consisting of a white and a red solid. (yield: 0.1569 g, 13.2%). Separation of the product mixture by TLC using different mobile phases was attempted. Mobile phases employed for this purpose were acetone, chloroform, cyclohexane, cyclohexene, toluene, abs. ethanol, dist. methanol and 1,1-dichloroethylene. Each trial was to unsuccessful as only one resulting spot in the associated TLC was seen in each case.

As no degree of separation at all was seen, reverse phase TLC was not attempted. As a result of the failure in the resolution of the mixture by TLC, it was unclear as to how to separate the components chromatographically as HPLC was unavailable at the time. The product was nevertheless characterised by microanalysis, ^{1}H NMR, ^{13}C NMR, DSC and FT-Infrared spectroscopy.

Synthesis of the iron(II) perchlorate complex of the ligand using the composite mixture was attempted with the idea that perhaps only one of the species would be amenable to this reaction from a kinetic viewpoint, thereby enabling the other to be washed off as an impurity (see complex synthesis section 2.6 in the main text). Quantitative amounts of the resulting compex(es) could not however be generated for characterisation due to insufficient precursor.

Table 1: Experimental versus theoretical microanalysis of the product mixture containing 2- and 3-MepyzNO (best fitting rows highlighted in yellow correspondingly).

Experimental (%)					Theoretical (%)				
Run	C	H	N	S	Waters	C	H	N	S
1	53.16	5.351	24.61	0	Anhydrous	54.54	5.492	25.44	0
2	53.71	5.668	24.85	0	-	-	-	-	0
Average	53.44	5.509	24.73	0	0.15 H_2O	53.23	5.629	24.83	0

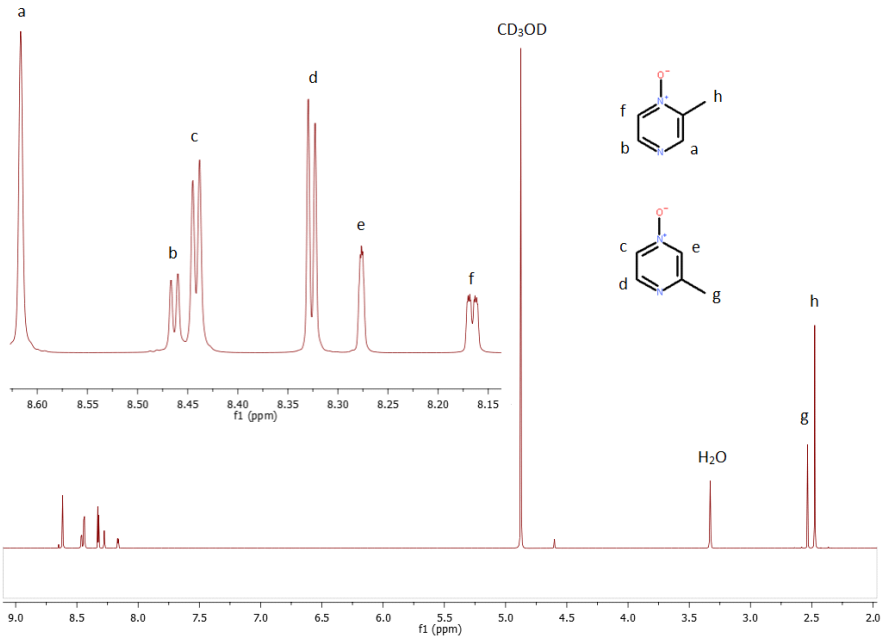

Figure 1.7. 600 MHz ^{1}H NMR spectrum of the 2- and 3-mepyzNO product mixture in CD_3OD; δ singlet 8.62 ppm (1H), doublet 8.46 ppm (1H, J = 4.2 Hz), doublet 8.44 ppm (1H, J = 4.2 Hz), doublet 8.33 ppm (1H, J = 4.2 Hz), singlet 8.28 ppm (1H), doublet 8.16 ppm (1H, J = 4.2 Hz), singlet 2.53 ppm (3H), singlet 2.48 ppm (3H). Enhanced view of aromatic region is included for clarity (top left).

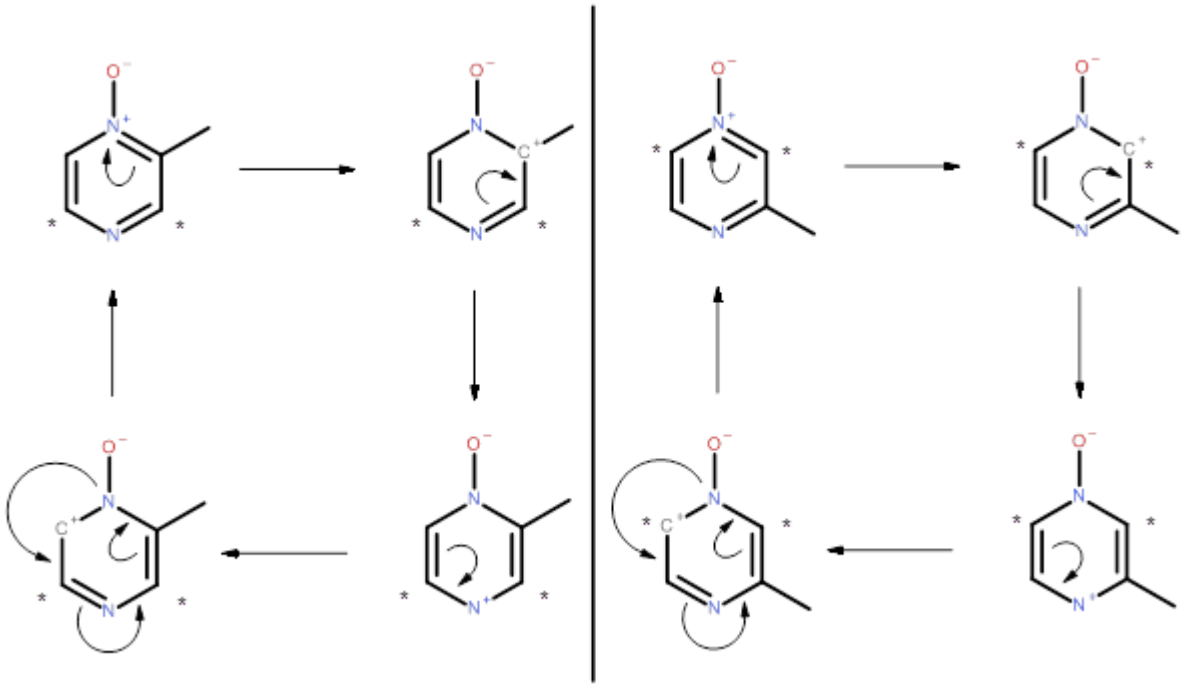

Figure 1.8: A theoretical treatment of the electronic resonance exhibited by 2-methylpyrazine-*N*-oxide (left) and 3-methylpyrazine-*N*-oxide (right) for the assignment of the ^{1}H NMR spectrum of the composite mixture. Resonance-induced charges are shown, as well as the shielded protons (asterisks) that result from inductive effects associated with the position of the methyl substituent.

The assignment of the ^{1}H NMR spectrum of the 2-mepyzNO/3-mepyzNO mixture was made by recourse to the various canonical forms that arise on inspection of the aromatic electronic resonance of the two products. This inspection afforded an idea of which protons are likely to be more shielded or deshielded relative to the other protons in the diazine heterocycle. As aromatic methyl (alkyl in general) substituents are known ortho-/para-directing activators, the positions marked with asterisks were thought to correspondingly experience a greater measure of shielding that those that are unmarked. The carbon atoms that inherit formal/partial positive charges during the resonance cycle, thereby deshielding their bonded protons, are also shown. The signals assigned to 2-mepyzNO by this method are; δ singlet 8.62 ppm (1H), doublet 8.46 ppm (1H, J = 4.2 Hz), doublet 8.16 ppm (1H, J = 4.2 Hz), and singlet 2.48 ppm (3H).

Those assigned to 3-MepyzNO are; doublet 8.44 ppm (1H, J = 4.2 Hz), doublet 8.33 ppm (1H, J = 4.2 Hz), singlet 8.28 ppm (1H), and singlet 2.53 ppm (3H). As these assignments were made from a purely logical and theoretical perspective, experimental evidence to verify them is still outstanding.

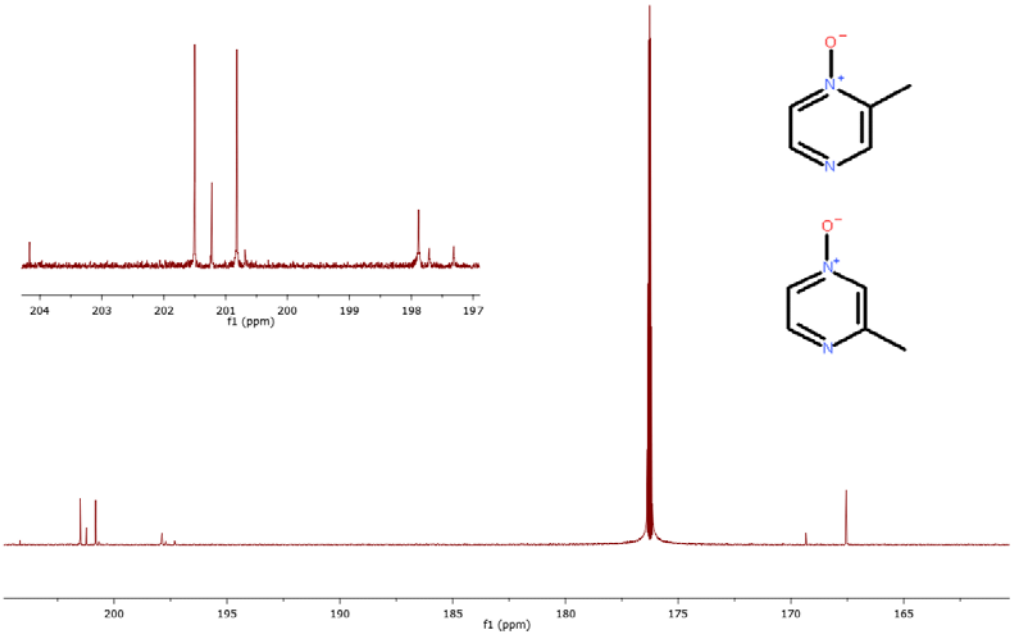

Figure 1.9: 600 MHz ^{13}C NMR spectrum of 2- and 3-mepyzNO product mixture in CD_3OD; δ 148.11 ppm (2C), 134.13 ppm (2C). Enhanced view of aromatic region is included for clarity (top left).

The assignment of the ^{13}C carbon spectrum of 2-mepyzNO/3-mepyzNO mixture could not be performed by the method outlined for the ^{1}H spectrum due the ambiguity that is characteristic of ^{13}C spectra. Nevertheless, the expectation that there should be exactly eight aromatic signals (four per product) and two in the aliphatic region (the two different methyl groups), was realised. This was deemed sufficient, when combined with the ^{1}H NMR data, to conclude that the two structural isomers were indeed both present.

Figure 1.10 shows the calorimetric thermal behaviour of the 2-mepyzNO and 3-mepyzNO mixture on heating. It was expected, since the NMR revealed two distinct product components, that the DSC experiment would likewise reveal two distinct melting points to reflect the different physical attributes of the two components. However, only one melting point was observed.

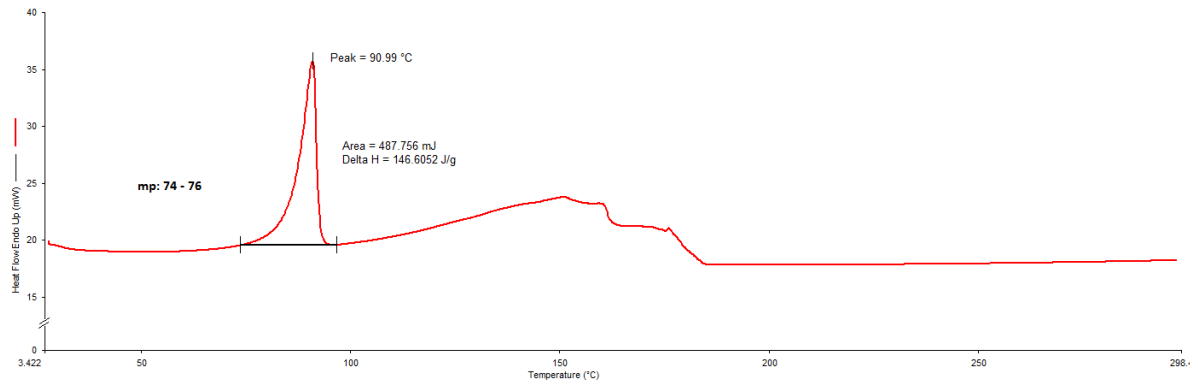

Figure 1.10: DSC thermogram (30 – 200 ^{o}C; 10^{o}.min^{-1}) of 2- and 3-mepyzNO product mixture (m.p.: 91 ^{o}C; ΔH: 16.3 kJ.mol^{-1}).

The relative broadness of the melting point endotherm (ΔT $\approx$ 20 ^{o}C) - in comparison with those of PyzNO (ΔT $\approx$ 5 ^{o}C) and BipyNO (ΔT $\approx$ 5 ^{o}C) in their respective DSC thermograms - is considered to be a reflection of the presence of both isomers.

The endotherm seen after the melting point has the same form as that seen in the DSC analyses of PyzNO and BipyNO. It was therefore concluded that it was due to the gradual evaporation of the resulting liquid MepyzNO mixture.

The mid-IR spectrum of the MepyzNO isomeric mixture is shown in Fig. 1.11. Although speculatively, the strong band at 1288 cm^{-1} and the medium strong band at 1215 cm^{-1} have been assigned as ν(NO) of 2-mepyzNO and ν(NO) of 3-mepyzNO, respectively. The assignment was made by recourse to Fig. 1.8. That is, 2-mePyzNO is expected to exhibit increased N-O double bond character due to the enhanced electron density of the *N*-oxide functional group's nitrogen atom; resulting from inductive effects associated with the neighbouring methyl group.

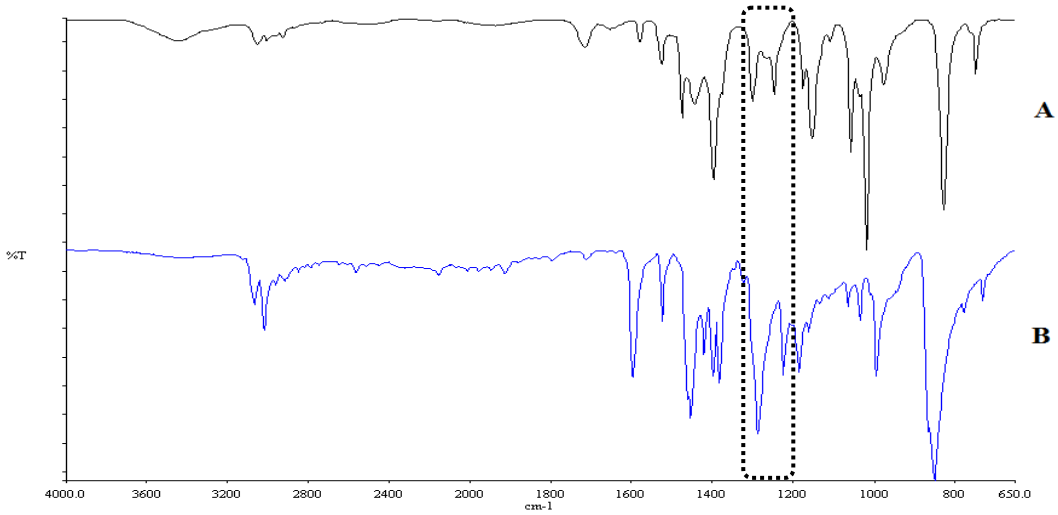

Figure 1.11: Mid-IR spectrum (4000.0 – 650.0 cm^{-1}) of the 2- and 3-mepyzNO product mixture after prep plate TLC (B). Included also is the spectrum of the precursor methylpyrazine (A) for comparison. The boxed region is where the *ν*(NO) vibration typically occurs.

Part 2

2.1 Hydration-induced colour change

A **B**

Figure 2.1: Photographs showing the red → yellow hydration-induced colour change as $[Fe_n(\mu_{1,1}\text{-}pyzNO)_{2n-2}(pyzNO)_{3n+2}](ClO_4)_{2n}$ (n = {1, 2}) (Complex1) transforms to $\{Fe(pyzNO)_5(ClO_4)_2(H_2O)_3\}$ (Complex5) (A); and as $[Fe_{2n}(\mu_{1,5}\text{-}pyzNO)_{2n-1}(pyzNO)_{8n+1}](ClO_4)_{4n}$ (Complex2) transforms to $[Fe(pyzNO)_4(H_2O)_2](ClO_4)_2{\cdot}2H_2O$ (Complex6) (B).

2.2 Crystal structure of $[Fe_{2n}(\mu_{1,5}\text{-pyzNO})_{2n-1}(pyzNO)_{8n+1}](ClO_4)_{4n}$ (Complex2) (alternative view)

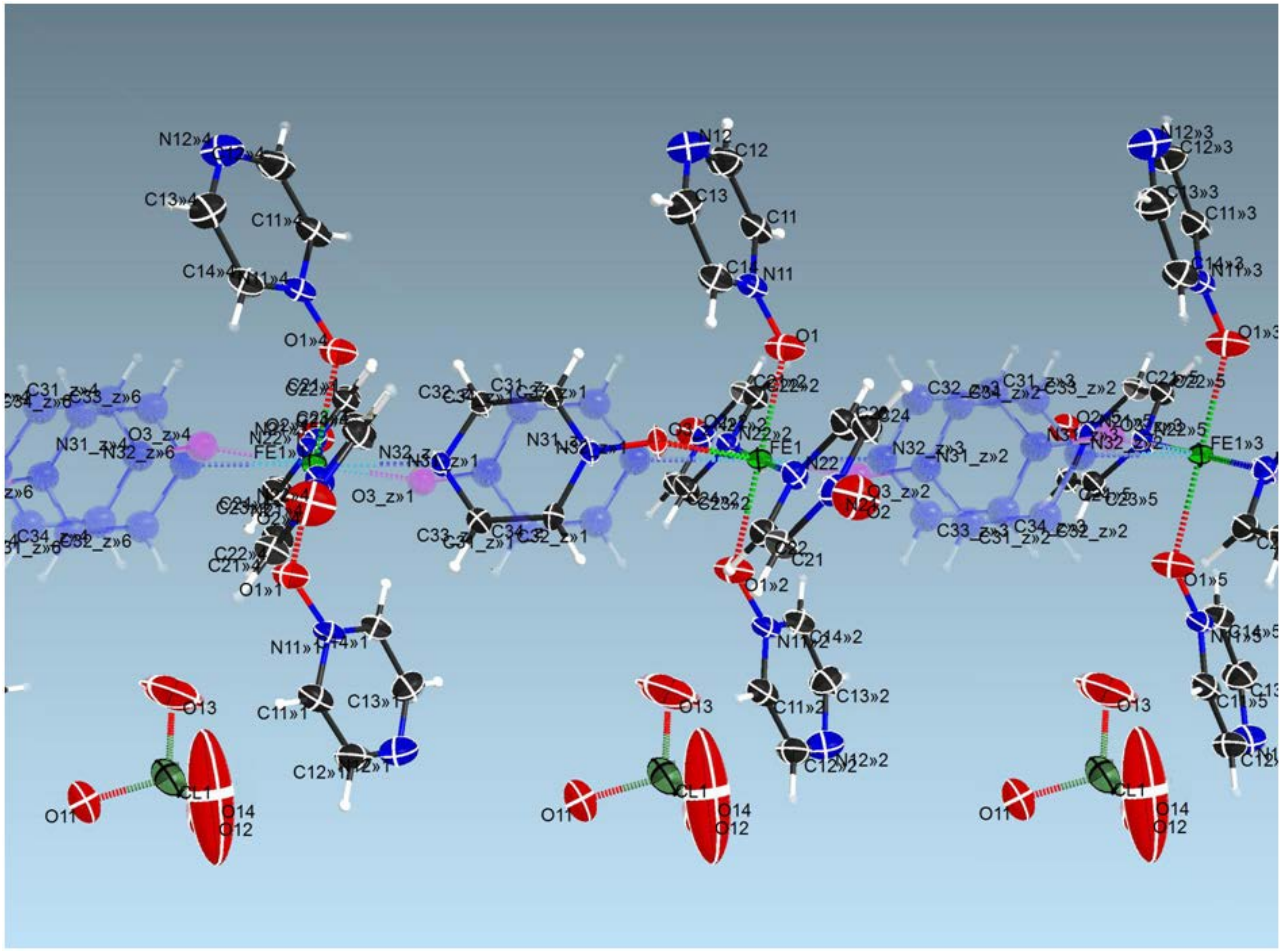

Figure 2.2: Alternative depiction of the crystal structure of $[Fe_{2n}(\mu_{1,5}\text{-pyzNO})_{2n-1}(pyzNO)_{8n+1}](ClO_4)_{4n}$ (Complex2).

2.3 High resolution XPS scans of the Cl 2p region:

2.3.1 $[Fe_{2n}(\mu_{1,5}\text{-}pyzNO)_{2n-1}(pyzNO)_{8n+1}](ClO_4)_{4n}$ (Complex2)

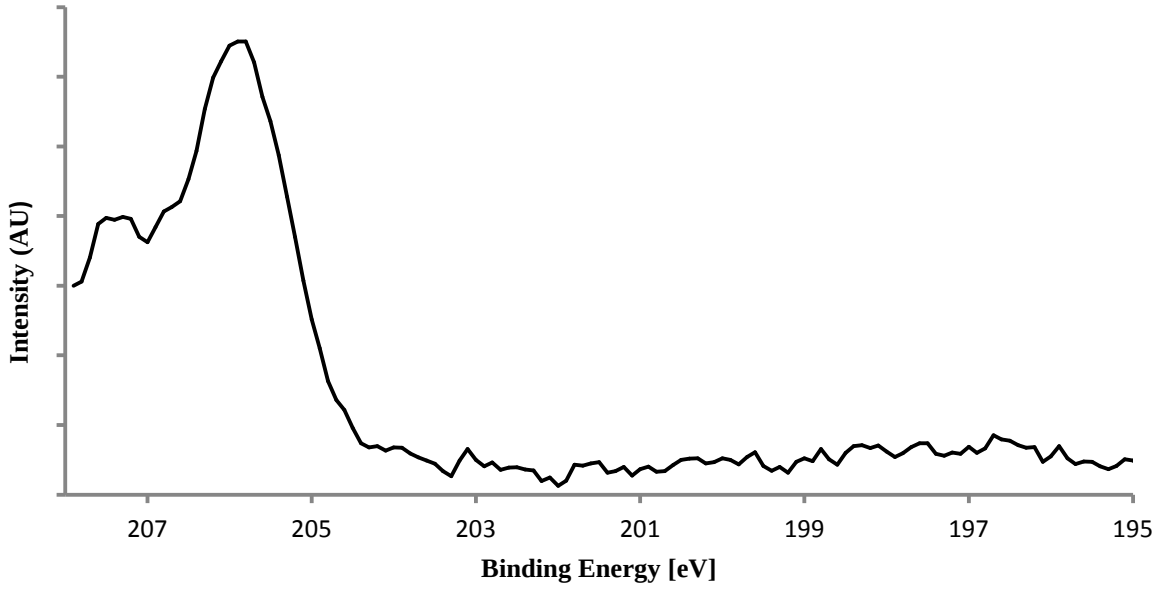

Figure 2.3: High resolution XPS scan of the Cl 2p region of $[Fe_{2n}(\mu_{1,5}\text{-}pyzNO)_{2n-1}(pyzNO)_{8n+1}](ClO_4)_{4n}$ (Complex2)

2.3.2 $[Fe(pyzNO)_4(H_2O)_2](ClO_4)_2{\cdot}2H_2O$

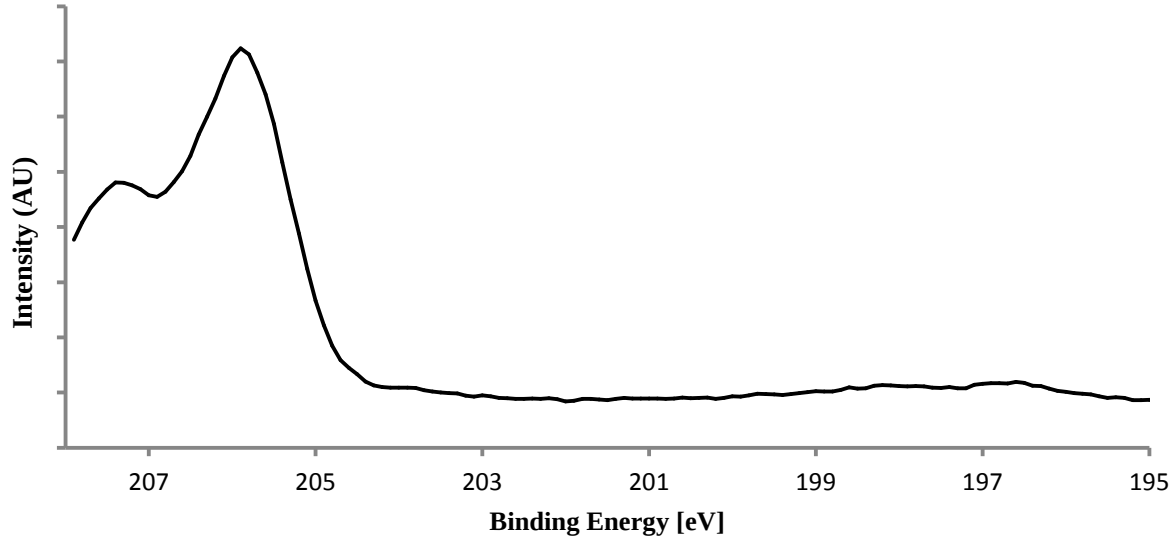

Figure 2.4: High resolution XPS scan of the Cl 2p region of $[Fe(pyzNO)_4(H_2O)_2](ClO_4)_2{\cdot}2H_2O$ (Complex6)

2.3.3 $[Fe_2(\mu_{1,1}\text{-bipyNO})_3(bipyNO)_2(MeOH)_4](ClO_4)_4 \cdot 2MeOH$

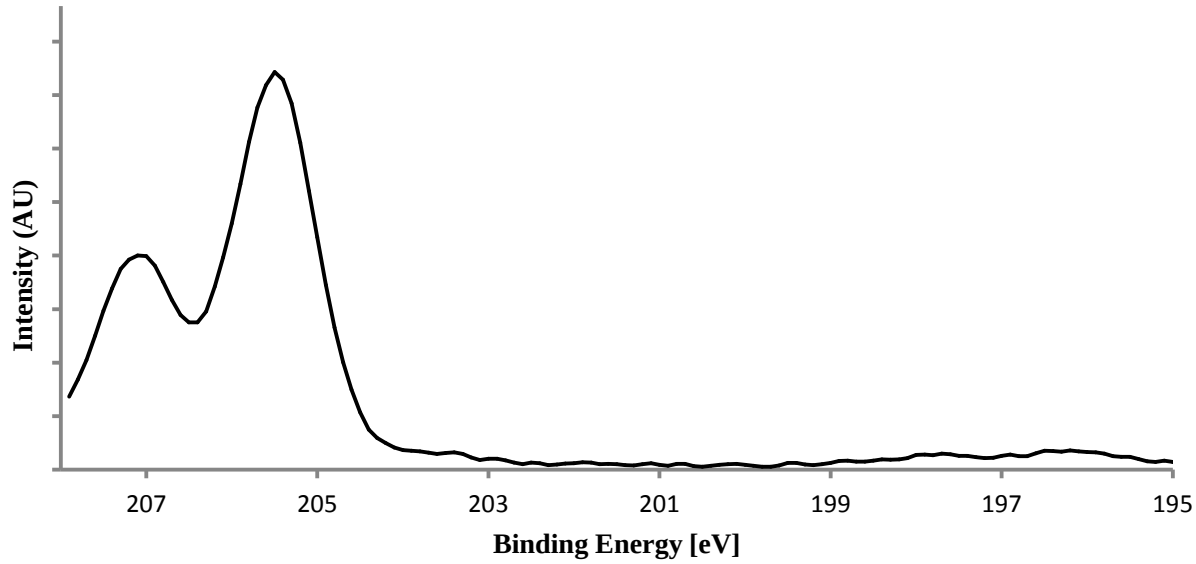

Figure 2.5: High resolution XPS scan of the Cl 2p region of $[Fe_2(\mu_{1,1}\text{-bipyNO})_3(bipyNO)_2(MeOH)_4](ClO_4)_4 \cdot 2MeOH$ (Complex4)

2.3.4 $[Fe(PyzNO)_6](ClO4)_2 \cdot 3etOH$

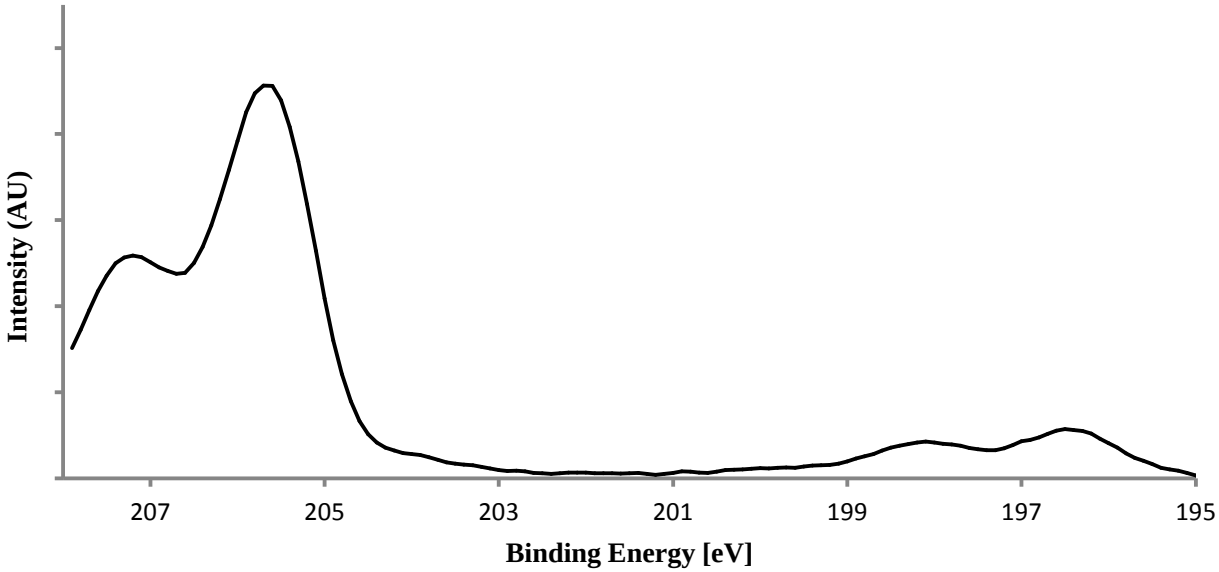

Figure 2.6: High resolution XPS scan of the Cl 2p region of $[Fe(PyzNO)_6](ClO_4)_2 \cdot 3etOH$ (Complex3)

2.4 UV/Vis Spectra in *dry* versus wet DMSO (H_2O:DMSO → 1:99 (v/v)):

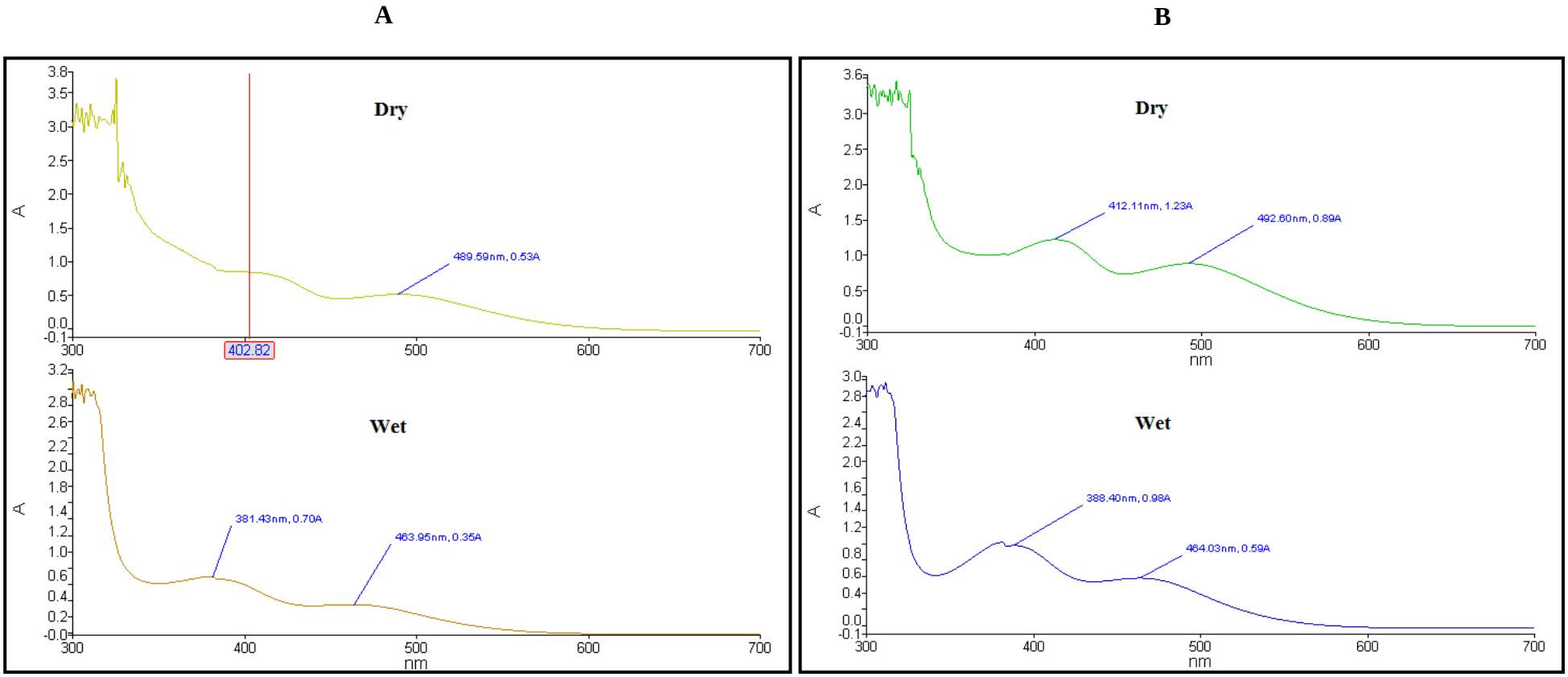

Figure 2.7: UV/Vis spectra (300 - 700 nm) of Complex1 (A), and Complex2 (B) in *dry* DMSO (top) versus wet DMSO (H_2O:DMSO → 1:99 (v/v)) (bottom).

2.5 Solvent studies: Full DSC thermograms (including decomposition):

$[Fe_{2n}(\mu_{1,5}\text{-}pyzNO)_{2n-1}(pyzNO)_{8n+1}](ClO_4)_{4n}$ and $[Fe(pyzNO)_6](ClO4)_2 \cdot 3EtOH$

The Full DSC thermal profiles, including decomposition exotherms, are shown in 2.8 (a) – (c). The decomposition characteristics are discussed in the main text solvent studies section (6.2). Methanol, ethanol and acetaldehyde thermograms were obtained in the 30 – 350 ^{o}C temperature, whilst the formaldehyde trial contains the 30 – 450 ^{o}C range.

The suppression of specific solvent desorption endotherms is noted, and is the result of scaling issues brought about by the very large decomposition exotherm in each case. Rescaling was performed where possible in order to preserve the characteristics of each event in terms of the resulting thermogram. The essential features of the decomposition step, as previously discussed, were however the principal focal point.

Fig. 2.9 (a) shows the false colour FT-IR EGA profile of the original (untreated) Complex2, and Figs. 2.9 (b) – (d) show the complex after exposure to different solvent vapour-saturated environments.

Figs 2.10 (a) – (c) show the full DSC thermal profile of Complex3 after exposure to various solvent vapour-saturated environments.

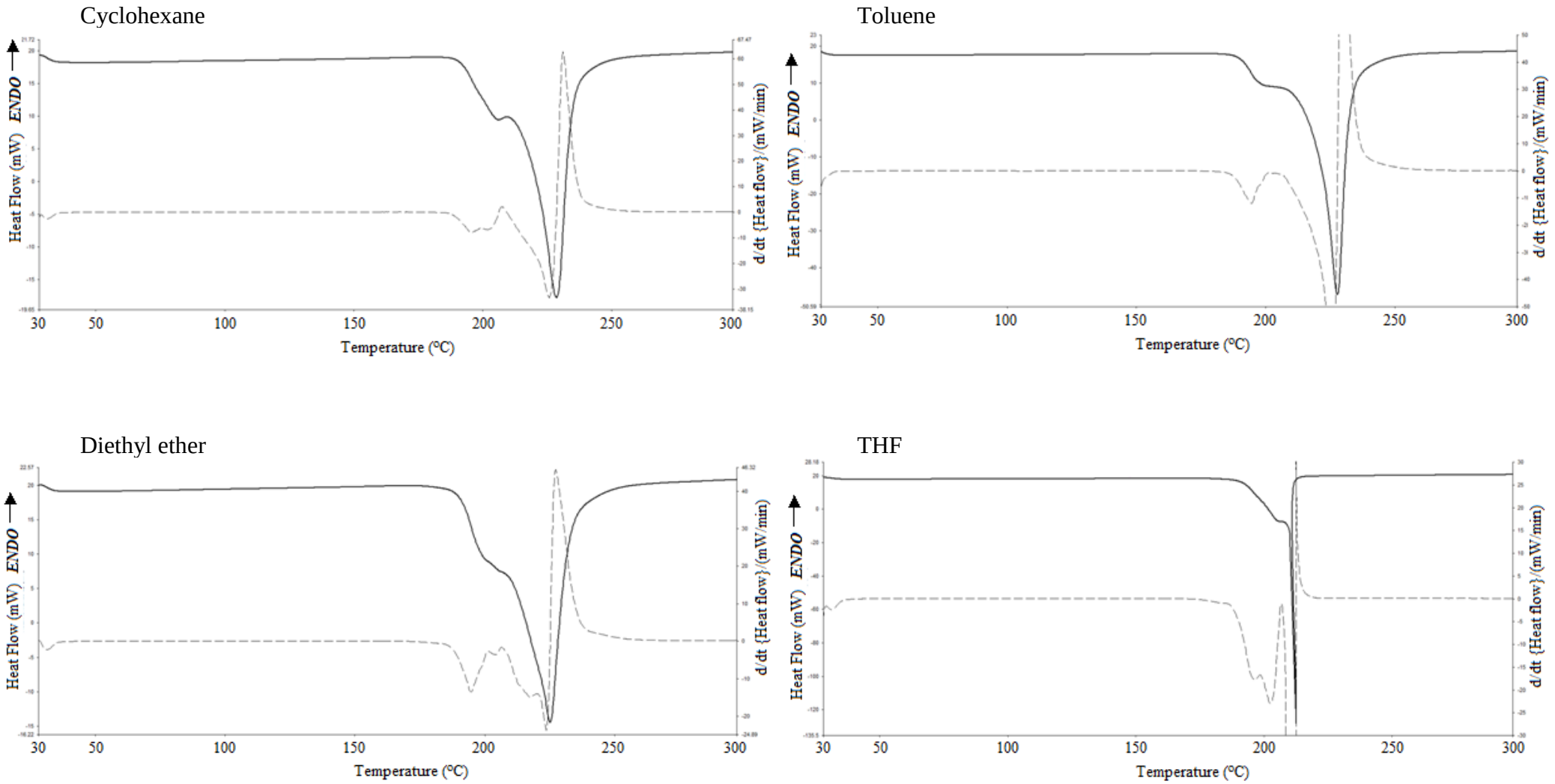

Figure 2.8 a.: Full DSC thermograms of $[Fe_{2n}(\mu_{1,5}\text{-pyzNO})_{2n-1}(pyzNO)_{8n+1}](ClO_4)_{4n}$) (Complex2 in various solvent vapour-saturated environments.

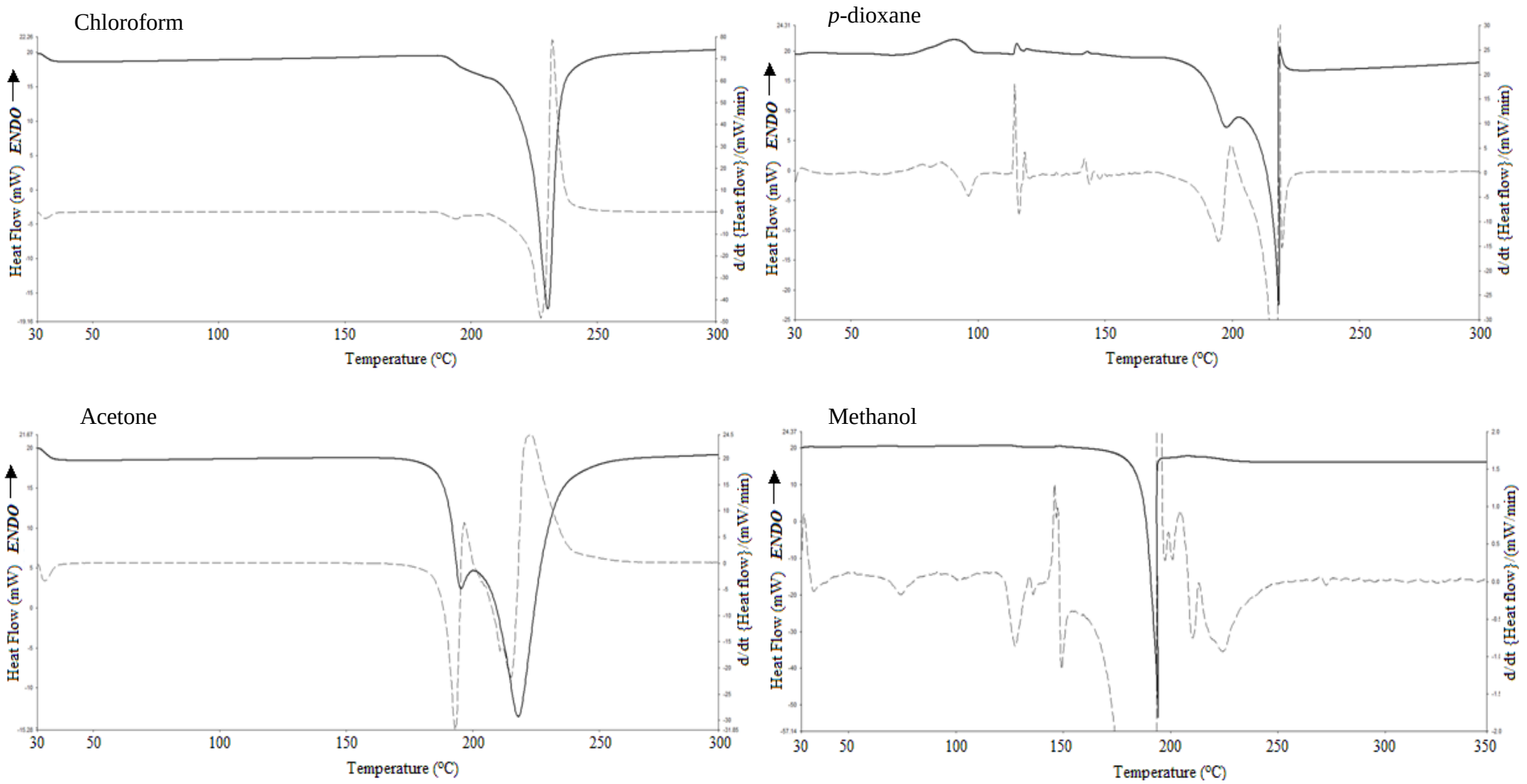

Figure 2.8 b.: Full DSC thermograms of $[Fe_{2n}(\mu_{1,5}\text{-pyzNO})_{2n-1}(pyzNO)_{8n+1}](ClO_4)_{4n}$ (Complex2) in various solvent vapour-saturated environments.

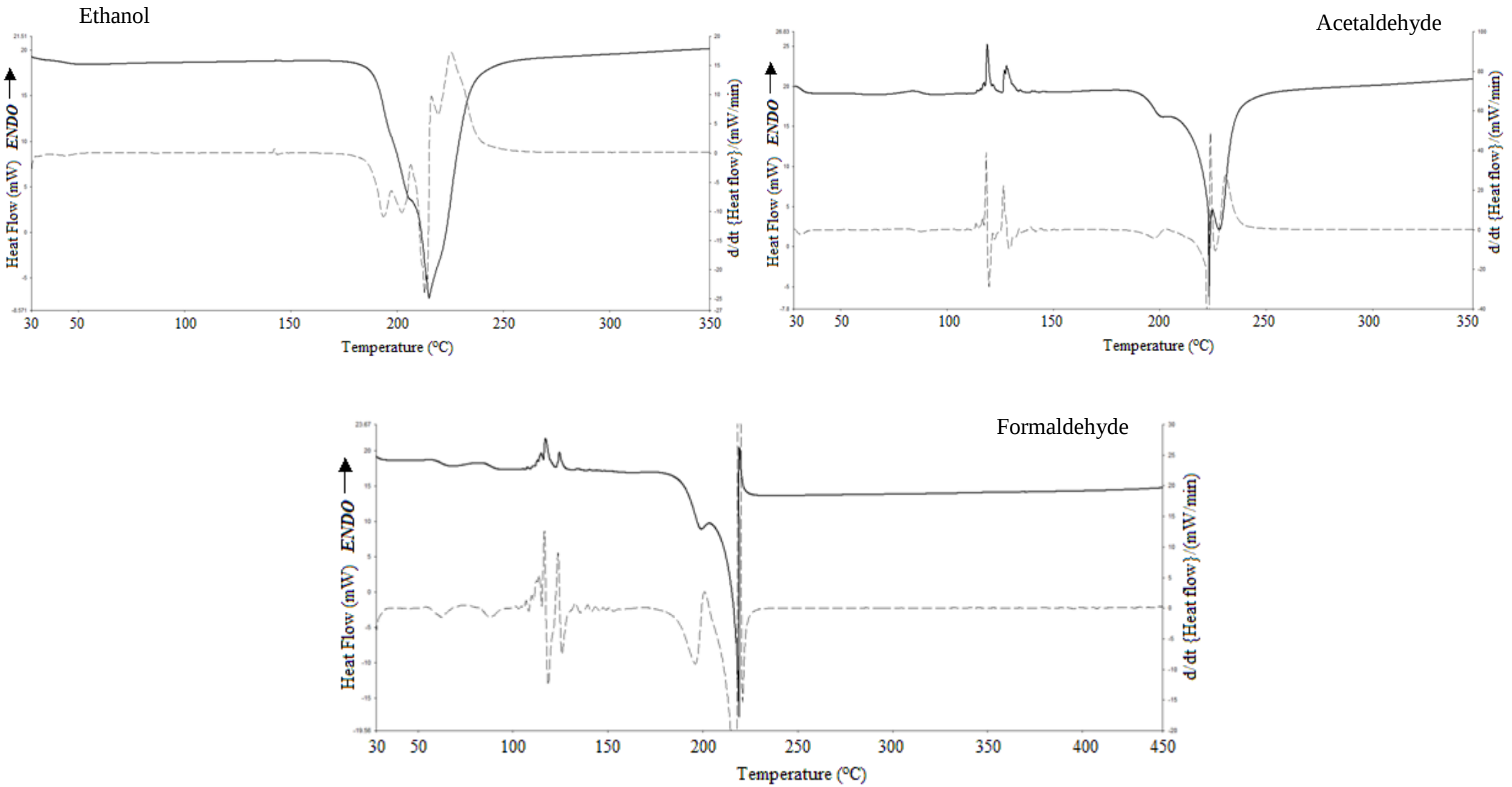

Figure 2.8 c.: Full DSC thermograms of $[Fe_{2n}(\mu_{1,5}\text{-pyzNO})_{2n-1}(pyzNO)_{8n+1}](ClO_4)_{4n}$ (Complex2) in various solvent vapour-saturated environments.

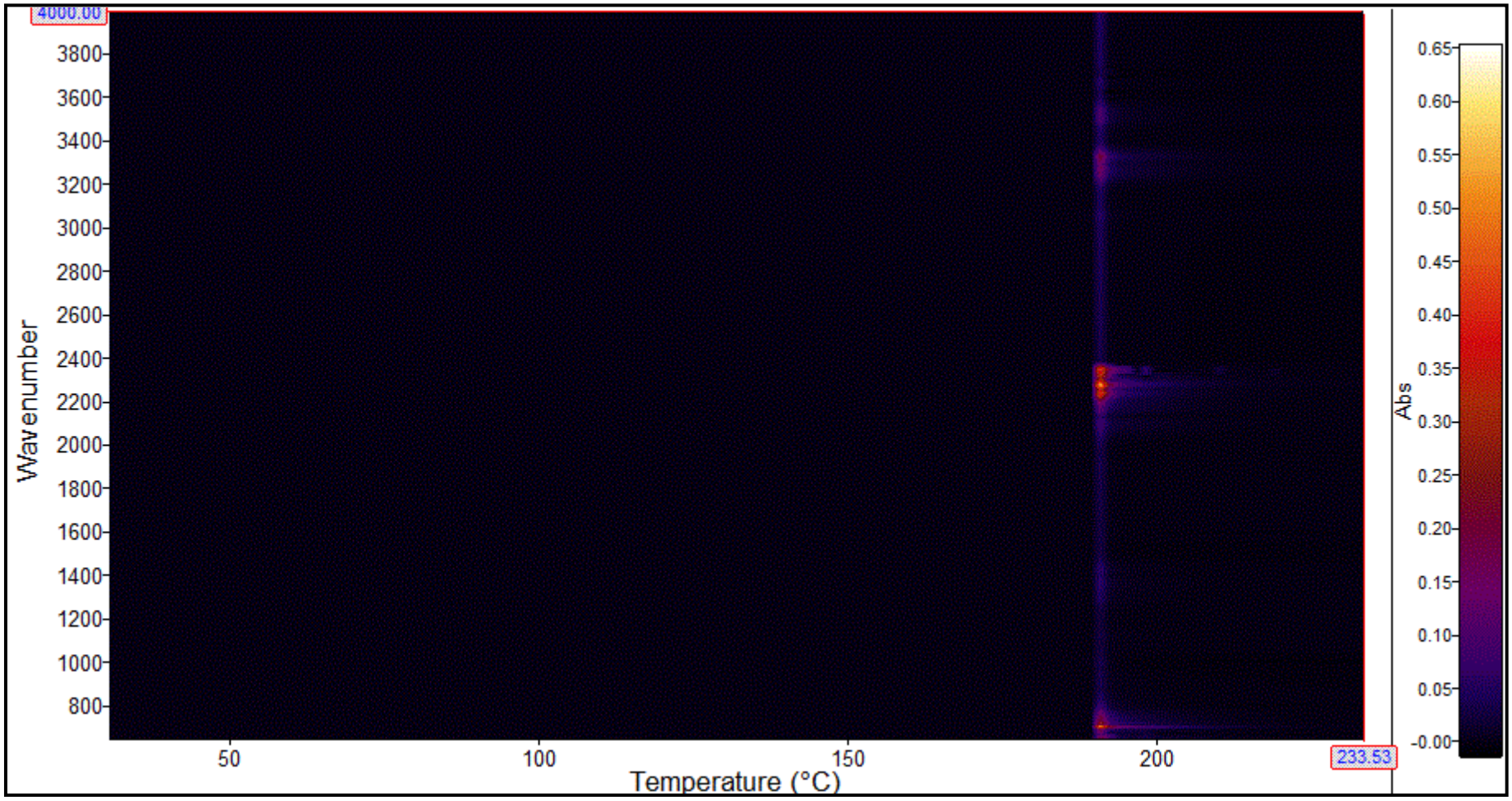

Figure 2.9 a: False colour EGA profile of the original (untreated) $[Fe_{2n}(\mu_{1,5}\text{-pyzNO})_{2n-1}(pyzNO)_{8n+1}](ClO_4)_{4n}$ complex.

Cyclohexane

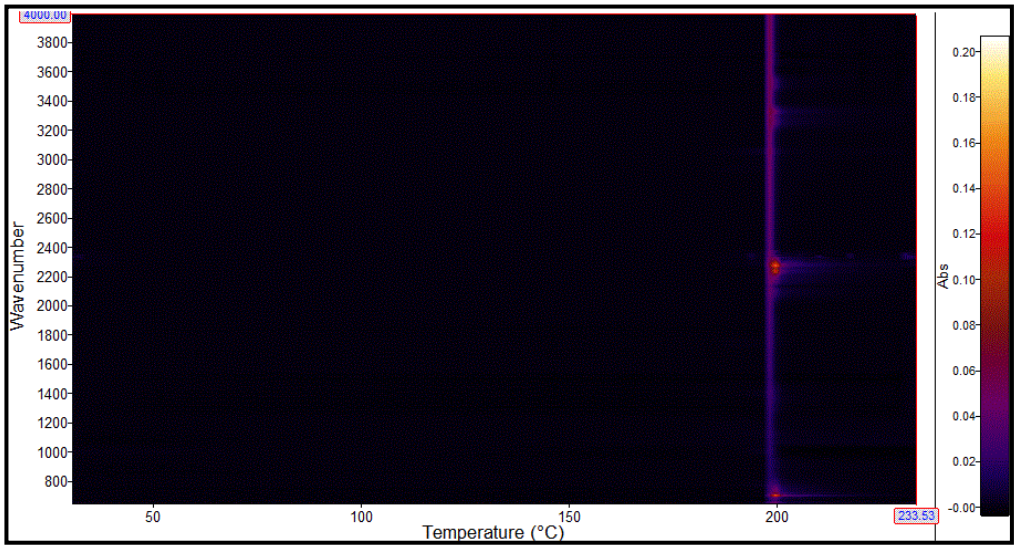

Toluene

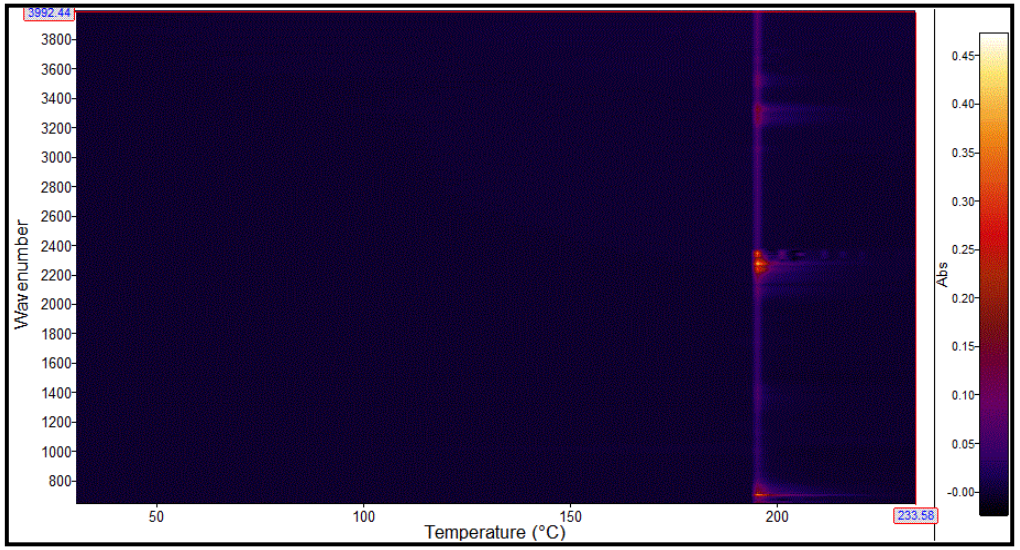

Diethyl ether

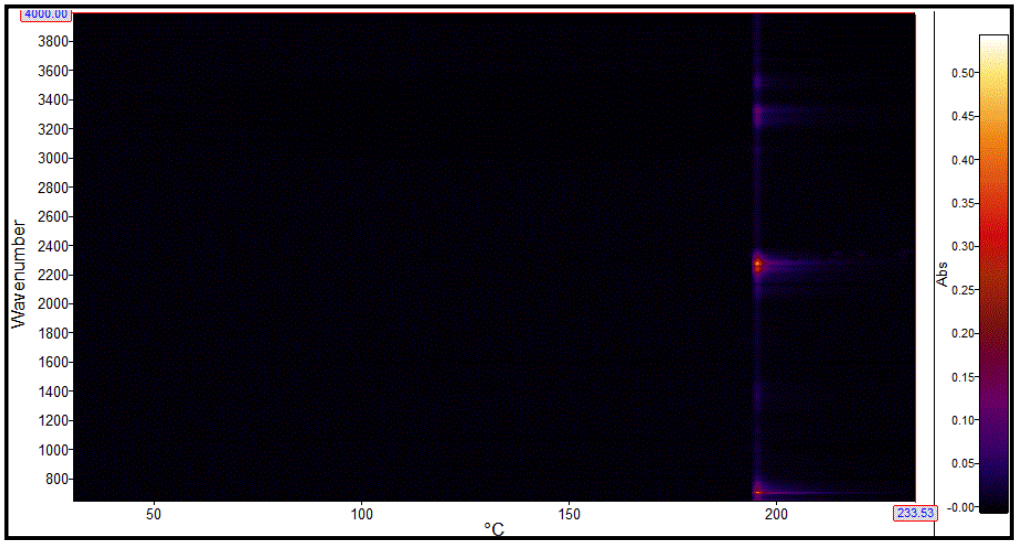

THF

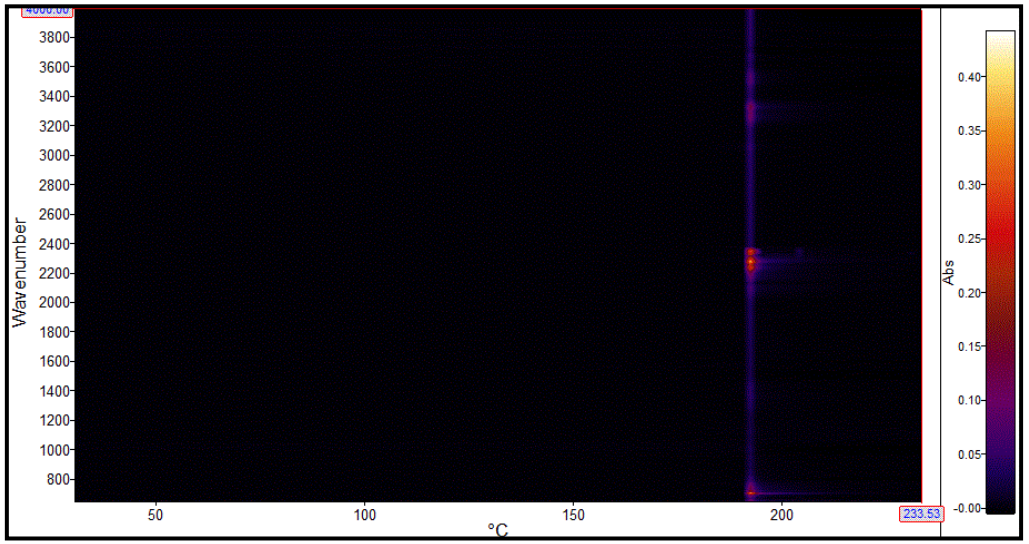

Figure 2.9 b: False colour EGA profile of $[Fe_{2n}(\mu_{1,5}\text{-pyzNO})_{2n-1}(pyzNO)_{8n+1}](ClO_4)_{4n}$ (Complex2) in various solvent vapour-saturated environments.

Chloroform

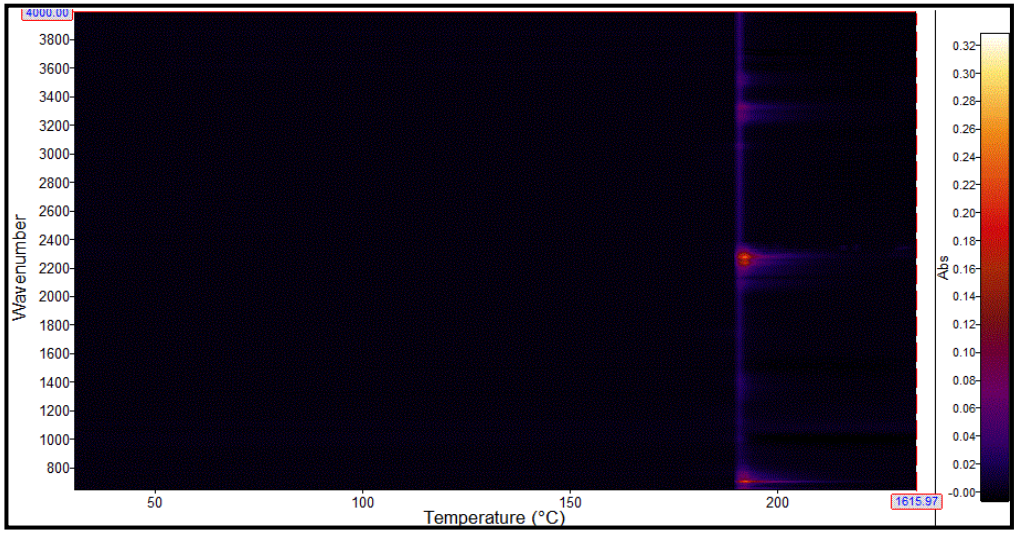

p-dioxane

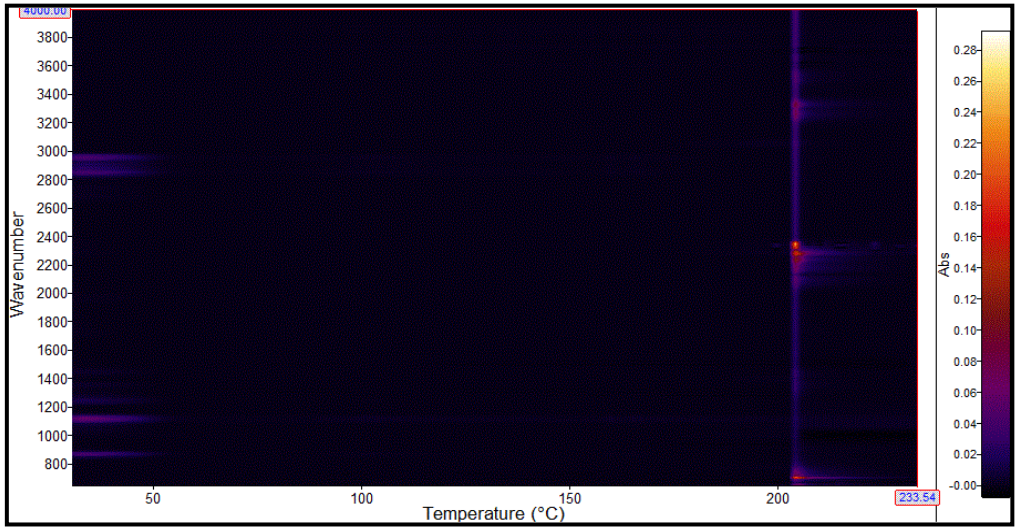

Acetone

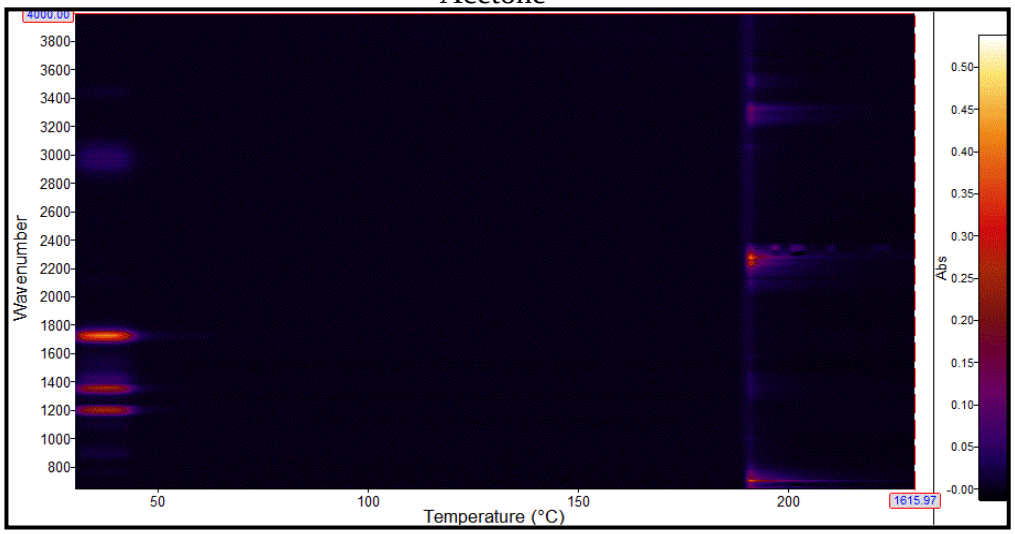

Methanol

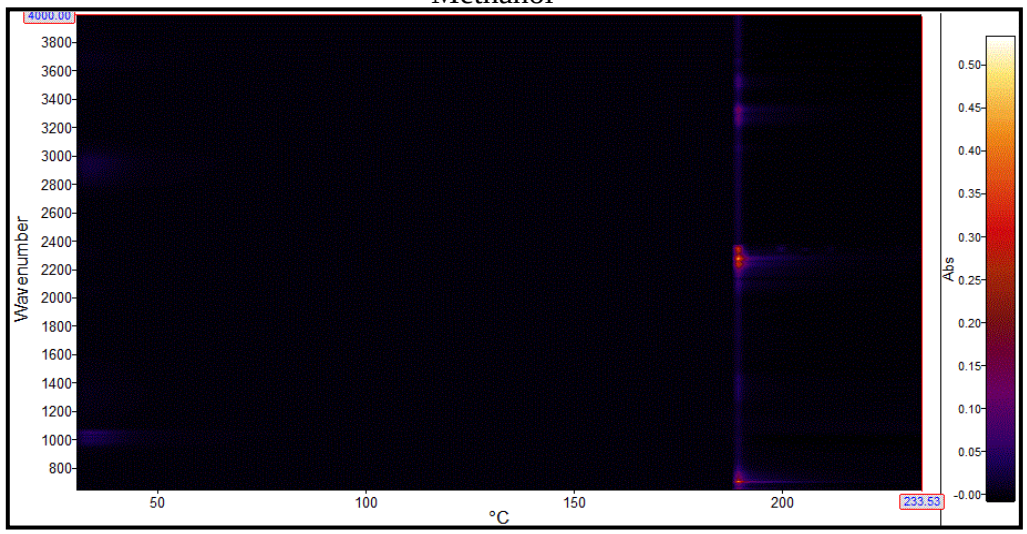

Figure 2.9 c: False colour EGA profile of $[Fe_{2n}(\mu_{1,5}\text{-pyzNO})_{2n-1}(pyzNO)_{8n+1}](ClO_4)_{4n}$ (Complex2) in various solvent vapour-saturated environments.

Ethanol

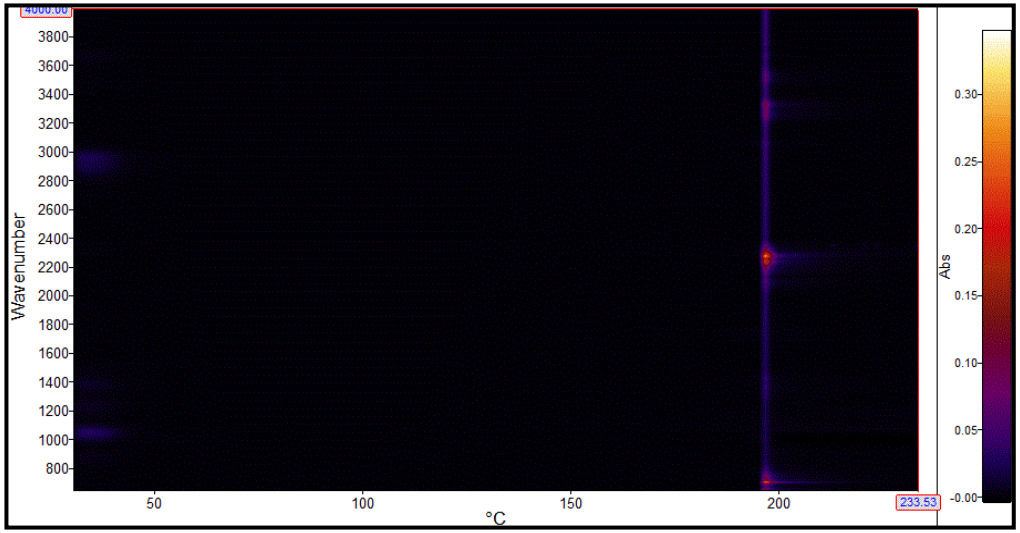

Acetaldehyde

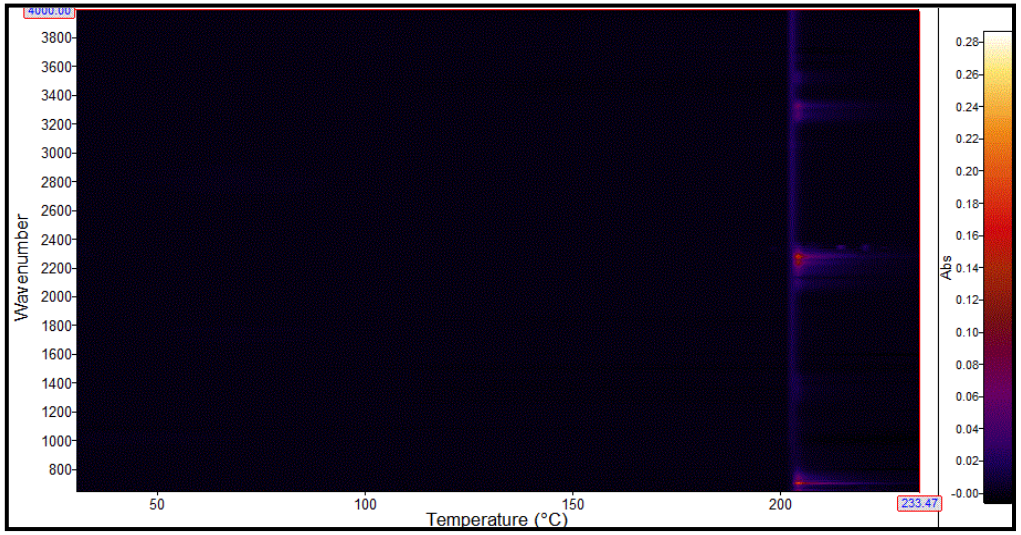

Formaldehyde

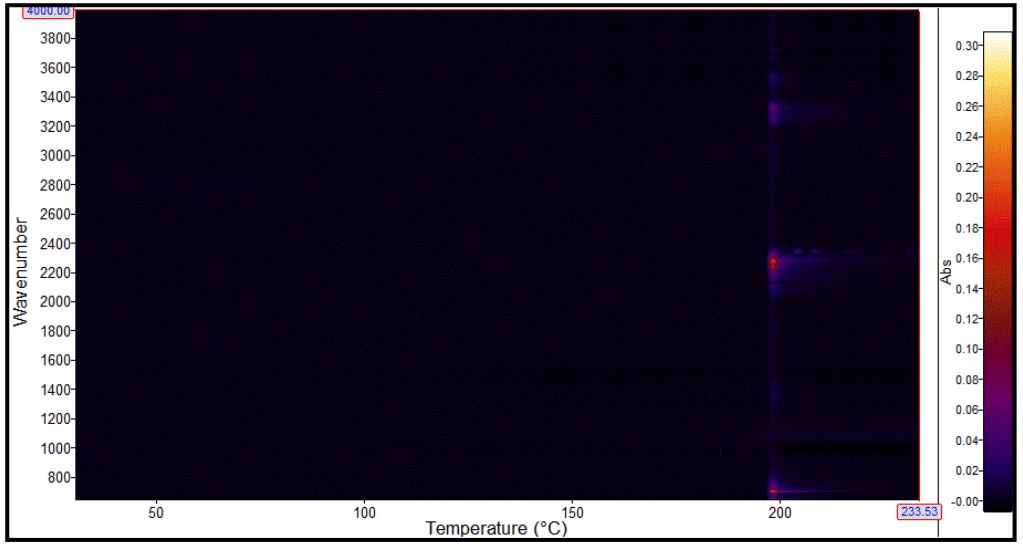

Figure 2.9 d: False colour EGA profile of $[Fe_{2n}(\mu_{1,5}\text{-}pyzNO)_{2n-1}(pyzNO)_{8n+1}](ClO_4)_{4n}$ (Complex2) in various solvent vapour-saturated environments.

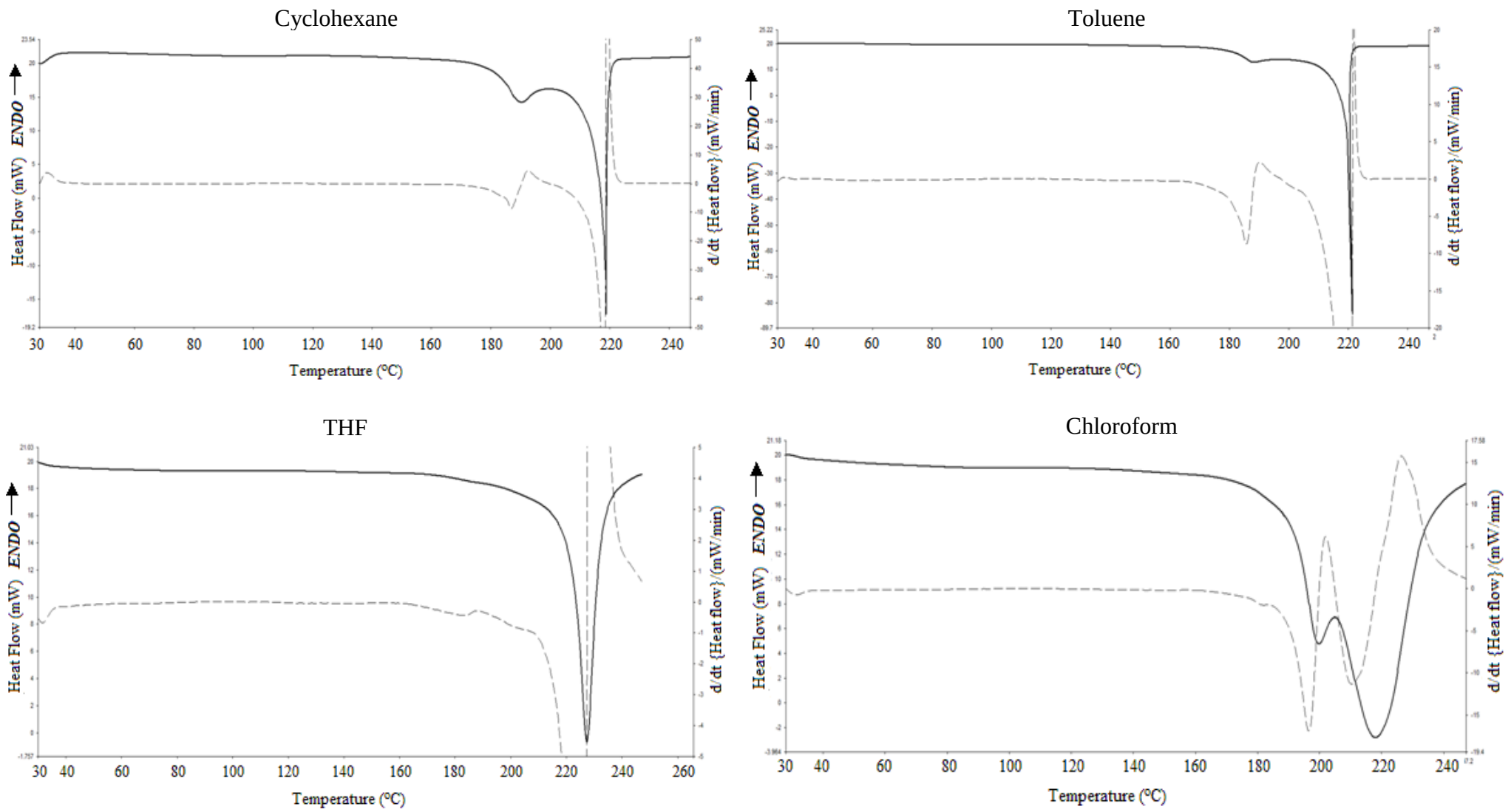

Figure 2.10 a: Full DSC thermograms of $[Fe(pyzNO)_6](ClO_4)_2 \cdot 3EtOH$ (Complex3) in various solvent vapour-saturated environments.

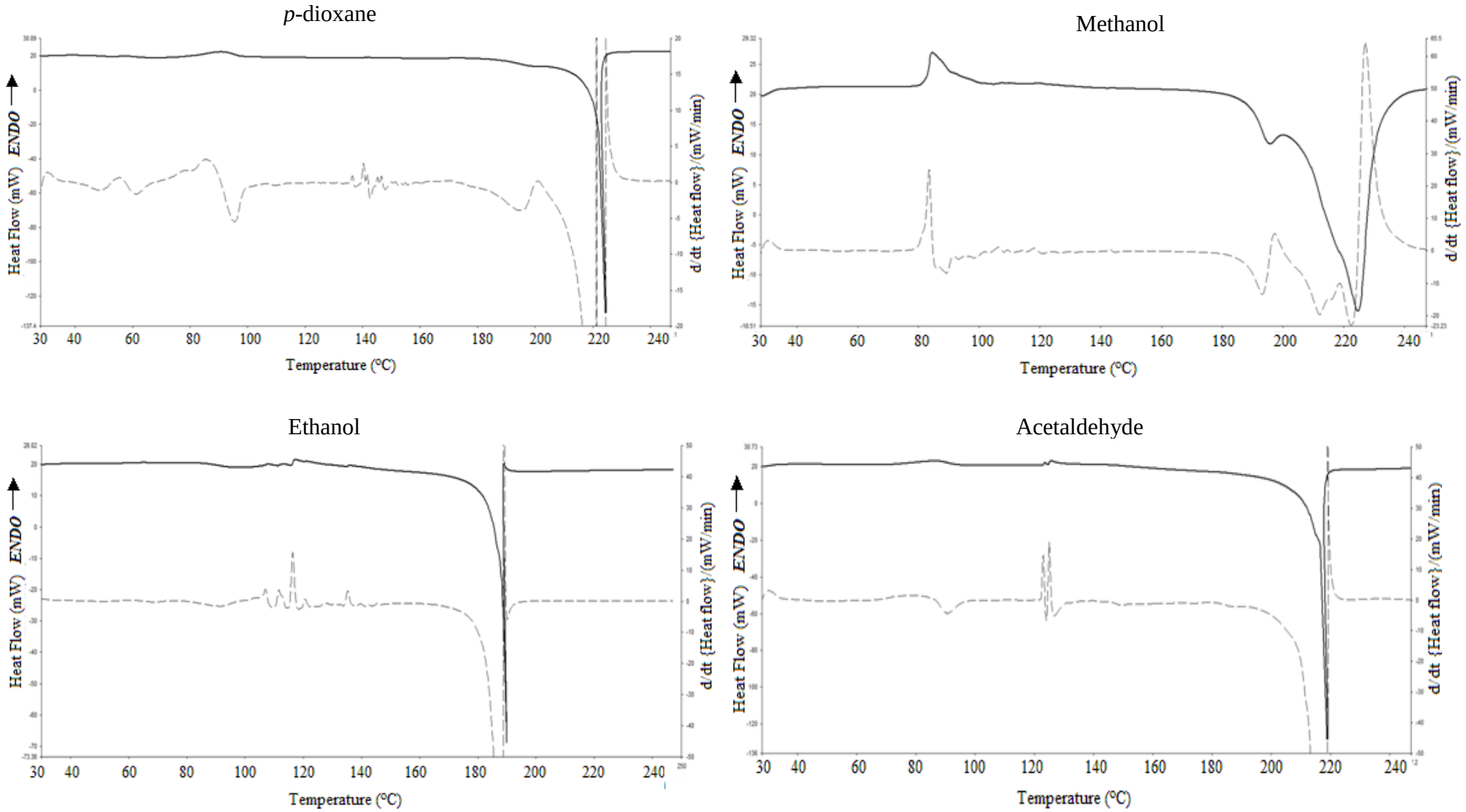

Figure 2.10 b: Full DSC thermograms of $[Fe(pyzNO)_6](ClO_4)_2 \cdot 3EtOH$ (Complex3) in various solvent vapour-saturated environments.

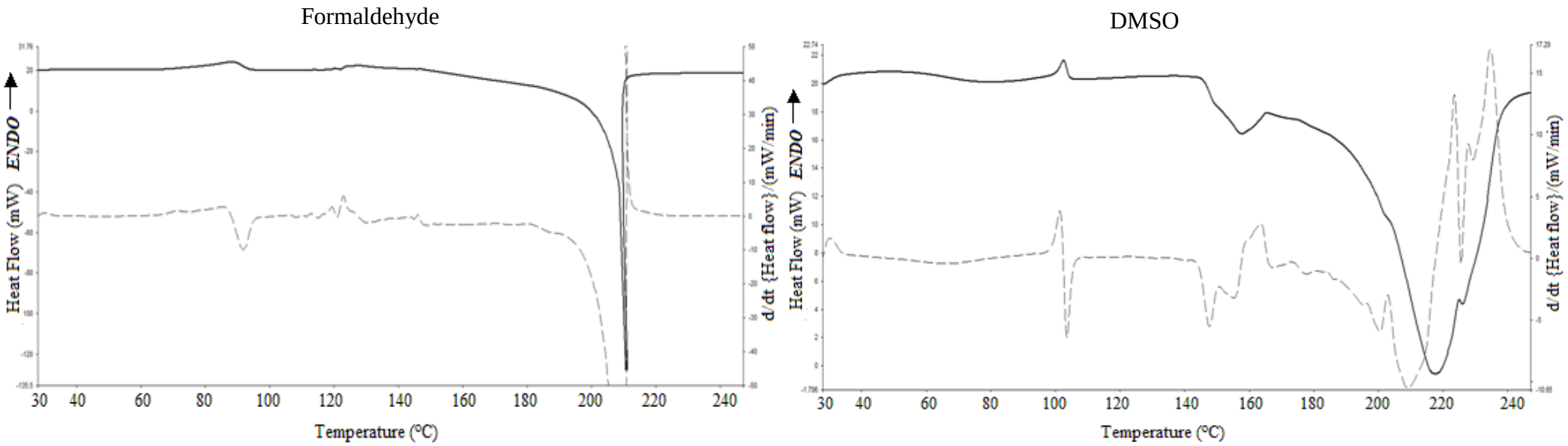

Figure 2.10 c: Full DSC thermograms of $[Fe(pyzNO)_6](ClO_4)_2 \cdot 3EtOH$ (Complex3) in formaldehyde and DMSO vapour-saturated environments.

2.6 Truncated TG thermogram of $[Fe_2(\mu_{1,1}\text{-bipyNO})_3(bipyNO)_2(MeOH)_4](ClO_4)_4 \cdot 2MeOH$

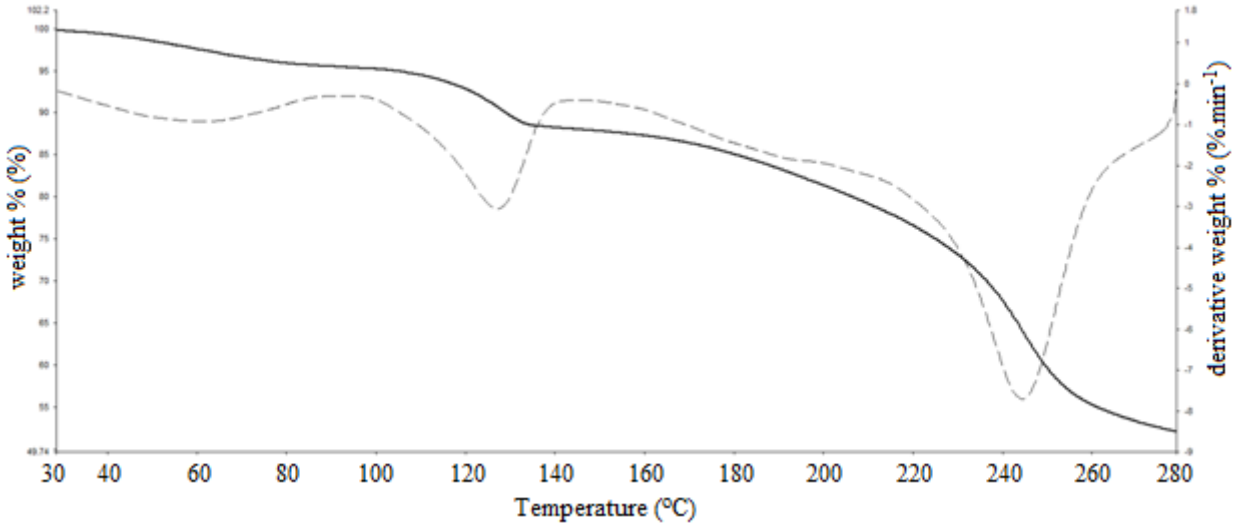

Figure 2.11: DSC thermogram (30 – 280 ^{o}C) of $[Fe_2(\mu_{1,1}\text{-bipyNO})_3(bipyNO)_2(MeOH)_4](ClO_4)_4 \cdot 2MeOH$ (Complex4)

References

[1] **Watkins, G.M**. (1987) *Ligand Isotope Vibrational Studies of Metal (II) Complexes*. Doctoral thesis. Cape Town: University of Cape Town.

[2] **Koelsch, C. F.; Gumprecht, W.H**. Some diazine *N*-oxides. *J. Org. Chem.* **23** (1958), 1603

[3] **Klein, B.; Berkowitz, J**. Pyrazines. I. Pyrazine *N*-oxides. Preparation and spectral characteristics. *J. Amer. Chem.* **81** (1959), 5160-5161

[4] **Popp, C. J.; Garlough, G. D**. Transition metal complexes of diazine *N*-oxides. *J. inorg. nucl. Chem.* **43** (1980), 501